Innovations in Wireless Bioelectronics for Precision Medicine, from Sustainable Sweat Sensing to Ingestible Gut Monitoring

Thesis by

Jihong Min

In Partial Fulfillment of the Requirements for

the Degree of

Doctor of Philosophy

CALIFORNIA INSTITUTE OF TECHNOLOGY

Pasadena, California

2024

(Defended November 13, 2023)

© 2024

Jihong Min
ORCID: 0000-0002-5788-1473

ACKNOWLEDGEMENTS

I would like to extend my deepest gratitude to Professor Wei Gao for offering the chance to conduct exciting research in the realm of wearable and ingestible devices. His invaluable support and guidance, as well as enthusiasm for research have been instrumental in shaping my journey as a researcher.

My appreciation goes to my thesis and candidacy committee members from Caltech: Professor Wei Gao, Professor Azita Emami, Professor Henry Lester, Professor Mikhail Shapiro, and Professor Axel Scherer. Their insightful feedback, encouragement, and collaborative efforts enriched my research experience.

Special thanks to my all lab colleagues, including, but not limited to, Yu Song, Minqiang Wang, Yiran Yang, Hyunah Ahn, Juliane Sempionatto, Jiaobing Tu, Changhao Xu, and Heather Lukas. Their contributions in co-leading research and review paper projects were invaluable.

Outside Caltech, I'm grateful to colleague Stepan Demchyshyn and Professor Martin Kaltenbrunner from Johannes Kepler University Linz. Our fruitful collaboration began when Stepan was a visiting student at Caltech.

On a personal note, heartfelt thanks to my parents, Kyoungil and Shinhae, for their unwavering support throughout my life. To my siblings, Junhong and Juhong, your joy and humor have always been my anchor. My friends from elementary school and university deserve special mention for their companionship and for traveling long distances to spend cherished moments with me.

Lastly, to my friends and labmates at Caltech: our shared experiences, from traveling, golfing, tennis, climbing, weightlifting, basketball, and soccer, have been a source of solace and joy amidst the rigors of research. Your camaraderie made my journey as a graduate student at Caltech all the more memorable.

ABSTRACT

Biofluids, constituting about 60% of the human body, serve as treasure troves of biomarkers such as metabolites and electrolytes, shedding light on individual health conditions. Although blood and urine tests have been routinely utilized, they are limited by their invasive and episodic nature. However, the promise of continuous and noninvasive access to other biofluids like sweat, GI fluids, and saliva paves the way for real-time, onsite health monitoring. This thesis delves into the untapped potential of wearable sensors and noninvasive biofluid analysis, emphasizing the importance of continuous and sustainable monitoring for predictive personal healthcare. Chapter 1 introduces the paradigm of biofluid sensing, focusing on sweat as a key candidate for personalized healthcare applications. Chapter 2 delves into the physiology of sweat glands, highlighting the composition of sweat and the mechanisms behind sweat extraction, either through natural exercise or iontophoretic stimulation. Chapter 3 embarks on the development of innovative sensors designed for detecting clinically pertinent biomarkers in sweat, a step forward in predictive health analytics. In Chapter 4, the spotlight is on system integration, as the study emphasizes the need for miniaturized and reliable wireless sensor devices that ensure minimal discomfort and maximum reliability. Chapters 5 and 6 delve into strategies for sustainably powering wearable devices from energy harvested from body motions and from ambient light, respectively. The final chapter, Chapter 7, extrapolates the aforementioned technologies for the realm of ingestible devices, adapting them for electrochemical sensing in alternate media, primarily gastrointestinal fluids. This allows for enhanced detection of gastrointestinal diseases and a deeper understanding of the intricate gut-brain axis. The ultimate vision of this research is to equip individuals with wearable and ingestible sensors that can seamlessly monitor a broad spectrum of clinically relevant biomarkers. This continuous monitoring, coupled with data analytics, will potentially catalyze a shift from reactive to predictive healthcare, ushering in an era of personalized therapeutic interventions. As wearable sweat and ingestible sensors become mainstream, a confluence of biosensing mechanisms, materials science, and flexible electronics is anticipated enable continuous and unobtrusive

acquisition of clinically relevant biomarkers over prolonged periods and large populations, further refining the nexus between health monitoring and precision medicine.

PUBLISHED CONTENT AND CONTRIBUTIONS

1. Min, J.; Tu, J.; Xu, C.; Lukas, H.; Shin, S.; Yang, Y.; Solomon, S. A.; Mukasa, D.; Gao, W. Skin-Interfaced Wearable Sweat Sensors for Precision Medicine. *Chemical Reviews* **2023**, 123 (8), 5049–5138. https://doi.org/10.1021/acs.chemrev.2c00823.

J.M., J.T., C.X., and H.L. contributed equally to this work. All authors prepared the figures and prepared the manuscript.

2. Wang, M.; Yang, Y.; Min, J.; Song, Y.; Tu, J.; Mukasa, D.; Ye, C.; Xu, C.; Heflin, N.; McCune, J. S.; Hsiai, T. K.; Li, Z.; Gao, W. A Wearable Electrochemical Biosensor for the Monitoring of Metabolites and Nutrients. *Nature Biomedical Engineering* **2022**. https://doi.org/10.1038/s41551-022-00916-z.

W.G., M.W., Y.Y., and J.M. initiated the concept and designed the studies; W.G. supervised the work; M.W., Y.Y., and J.M. led the experiments and collected the overall data; Y.S., J.T., D.M., C.Y., and C.X. contributed to sensor characterization, validation and sample analysis; N.H. contributed to the signal processing and app development. J.S.M., T.K.H., and Z.L. contributed to the design of the human studies. W.G., M.W., Y.Y., and J.M. co-wrote the paper. All authors contributed to the data analysis and provided feedback on the manuscript.

3. Min, J.; Demchyshyn, S.; Sempionatto, J. R.; Song, Y.; Hailegnaw, B.; Xu, C.; Yang, Y.; Solomon, S.; Putz, C.; Lehner, L. E.; Schwarz, J. F.; Schwarzinger, C.; Scharber, M. C.; Shirzaei Sani, E.; Kaltenbrunner, M.; Gao, W. An Autonomous Wearable Biosensor Powered by a Perovskite Solar Cell. *Nature Electronics* **2023**, *6* (8), 630–641. https://doi.org/10.1038/s41928-023-00996-y.

W.G., J.M., M.K., and S.D. initiated the concept and designed the studies. J.M. and S.D. led the experiments and collected the overall data. J.R.S., Y.S., B.H., C.X., Y.Y., and S.S. contributed to the wearable device characterization, validation and sample analysis. B.H., C.P., L.L., M.S., and S.S. contributed to the solar module development, fabrication and characterization. S.D., B.H., J.F.S., and C.S. contributed to the experimental design and characterization of Pb leakage test for the solar cell module. E.S.S. contributed to the cell viability and metabolic activity characterization. J.M., S.D., W.G., and M.K. co-wrote the paper. All authors contributed to the data analysis and provided feedback on the manuscript.

4. Tu, J.; Min, J.; Song, Y.; Xu, C.; Li, J.; Moore, J.; Hanson, J.; Hu, E.; Parimon, T.; Wang, T.-Y.; Davoodi, E.; Chou, T.-F.; Chen, P.; Hsu, J. J.; Rossiter, H. B.; Gao, W. A Wireless Patch for the Monitoring of C-Reactive Protein in Sweat. *Nature Biomedical Engineering* **2023**, *7* (10), 1293–1306. https://doi.org/10.1038/s41551-023-01059-5.

W.G. and J.T. initiated the concept and designed the overall studies. W.G. supervised the work. J.T., J. M., and Y.S. led the experiments and collected the overall data. C.X., J.L., T.-Y.W., E.D., and T.-F.C. contributed to sensor characterization and validation. J. Moore, J.H., E.H., T.P., P.C., J.J.H., and H.B.R. contributed to the design of the human trials and to the system's evaluation in the participants. All authors contributed to data analysis and provided feedback on the paper.

5. Ye, C.; Wang, M.; Min, J.; Tay, R. Y.; Lukas, H.; Sempionatto, J. R.; Li, J.; Xu, C.; Gao, W. A Wearable Aptamer Nanobiosensor for Non-Invasive Female Hormone Monitoring. *Nature Nanotechnology* **2023**. https://doi.org/10.1038/s41565-023-01513-0.

W.G. and C.Y. initiated the concept and designed the overall studies. W.G. supervised the work. C.Y. and M.W. led the experiments and collected the overall data. J.M., R.Y.T., H.L., J.R.S., and C.X. contributed to sensor characterization and validation. J.L. contributed to the numerical simulation. All authors contributed the data analysis and provided feedback on the manuscript.

6. Song, Y.; Min, J.; Yu, Y.; Wang, H.; Yang, Y.; Zhang, H.; Gao, W. Wireless Battery-Free Wearable Sweat Sensor Powered by Human Motion. *Science Advances* **2020**, *6* (40), eaay9842. https://doi.org/10.1126/sciadv.aay9842.

W.G., Y.S., and H.Z. initiated the project. W.G. supervised the studies. Y.S. and J.M. led the experiments and collected the overall data. J.M., Y.S., and Y.Yu contributed to the system development, fabrication, and characterization. J.M. performed the electronic circuit design and test. Y.S. and H.W. contributed to FTENG preparation and characterization. Y.S. and Y.Yu contributed to sensor preparation and characterization. W.G., Y.S., J.M., and Y.Yang contributed to data analysis and cowrote the paper. All authors provided feedback on the manuscript.

7. Yu, Y.; Nassar, J.; Xu, C.; Min, J.; Yang, Y.; Dai, A.; Doshi, R.; Huang, A.; Song, Y.; Gehlhar, R.; Ames, A. D.; Gao, W. Biofuel-Powered Soft Electronic Skin with Multiplexed and Wireless Sensing for Human-Machine Interfaces. *Science Robotics.* **2020**, *5* (41), eaaz7946. https://doi.org/10.1126/scirobotics.aaz7946.

W.G. and Y.Y. conceived the project. W.G. supervised the studies and Y.Y. led the experiments. J.N., C.X., and Y.Y. contributed to the system development, fabrication, and characterization; J.M., A.D., and R.D. contributed to the electronic circuit design and test. A.H. and Y.S. contributed to sensor preparation and characterization. R.G. and A.D.A. contributed to the prosthesis control study. Y. Yu, Y. Yang, and W.G. contributed the data analysis and co-wrote the paper. All authors provided feedback on the manuscript.

8. Min, J.; Gao, W. Battery-Free Wearable Electrochemical Sweat Sensors. In *2023 IEEE International Flexible Electronics Technology Conference (IFETC)*; IEEE: San Jose, USA, CA, USA, **2023**; pp 1–5. https://doi.org/10.1109/IFETC57334.2023.10254891.

J.M. and W.G. prepared the manuscript and the figures.

TABLE OF CONTENTS

Acknowledgements iii
Abstract iv
Published Content and Contributions vi
Table of Contents viii
List of Illustrations and/or Tables x
Abbreviations 13
Chapter 1. Introduction 17
1.1 Biosensors for Health Monitoring and Disease Diagnostics 18
1.2 Electrochemical Biofluid Sensing for Precision Medicine 20
1.3 Challenges and Objectives 21
Chapter 2. Sweat Secretion Dynamics and Continuous Sweat Extraction 25
2.1 Sweat Gland Structure 27
2.2 Sweat Secretion Mechanisms 30
2.3 Sweat Induction Methods 32
2.4 Sweat Extraction Methods 34
Chapter 3. Novel Electrochemical Approaches for Sweat Sensing 42
3.1 Molecularly Imprinted Polymer Sensors for Nutrient Monitoring 45
3.2 Immunosensor for Detection of C-reactive Protein in Sweat 67
3.3 Aptasensor for Non-invasive Female Hormone Monitoring 74
Chapter 4. System Level Integration and Powering of Wearables 86
4.1 Analog Interface 88
4.2 Signal Processing and Wireless Communications 90
4.3 Power Management 91
Chapter 5. Harvesting Energy from Body Motions 93
5.1 Background 94
5.2 Results 97
5.3 Discussion 109
5.4 Methods 110
5.5 Supporting Information 113
5.6 Harvesting Energy from Human Sweat 126
Chapter 6. Harvesting Energy from Ambient Light 130
6.1 Background 131
6.2 Results 135
6.3 Discussion 147
6.4 Methods 148
6.5 Supporting Information 157
Chapter 7. Ingestible Sensors for Exploring the Gut 206
7.1 Background 207
7.2 Sensor Array for Multiplexed Monitoring of GI Biomarkers 210
7.3 System Level Integration of Bioelectronic System 213
7.4 Future Work and Outlook 215

Bibiliography 218

LIST OF ILLUSTRATIONS AND/OR TABLES

Figure number *Page*

1-1. Wireless biofluid sensor network for continuous and noninvasive health monitoring. 19
1-2. Challenges in wearable sweat sensors for personalized healthcare. 23
2-1. Structure of the skin, including apocrine and eccrine sweat glands. 26
2-2. The secretory coil and sweat duct of the eccrine sweat gland. 29
2-3. Sweat stimulation pathways. 30
2-4. Iontophoresis-based sweat induction. 33
2-5. Flexible laser-engraved iontophoresis patch for on demand sweat extraction. 37
2-6. On-body evaluation of the wearable device's light-powered iontophoresis and sweat processing system at rest. 39
3-1. Biomimetic wearable biosensor for detection of circulating nutrients in sweat. 46
3-2. Schematic of the preparation procedure and detection mechanism of the LEG-MIP AA sensors. 48
3-3. Direct detection of electroactive molecules using LEG-MIP sensors. 49
3-4. Selectivity studies of the LEG-MIP sensors for detecting two electroactive amino acids: Trp and Tyr. 49
3-5. Evaluation of the effect of incubation time and sample volume on the LEG-MIP sensor performance. 50
3-6 Indirect molecular detection using LEG-RAR-MIP sensors. 51
3-7. LSV voltammograms of the LEG-PB-MIP sensors for indirect detection of all nine essential amino acids. 52
3-8. LSV voltammograms of the LEG-PB-MIP sensors for indirect detection of multiple vitamins, metabolites, and lipids. 53
3-9. LSV voltammograms and the corresponding calibration curves of the LEG-PB-MIP sensor for indirect detection of chemotherapy drugs (three cancer drugs: cyclophosphamide, busulfan, and mycophenolic acid) and hormones (i.e., cortisol). 54
3-10. Wearable system evaluation across activities toward prolonged physiological and nutritional monitoring. 55
3-11. Continuous on-body Trp and Tyr analysis with real-time sensor calibrations using a wearable sensor array on three subjects during a constant-load cycling exercise. 56
3-12. Automated voltammogram analysis. 57
3-13. Dynamic monitoring of central fatigue using the Trp/BCAA sensor array patches. 58
3-14. Iontophoresis-based continuous on-body Trp and Tyr analysis using a wearable sensor array with and without supplement intake (Subject 2). 59
3-15. Iontophoresis-based continuous on-body Trp and Tyr analysis using a wearable sensor array with and without supplement intake (Subject 3). 60
3-16. Iontophoresis-based continuous on-body Trp and Tyr analysis using a wearable sensor array with and without supplement intake (Subject 4). 61

3-17. Tyr and Trp levels in continuous on-body Trp and Tyr sensing using wearable sensor arrays with and without supplement intake. 62
3-18. Sweat rate and the concentrations of amino acids (Trp here) and Na^+ on human subjects. 63
3-19. Wearable electrochemical nanobiosensor for automatic, non-invasive, and wireless inflammation monitoring. 69
3-20. The integrated wireless wearable electronics for CRP sensing. 70
3-21. On-body evaluation of the multiplexed wearable patch toward non-invasive automatic inflammation monitoring. 72
3-22. On-body evaluation of the wearable sensor on a healthy subject and a post-covid subject. 73
3-23. Influence of solution pH in peak potential and current of the redox molecule thionine. 73
3-24. Influence of the pH, ionic strength, and temperature on the CRP sensor reading. 74
3-25: A wearable nanobiosensor based on strand-displacement aptamer switch for non-invasive reagentless female reproductive hormone analysis. 75
3-26. Schematic of the reagentless electrochemical aptamer sensor based on competitive redox probe displacement and recapture. 76
3-27. Performance of the reagentless electrochemical aptamer sensor. 77
3-28. Incubation and regeneration of reagentless electrochemical aptamer sensor. 78
3-29. Electric field enhanced rapid estradiol analysis. 79
3-30. Rapid estradiol analysis with the assistance of an external electric field. 80
3-31. Sensor regeneration in artificial sweat. 80
3-32. Schematic about the in vitro sensor regeneration process. 81
3-33. Evaluation of the wearable sensor for non-invasive female hormone monitoring in human participants. 83
3-34. On-body wearable multiplexed physicochemical sensing and estradiol quantification in three male human subjects. 84
4-1. Electronic system block diagram of wearable sweat sensors. 87
5-1. Battery-free FWS^3 for wireless and noninvasive molecular monitoring. 96
5-2. Characterization of the FTENG for energy harvesting from human motion. 100
5-3. Characterization of the microfluidic-based biosensor patch in vitro. 102
5-4. System-level integration and evaluation of the FWS^3. 104
5-5. On-body evaluation of the FWS^3 for wireless, dynamic perspiration analysis. 108
5-6. Flexible nanoengineered BFC array for efficient energy harvesting. 127
5-7. Perspiration-powered soft electronic skin (PPES) for multiplexed wireless sensing. 127
5-8. System-level integration and evaluation of the PPES. 128
5-9. On-body evaluation of the PPES toward personalized metabolic monitoring. 129
6-1. Schematics and images of the ambient light-powered battery-free lab on the skin. 134
6-2. Design and characterization of the flexible perovskite solar cell. 137
6-3. System design and characterization of the wearable device for energy harvesting and autonomous multimodal biosensing. 140
6-4. On-body evaluation of the wearable device for prolonged and cross-activity perspiration analysis. 146

7-1. PillTrek, an ingestible electrochemical platform for continuous, multiplexed gastrointestinal fluid analysis.....209
7-2. Ingestible sensor array for multiplexed detection of gastrointestinal biomarkers.....211
7-3. Compact ingestible electronic system for prolonged wireless operation in GI tract.. 213

ABBREVIATIONS

AA	amino acid
AC	alternating current
ADC	analog to digital converter
AFE	analog frontend
APBA	aminophenylboronic acid
AQCA	anthraquinone-2-carboxylic acid
AQCA	redox-active nanoreporters
BCAA	branched-chain amino acid
BFC	biofuel cell
BLE	Bluetooth low energy
CA	control amplifier
CNS	central nervous system
COVID-19	corona virus 2019
CV	cyclic voltammetry
CVD	cardiovascular disease
DAC	digital to analog converter
DC	direct current
DPV	differential pulse voltammetry
FCC	Federal Communications Commission

FPCB	flexible printed circuit board
FPSC	flexible perovskite solar cell
FTENG	freestanding-mode triboelectric nanogenerator
GI	gastrointestinal
GPIO	general-purpose input/output
IBD	inflammatory bowel disease
IBS	irritable bowel syndrome
Ile	isoleucine
InAmp	instrumentation amplifier
Leu	leucine
MIP	molecularly imprinted polymer
NFC	near field communication
OCPT	open circuit potentiometry
PB	prussian blue
PCB	printed circuit board
PCBM	[6,6]−phenyl-C61-butyric acid methyl-ester
PENG	piezoelectric nanogenerator
PET	polyethylene terephthalate
Phe	phenylanaline
PMIC	power management integrated circuit

PTFE	polytetrafluoroethylene
SC	solar cell
SIF	simulated intestinal fluid
SoC	system-on-chip
SPI	serial peripheral interface
SWV	square wave voltammetry
TENG	triboelectric nanogenerator
TIA	transimpedance amplifier
Trp	tryptophan
Tyr	tyrosine
UART	universal asynchronous receiver-transmitter

Chapter 1

INTRODUCTION

Materials from this chapter appear in "Min, J.; Tu, J.; Xu, C.; Lukas, H.; Shin, S.; Yang, Y.; Solomon, S. A.; Mukasa, D.; Gao, W. Skin-Interfaced Wearable Sweat Sensors for Precision Medicine. *Chemical Reviews* **2023**, 123 (8), 5049–5138. https://doi.org/10.1021/acs.chemrev.2c00823."

The quest for health and wellness is a journey that mankind has embarked upon ages ago. In recent times, this journey has seen the confluence of technology and biology in unprecedented ways. The advent of biosensors and their applications in health monitoring and disease diagnostics epitomizes this confluence. This chapter delves into the development of biosensors, their potential in reshaping precision medicine, and the challenges we face in making these devices mainstream.

1.1 Biosensors for Health Monitoring and Disease Diagnostics

From their inception as rudimentary step-counters, wearable biosensors have undergone a transformative journey. Today, they are among the foremost tools for personal health monitoring. This rapid development has largely been fueled by societal shifts, such as increasing urbanization, and a growing global emphasis on preventive health measures.

The earlier versions of wearable devices were limited in their scope. Devices like pedometers simply counted steps, giving users a basic idea of their activity levels. Over time, as the demand for detailed health metrics grew, the technology underpinning these devices advanced dramatically. Modern wearables now incorporate sophisticated sensors that can monitor a myriad of biometrics. Today, these devices not only capture heart rate, blood oxygen levels, and sleep cycles but are also being developed to analyze biochemical signals, promising even more detailed insights into an individual's health.

Importantly, traditional gold-standard health screening in biofluids like blood and urine have always posed challenges in continuous and non-invasive monitoring. In contrast, fluids such as sweat, GI contents, and saliva offer a more accessible avenue for persistent health surveillance. Their non-invasive nature paves the way for innovative sensing devices like wearable mouthguard sensors for saliva, ingestible capsule sensors for GI fluids, and wearable devices for sweat (**Fig. 1-1**). This shift in fluid preference is a paradigm change, setting the stage for more efficient and patient-friendly diagnostics.

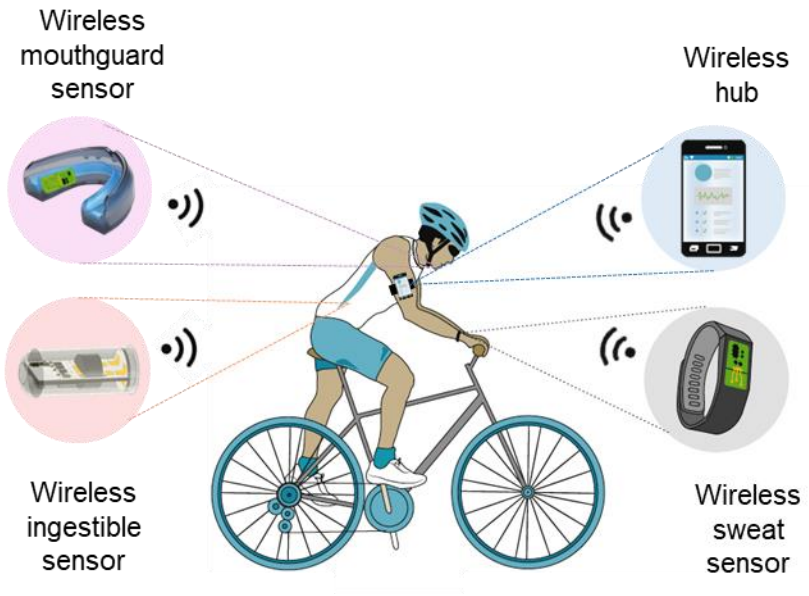

Figure 1-1. Wireless biofluid sensor network for continuous and noninvasive health monitoring.

One avenue of significant promise in wearable tech is sweat analysis. While often overlooked, sweat contains a wealth of biomolecular data. By analyzing sweat, it is possible to derive valuable information about a person's electrolyte balance, hydration status, and even certain metabolic markers. As the field progresses, researchers are working to enhance wearable devices to continuously monitor and analyze these molecular indicators, offering real-time insights into one's health.

Parallel to the advancements in wearables, the realm of ingestible biosensors has seen remarkable progress. The human gastrointestinal (GI) tract is an intricate system with numerous biochemical processes occurring simultaneously. Traditional diagnostic tools for the GI tract, such as endoscopes, offer limited insights, being invasive and restricted in their reach.

Enter ingestible biosensors. These tiny devices, often shaped like pills, are engineered with advanced cameras, a myriad of sensors, and transmitters. They travel through the GI tract, collecting data and potentially detecting diseases or imbalances at their earliest stages. Their

unique ability to access and transmit information from hard-to-reach areas, like the small intestine, marks a significant leap in diagnostic capabilities. The aspiration for these sensors is not just real-time imaging, though that in itself is groundbreaking. The vision extends to molecular diagnostics within the GI environment. Given that the tract is flush with body fluids and gases rich in biomarkers, it presents an unparalleled opportunity for in-depth health analysis.

As we move forward, both wearable and ingestible biosensors stand as pivotal tools in revolutionizing health diagnostics. They promise early detection, precise diagnosis, and a chance for interventions tailored to individual needs. In the forthcoming sections, we will delve deeper into the intricate mechanisms of in situ electrochemical biofluid sensing, discussing its implications for precision medicine, and unpacking the associated challenges and research objectives.

1.2 Electrochemical Biofluid Sensing for Precision Medicine

The human body is a rich reservoir of biofluids, each teeming with a wealth of molecular information. From blood and urine to sweat and tears, these fluids are more than mere byproducts of physiological processes; they are invaluable data sources, offering profound insights into an individual's health. Over the years, as our understanding of these biofluids has deepened, so has the realization of their potential as diagnostic tools.

At the crux of this diagnostic revolution is electrochemical sensing. This technique involves detecting changes in an electric current or voltage in response to chemical reactions. When applied to biofluid analysis, electrochemical sensors offer the possibility of real-time, continuous monitoring of various biochemical markers. The beauty of this approach lies in its ability to non-invasively assess a plethora of indicators, from glucose and lactate levels to hormone imbalances and trace metabolites.

One remarkable advantage of electrochemical sensing is its adaptability. The sensors can be fine-tuned to detect specific analytes, allowing for a broad spectrum of applications. They

can be incorporated into wearable devices to continuously monitor sweat or even crafted into ingestible tools for a deep dive into GI biochemistry.

The real allure of electrochemical biofluid sensing, however, is not just in its diagnostic capabilities but also in its potential to usher in an era of precision medicine. In an age where technology often outpaces its practical application, this technique offers tangible hope. As these sensors continue to refine their detection accuracy, they will generate vast datasets. When these datasets are combined with advanced analytics and machine learning, it becomes possible to predict disease onset, tailor medical interventions to individual biochemical profiles, and even preemptively address potential health issues.

Of course, like any evolving technology, electrochemical biofluid sensing is not without its challenges. There are hurdles related to ensuring consistent biofluid sampling, developing reliable sensors apt for detecting a wide array of biomarkers of interest, and engineering compact electronic systems for signal processing and data communication that can be sustainably powered. Yet, as research progresses, solutions to these challenges are emerging, propelling us towards a future where personal health monitoring and interventions are not just possible but are tailored to the unique biochemistry of each individual.

1.3 Challenges and Objectives

Wearable sweat sensors have emerged as a potent solution in the realm of continuous health monitoring. Advances in sensor technologies, materials sciences, and electronics lead to the advent of the first fully integrated multiplexed wearable sweat sensor in 2016, and since then, numerous wearable sweat sensing systems have been developed.[1] These devices typically utilize integrated electrochemical sensor arrays, converting sweat analyte concentrations into discernible electrical signals. With the aid of intricate electronic circuitry, they can adeptly process and transmit pivotal health data in real-time. However, their path to universal adoption is laden with challenges.

The continuity and reliability of sweat sensor data are fundamental for achieving continuous health monitoring. Effective sweat sampling is the first step toward achieving continuous and accurate biomarker analysis. Early sweat sampling methods for analyzing biomarkers in sweat were often confounded by discrepancies due to skin contamination, sweat evaporation, sweat stimulation methods, and sweat rate effects. In addition, sweat stimulation was primarily achieved physically through exercise or thermal stress, leading to large variations in sweat rate and limiting sweat collection to very specific scenarios. Chemical sweat stimulation methods, as well as efficient sweat collection materials and microfluidic designs can minimize fouling of sweat samples and extend the use of sweat sensors to sedentary and everyday scenarios. Ultimately, highly precise, specific, and stable sweat sensors for detecting a wide range of biomarkers need to be developed or improved upon. These sensors should also be supported by calibration sensors that simultaneously analyze variables that can potentially influence sensor readings or sweat content, such as skin temperature, sweat electrolyte balance, and sweat rate. On the power front, the dual demands of data transmission and complex electrochemical instrumentation contribute to substantial energy consumption that often require rigid and bulky lithium batteries. Lastly, the extensive continuous data gathered by sweat sensors can be processed using big-data and cloud computing techniques. This analysis provides a deeper understanding of biomarker levels, ultimately leading to personalized healthcare solutions (**Fig 1-2**).

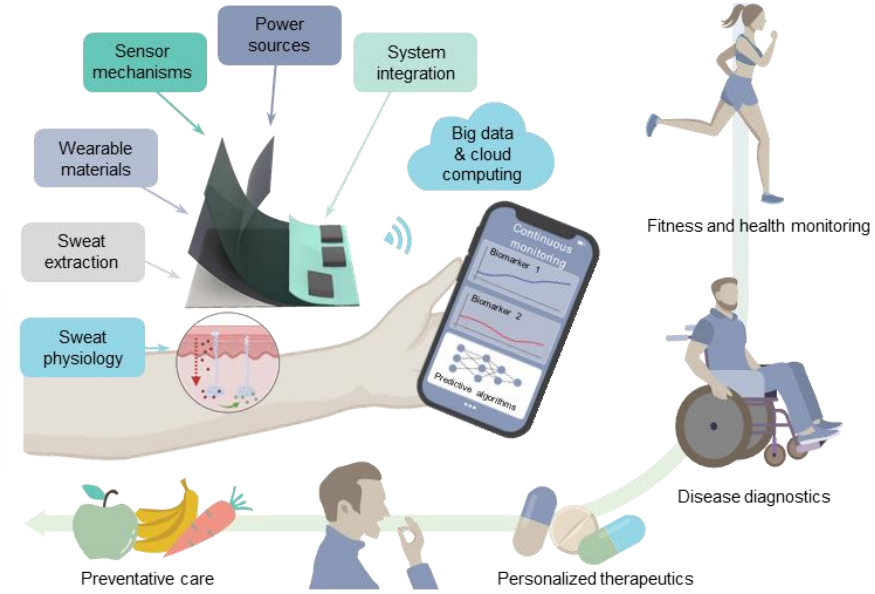

Figure 1-2. Challenges in wearable sweat sensors for personalized healthcare.

In parallel, ingestible devices designed for intestinal fluid analysis have shown promising potential. Their primary objective is the molecular examination of intestinal fluids within the GI tract—a region rich in diverse biochemical markers. However, their deployment is fraught with challenges. First is the issue of miniaturized system design: how to encapsulate intricate technological components within the confined space of a digestible capsule. This includes not just the primary sensor, but also power sources, transmission systems, and data storage solutions. The unique environment of the GI tract brings forth the need for novel biosensor design. Traditional sensors may not suffice due to the distinct conditions within the tract. Consequently, the development of specialized sensors that maintain high sensitivity and specificity in this environment is essential. Protection of these biosensors is another significant concern. The GI tract, by nature, has varying pH levels, enzymes, and other substances that can adversely affect sensor materials and electronics. Ensuring longevity and effectiveness in such a milieu necessitates innovative protection strategies for these biosensors, shielding them from potential degradation or interference.

Combining the advancements of wearable and ingestible sensor technologies, the future of personalized, continuous health monitoring is on the horizon. Yet, as these domains expand, the scientific community must concurrently address inherent challenges to realize the full potential of these revolutionary tools. The subsequent sections delve into the origins of these challenges and detail the development of innovative prototype wearable and ingestible devices to surmount these barriers. Chapter 2 offers an in-depth exploration of the physiology of sweat glands. It meticulously dissects the composition of sweat and delves into the mechanisms underlying sweat extraction—whether it is evoked through natural exercise or facilitated via iontophoretic stimulation. Chapter 3 shifts focus to the cutting-edge domain of sensor technology. Here, we chart the development of innovative sensors, meticulously tailored for the detection of clinically relevant biomarkers in sweat. This signifies a monumental stride towards the realm of predictive health analytics. Chapter 4 illuminates the paramount importance of system integration. The narrative emphasizes the impending necessity for the advent of miniaturized, wireless sensor devices. Powering these devices sustainably through energy harvesters is not just a technical ambition but a cornerstone for the next generation of wearables. Such devices are envisioned to redefine the wearable landscape, minimizing user discomfort while optimizing reliability. Finally, Chapter 5 takes the technologies and principles elaborated in the previous chapters and recontextualizes them for the universe of ingestible devices. The focus here is on the adaptation of these technologies for electrochemical sensing in different environments, with a primary emphasis on GI fluid.

Chapter 2

SWEAT SECRETION DYNAMICS AND CONTINUOUS SWEAT EXTRACTION

Materials from this chapter appear in "Min, J.; Tu, J.; Xu, C.; Lukas, H.; Shin, S.; Yang, Y.; Solomon, S. A.; Mukasa, D.; Gao, W. Skin-Interfaced Wearable Sweat Sensors for Precision Medicine. *Chemical Reviews* **2023**, 123 (8), 5049–5138. https://doi.org/10.1021/acs.chemrev.2c00823.", "Wang, M.; Yang, Y.; Min, J.; Song, Y.; Tu, J.; Mukasa, D.; Ye, C.; Xu, C.; Heflin, N.; McCune, J. S.; Hsiai, T. K.; Li, Z.; Gao, W. A Wearable Electrochemical Biosensor for the Monitoring of Metabolites and Nutrients. *Nature Biomedical Engineering* **2022**. https://doi.org/10.1038/s41551-022-00916-z.", and " Min, J.; Demchyshyn, S.; Sempionatto, J. R.; Song, Y.; Hailegnaw, B.; Xu, C.; Yang, Y.; Solomon, S.; Putz, C.; Lehner, L. E.; Schwarz, J. F.; Schwarzinger, C.; Scharber, M. C.; Shirzaei Sani, E.; Kaltenbrunner, M.; Gao, W. An Autonomous Wearable Biosensor Powered by a Perovskite Solar Cell. *Nature Electronics* **2023**, *6* (8), 630–641. https://doi.org/10.1038/s41928-023-00996-y."

Sweat is produced from glands located deep within the skin, the body's largest organ by surface area. The skin has a stratified structure including the stratum corneum, epidermis, dermis, and hypodermis. The dermis is the major component of the skin containing blood vessels, nerve endings, and the base of sweat glands, sebaceous glands, and hair follicles (**Fig. 2-1**). The average eccrine sweat gland density is 200/cm^2, but this varies between individuals and across the body with the highest density among the palms and soles (~400/cm^2).[2,3] The total number of eccrine sweat glands is on the order of 1.6–5 million.[2]

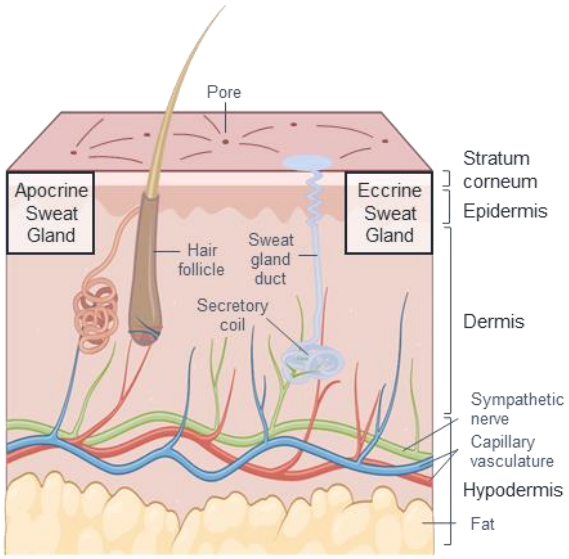

Figure 2-1. Structure of the skin, including apocrine and eccrine sweat glands.

Sweat plays a very important role in maintaining the body's core temperature, providing a means of thermoregulation. Should body core temperatures rise above 40℃ without modulation, there is a risk of protein denaturation, cell death, and subsequent organ failure.[2] Beyond thermal regulation, sweat also participates in skin homeostasis. Moisturizing factors in sweat, such as lactate and urea, maintain the plasticity and barrier integrity of the stratum corneum. Secretion of antimicrobial compounds such as dermcidin, lactoferrin, lysozymes, and immunoglobulin E (IgE) antibodies contributes to the skin's first line of defense against infection.[4] The loss of sweat glands after severe damage as in the case of burn victims

presents new challenges in regenerative wound healing and demands further research into sweat gland physiology.

Eccrine sweat glands secrete a highly filtered, aqueous fluid composed of electrolytes, metabolites, and additional molecules. Apocrine sweat glands secrete a viscous fluid containing lipids, proteins, steroids, and ions, by exocytosis in the apocrine gland coil.[5] Volatile organic compounds from apocrine secretions act as pheromones.[2] Apocrine and eccrine sweat glands are differentially stimulated. The apocrine sweat gland responds strongly to emotional stimuli and sympathomimetic drugs via adrenergic innervation, but does not respond to cholinergic or thermal stimulation like the eccrine sweat gland.[4,6] The apoeccrine sweat gland shares properties of both eccrine and apocrine glands; it may develop during puberty in the axillae region from existing eccrine sweat glands. The gland retains an eccrine-like sweat duct but has an apocrine-like secretory tubule. Apoeccrine sweat ultimately resembles aqueous eccrine sweat and arises from an intermediate type of stimulation.[7]

In this section, the physiology of eccrine sweat is elucidated, tracing its journey from stimulated innervation to eventual secretion. The development and structure of sweat glands are detailed, emphasizing their integral role in thermoregulation and metabolic waste removal. This section further delves into methods of sweat induction, whether through natural stimuli like exercise or through controlled processes such as iontophoretic stimulation. Concluding the section, advances in sweat extraction are explored, highlighting the potential of microfluidic systems in revolutionizing sweat collection and analysis.

2.1 Sweat Gland Structure

The eccrine sweat tubule is a conduit for sweat and electrolyte exchange 4–8 mm in length. At the base, the secretory coil is 500–700 μm in size with a lumen inner diameter of 30–40 μm and a coil outer diameter of 60–120 μm.[2] The secretory coil is interwoven with capillaries for vascular exchange and sudomotor nerve fibers for autonomic modulation.[3,8] The secretory tubule straightens into the dermal duct with an inner diameter of 10–20 μm and

outer diameter of 50–80 μm composed of two to three layers of epithelial cells.[2] The sweat duct is straight from the dermis to the epidermis, and then transitions to a helical structure in the epidermis that terminates in the stratum corneum. The number of turns of the helical duct varies from 4–6 and varies proportionally to the stratum corneum thickness, yet the pitch angle remains constant across sweat glands.[9] The helical structure makes the sweat duct act as a helical antenna resulting in resonance behavior. Sweat duct dimensions, density, distribution, and the dielectric properties of the stratum corneum all determine the resonant frequency and subsequent skin-THz wave interactions. The duct length varies from 150–600 μm and varies proportionally to the stratum corneum thickness.[9] The sweat duct widens into the acrosyringium, a pore on the outer surface. The acrosyringium is composed of epithelial cells with no clear distinction or border to the epidermis. The lumen has a diameter of 20–60 μm and may also contain cornified cells.[2]

Humans are born with almost all their sweat glands, with gland development occurring mostly during the first two trimesters. This is one explanation for higher observed duct densities in children than adults.[9] The sweat gland develops from a group of multipotent $K14^+$ progenitors, descendants of epidermal stem cells. It grows downward as a straight duct, stratifying in the lower half to proliferative $K14^{low}/K18^+$ suprabasal progenitors. The $K14^{low}/K18^+$ suprabasal progenitors develop into luminal cells, while the remaining $K14^+$ progenitors give way to myoepithelial cells.[10] Although sweat glands have limited turnover and proliferation capabilities, there is some promise of regeneration. Stem cells associated with secretory luminal and myoepithelial cells were found to promote epidermis and sweat gland regeneration when amplified and seeded in the wound bed.[11] Additionally, the use of three-dimensional (3D) bioprinting matrices has been studied for sweat gland morphogenesis with tissue-level self-organization.[12]

The secretory coil and duct define the two major steps of sweat generation: isotonic secretion and salt reabsorption (**Fig. 2-2**). Ductal cells facilitate transcellular reabsorption with mitochondria-rich basal cells contributing to uptake. The secretory coil is made up of basal myoepithelial cells and luminal clear and dark cells, named for their appearance in eosin,

toluidine blue, and methylene blue stains.[2] Myoepithelial cells strengthen the structure of the secretory coil and create a microenvironment for gland stem cell differentiation.[13] Clear cells contain many mitochondria suggesting that they facilitate most of the active sweat secretion and osmotic flow.[2] Dark cells are granular, containing many vesicles. Dark cells are more involved in the secretion of proteins, including periodic acid-Schiff (PAS)-positive diastase-resistant glycoproteins, dermicidin, and sialomucin.[13] The interdependent relationship between clear and dark cells requires further investigation.

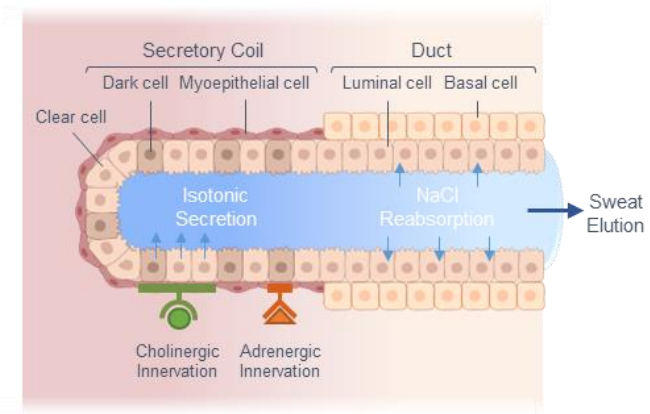

Figure 2-2. The secretory coil and sweat duct of the eccrine sweat gland. Isotonic secretion and reabsorption occur, respectively, at the secretory coil and sweat duct to produce a hypotonic aqueous fluid.

Sweat secretion is stimulated by adrenergic and cholinergic innervation (**Fig. 2-3**). The sudomotor response involves several adenosine triphosphate (ATP)-dependent steps, and is suppressed by ouabain and metabolic inhibitors.[3] When the secretory cell is stimulated, a signaling cascade occurs involving Ca^{2+} or cyclic adenosine monophosphate (cAMP) as second messengers to trigger the efflux of Cl^- into the lumen of the secretory coil. Na^+ is pumped out at the basolateral membrane and diffuses down its electrochemical gradient into the lumen. The buildup of electrolytes in the lumen renders it hypertonic with respect to the cytosol; this osmotic gradient drives the primary sweat solution out of the cell and into the secretory lumen. Advective mass transport drives fluid up the eccrine sweat duct. Along the sweat duct, luminal cells reabsorb ions to produce a hypotonic sweat solution.

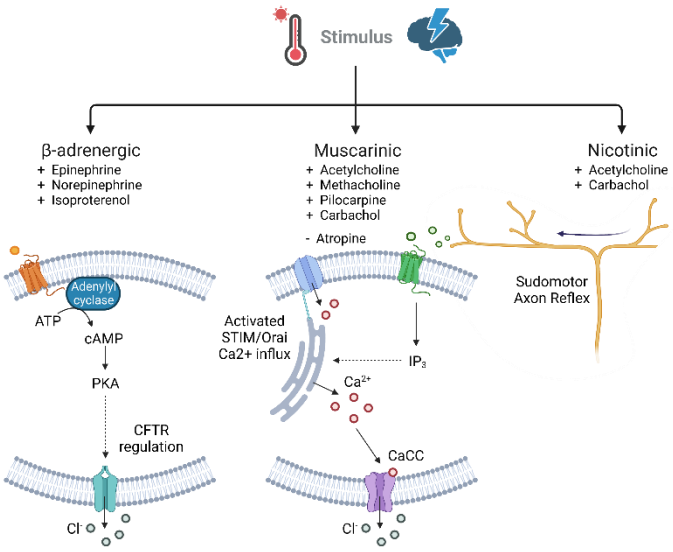

Figure 2-3. Sweat stimulation pathways. Sweat is stimulated primarily through β-adrenergic and muscarinic innervation. β-adrenergic and muscarinic signaling pathways use cAMP and Ca2+ as second messengers, respectively, to activate chloride channels. Activation of nicotinic receptors may amplify the sweating response beyond the localized region via the sudomotor axon reflex.

2.2 Sweat Secretion Mechanisms

Thermoregulatory sweating is an autonomic response to signals from thermoreceptors in the preoptic-anterior hypothalamus area. Upon an increase in core temperature, thermoreceptors send through efferent pathways to postganglionic sympathetic neurons in the dermis.[3] Cholinergic nerve fibers around the secretory coil release acetylcholine, thus activating muscarinic receptors on the membrane of the eccrine secretory cell. Activation of muscarinic G-protein-coupled receptors (GPCRs) increases intracellular inositol trisphosphate (IP_3). IP_3 binds to receptors on the endoplasmic reticulum (ER) membrane to release Ca^{2+} into the cytosol.[14] Stromal interaction molecule protein, stromal interaction molecule 1 (STIM1), monitors the ER Ca^{2+} levels, and when Ca^{2+} stores are depleted STIM1 induces store-operated Ca^{2+} entry by binding to and activating Orai, a Ca^{2+} channel on the plasma

membrane.[14] This influx of Ca^{2+} mediates the exchange of electrolytes resulting in sweat secretion.

Sweating is also adrenergically stimulated under the "fight or flight" response. The physical reaction to stress, anxiety, fear, and pain occurs mostly in the palms, soles, and axillary region and may have the selective advantage of increasing palmoplantar friction for fleeing.[2] "Emotional" sweating is controlled by the limbic system and efferent signals are sent to adrenergic nerve fibers in the sweat secretory coil. Release of epinephrine and norepinephrine in signaling stimulates α- and β-adrenoreceptors in sweat secretory cells. A synthetic sympathomimetic drug, isoproterenol, selectively stimulates β-adrenoreceptors and has been used to further differentiate the two pathways. β-adrenergic stimulation is the dominant pathway in emotional sweating. The magnitude of stimulated sweat secretion (measured by secretory rate) is 4:2:1 for cholinergic, β-adrenergic, and α-adrenergic pathways, respectively.[15] α-adrenergic stimulation results in Ca^{2+} influx similar to cholinergic pathways. β-adrenergic GPCRs activate adenylyl cyclase and increase the intracellular concentration of cAMP. cAMP activates protein kinase A (PKA), which in turn mediates Cl^- secretion by opening the cystic fibrosis transmembrane conductance regulator (CFTR).[16,17] In the case of cystic fibrosis, CFTR is defective or absent, resulting in blocked CFTR Cl^- secretion during β-adrenergic stimulation and inhibited Cl^- reabsorption. A "ratiometric" sweat rate test comparing adrenergic and cholinergic sweat rates may be used to assess CFTR functional activity.[18]

Sweat may be generated at the periphery of a stimulated region via the sudomotor axon reflex (**Fig. 2-3**). Nicotinic agonists interact with receptors on postganglionic sudomotor terminals at the base of the sweat gland, causing antidromic axonal conduction towards a branch point followed by orthograde conduction down the branching fibers. Acetylcholine is then released at the nerve terminals and binds to muscarinic receptors on the eccrine sweat gland, resulting in sweat secretion similar to the direct iontophoretic response.[3,19] The spatial extension of this sweating could be millimeters beyond the periphery of the stimulation region.[20] The sudomotor axon reflex may be used to assess autonomic nervous system disorders, such as

diabetic neuropathy.[3,21] The sudomotor axon reflex may also be used to separate drug-induced sweat stimulation and sweat sampling regions to prevent cross-contamination.[19] The sudomotor axon response has a longer latency than the direct cholinergic response by about 5 s, which accounts for axonal conduction and neuroglandular transmission. The sudomotor axon response and direct response produce similar sweat volumes in the presence of nicotinic agonists. In contrast to the direct stimulated sweat response, which continues over an hour after cessation of the stimulus, the sudomotor axon response returns to baseline 3–5 minutes after stimulus cessation.[22]

The sweat rate is modulated in part by non-uniform, localized activation. Under mental stress, sweat production of adjacent sweat glands varied strongly.[23] The cumulative sweating response controlled by the sympathetic nerve is discretized into active and inactive sweat glands.[23] The sweat rate in healthy individuals ranges from 0.2–1 μL/cm^2/min.[24,25] At an average sweat gland density of 200/cm^2, this equals 1–5 nL/gland/min. Sweat rate is affected by local skin temperature.[2] Sweat stimulated pharmacologically may also further increase the sweat rate to approximately 10 nL/gland/min.[26] Sweat rate decay and cessation occur in part due to the subcutaneous elimination of the sweat stimulant (e.g., acetylcholinesterase).[3,27] Interindividual variations in sweat rate are likely due to differences in the function and responsiveness of the sweat gland.[28] Many factors may influence the sweat response including gender, physical fitness, menstrual cycle, and circadian rhythm.[2] Intraindividual regional variations in observed sweat rate may be associated with variations in sweat gland density and distribution.[9,28] For example, the forehead has a high density of sweat glands and has the highest tested sweat rate region during both active and passive thermal sweating.[28,29]

2.3 Sweat Induction Methods

2.3.1 Thermally-Induced, Exercise-Induced, and Natural Sweat

Sweat can be induced in various manners, such as thermal stimulation, exercise, natural secretion, and iontophoresis. For thermal stimulation, subjects are placed in a heating environment (e.g., sauna bathing) to induce a thermal sweating session at a skin temperature

of 40-41 °C, with a full-body sweat production of 0.6-1 kg/h.[30–32] Exercise-induced sweat is prevalent in many studies; however, the sweat rate could fluctuate with respect to different exercises and exercise intensities. Some common exercises include treadmill running and stationary biking, in which the exercise intensity could be controlled and recorded. As thermal and exercise induction could impose constraints on subjects' physical conditions and testing environment, there is an increasing trend in using naturally occurring sweat for downstream sensing.[33–38] The naturally secreted sweat, also called "background sweat," occurs during regular routines and entails relatively low sweat rates around 10 times lower than exercise sweat rate.[36]

2.3.2 Iontophoresis-Induced Sweat

Iontophoresis is a procedure where a small current delivers a cholinergic drug loaded in hydrogel into the skin. Two pieces of hydrogels are attached to the skin; the anode hydrogel contains a cholinergic agent while the cathode hydrogel contains electrolytes to facilitate current flow (**Fig. 2-4**). As the cholinergic agent stimulates the muscarinic 3 (M3) receptors on sweat glands, a direct sweat response is elicited. Depending on nicotinic receptor specificity, the iontophoretic drug may induce peripheral sudomotor axon reflex sweating.[19]

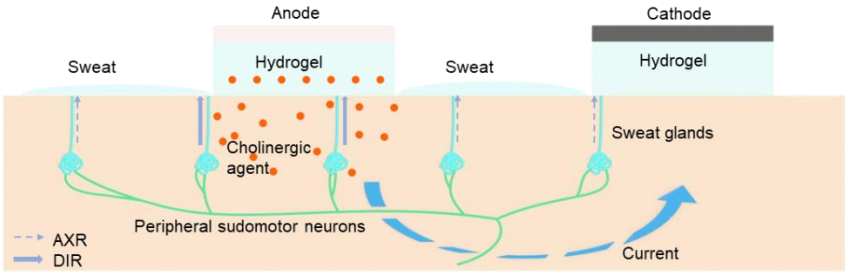

Figure 2-4. Iontophoresis-based sweat induction. AXR: Axon-reflex mediated sweating. DIR: direct stimulated sweating

Different cholinergic agonists could be used to induce sweating and the sweating response varies in duration and area, determined by the receptor activity and susceptibility to acetylcholinesterase (AChE) hydrolysis. Acetylcholine and methacholine are hydrolyzed by

AChE and thus have a shorter sweating duration. On the other hand, the nicotinic activity of the cholinergic agents affects the indirect axon-reflex sweating and thus the area of the sweat response. For example, the β-methyl group of bethanechol limited the nicotinic activity and thus the sweating response is highly localized and mostly direct sweating underneath the placement of the iontophoresis gel. Detailed studies and summaries of the receptor activities and sweating response can be found in previous literature.[22,26,39,40]

2.3.3 Sweat Composition by Different Induction Methods

The composition of sweat may vary across sweat induction methods. Firstly, the pH of sweat tends to be higher in iontophoresis-induced sweat compared to thermogenic sweat.[41] High sweat rates and low ductal HCO_3^- reabsorption may contribute to this higher pH. Ca^{2+} and Mg^{2+} levels were observed to be higher in sweat obtained from the sauna than in sweat obtained from exercise.[42] Recent metabolomic studies also revealed variations in lipid profiles[43] and metabolites[34] among iontophoresis-induced, exercise-induced, and natural sweat, including notable variations in L-alanine, pyruvate, L-aspartate, BCAAs, asparagine, lysine, and fumarate concentrations.[34] The stability of metabolites in sweat also plays a critical role in the quantitation process; sweat metabolite stability was shown to last for 90 min at simulated body temperature.[44] For natural sweat at a much slower sweat rate, it is suggested that quantitation results may be compromised due to metabolic quenching of enzymatic reactions and metabolite stability, an issue especially relevant for untargeted metabolomics analysis.[45] For targeted metabolomics analysis, such as drug tests, controlled stability studies should be done to achieve repeatable quantitation within the applicable detection range.[46] Moreover, tissue-dependent factors (e.g., keratin amount and thickness of stratum corneum) affect the iontophoresis response between individuals and at different body locations, potentially also impacting the sweat composition.[45]

2.4 Sweat Extraction Methods

Over the past decade, various iontophoresis devices have been developed for wearable sweat induction. The commercially available Macroduct system is Food and Drug Administration (FDA)-approved for iontophoresis-based sweat induction for cystic fibrosis diagnosis and

uses pilocarpine as the cholinergic agonist. After initial current ramping, a constant current is administered to pilocarpine gel discs strapped onto the arm. The device automatically ramps down the current and shuts down after 5 min. Although the device provides customizable options with the straps for stimulation at different locations on extremities and across different age groups (babies to adults), the system remains bulky and unsuitable for regular wear. Similar systems could be achieved for initial prototype testing with an iontophoresis device and custom lab-made hydrogels loaded with selected cholinergic agonists.[37]

Upon sweat induction, proper sweat collection is required such that low volumes of sweat produced are efficiently harvested for analysis[47]. Historically, sweat was sampled without a transporting mechanism (i.e., microfluidic system). Several materials have been used for sweat collection with no microfluidic system, which can wick (e.g., rayon[1,48–51], paper[52], textile[53], absorbent pad or sponge[54–57], hydrogel[37,38,58–60]) or capture (e.g., glove[36], sweatband[61]) the sweat directly on the sensing system.

Although direct sweat sampling using absorbent materials is simple and easy to implement, there are limitations to be resolved.[62] Direct sweat sampling limits the capability of biosensor due to mixing and carry-over between new sweat and old sweat, resulting in contaminating sweat samples. For instance, with the bulk rayon material (e.g., regenerated cellulose), it is hard to rapidly capture a change in the analyte concentration.[63–65] Without a system for continuous sweat flow to refresh sensing sample and control of sample evaporation and volume, the biosensor may yield less reliable continuous reading and should serve as single-use only device. Microfluidics enables a continuous sweat flow through microfluidic channels and encapsulated sensing chambers or reservoirs and therefore resolves the limits.[62,66] With the use of microfluidics, microliter sampling volumes can be collected at the sensor surface to generate the same quality of response compared to bulk solution analysis.[66,67]

2.4.1 Laser-Engraved Iontophoresis Patch for On-demand Sweat Induction

In our lab, we developed a flexible laser-engraved iontophoresis patch with a much smaller form factor was developed with small hydrogels containing muscarinic agent carbachol cast onto laser-engraved graphene electrodes, and on-demand sweat induction was achieved by utilized a flexible printed circuit board (FPCB) (**Fig. 2-5a**).[67] Carbachol was selected from various muscarinic agents as it allows the most efficient, repeatable, and long-lasting sweat secretion from the surrounding sweat gland thanks to its additional nicotinic effects[68] (**Fig. 2-5b-d**). In contrast, the classic sweat inducing agent – pilocarpine – used by the standard sweat test and previously reported wearable systems[69–71] offers only a short period of sweat and very limited sweat rate from the neighboring sweat glands (**Fig. 2-5b-d**). Furthermore, sampling the mixture of the leaked sweat underneath the pilocarpine gel and the gel fluid could result in substantial wearable sensor errors and fail to provide real-time information due to the absence of efficient sweat refreshing. A very small current (50–100 μA) is used for our iontophoresis module, as compared to commonly used 1–1.5 mA[69–71], greatly reducing the risks of skin irritation. To maximize the efficiency of low-volume sweat sampling and improve the temporal resolution of wearable sensing, a compact and flexible microfluidic module was carefully designed to isolate sweat sampling areas from iontophoresis gels. With the optimized design for sweat induction and sampling, sweat can be conveniently induced locally and readily sampled with the multi-inlet microfluidics over a prolonged period (**Fig. 2-5c,e**).

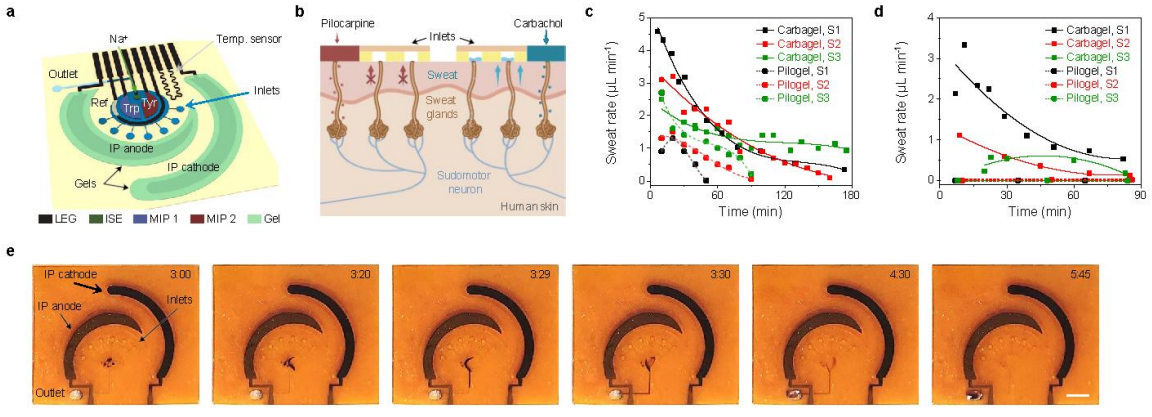

Figure 2-5. Flexible laser-engraved iontophoresis patch for on demand sweat extraction. a, Illustration of a multi-functional wearable sensor patch. **b**, Schematic of localized sweat sampling based on iontophoretic sweat extraction with muscarinic agents: pilocarpine and carbachol. **c**,**d**, Localized sweat rates measured from the stimulated (**c**) and surrounding (**d**) skin areas after a 5-min iontophoresis with pilocarpine and carbachol. Solid and dashed curves represent quadratic-fit trendlines. S, subject. **e**, On-body evaluation of the optimized flexible microfluidic patch for efficient carbachol-based iontophoretic sweat induction and surrounding sampling at rest. Timestamps represent the period (min) after a 5-min iontophoresis session. Black dye was used in the reservoir to facilitate the direct visualization of sweat flow in the microfluidics. Scale bar, 3 mm.

Fabrication and characterization of microfluidic channels. The microfluidic module was fabricated using a 50 W CO2 laser cutter (Universal Laser System). Briefly, layers of double-sided and single-sided medical adhesives (3M) were patterned with channels, inlets, the iontophoresis gel outlines and reservoirs. For all microfluidic layers, the iontophoresis gel outlines were patterned to enable the current flow from the top polyimide electrode layer. The bottom layer, which is the double-sided adhesive layer in contact with the skin (accumulation layer), was patterned with a sweat accumulation well (3M 468MP, laser parameter: power 60%, speed 90%, PPI 1000). The second layer (the inlets layer), in contact with the accumulation layer, was patterned with the multiple inlets (12 μm thick Polyethylene terephthalate (PET), laser parameter: power 20%, speed 100%, PPI 1000). The third layer (channel layer), in contact with the inlets layer, was patterned with microfluidic channels (Adhesives Research 93049, laser parameter: power 45%, speed 100%, PPI 1000). The fourth layer (reservoir layer), sandwiched between the channel layer and the electrode polyimide layer, was patterned with the reservoir and the outlet (3M 468MP, laser parameter: power 60%, speed 90%, PPI 1000). The reservoir is an ellipse with a 5.442 mm major axis and a 4.253 mm minor axis to fully enclose the active sensing area. The thickness of the channel layer is ~0.1 mm (Adhesives Research 93049) and the thickness of the reservoir layer is 0.13 mm (3M 468MP). The reservoir area is 18.17 mm2, and thus the reservoir

volume can be calculated as the area multiplied by the thickness of the reservoir layer (0.13 mm) which totals 2.36 μL.

Fabrication of agonist agent hydrogels. Hydrogels containing muscarinic agent carbachol was prepared as follows: Briefly, for anode gel, agarose (3% w/w) was added into deionized water and then heated to 250 °C under constant stirring. After the mixture was fully boiled and became homogenous without agarose grains, the mixture was cooled down to 165 °C and 1% carbachol was added to the above mixture. Subsequently, the cooled mixture was slowly poured into pre-made cylindrical molds or into assembled microfluidic patch and solidified for 10 min at 4 °C. The cathode gel was prepared similarly except that NaCl (1% w/w) was used instead of carbachol.

2.4.2 Iontophoresis Patch for Continuous Sweat Induction and Sweat Rate Monitoring

In developing a state-of-the-art sweat analysis system, the variabilities of iontophoresis-induced sweat rates and their durations, which are inherently dependent on individual physiological differences, were meticulously considered. Recognizing sweat as a significant biomarker, intrinsically linked to the secretion of various other essential biomarkers, a critical aspect of the analytical process involves determining whether the sensor reservoir is continuously refreshed, indicative of ongoing sweat production. To address this, a specialized microfluidic sweat processing module was devised, incorporating a sophisticated application of carbachol-based iontophoresis, enhancing the efficiency of sweat induction. This was seamlessly paired with a dedicated sweat rate sensor, allowing for a robust and comprehensive analysis. Such an integration facilitated a nuanced monitoring process where, following a singular sweat induction event, the system could adeptly extract and monitor sweat rates for an extended period, ensuring over three hours of consistent and insightful data acquisition (**Fig. 2-6**). Notably, this iontophoretic sweat processing system is powered fully by a perovskite solar cell and will be discussed in more detail in Chapter 6.

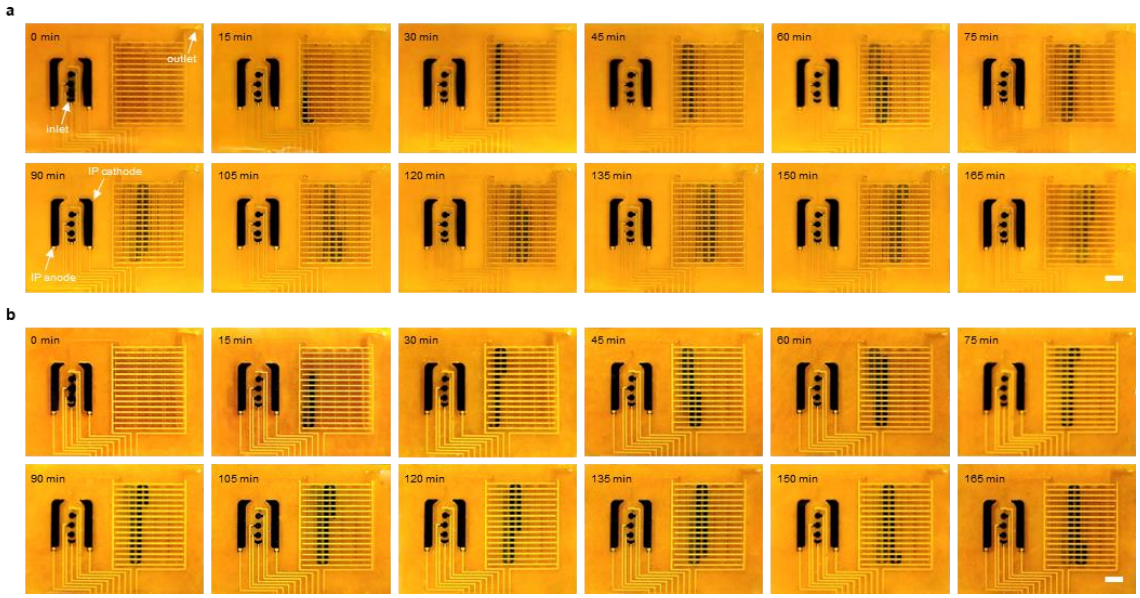

Figure 2-6. On-body evaluation of the wearable device's light-powered iontophoresis and sweat processing system at rest. a,**b**, Time-lapsed photos in minutes after 10 minutes of iontophoresis under bright laboratory light for two subjects. Blue dye was placed on the sweat accumulation layer to visualize the sweat filling the biosensor and sweat rate sensor reservoirs at rest. Scale bars, 3 mm.

Design considerations and optimization of microfluidic sweat processing system. The design goal for the microfluidic sweat processing system was to develop a system that can induce and extract the sweat for prolonged durations above a minimal threshold flow rate while consuming minimal amounts of power. Trade-offs between power consumption for iontophoresis and the size of the carbagels, geometric location and orientation of the gels with respect to the sweat accumulation reservoir, and distance between the gels and sweat accumulation reservoir were considered. The power consumption of the iontophoresis circuit is positively correlated to the total current applied and the compliance voltage of the constant current source. As iontophoretic current density is positively correlated with regional sweat rate, power consumption could be minimized by minimizing the area of the carbagel. On the other hand, while carbachol can stimulate neighboring sweat glands, if the carbagel is too small, the sweat gland density around the gel can be low, generating low sweat volume. The

next factor considered was the orientation of the gels with respect to the sweat accumulation reservoir. We found that locating the sweat accumulation reservoir between the anode and cathode can maximize extraction efficiency as the majority of the drug is delivered across the anode and cathode. Another factor considered was the distance between the gels. If the anode and cathode are too close, the drug delivery area may be too small and it is possible that not enough sweat glands are activated. However, increasing the inter-gel distance above a certain extent does not increase sweat gland activation and only increases the impedance between the two carbagels, which necessitates a higher compliance voltage and power consumption for the iontophoresis circuit. Regarding the distance between the carbagels and the sweat accumulation reservoir, sweat extraction improved when the sweat accumulation reservoir was closer to the anodic carbagel (where the drug is loaded). However, if the distance between the gel and accumulation reservoir was closer than 1 mm, the adhesive would have difficulty maintaining the sweat within the sweat accumulation reservoir and sweat would leak at times. With all these considerations in mind, our final carbagel area was 15 mm^2 per electrode, distance between the carbagels was 4 mm, and the distance between the carbagel and the sweat accumulation reservoir was 1.2 mm. A current of 55 μA was delivered for iontophoretic stimulation as lower currents did not result in sufficient sweat output, and higher currents lead to an increased power consumption and did not necessarily result in a longer stimulation duration.

The final microfluidic sweat processing system consists of three main layers, the sweat accumulation layer, the channel layer, and the reservoir layer. All layers of the microfluidic system contain two large cutouts for holding the carbagels. In addition to these cutouts, the accumulation layer (0.13 mm) contains a well (same dimensions as the sensor reservoir) for sweat accumulation; the channel layer (0.64 mm) contains a sweat rate channel (36 μL or 95 μL capacity) for processing high volumes of sweat and a counter electrode-shaped inlet to transport the accumulated sweat into the sensor reservoir; and the reservoir layer (0.13 mm) contains a compact sensor reservoir (1.1 μL capacity) to enable rapid refreshing of sweat and a microfluidic channel to flush out the sweat through the sweat rate channel.

Chapter 3

NOVEL ELECTROCHEMICAL APPROACHES FOR SWEAT SENSING

Materials from this chapter appear in "Min, J.; Tu, J.; Xu, C.; Lukas, H.; Shin, S.; Yang, Y.; Solomon, S. A.; Mukasa, D.; Gao, W. Skin-Interfaced Wearable Sweat Sensors for Precision Medicine. *Chemical Reviews* **2023**, 123 (8), 5049–5138. https://doi.org/10.1021/acs.chemrev.2c00823.", "Wang, M.; Yang, Y.; Min, J.; Song, Y.; Tu, J.; Mukasa, D.; Ye, C.; Xu, C.; Heflin, N.; McCune, J. S.; Hsiai, T. K.; Li, Z.; Gao, W. A Wearable Electrochemical Biosensor for the Monitoring of Metabolites and Nutrients. *Nature Biomedical Engineering* **2022**. https://doi.org/10.1038/s41551-022-00916-z.", " Tu, J.; Min, J.; Song, Y.; Xu, C.; Li, J.; Moore, J.; Hanson, J.; Hu, E.; Parimon, T.; Wang, T.-Y.; Davoodi, E.; Chou, T.-F.; Chen, P.; Hsu, J. J.; Rossiter, H. B.; Gao, W. A Wireless Patch for the Monitoring of C-Reactive Protein in Sweat. *Nature Biomedical Engineering* **2023**, *7* (10), 1293–1306. https://doi.org/10.1038/s41551-023-01059-5.", and " Ye, C.; Wang, M.; Min, J.; Tay, R. Y.; Lukas, H.; Sempionatto, J. R.; Li, J.; Xu, C.; Gao, W. A Wearable Aptamer Nanobiosensor for Non-Invasive Female Hormone Monitoring. *Nature Nanotechnology* **2023**. https://doi.org/10.1038/s41565-023-01513-0."

Sweat is an information-rich biofluid containing many molecules that can serve as biomarkers. Sweat is composed of various electrolytes, metabolites, hormones, proteins, and peptides (**Table 1**). Sweat samples may be analyzed using metrics such as biomarker concentrations, biomarker flux, sweat rate, sweat pH, and ionic strength to provide important information as they correlate to health. In some cases, biomarker flux may represent a better metric of analysis since it accounts for the dynamic water flux, which may affect concentration measurements. Biomarker flux may be calculated using the product of sweat rate and biomarker concentration.[72] Recent reports have shown promising correlations between the levels of a number of sweat and blood analytes,[8] indicating the great potential of using sweat as an alternative source for personalized healthcare. Since sweat is readily available for noninvasive sampling, sweat is an attractive biofluid for point-of-care (POC), at-home, and continuous diagnostics. Moreover, new biomarker discovery for precision medicine can be greatly facilitated by the continuous, large sets of data collected through non-invasive sweat analysis in daily activities.[73]

Table 3-1. Composition of sweat.

Biomarkers			Sweat concentration (mM)	Blood concentration (mM)	Molecular weight (Da)	References
Electrolytes	Sodium		10–100	135–150	23	29,42,74,75
	Chloride		10–100	97–107	35	29,56,76
	Potassium		1–20	3.5–5	39	29,77,78
	Ammonium		0.5–8	0.01–0.4	18	79,80
Metabolites	Lactate		5–60	0.5–25	90	29,81–88
	Glucose		0.01–0.3	3.3–17.3	180	89–91
	Urea		2–40	1.8–7.1	60	87,90,92–94
	Uric acid		0.02–0.1	0.1–0.5	168	66,92–95
	Creatinine		0.01–0.03	0.065–0.12	113	92,93,96
Minerals	Calcium		0.2–2	2.2–2.7	30	97–100
	Magnesium		0.02–0.4	0.7–0.95	24	97–100
	Iron		0.0001–0.03	0.006–0.027	56	97–100
	Zinc		0.0001–0.02	0.01–0.017	65	97–100
Nutrients	Amino acids	Tyrosine	0.2–0.4	0.055–0.3	181	67,101–103
		Tryptophan	0.055–0.08	0.02–0.091	204	67,101–103
		BCAAs[a]	0.2–1	0.2–1.2	117–131	67,101–103
	Vitamin C		$0.01–50\times10^{-3}$	$2.8–200\times10^{-3}$	176	104,105
Hormones	Cortisol		$0.1–20\times10^{-3}$	$0.07–690\times10^{-3}$	362	106–108
	Testosterone		$0.8–1.6\times10^{-6}$	$0.5–35\times10^{-6}$	288	109
	Dehydroepiandrosterone		$6.9–455\times10^{-6}$	$0.35–11.91\times10^{-3}$	288	109
	Neuropeptide Y		$1.9–6.8\times10^{-10}$	$1.4–6.1\times10^{-10}$	4272	110
Proteins	C-reactive protein		$4.2–250\times10^{-9}$	$7–29\times10^{-6}$	120,000	
	Cytokines	Interleukin 6	$3.7–6.9\times10^{-10}$	$2.4–5.6\times10^{-10}$	21,000	110,111

	Interleukin 8	$1.8–7.2\times10^{-10}$	$1.5–6.5\times10^{-10}$	8452	111,112
Substances	Ethanol	2.5–22.5	2–22.5	46	113
	Acetaminophen	$<50\times10^{-3}$	$66–132\times10^{-3}$	151	114
	Levodopa	$<2.5\times10^{-3}$	$<5\times10^{-3}$	197	115

[a]BCAAs: branched-chain amino acids

Most wearable sweat sensors currently in use primarily utilize potentiometric ion-selective electrodes or amperometric enzyme electrodes. This conventional approach essentially limits the detection spectrum to a select few electrolytes (Na+, Cl-, K+, NH4+) and metabolites (lactate, glucose, urea, creatinine). Thus, many clinically relevant nutrients and metabolites in sweat are rarely explored and undetectable by existing wearable sensing technologies. In addition to the aforementioned electrolytes and metabolites, sweat a rich source of various other informative biomarkers such as amino acids (tyrosine, tryptophan, BCAAs) and proteins & hormones (cytokines, cortisol, CRP, estradiol), which are incredibly insightful for broader health analysis.

Innovation is the key to overcoming these current technological limitations. Thus, we have pioneered the development of novel sweat sensors, utilizing alternative electrochemical transduction mechanisms, enabling them to detect an expanded array of biomarkers. Our advanced sensors incorporate diverse recognition elements coupled with intricate electrochemical detection techniques. For instance, we have employed molecularly imprinted polymer sensors paired with differential pulse voltammetry for personalized nutrition monitoring, graphene-gold nanoparticle modified immunosensors paired with square wave voltammetry for systemic inflammation monitoring, and aptamer sensors paired with square wave voltammetry for monitoring female hormones.

In discussing these advancements, particular attention is devoted to each sensor system's unique contributions to the field. Besides, it is crucial to consider personal variations like sweat rate or pH, which can invariably influence biomarker secretion, possibly confounding sensor readings. To mitigate this, we have devised wearable platforms capable of multiplexed measurements. These platforms are meticulously designed to consider and adjust for variations such as skin temperature, sweat pH, and ionic strength, ensuring a more reliable

and accurate analysis. However, it is important to note that the integration of these advanced measurement techniques and the expansion of measurement channels does inherently increase the electronic circuit's power consumption. This vital aspect of power consumption and its implications will be explored comprehensively in the subsequent section.

3.1 Molecularly Imprinted Polymer Sensors for Nutrient Monitoring

3.1.1 Background

Circulating nutrients are essential indicators for overall health and body function[116]. Amino acids (AAs), sourced from dietary intake, gut microbiota synthesis, and influenced by personal lifestyles, are important biomarkers for a number of health conditions (**Fig. 3-1a**)[117]. Elevated branched-chain amino acids (BCAAs) including leucine (Leu), isoleucine (Ile), and valine (Val), are associated with obesity, insulin resistance, and the future risk of type 2 diabetes mellitus (T2DM), cardiovascular diseases (CVDs), and pancreatic cancer[118–120]. Deficiencies in AAs (e.g., arginine and cysteine) could hamper the immune system by reducing immune-cell activation[121]. Tryptophan (Trp), tyrosine (Tyr) and phenylalanine (Phe) are precursors of serotonin and catecholamine neurotransmitters (dopamine, norepinephrine, and epinephrine), respectively, and play an important role in the function of complex neural systems and mental health[122,123]. A number of metabolic fingerprints (including Leu, Phe, and vitamin D) are linked to corona virus 2019 (COVID-19) severity[124,125]; health disparities in nutrition also correlate well with the alarming racial and ethnic disparities that are worsened by COVID-19 vulnerability and mortality[126]; moreover, organ and tissue dysfunction induced by SARS-CoV-2 could result in an increased incidence of cardiometabolic diseases[127].

Here we present a universal wearable biosensing strategy based on a judicious combination of the mass-producible laser-engraved graphene (LEG), electrochemically synthesized redox-active nanoreporters (RARs), biomimetic molecularly imprinted polymer (MIP)-based 'artificial antibodies,' as well as unique *in situ* regeneration and calibration technologies (**Fig. 3-1b**). Unlike bioaffinity sensors based on antibodies or classic MIPs

which are generally one-time use and require multiple washing steps in order to transduce the bioaffinity interactions in standard ionic solutions[128,129], this approach enables the first demonstration of sensitive, selective, and continuous monitoring of a wide range of trace-level biomarkers in biofluids including all nine essential AAs as well as vitamins, metabolites, and lipids commonly found in human sweat. Seamless integration of this unique approach with *in situ* signal processing and wireless communication leads to a powerful wearable sweat sensing platform 'NutriTrek' that is able to perform personalized and non-invasive metabolic and nutritional monitoring toward timely intervention (**Fig. 3-1b**). The incorporation of the carbachol iontophoresis-based sweat induction and efficient microfluidic-based surrounding sweat sampling enables prolonged autonomous and continuous molecular analysis with high temporal resolution and accuracy across activities, during physical exercise and at rest. Using five essential or conditionally essential AAs (i.e., Trp, Try, and three BCAAs (Leu, Ile, Val)) as exemplar nutrients, we corroborated the system in several human trials by enrolling both healthy subjects and patients toward personalized monitoring of central fatigue, standard dietary intakes, nutrition status, metabolic syndrome risks, and COVID-19 severity.

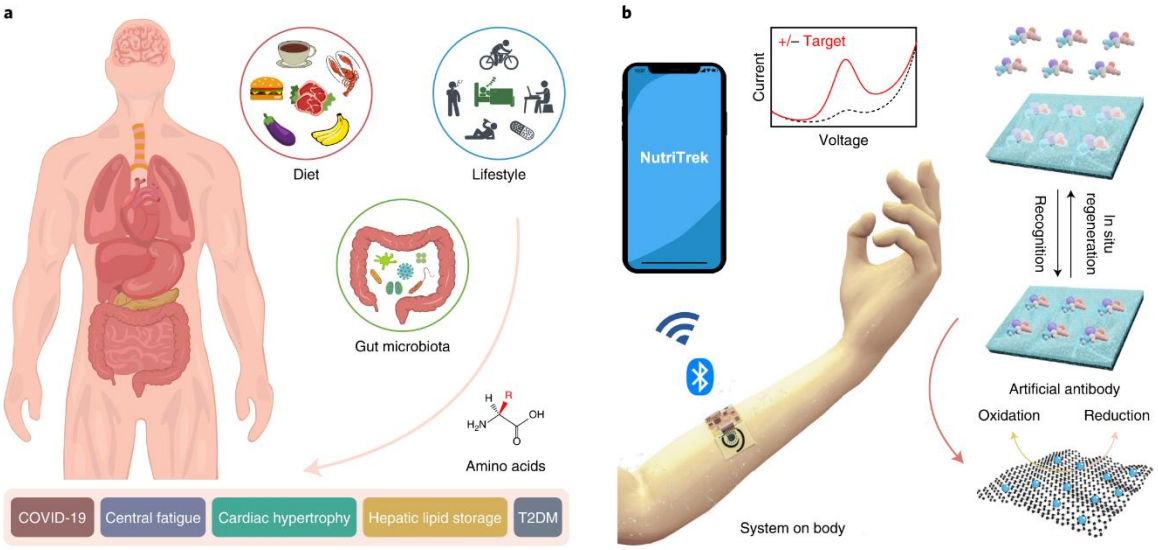

Figure 3-1. Biomimetic wearable biosensor for detection of circulating nutrients in sweat. a, Circulating nutrients such as amino acids are associated with various physiological

and metabolic conditions. **b**, Schematic of the wearable 'NutriTrek' that enables metabolic monitoring through a synergistic fusion of laser-engraved graphene, redox-active nanoreporters, and biomimetic 'artificial antibodies.'

3.1.2 Biomimetic sensor design and evaluation for universal metabolic and nutritional analysis

Universal detection of AAs and other metabolites/nutrients with high sensitivity and selectivity was achieved through careful design of the selective binding MIP layer on the LEG. MIPs are chemically synthesized biomimetic receptors formed by polymerizing functional monomer(s) with template molecules. Although MIP technology has been proposed for sensing, separation and diagnosis[129,130], it has not yet been demonstrated for continuous wearable sensing as classic MIP sensors require washing steps for sensor regeneration and the detection is generally performed in standard buffer or redox solutions. In our case, the functional monomer (e.g., pyrrole) and crosslinker (e.g., 3-Aminophenylboronic acid) initially form a complex with the target molecule; following polymerization, their functional groups are embedded in the polymeric structure on the LEG; subsequent extraction of the target molecules reveals binding sites on the LEG-MIP electrode that are complementary in size, shape, and charge to the target analyte (**Fig. 3-2**). Two detection strategies - direct and indirect - are designed based on the electrochemical properties of the target molecules (**Fig. 3-3**).

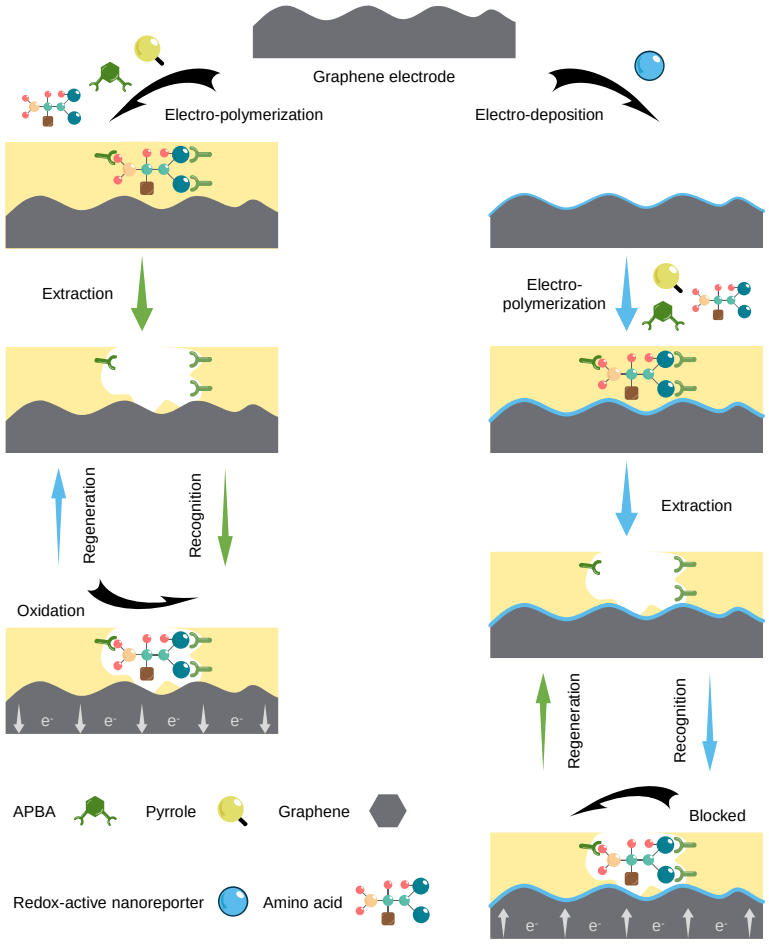

Figure 3-2. Schematic of the preparation procedure and detection mechanism of the LEG-MIP AA sensors. Left panel, electroactive AA sensor with direct detection mechanism; Right panel, AA sensor with indirect detection mechanism.

For electroactive molecules in sweat, the oxidation of bound target molecules in the MIP template can be directly measured by differential pulse voltammetry (DPV) in which the peak current height correlates to analyte concentration (**Fig. 3-3a**). Considering that multiple electroactive molecules can be oxidized at similar potentials, this LEG-MIP approach addresses both sensitivity and selectivity issues. For example, Tyr and Trp, two AAs with close redox potentials (~0.7 V), could be detected selectively with this strategy (**Fig. 3-3b,c** and **Fig. 3-4**). Linear relationships between peak height current densities and target concentrations with sensitivities of 0.63 $\mu A\,\mu M^{-1}\,cm^{-2}$ and 0.71 $\mu A\,\mu M^{-1}\,cm^{-2}$,

respectively, for the LEG-MIP Tyr and Trp sensors were observed. It is worth noting that choices of monomer/crosslinker/template ratios and incubation periods have substantial influences on sensor response while sample volume does not (**Fig. 3-5**). The Tyr and Trp sensors can be readily and repeatably regenerated *in situ* without any washing step with a high-voltage amperometry (IT) that oxidizes the bound targets at their redox potentials (**Fig. 3-3d**).

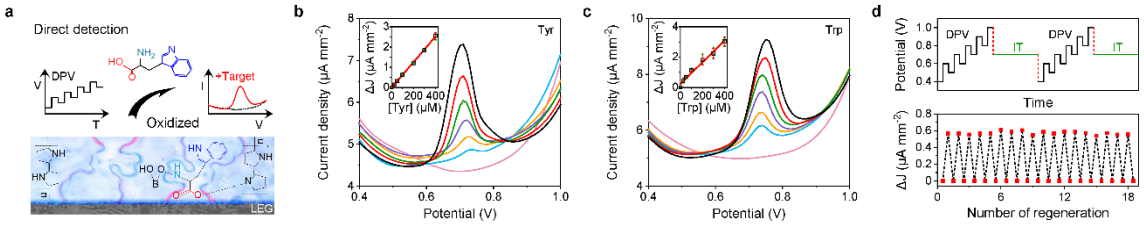

Figure 3-3. Direct detection of electroactive molecules using LEG-MIP sensors. a, Schematic of operation for direct detection. **b**,**c**, DPV voltammograms of the LEG-MIP sensors for direct Tyr (**b**) and Trp (**c**) detection. Insets, the calibration plots. ΔJ, peak height current density. **d**, *In situ* continuous sensing and regeneration of an LEG-MIP Trp sensor in 50 μM Trp.

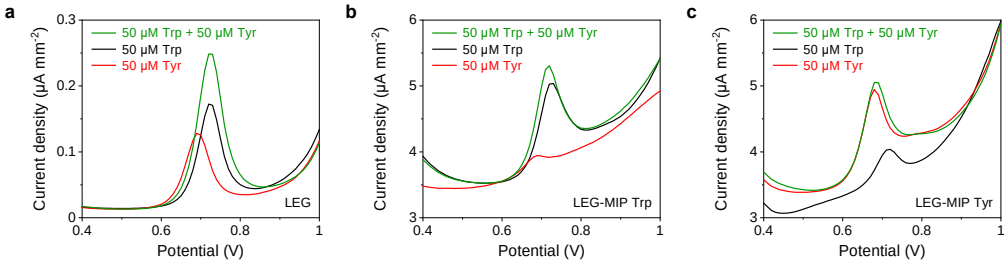

Figure 3-4. Selectivity studies of the LEG-MIP sensors for detecting two electroactive amino acids: Trp and Tyr. a–c, DPV voltammograms of a bare LEG electrode (**a**), an LEG-MIP Trp electrode (**b**), and an LEG-MIP Tyr electrode (**c**) in 50 μM Trp, 50 μM Tyr, and 50 μM Trp + 50 μM Tyr.

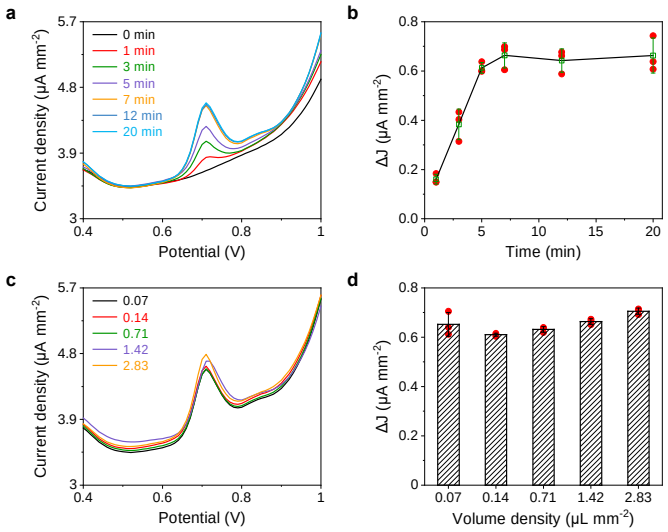

Figure 3-5. Evaluation of the effect of incubation time and sample volume on the LEG-MIP sensor performance. a,**b**, DPV voltammograms (**a**) and current density of the peak height (ΔJ) (**b**) of the Trp sensors in 50 μM Trp with varied 1–20 min incubation time. **c**,**d**, DPV voltammograms (**c**) and current density of the peak height (ΔJ) (**d**) of the Trp sensors in 50 μM Trp with varied sample volumes. Error bars in **b** and **d** represent the s.d. from 3 sensors.

As the majority of metabolites and nutrients (e.g., BCAAs) are non-electroactive and cannot easily be oxidized under operational conditions, we herein utilize an indirect detection approach involving an RAR layer sandwiched between the LEG and MIP layers to enable rapid quantitation (**Fig. 3-6a**). The selective adsorption of the target molecules onto the imprinted polymeric layer decreases the exposure of the RAR to the sample matrix. Controlled-potential voltammetric techniques such as DPV or linear sweeping voltammetry (LSV) can be applied to measure the RAR's oxidization or reduction peak, where the decrease in peak height current density corresponds to an increase in analyte levels. For example, using Prussian Blue nanoparticles (PBNPs) as the RAR, we developed a MIP-LEG Leu sensor with a log-linear relationship between the peak height decrease and Leu concentration and a sensitivity of 702 nA mm^{-2} per decade of concentration (**Fig. 3-6b**). We established this approach to quantify the physiologically relevant range of all nine essential

AAs (i.e., Leu, Ile, Val, Trp, Phe, histidine (His), lysine (Lys), methionine (Met), and threonine (Thr)) (**Fig. 3-6c** and **Fig. 3-7**) as well as a number of vitamins, metabolites, and lipids (vitamins B_6, C, D_3, and E, glucose, uric acid, creatine, creatinine, and cholesterol) (**Fig. 3-6d** and **Fig. 3-8**). In addition to these nutrients and metabolites, this approach can be easily reconfigured to enable the monitoring of a broad spectrum of biomarkers ranging from hormones (e.g., cortisol) to drugs (e.g., chemotherapy medications) (**Fig. 3-9**). Most of these targets are undetectable continuously by any existing wearable technology. Considering that a total level of multiple nutrients (e.g., total BCAAs) is often an important health indicator, a multi-template MIP approach can be used to enable accurate and sensitive detection of the total concentration of multiple targets with a single sensor (**Fig. 3-6e,f**). These indirect LEG-RAR-MIP sensors can be regenerated *in situ* upon constant potential applied to the working electrode repels the bound target molecules from the MIP layer with prolonged re-usability (**Fig. 3-6g**). The LEG-MIP sensors show stable responses during repeatable use: The PBNPs-based RAR showed stable redox signals throughout 60 repetitive cyclic voltammetry (CV) scans (**Fig. 3-6h**)

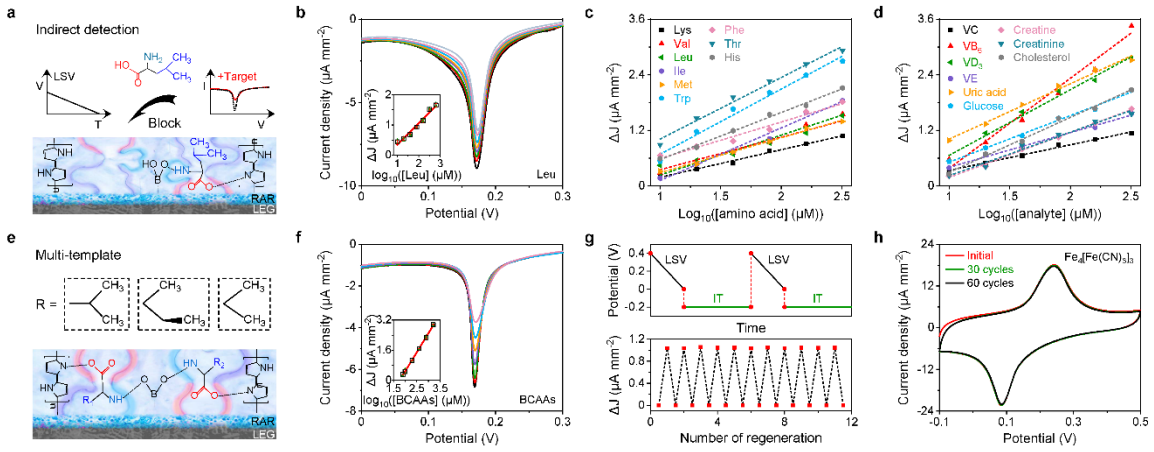

Figure 3-6 Indirect molecular detection using LEG-RAR-MIP sensors. a, Schematic of operation for indirect detection. **b**, LSV voltammograms of indirect Leu detection with LEG-PBNP-MIP sensors. Inset, the calibration plot. **c**,**d**, Indirect detection of all essential AAs (**c**) and multiple vitamins, lipids, and metabolites (**d**) using LEG-PBNP-MIP sensors. **e**, Schematic of multi-MIP AA sensors. **f**, LSV voltammograms of a LEG multi-MIP sensor

for BCAA quantification. Inset, the calibration plot. **g**, *In situ* continuous sensing and regeneration of an LEG-PBNP-MIP Leu sensor in 50 µM Leu. **h**, Repetitive CV scans of an LEG-PBNP electrode in 0.1 M KCl.

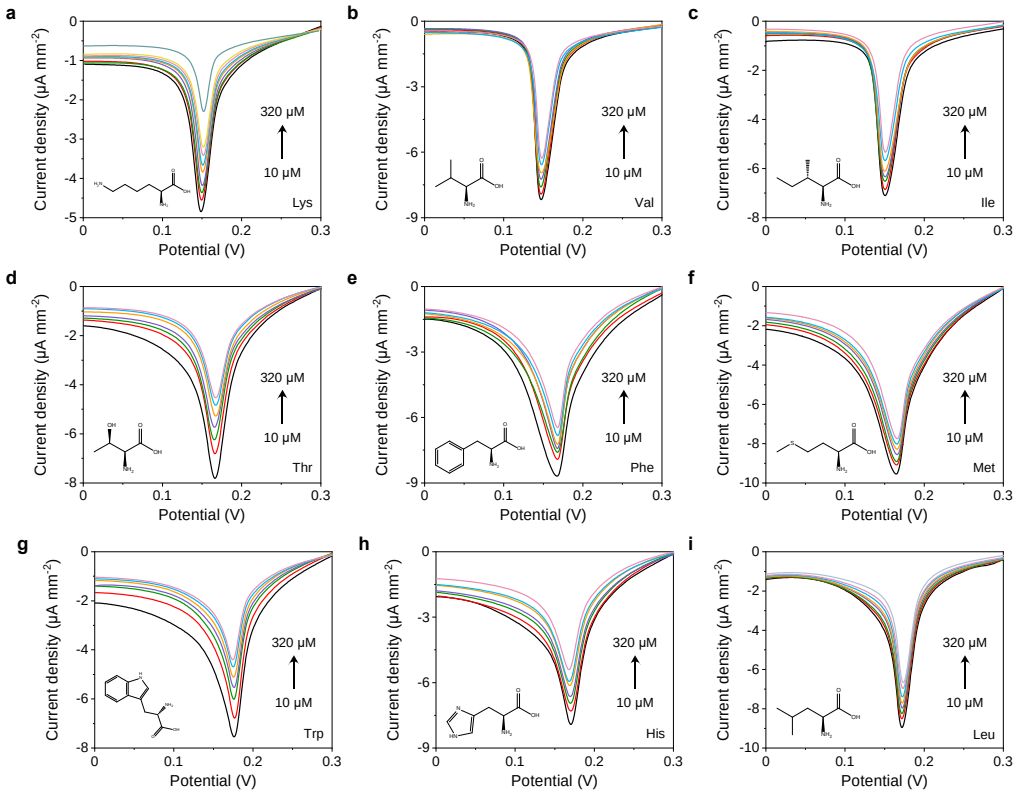

Figure 3-7. LSV voltammograms of the LEG-PB-MIP sensors for indirect detection of all nine essential amino acids.

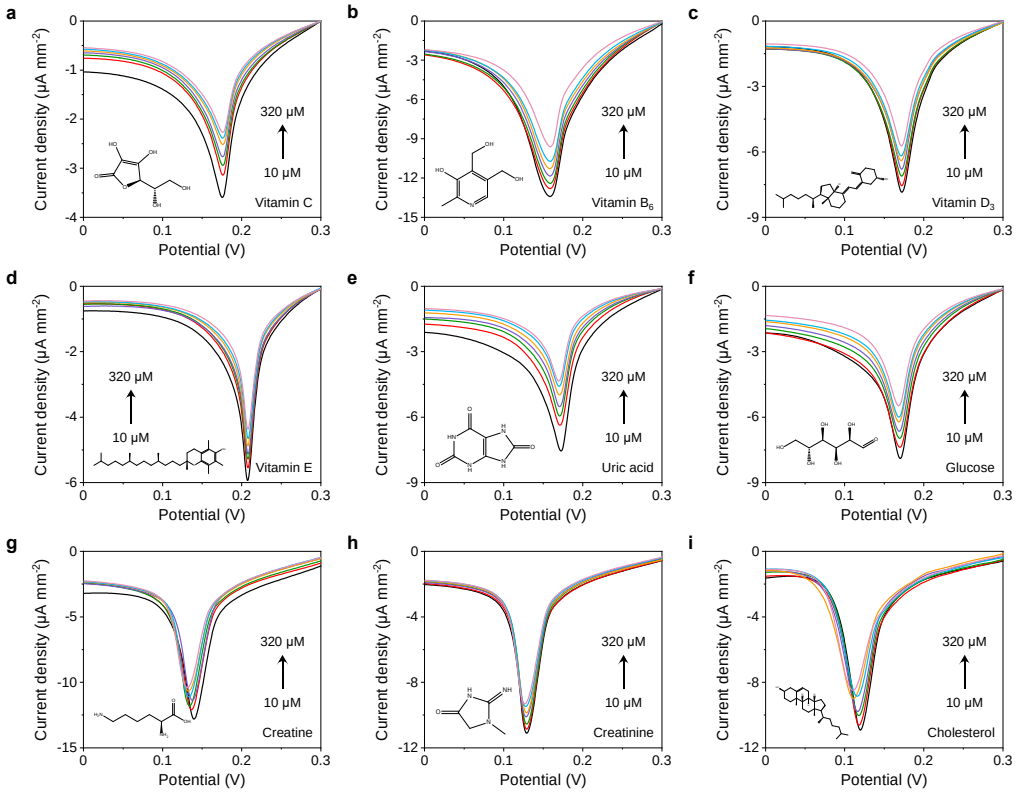

Figure 3-8. LSV voltammograms of the LEG-PB-MIP sensors for indirect detection of multiple vitamins, metabolites, and lipids.

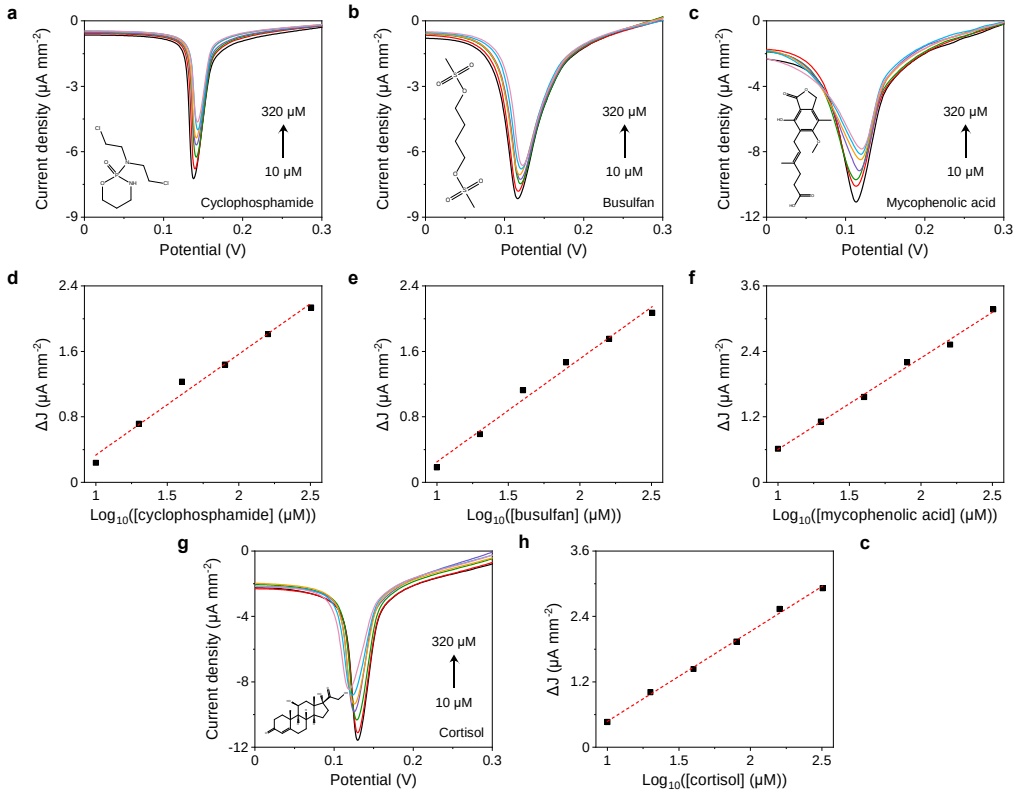

Figure 3-9. LSV voltammograms and the corresponding calibration curves of the LEG-PB-MIP sensor for indirect detection of chemotherapy drugs (three cancer drugs: cyclophosphamide, busulfan, and mycophenolic acid) and hormones (i.e., cortisol).

3.1.3 Evaluation of the wearable system for dynamic physiological and nutritional monitoring

Evaluation of the wearable system was conducted first *via* sensing of sweat Trp and Tyr in human subjects during a constant-load cycling exercise trial (**Fig. 3-10a-d** and **Fig. 3-11**). The DPV data from the sensors were wirelessly transmitted along with temperature and Na^+ sensor readings to the mobile app that automatically extracted the oxidation peaks using a custom developed iterative baseline correction algorithm (**Fig. 3-10e** and **Fig. 3-12**) and performed calibration for the accurate quantification of sweat Tyr and Trp. Considering that AAs (e.g., Try and BCAAs) play a crucial role in central fatigue during physical exercise[131],

a flexible Trp and BCAA sensor array was used to monitor the AA dynamics during vigorous exercise (**Fig. 4f–j** and **Fig. 3-13**). Both Trp and BCAA levels decreased during the exercise due to the serotonin synthesis and BCAA ingestion, respectively. The increased sweat Trp/BCAA ratio was observed which could potentially serve as an indicator for central fatigue, in agreement with a previous report on its plasma counterpart[131].

The wearable iontophoresis-integrated patch enables daily continuous AA monitoring at rest beyond the physical exercise. As illustrated in **Fig. 4k–o** and **Figs. 3-14-17**, rising Trp and Tyr levels in sweat were observed from all four subjects after Trp and Tyr supplement intake while the readings from the sensors remained stable during the studies without intake. Such capability opens the door for personalized nutritional monitoring and management through personalized sensor-guided dietary intervention. It should be noted that our pilot study showed that sweat nutrient and electrolyte levels were independent of sweat rate changes during the carbachol-based iontophoresis-induced sweat (**Fig. 3-18**).

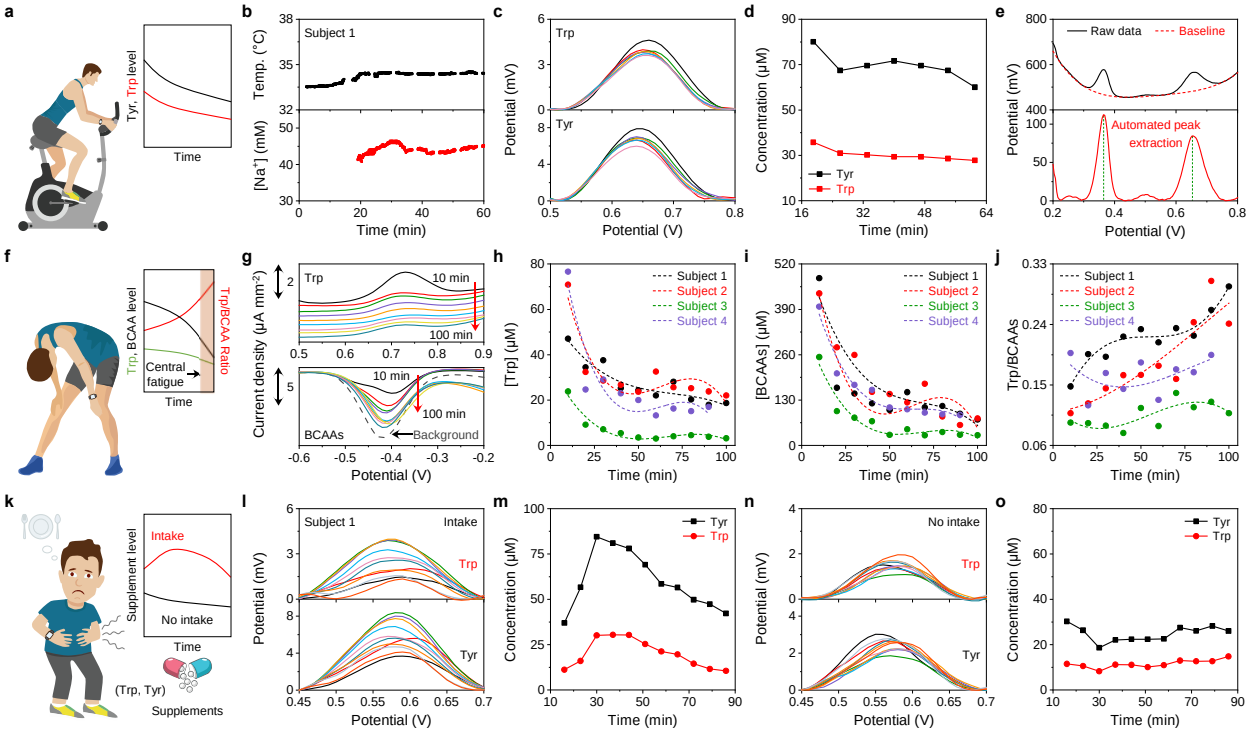

Figure 3-10. Wearable system evaluation across activities toward prolonged physiological and nutritional monitoring. a–d, Continuous on-body Trp and Tyr analysis

using a wearable sensor array with real-time sensor calibrations during cycling exercise. **e**, Custom voltammogram analysis with an automatic peak extraction strategy based on a polynomial fitting and cut-off procedure. **f–j**, Dynamic sweat Trp and BCAA analysis during physical exercise toward central fatigue monitoring. **k–o**, Dynamic analysis of sweat AA levels with and without Trp and Tyr supplement intake at rest toward personalized nutritional monitoring.

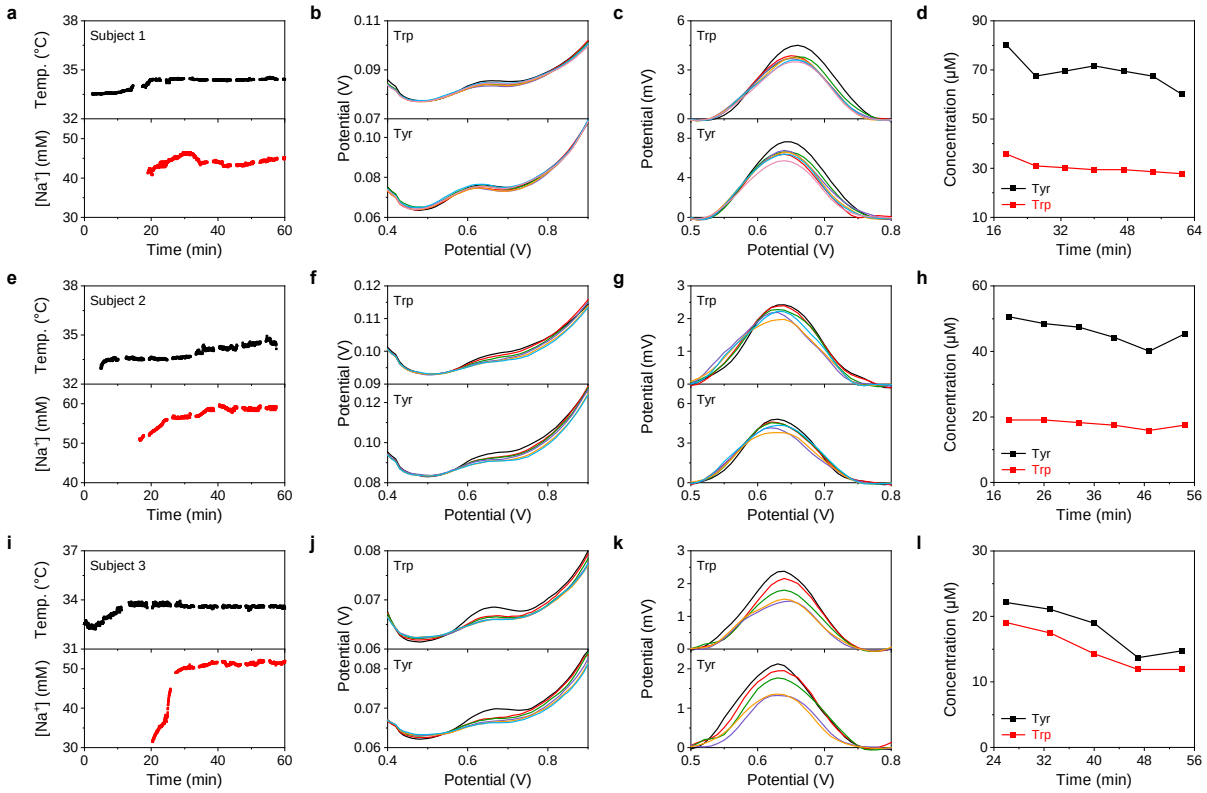

Figure 3-11. Continuous on-body Trp and Tyr analysis with real-time sensor calibrations using a wearable sensor array on three subjects during a constant-load cycling exercise. b,**f**,**j** represent the raw signals obtained from the on body measurement while **c**,**g**,**k** represent the corresponding data obtained with automated voltammogram analysis.

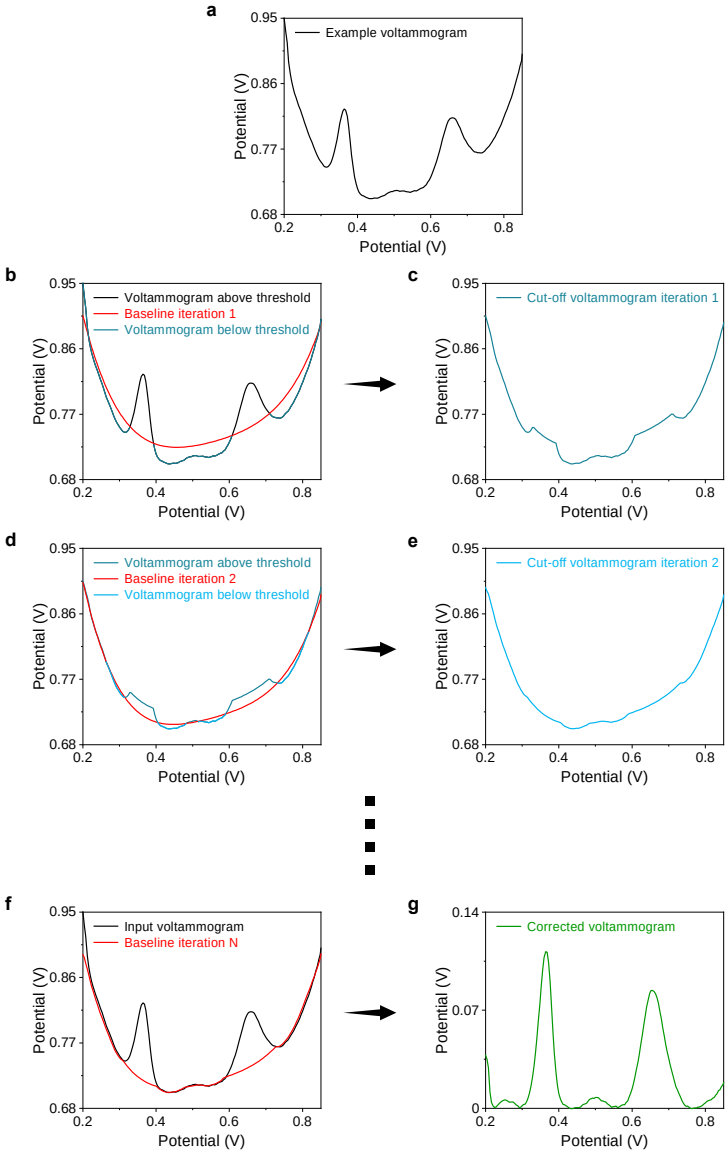

Figure 3-12. Automated voltammogram analysis. A sample input voltammogram (**a**) is approximated by a polynomial baseline that acts as a threshold (**b**) for the input voltammogram. The voltammogram below the threshold is retained, while the voltammogram above the threshold is replaced by the polynomial baseline to generate the first iteration cut-off voltammogram (**c**). The polynomial fitting and cutting-off procedure is iterated a specified number of times (**d**,**e**). After the iterative baseline correction, the original input voltammogram is subtracted by the final baseline to yield a corrected

voltammogram (**f**,**g**). A simple peak detection algorithm is employed to calculate the peak height and location of the corrected voltammogram.

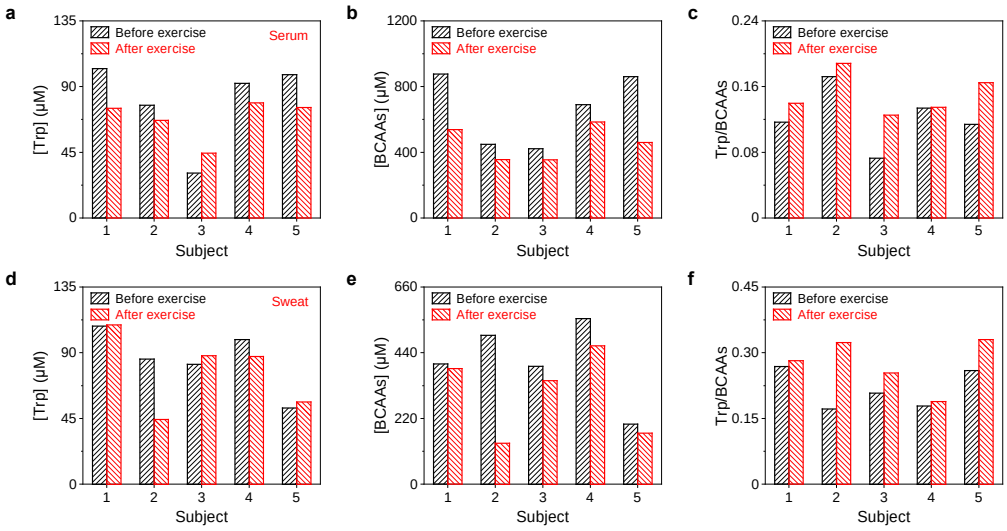

Figure 3-13. Dynamic monitoring of central fatigue using the Trp/BCAA sensor array patches. **a–c**, BCAA (**a**), Trp (**b**) and Trp/BCAA ratio (**c**) before exercise and after vigorous exercise until fatigue in human serum. **d–f**, BCAA (**d**), Trp (**e**) and Trp/BCAA ratio (**f**) before exercise and after vigorous exercise until fatigue in iontophoresis sweat.

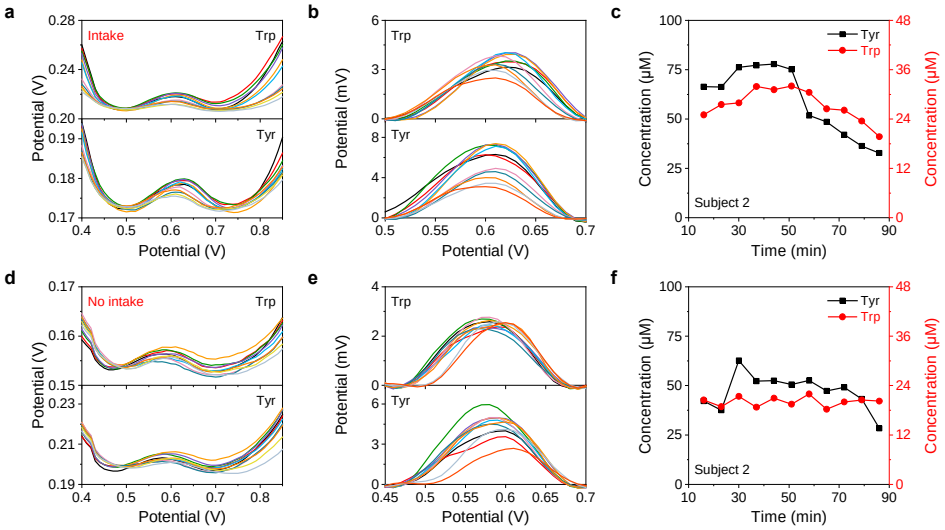

Figure 3-14. Iontophoresis-based continuous on-body Trp and Tyr analysis using a wearable sensor array with and without supplement intake (Subject 2). a–c, The raw voltammograms (**a**), automatically corrected voltammograms (**b**), and calibrated biomarker trends (**c**) collected during an on-body study with the supplement intake (Trp and Tyr, 1 g each). **d–f**, The raw voltammograms (**d**), automatically corrected voltammograms (**e**), and calibrated biomarker trends (**f**) collected during an on-body study without the supplement intake.

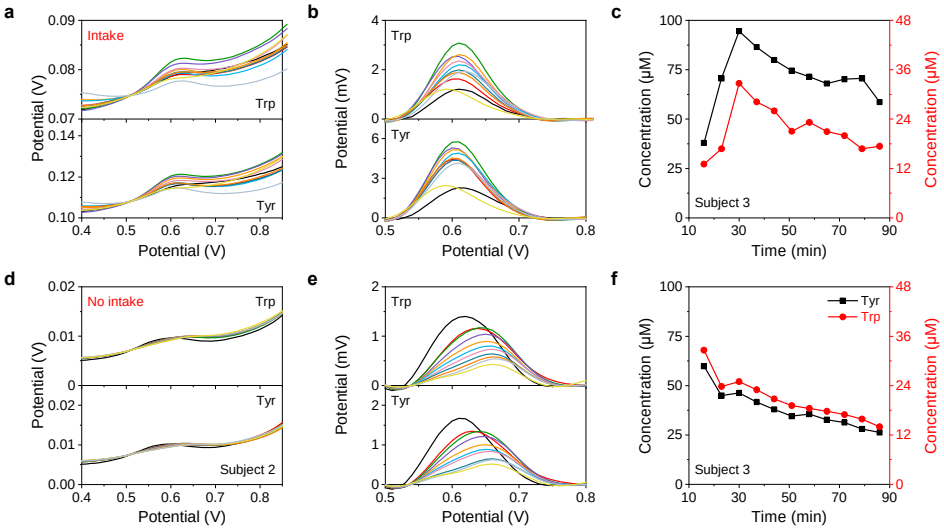

Figure 3-15. Iontophoresis-based continuous on-body Trp and Tyr analysis using a wearable sensor array with and without supplement intake (Subject 3). a–c, The raw voltammograms (**a**), automatically corrected voltammograms (**b**), and calibrated biomarker trends (**c**) collected during an on-body study with the supplement intake (Trp and Tyr, 1 g each). **d–f**, The raw voltammograms (**d**), automatically corrected voltammograms (**e**), and calibrated biomarker trends (**f**) collected during an on-body study without the supplement intake.

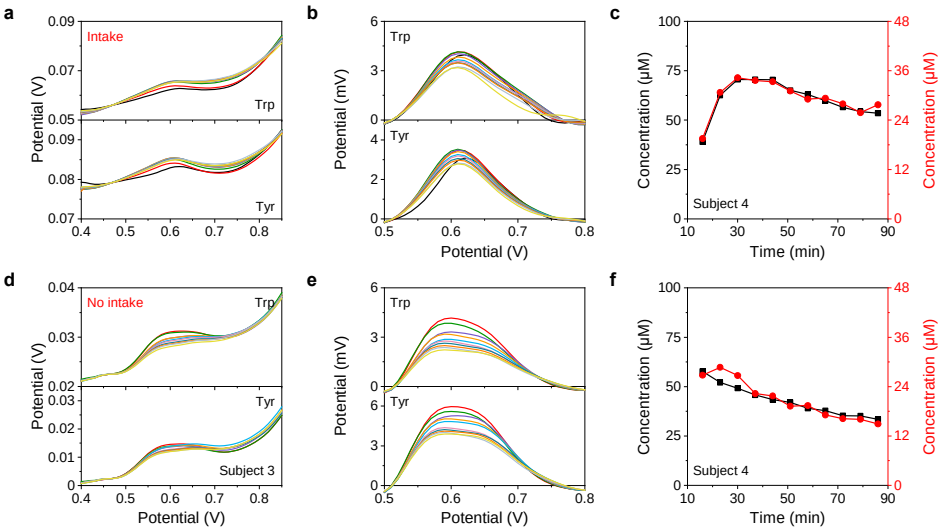

Figure 3-16. Iontophoresis-based continuous on-body Trp and Tyr analysis using a wearable sensor array with and without supplement intake (Subject 4). a–c, The raw voltammograms (**a**), automatically corrected voltammograms (**b**), and calibrated biomarker trends (**c**) collected during an on-body study with the supplement intake (Trp and Tyr, 1 g each). **d–f**, The raw voltammograms (**d**), automatically corrected voltammograms (**e**), and calibrated biomarker trends (**f**) collected during an on-body study without the supplement intake.

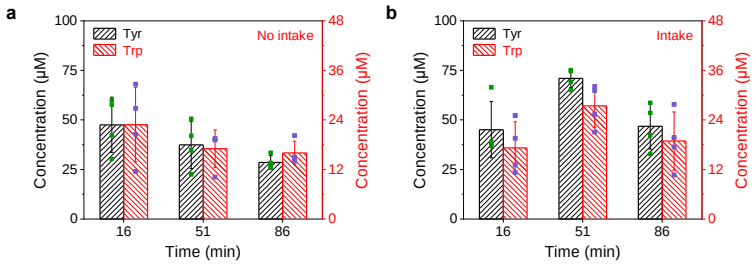

Figure 3-17. Tyr and Trp levels in continuous on-body Trp and Tyr sensing using wearable sensor arrays with and without supplement intake. Bars indicate the mean value of target; error bars represent the s.d. of measurements from all the subjects (n= 4).

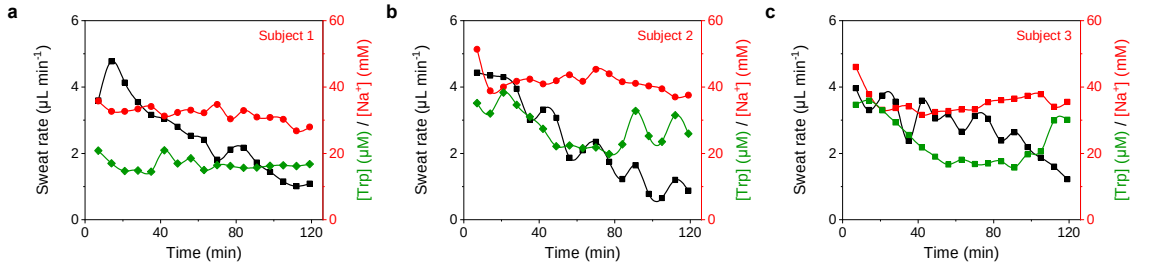

Figure 3-18. Sweat rate and the concentrations of amino acids (Trp here) and Na^+ on human subjects. The sweat was induced with the proposed carbachol-based iontophoresis.

3.1.4 Discussion

By integrating the mass-producible LEG, electrochemically synthesized RARs, and biomimetic 'artificial antibodies,' we have demonstrated a powerful universal wearable biosensing strategy that can achieve selective detection of an unprecedentedly broad range of biomarkers (including all essential AAs, vitamins, metabolites, lipids, hormones and drugs) and reliable *in situ* regeneration. Furthermore, to enable continuous and on-demand metabolic and nutritional monitoring across the activities, we have integrated the LEG-MIP sensor array and iontophoresis-based sweat induction into a wireless wearable platform, with optimized multi-inlet microfluidic sudomotor axon reflex sweat sampling, *in situ* signal processing, calibration, and wireless communication. Using this telemedicine platform, we have demonstrated the first-ever wearable and continuous monitoring of postprandial AA responses to identify risks for metabolic syndrome. The high correlation between sweat and serum BCAAs shows great promise of this platform towards metabolic syndrome risk monitoring. The significant difference in Leu between COVID-19 positive and negative blood samples indicates the potential of using this technology for at-home COVID-19 management. We envision that this wearable platform could play a crucial role in the realization of precision nutrition through continuous monitoring of circulating biomarkers and enabling personalized nutritional intervention. This platform could also be reconfigured to continuously monitor a variety of other biomarkers toward a wide range of personalized preventive, diagnostic, and therapeutic applications.

3.1.5 Methods

Fabrication and preparation of the LEG sensors. The LEG electrodes were fabricated on a polyimide film with a thickness of 75 μm (DuPont) with a 50 W CO_2 laser cutter (Universal Laser System). When engraving the PI with a CO_2 laser cutter, the absorbed laser energy is converted to local heat and thus leads to a high localized temperature (>2500 °C), chemical bonds in the PI network are broken and thermal reorganization of the carbon atoms occurs, resulting in sheets of graphene structures. The optimized parameters for the graphene electrodes and electronic connections were power 8%, speed 15%, points per inch (PPI) 1000 in raster mode with 3-time scan. For the active sensing area of the temperature sensor, the optimized parameters were power 3%, speed 18%, PPI 1000 in vector mode with 1-time scan. To prepare the reference electrode, Ag was first modified on the corresponding graphene electrode by multi-current electrodeposition with electrochemical workstation (CHI 832D) at -0.01 mA for 150 s, -0.02 mA for 50 s, -0.05 mA for 50 s, -0.08mA for 50 s, and -0.1 mA for 350 s using a plating solution containing 0.25 M silver nitrate, 0.75 M sodium thiosulfate and 0.5 M sodium bisulfite. 0.1 M $FeCl_3$ solution was further dropped on the Ag surface for 30 s to obtain the Ag/AgCl electrode, and then 3 μL PVB reference cocktail prepared by dissolving 79.1 mg of PVB, 50 mg of NaCl in 1 mL of methanol was dropped on the Ag/AgCl electrode and dried overnight. The Na^+ selective electrode was prepared as follows: 0.6 μL of Na^+ selective membrane cocktail prepared by dissolving 1 mg of Na ionophore X, 0.55 mg Na-TFPB, 33 mg PVC and 65.45 mg DOS into 660 μL of THF was drop-casted onto the graphene electrode and dried overnight. To obtain the desired stable Na^+ sensing performance for long-term continuous measurements, the obtained Na^+ sensor was conditioned overnight in 100 mM NaCl.

All the MIP layers are synthesized by electro-polymerization. The polymerization solution was prepared by dissolving 5 mM template (e.g., target amino acid), 12.5 mM aminophenylboronic acid (APBA) and 37.5 mM pyrrole into 0.01 M phosphate buffer saline (PBS) (pH=6.5). For multi-MIP BCAA sensor, 5 mM of each target (i.e., Leu, Ile, and Val) was used. Prior to MIP deposition, the LEG was activated in 0.5 M H_2SO_4 with CV scans for 60 segments (-1.2–1 V with a scan rate of 500 mV s^{-1}). For the direct-detection LEG-MIP

sensors, the target imprinted polymer was electrochemically synthesized on the LEG electrode with CV deposition (0–1 V for 10 cycles, 50 mV s^{-1}) using the prepared polymerization solution. The target molecules were extracted by soaking the electrode into an acetic acid/methanol mixture (7:3 v/v) for 1 hour. Subsequently, the resulting electrode was immersed into 0.01 M phosphate buffer saline (pH=6.5) for repetitive CV scans (0.4–1 V with a scan rate of 50 mV s^{-1}) until a stable response was obtained. For LEG-non-imprinted polymer (NIP), the electrode was prepared following the same procedure as LEG-MIP except that there was no template added in the polymerization solution.

For the indirect-detection MIP sensors, electrochemically synthesized redox-active nanoreporters (RARs) (e.g., Prussian Blue nanoparticles (PBNPs) or anthraquinone-2-carboxylic acid (AQCA)) was first modified on the LEG electrode. The PBNPs RAR on the LEG was prepared with cyclic voltammetry (20 cycles) (-0.2 to 0.6 V with a scan rate of 50 mV s^{-1}) in an aqueous solution containing 3 mM $FeCl_3$, 3 mM $K_3Fe(CN)_6$, 0.1 M HCl and 0.1 M KCl. A PBNP layer with appropriate redox signal is necessary to produce a good sensitivity for the final MIP sensors; to achieve this stable and suitable redox signal, the LEG-electrode was rinsed with distilled water after the initial Prussian blue (PB) deposition and the PB electrodeposition step was repeated for two more times until a stable 70 µA LSV peak in 0.1 M KCl solution was achieved. Subsequently, the LEG-PB was rinsed with distilled water and immersed into a solution containing 0.1 M HCl and 0.1 M KCl for repetitive CV scans (-0.2–0.6 V with a scan rate of 50 mV s^{-1}) until a stable response was obtained. To prepare the AQCA RAR on the LEG, the LEG electrode was first incubated in 50 µL PBS (pH=6.5) with 5 mM AQCA at 4 ºC overnight. Subsequently, the LEG-AQCA was rinsed with distilled water and immersed into a phosphate buffer solution for repetitive CV scans (-0.8–0 V with a scan rate of 50 mV s^{-1}) until a stable response was obtained. For the indirect-detection LEG-PB-MIP sensors, an additional PB activation process was conducted right after the template extraction (IT scan at 1 V in 0.5 M HCl for 600 s), followed by an LEG-PB-MIP sensor stabilization process in 0.1 M KCl (CV scans at -0.2–0.6 V with a scan rate of 50 mV s^{-1}). It should be noted that for the LEG-AQCA-MIP sensor, only 3 CV cycles polymerization was used to prepare the MIP layer, and the sensor was stabilized in 0.01 M

phosphate buffer saline (PBS) (pH=6.5) (CV scans at -0.8–0 V with a scan rate of 50 mV s^{-1}).

System evaluation during exercise. To validate the wearable sensor system, we conducted constant-load cycling exercise on healthy subjects. The subjects reported to the lab after fasting overnight and were given a standardized protein drink (Fairlife, Core Power Elite). The subjects' foreheads and necks were cleaned with alcohol swabs and gauze before the sensor patches were placed on the body. A stationary exercise bike (Kettler Axos Cycle M-LA) was used for cycling trials. The subjects cycled at 60 rpm for 60 min or until fatigue. During the on-body trial, the data from the sensor patches were wirelessly sent to the user interface via Bluetooth. When the subjects started biking, the sensor system continuously acquired and transmitted temperature and sodium sensor data. Every minute, the electronic system initiated a transient voltage bias between the reference and working electrodes. When the bias triggered a current above an experimentally determined threshold, the system would start a CV cleaning cycle and then the first DPV scan as the initial background without target incubation. The DPV scan was repeated 7 min later as the post-incubation curve. Between the two scans, sodium and temperature sensor data were continuously recorded. Right after the post-incubation DPV, another cycle started with a IT cleaning/regeneration step, followed by an initial background DPV scan. The collected temperature, sodium, and DPV data were wirelessly transmitted to a user device via Bluetooth in real-time, where the molecular data was extracted, calibrated, and converted to concentration levels. Sweat samples were collected periodically from the subjects during the studies using centrifuge tubes. The sweat samples were then frozen at −20 °C for further testing and validation via electrochemical test with the biosensors and GC-MS analysis.

System evaluation with Tyr/Trp supplement intake. The subjects reported to the lab after fasting overnight. The subjects' arms were cleaned with alcohol swabs and gauze before the sensor patches were placed on the body. The subjects were provided Tyr and Trp supplement (1 g each) for the intake study. In contrast, the control study was performed on the subjects

without any supplementary intake. A 5-min iontophoresis was applied on the subjects. The sensor data recording process was the same as exercise-based human trials.

3.2 Immunosensor for Detection of C-reactive Protein in Sweat

3.2.1 Background

Real-time monitoring of inflammatory proteins allows remote disease progression tracking and early intervention, thus improving patient outcomes and lowering economic burdens in chronic diseases. However, most current commercial protein sensing technologies rely on invasive blood draws and require lengthy target incubation and labor-intensive washing steps to reach picomolar-level sensitivity. Although sweat is a non-invasive source for disease monitoring, wearable immunosensing is complex and sweat protein secretion is extremely underexplored, presenting a major challenge for personalized inflammation monitoring. Here, we present a wearable nanoengineered electrochemical biosensing technology that allows real-time and non-invasive analysis of a crucial inflammatory biomarker, C-reactive protein (CRP). Highly sensitive, selective, and fully automatic *in situ* inflammatory protein analysis across human activities was realized through seamless integration of a mesoporous graphene-gold nanoparticle modified immunosensor (coupled with thionine-tagged detector antibody-conjugated gold nanoparticles for signal transduction and amplification), autonomous sweat gland-driven microfluidics, and multimodal graphene sensor calibration. Through *in vitro* and *in vivo* clinical studies, we confirmed the presence and identified substantially elevated sweat CRP levels from patients with heart failure, chronic obstructive pulmonary disease, and active and past infections (e.g., COVID-19). We obtained a high correlation between sweat and blood CRP levels, demonstrating the potential of this technology toward non-invasive chronic disease management.

3.2.2 Design of the wearable microfluidic LEG-AuNPs biosensor

Key components of the wearable sensor are a skin-interfaced flexible, disposable, multimodal microfluidic biosensor patch fabricated on a polyimide (PI) substrate *via* CO_2 laser engraving and a FPCB for iontophoretic sweat induction, sensor data acquisition and wireless communication (**Fig. 3-19b**). The sensor array consists of an electrodeposited

AuNPs-decorated LEG working electrode immobilized with anti-CRP capture antibodies (cAb), a Ag/AgCl reference electrode, an LEG counter electrode for sweat CRP capturing and electrochemical analysis, an LEG-based impedimetric ionic strength sensor, a LEG-polyaniline-based potentiometric sweat pH sensor, and a strain-insensitive resistive graphene temperature sensor. Considering that the potential users of this technology include sedentary and immobile patients, an iontophoresis module (based on a pair of LEG electrodes) is incorporated for on-demand delivery of cholinergic agonist carbachol from the carbachol hydrogel (carbagel) for autonomous sweat stimulation throughout daily activities without the need for vigorous exercise. A cost-effective and flexible microfluidic module is assembled by stacking laser-cut medical adhesives and polyethylene terephthalate (PET) for efficient sweat sampling (**Fig. 3-19c**). The miniaturized FPCB interfaces compactly on top of the microfluidic sensor patch to form the fully integrated wearable system (**Fig. 3-19d**). Powered by a small on-board lithium battery, the wearable system is able to wirelessly communicate with a user interface *via* Bluetooth Low Energy (**Fig. 3-20**).

In order to realize automatic wearable CRP detection *in situ*, the microfluidic module comprises a reagent reservoir for the storage of the labeled anti-CRP dAbs-conjugated AuNPs, a serpentine mixing channel for mixing of dAb with sweat CRP, and a detection reservoir for the capture and quantification of sweat CRP (**Fig. 3-19e**). The redox molecule, TH, is used to label the nanoparticle conjugates to achieve direct electrochemical sensing. As the autonomously induced sweat flows into the microfluidics, the deposited dAbs conjugated AuNPs are reconstituted within the reagent reservoir (I) and routed along with sweat through a serpentine passive mixer to facilitate the dynamic binding between sweat CRP and dAb (II). As the mixture enters the detection reservoir, it slowly fills the chamber before exiting *via* the outlet; the detection reservoir has an optimized size to allow sufficient time for CRP-dAb to bind with anti-CRP cAb functionalized LEG-AuNPs working electrode (III). Subsequently, a fresh sweat stream continues to refresh the microfluidics to achieve passive label removal (IV). Square wave voltammetry (SWV) is used to measure the amount of TH bound to the working electrode surface. Since TH molecules are directly conjugated to CRP dAb-immobilized AuNPs, their amount bound is directly correlated to the amount of

CRP ‘sandwiched’ between cAbs at the electrode surface and dAb-immobilized AuNPs, and consequently, the initial concentration of CRP in solution.

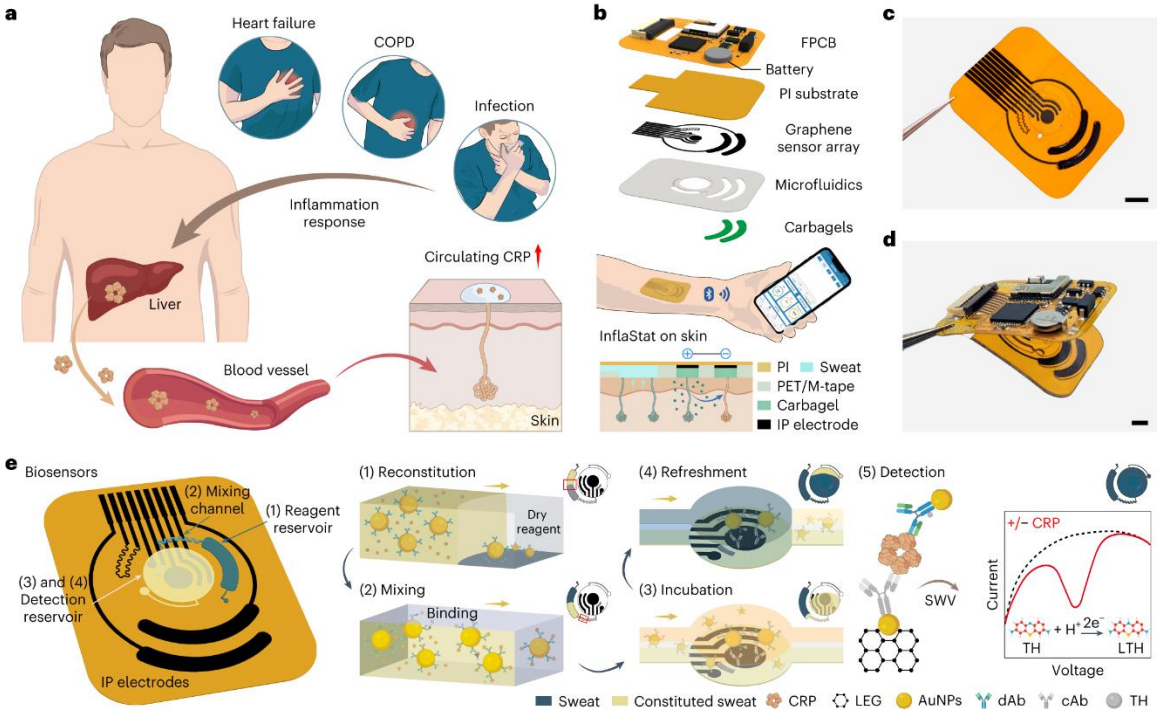

Figure 3-19. **Wearable electrochemical nanobiosensor for automatic, non-invasive, and wireless inflammation monitoring. a**, Circulating C-reactive protein (CRP), released from inflammatory responses, is closely related to various chronic and acute health conditions and could be secreted *via* the sweat gland. COPD, chronic obstructive pulmonary disease. **b**, Schematic of the skin-interfaced multimodal wearable nanobiosensor that contains an iontophoretic module for localized sweat extraction on-demand, a microfluidic module for automated sweat sampling and reagent routing, and a flexible laser-engraved graphene (LEG) multimodal sensor array for multiplexed sensing of sweat CRP, pH, temperature, and ionic strength. PI, polyimide; carbagel, carbachol hydrogel; PET/M-tape, polyethylene terephthalate/medical tape; IP, iontophoresis. **c**,**d**, Optical images of a disposable microfluidic graphene sensor patch (**c**) and a vertical stack assembly of the fully integrated wireless wearable system (**d**). Scale bars, 0.5 cm. **e**, The mechanism of *in situ* microfluidic sweat CRP analysis that involves fully-automatic sweat sampling, reagent routing, and detection. AuNPs, gold nanoparticles; cAb, capture

antibody; dAb, detector antibody; SWV, square wave voltammetry; TH, thionine; LTH, leuco thionine.

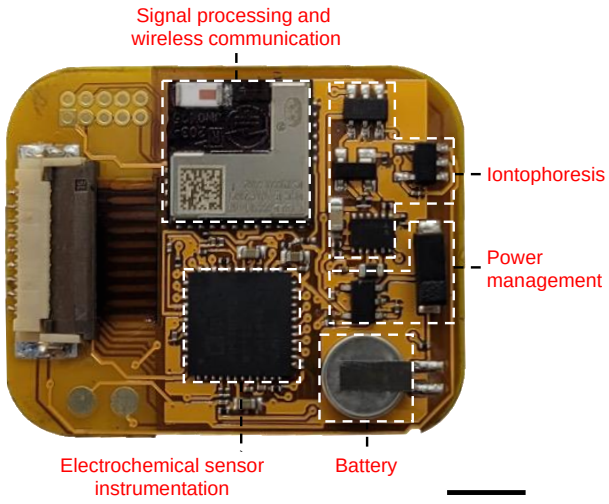

Figure 3-20. **The integrated wireless wearable electronics for CRP sensing.** Scale bar, 5 mm.

3.2.3 System integration and on-body evaluation of the wearable biosensor

The fully integrated wearable inflammation monitoring system, InflaStat, is designed based on vertical stack assembly of a flexible microfluidic sensor patch and an FPCB and can be comfortably worn by the subjects (**Fig. 3-21a**). As illustrated in electronic circuit block diagram and schematic in **Fig. 3-21b**, the FPCB is able to perform current-controlled iontophoresis, multiplexed multimodal electrochemical measurements (including voltammetry, impedimetry, and potentiometry), signal processing, and wireless communication. The integrated system could also accurately obtain the dynamic responses of the integrated LEG-based pH, ionic strength, and skin temperature sensors for real-time CRP sensor calibration (**Fig. 3-21c–f**). The InflaStat is designed to have good mechanical flexibility and stability toward practical usage during various physical activities.

Clinical on-body evaluation of the wearable system was performed on healthy subjects (involving both never smokers and current smokers) as well as patients with COPD and post-COVID-19 infection (**Fig. 3-21g–l** and **Fig. 3-22**). During the on-body trials, the wearable

system laminates conformally on the subject's arm, chemically induces and analyzes sweat, and acquires inflammatory biomarker information non-invasively and wirelessly (**Fig. 3-21g**). The obtained sensor data can be displayed on a custom developed mobile app in real-time (**Fig. 3-21h**). In situ pH, temperature, and CRP sensor readings are acquired after the ionic strength sensor indicate full refreshment of the detection reservoir (**Fig. 3-21h-l**). It should be noted that the TH's reduction peak for the CRP sensor appears at a slightly shifted potential given the variations in sweat pH (**Fig. 3-23**). The CRP concentration was converted in the mobile app based on the obtained SWV voltammogram and the corresponding real-time obtained ionic strength, pH, and temperature values (**Fig. 3-24**). As expected, an elevated CRP level was observed from the current smokers as compared with the never smokers in healthy subjects. The CRP levels in the COPD patients and post-COVID subjects were substantially greater than those of non-smoking healthy subjects, suggesting the promise of using the InflaStat in practical non-invasive systemic inflammation monitoring and disease management applications.

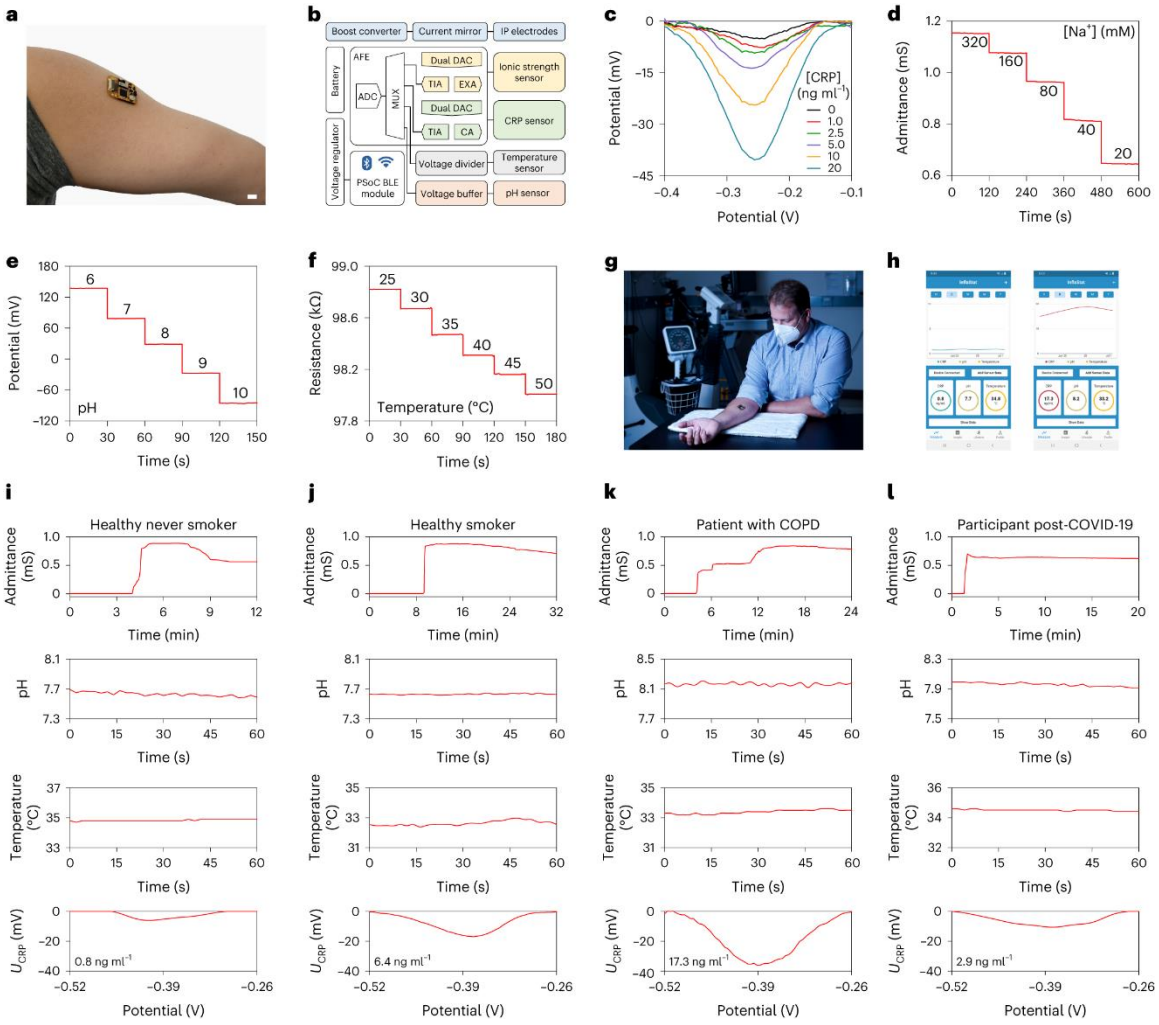

Figure 3-21. **On-body evaluation of the multiplexed wearable patch toward non-invasive automatic inflammation monitoring. a**, Image of a fully integrated wearable sensor on the arm of a human subject. Scale bar, 1 cm. **b**, Block diagram of the electronic system of the InflaStat. **c–f**, Calibration plots obtained using the wearable system from the CRP (**c**), ionic strength (**d**), pH (**e**) and temperature (**f**) sensors. Error bars represent the s.d. from 3 sensors. g, Photograph of a subject wearing the sensor patch during a clinical study. **h**, Custom mobile application for real-time data acquisition and display toward inflammation tracking. **i–l**, On-body multiplexed physicochemical analysis and CRP analysis with real-time sensor calibrations using the wearable sensor from a healthy never smoker (**i**), a healthy smoker (**j**), a COPD patient (**k**) and a post-COVID subject (**l**).

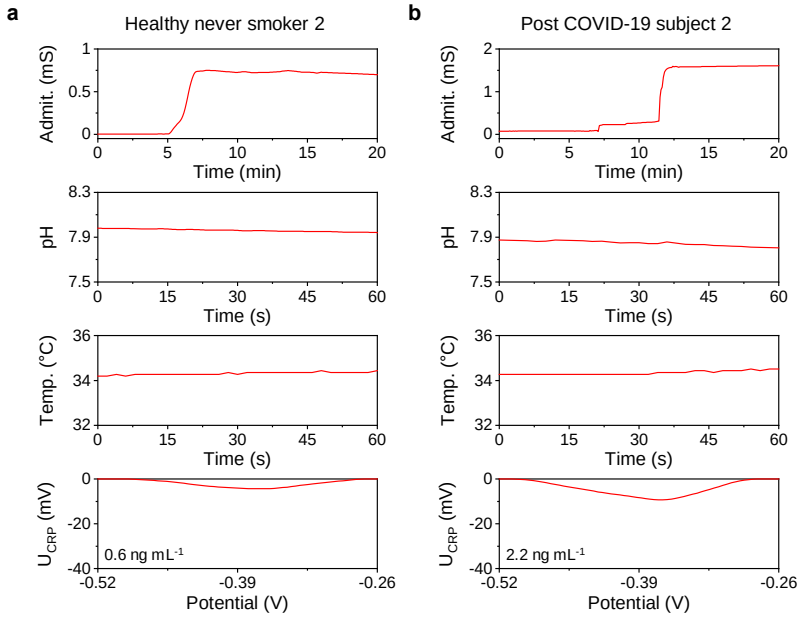

Figure 3-22. On-body evaluation of the wearable sensor on a healthy subject and a post-COVID subject.

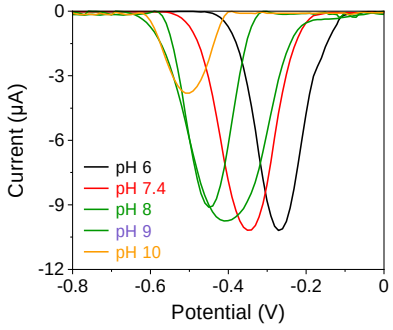

Figure 3-23. Influence of solution pH in peak potential and current of the redox molecule thionine. SWV voltammograms were obtained using the LEG electrodes in 5 µM TH in 1X PBS.

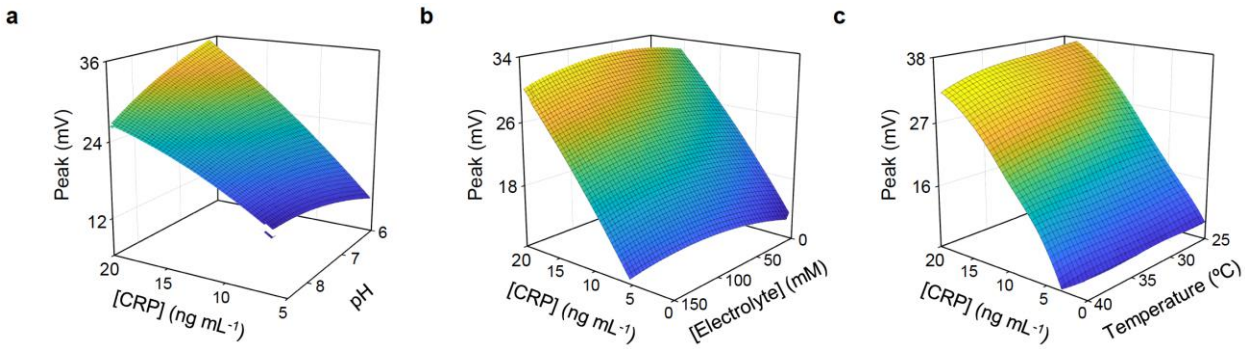

Figure 3-24. **Influence of the pH, ionic strength, and temperature on the CRP sensor reading. a–c**, Color maps showing the dependence of the CRP sensor response on pH (**a**), electrolyte (**b**), and temperature (**c**) levels.

3.3 Aptasensor for Non-invasive Female Hormone Monitoring

3.3.1 Background

Personalized monitoring of female hormones (for example, oestradiol) is of great interest in fertility and women's health. However, existing approaches usually require invasive blood draws and/or bulky analytical laboratory equipment, making them hard to implement at home. Here we report a skin-interfaced wearable aptamer nanobiosensor based on target-induced strand displacement for automatic and non-invasive monitoring of oestradiol via in situ sweat analysis. The reagentless, amplifcation-free and 'signal-on' detection approach coupled with a gold nanoparticle-MXene-based detection electrode ofers extraordinary sensitivity with an ultra-low limit of detection of 0.14 pM. This fully integrated system is capable of autonomous sweat induction at rest via iontophoresis, precise microfuidic sweat sampling controlled via capillary bursting valves, real-time oestradiol analysis and calibration with simultaneously collected multivariate information (that is, temperature, pH and ionic strength), as well as signal processing and wireless communication with a user interface (for example, smartphone) (**Fig. 3-25**). We validated the technology in human participants. Our data indicate a cyclical fuctuation in sweat oestradiol during menstrual cycles, and a high correlation between sweat and blood oestradiol was identifed. Our study

opens up the potential for wearable sensors for non-invasive, personalized reproductive hormone monitoring.

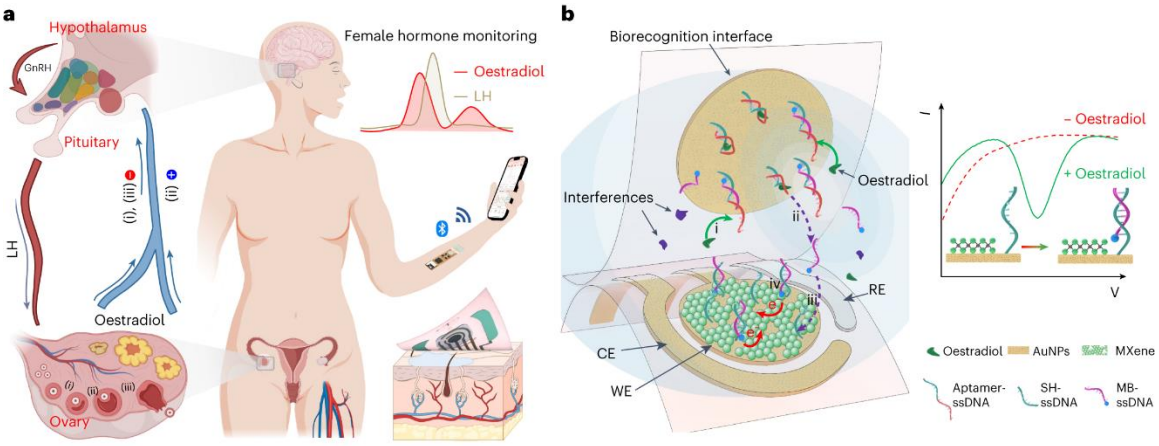

Figure 3-25: A wearable nanobiosensor based on strand-displacement aptamer switch for non-invasive reagentless female reproductive hormone analysis. a, Female hormones play an important role in women's health; non-invasive monitoring of oestradiol can be realized through sweat analysis using a skin-interfaced wearable sensor: (i) follicular phase; (ii) ovulation; (iii) luteal phase. GnRH, gonadotropin-releasing hormone; LH, luteinizing hormone; +, stimulatory effect; −, inhibitory effect. **b**, The reagentless in situ quantification of oestradiol using a AuNPs–MXene sensor coupled with a target-induced strand-displacement aptamer switch. i to iv represent recognition of the oestradiol molecule by the aptamer on the biorecognition interface (i), targetrecognition-induced strand displacement to release the MB-ssDNA (ii), recapture of thereleased MB-ssDNA by the SH-ssDNA on the working electrode (WE) (iii), and electrochemicalquantification of the methylene blue from the recaptured MB-ssDNA on the working electrode (iv). CE, counter electrode; RE, reference electrode.

3.3.2 Design and characterization of the oestradiol nanobiosensor.

The reagentless oestradiol sensor design was based on a strand-displacement aptamer switch. At the biorecognition interface, the oestradiol aptamer-ssDNA is immobilized on a AuNPs-

decorated surface, forming a partially hybridized duplex with an MB-ssDNA probe molecule, which acts as a competitive redox probe (**Fig. 3-26a**). Considering that a short MB-ssDNA with weak but selective affinity reaction to the oestradiol aptamer is desired for efficient target-induced strand-displacement reaction, a 25-base MB-ssDNA was selected on the basis of secondary structure analysis of the oestradiol aptamer[132]: a substantial hybridization reaction was obtained from the 25-base MB-ssDNA but not from the molecules with 24 or fewer bases. On the detection working electrode, a capture thiolated ssDNA (SH-ssDNA) molecule, the antisense strand of the MB-ssDNA probe molecule, is immobilized on a AuNPs–MXene electrode. In the presence of oestradiol, the MB-ssDNA is released by the aptamer-ssDNA because of the higher affinity of the aptamer to oestradiol than the partially hybridized sequence[133], and then anneals to the complementary sequence at the working electrode (**Fig. 3-26**). The recaptured MB-ssDNA probe molecules can be quantified by the redox signal measured electrochemically via a square wave voltammogram (SWV). The reagentless 'signal-on' detection approach, coupled with highly sensitive low-background SWV measurements, offers extraordinary sensitivity and applicability for ultra-low-level sweat oestradiol analysis in situ[134].

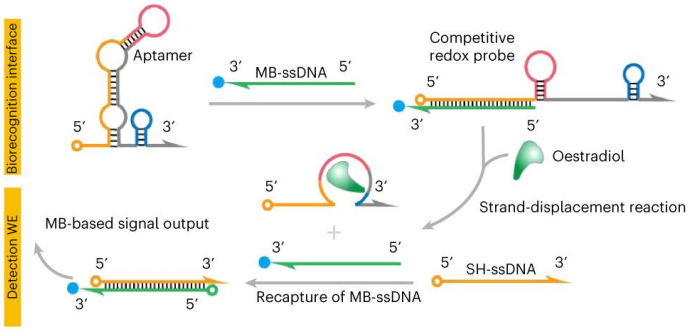

Figure 3-26. Schematic of the reagentless electrochemical aptamer sensor based on competitive redox probe displacement and recapture.

The sensor performance was evaluated by SWV in artificial sweat (0.2× PBS, pH 7.4) containing physiologically relevant oestradiol levels (0.1–100 pM) (**Fig. 3-27a**). The sensor exhibited a log-linear relationship between peak current density height of the SWV

voltammograms and target concentrations with an ultra-low limit of detection of 0.14 pM (**Fig. 3-27b**). The oestradiol sensor demonstrated high selectivity to oestradiol over a variety of potential interferences present at much higher concentrations (**Fig. 3-27c**). The accuracy of the aptamer sensors for sweat oestradiol analysis was validated by the enzyme-linked immunosorbent assay (ELISA) using iontophoresis-induced sweat samples (**Fig. 3-27d**), and a high linear correlation coefficient of 0.921 between the ELISA and biosensor results was obtained.

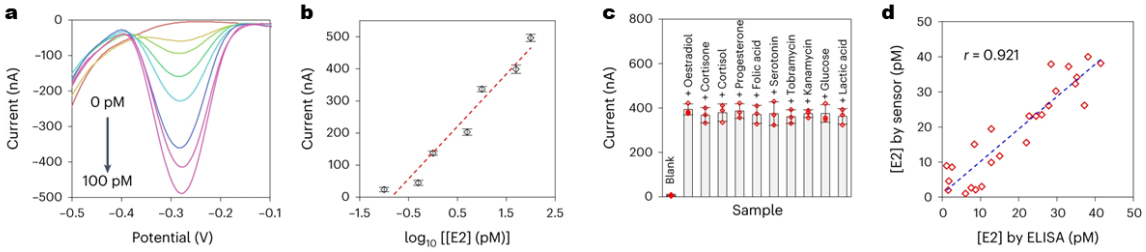

Figure 3-27. **Performance of the reagentless electrochemical aptamer sensor a**,**b**, SWV response of the aptamer oestradiol sensors in artificial sweat (0.2× PBS, pH 7.4) with 0, 0.1, 0.5, 1, 5, 10, 50 and 100 pM of oestradiol (**a**) and the corresponding calibration plot based on the peak current height of the SWV voltammograms (**b**). Each SWV voltammogram was obtained from an independent oestradiol sensor (total eight sensors) in **a**. E2, oestradiol. Error bars represent the s.d. of the mean from three sensors. **c**, Selectivity of the aptamer sensor to potential interferences (50 pM) in human sweat. Error bars represent the s.d. of the mean from three sensors. **d**, Validation of the aptamer sensor towards oestradiol quantification in iontophoresis-induced human sweat samples with ELISA (n = 25). The dashed line represeonts the linear-fit trendline. r, linear correlation coefficient.

Considering that the optimal incubation time for the competitive interaction and recapture is over 60 min, we explored the use of an external electric field (a positive potential bias between the working and counter electrodes before incubation) to reduce the incubation periods for rapid oestradiol analysis. Since ssDNA is negatively charged, applying a positive

potential at the working electrode results in electrophoresis-based enhanced transport of the released MB-ssDNA redox probe across the sensing gap and substantially reduces the necessary incubation time (**Fig. 3-29a**,**b**). As a result, electrochemical measurements reveal a substantially enhanced sensor signal after a 10 min incubation period with the application of a bias potential (1 min duration at +0.5 V before incubation) (**Fig. 3-28a** and **Fig. 3-30**), in agreement with the numerical simulation results (**Fig. 3-28b** and **Fig. 3-29c,d**). It should be noted that the hybridized MB-ssDNA dominates the signal of the final measurement while electrostatic adsorption or chelation of MB-ssDNA onto the positively charged detection working electrode only contributes to a small portion of the final measurement result. Considering that all free MB-ssDNA molecules result from the selective oestradiol-induced strand-displacement reaction, such electrostatic adsorption only contributes positively to sensitivity without compromising sensor selectivity. The oestradiol sensor can be readily regenerated in deionized water (**Fig. 3-28c**) or in acidic conditions (**Fig. 3-31**) after 1 min of incubation to perform repetitive oestradiol quantification (**Fig. 3-28d**). Successful oestradiol sensing and sensor regeneration showed only 6.2% signal drift after five cycles of repetitive measurement and/or regeneration (**Fig. 3-28d** and **Fig. 3-32**).

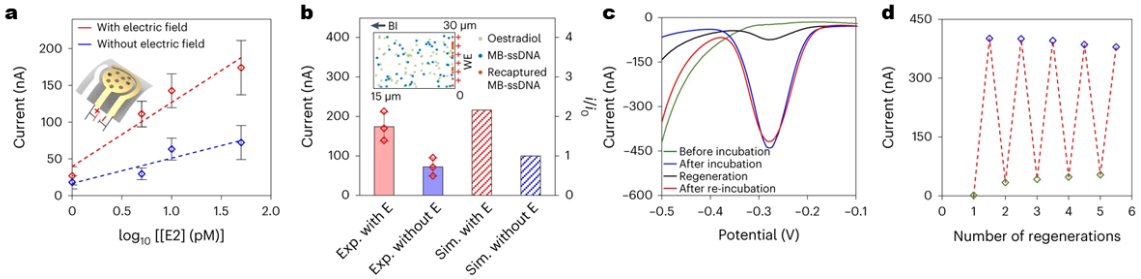

Figure 3-28. Incubation and regeneration of reagentless electrochemical aptamer sensor. a, Calibration plots of the aptamer sensors with 10 min of incubation measured with and without the assistance of an external electric field. Error bars represent the s.d. of the mean from three sensors. **b**, Experimental and simulation results of the sensor response with and without the assistance of an external electric field after 10 min of incubation. The inset shows simulated molecular diffusion and recapture of MB-ssDNA around the working electrode. Exp., experimental result; Sim., simulation result; E, electric field; BI,

biorecognition interface. Error bars represent the s.d. of the mean from three sensors. **c**,**d**, The SWV voltammograms (**c**) and the corresponding peak current height (**d**) showing the regeneration and repetitive use of the aptamer oestradiol sensors with 50 pM of oestradiol. Error bars represent the s.d. of the mean from three sensors.

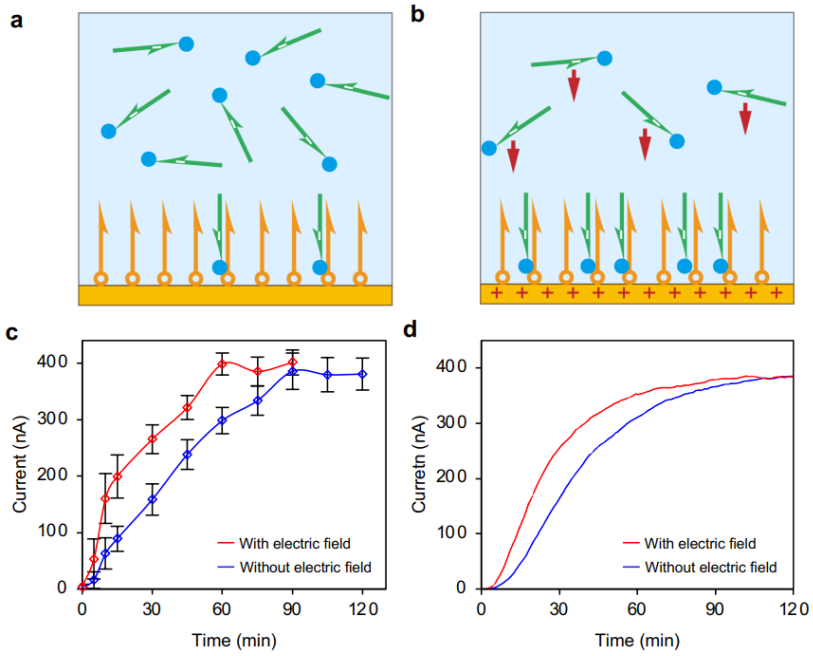

Figure 3-29. Electric field enhanced rapid estradiol analysis. a,**b**, Schematic illustration of the enhanced MB-ssDNA transport process toward the working electrode without (**a**) and with (**b**) an external electric field. **c**,**d**, The peak current height of the SWV voltammograms of the estradiol sensors (**c**) and numerically simulated sensor performance (**d**) under varying incubation time with and without the assistance of an external electric field. Error bars represent the s.d. of the mean from three sensors.

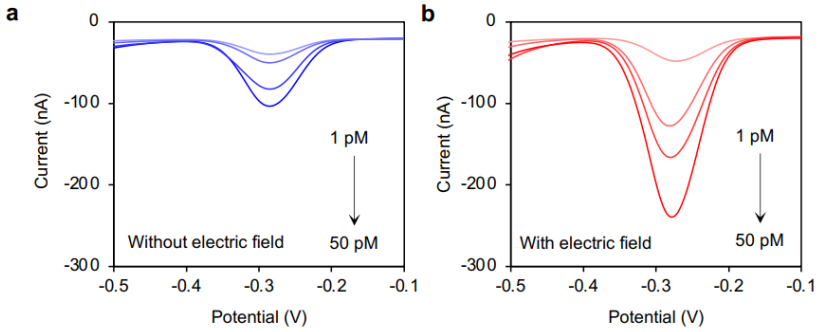

Figure 3-30. Rapid estradiol analysis with the assistance of an external electric field. **a**,**b**, SWV voltammograms obtained with 10-minute incubation of the estradiol sensors in 1, 5, 10, 50 pM estradiol without (**a**) and with (**b**) the assistance of an external electric field.

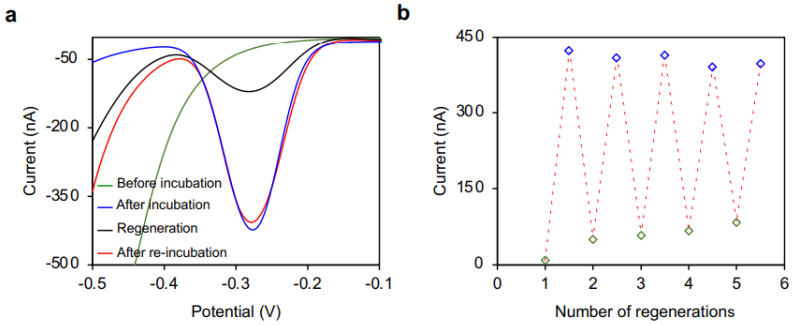

Figure 3-31. Sensor regeneration in artificial sweat. a,**b,** SWV voltammograms (**a**) of the estradiol sensors for detection of 50 pM estradiol in artificial sweat (0.2x PBS, pH 7.4) and regeneration through 1-minute rinse using artificial sweat (0.2x PBS, pH 5), and the corresponding peak current height (**b**) showing the regeneration and repetitive use of the estradiol sensors.

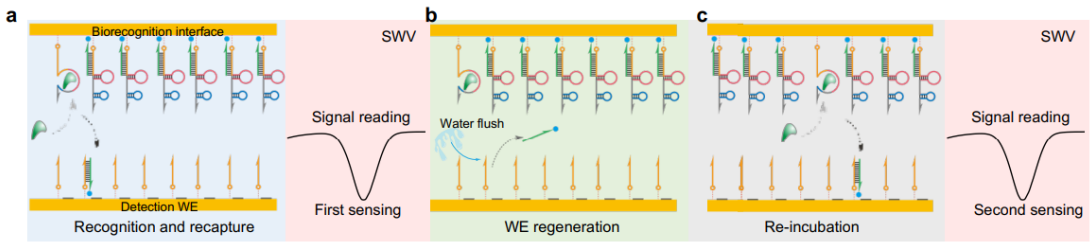

Figure 3-32. Schematic about the in vitro sensor regeneration process

Considering that the large interindividual variability in sweat compositions (that is, pH and ionic strength) could have a major influence on the target recognition and electrochemical measurement, a polyaniline-based potentiometric pH sensor and an impedimetric ionic strength sensor were developed and integrated into the sensor patch. In vitro sensor evaluation revealed linear relationships between the measured potential and pH for the pH sensor, and between measured admittance and electrolyte levels for the ionic strength sensor.

3.3.3 In vivo evaluation of the wearable oestradiol sensor

During a menstrual cycle, oestradiol level in the blood rises and falls twice as illustrated in **Fig. 3-33a**: it gradually increases in the mid-follicular phase and reaches the highest point right before ovulation; then the oestradiol level drops quickly after ovulation, followed by a secondary rise during the mid-luteal phase and a secondary decrease at the end of the menstrual cycle[135]. Compared to invasive and lengthy blood assay, analysing sweat oestradiol using wearable technology offers a highly attractive approach for remote at-home female hormone monitoring (**Fig. 3-33a**). To validate the clinical values of the sweat oestradiol measured by the sensor, human studies were conducted over two consecutive menstrual cycles on two healthy female participants by simultaneously monitoring urine luteinizing hormone, body temperature and blood oestradiol (**Fig. 3-33b**,**c**). The results revealed that oestradiol levels in both sweat and serum reached the peak right before the ovulation while the urine luteinizing hormone and temperature levels peaked during the ovulation period, confirming oestradiol's potential for early ovulation prediction. The main and secondary rise of the oestradiol was also observed in both sweat and serum in all menstrual cycles. This indicates that sweat oestradiol follows cyclical fluctuation during the menstrual cycles. In addition, a strong correlation coefficient of 0.837 was identified between sweat and blood oestradiol levels from the pilot study (**Fig. 3-33d**), suggesting the high potential of sweat oestradiol as a non-invasive biomarker for fertility and ovulation monitoring.

On-body evaluation of the wearable technology for real-time in situ oestradiol analysis was performed on three female participants on day 5, day 13 and day 20 during a menstrual cycle with the sensor patch conformally attached onto the skin (**Fig. 3-33e**). During the study, sweat was induced via the built-in iontophoresis module, and sampled by the microfluidics. Multiplexed sensor data were collected wirelessly using a user interface (**Fig. 3-33f–h**). The calibrated oestradiol levels were converted in real time and displayed in a custom-developed mobile app based on the obtained multimodal data (**Fig. 3-33e**). As expected, the lowest oestradiol levels were observed on day 5 whereas the highest values appeared on day 13 in all participants; moderate oestradiol levels were observed on day 20 due to the secondary rise of the oestradiol during the menstrual cycle. Additional control studies were performed on three male participants; very low oestradiol levels were obtained on all participants with no apparent fluctuations (**Fig. 3-34**).

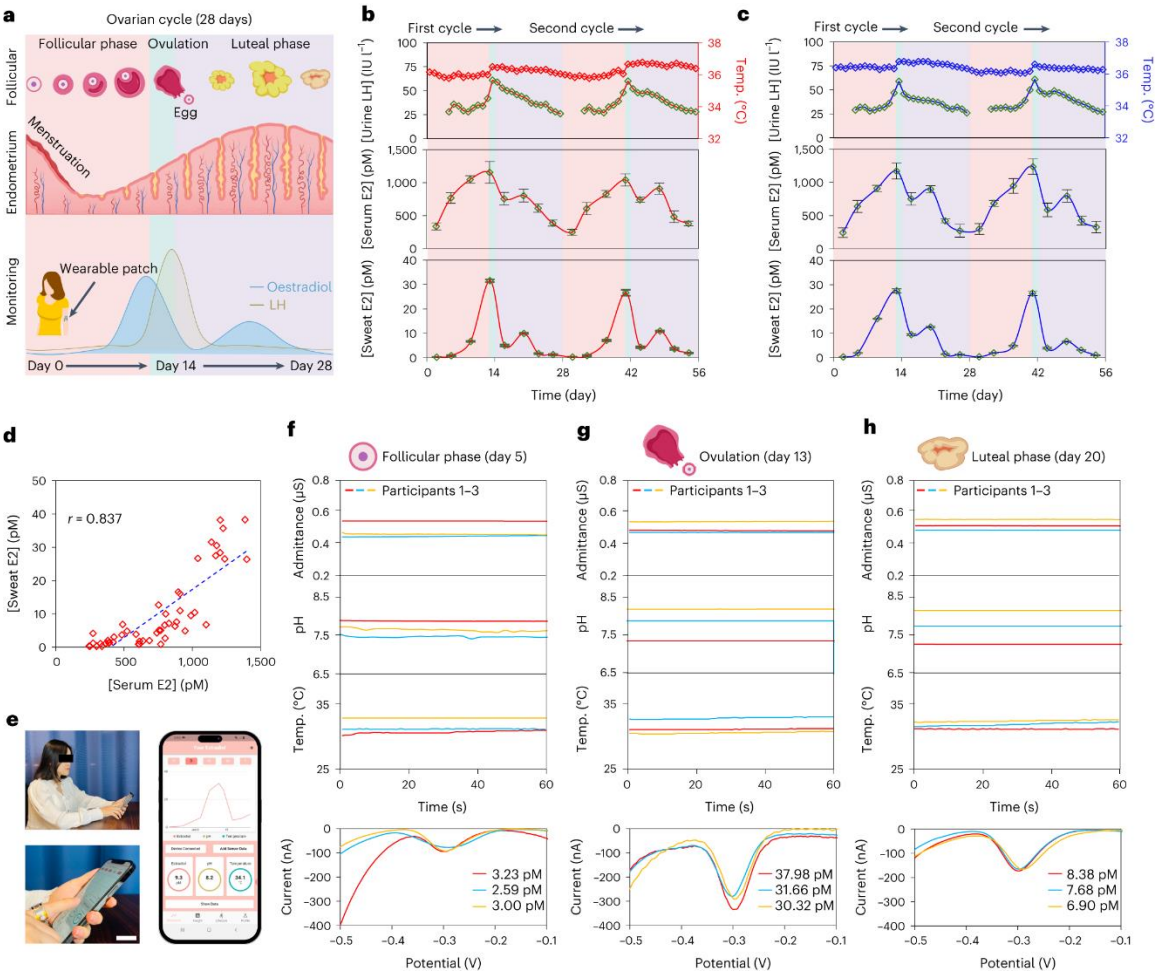

Figure 3-33. Evaluation of the wearable sensor for non-invasive female hormone monitoring in human participants. **a**, Hormonal fluctuations over the menstrual cycle. **b**,**c**, Continuous female hormone monitoring for two menstrual cycles in two female participants. Urine luteinizing hormone (LH) levels were tested by the commercial LH strips kit while oestradiol levels in serum and sweat were tested by the ELISA and the aptamer sensors, respectively. Error bars represent the s.d. of the mean from three measurements. Participant 1 was female, 32 years old (**b**) and participant 2 was female, 28 years old (**c**). **d**, Correlation of oestradiol levels between human sweat and serum ($n = 51$). Dashed line represents the linear-fit trendline. **e**, Optical images of a female human participant wearing the wireless wearable sensor during an on-body test. The collected data were wirelessly sent to a smartphone and displayed in the custom-developed mobile app. Scale bar, 1 cm. **f–h**, On-body multiplexed physicochemical sensing and

oestradiol quantification with real-time sensor calibrations using the wearable aptamer sensor in the follicular (**f**), ovulation (**g**) and luteal (**h**) phases of menstrual cycles for three female human participants. Participant 1 was female, 31 years old; participant 2 was female, 28 years old and participant 3 was female, 32 years old. Temp., temperature.

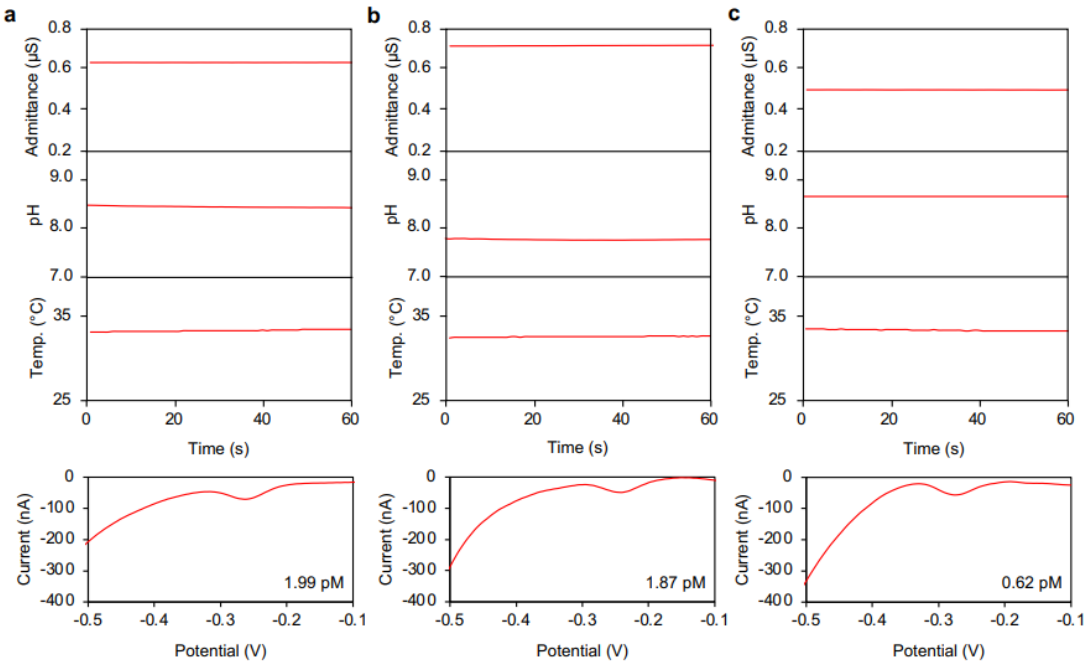

Figure 3-34. On-body wearable multiplexed physicochemical sensing and estradiol quantification in three male human subjects. Male subjects were used here as the control (compared to the female subjects in **Fig. 3-33**).

Chapter 4

SYSTEM LEVEL INTEGRATION AND POWERING OF WEARABLES

Materials from this chapter appear in "Min, J.; Tu, J.; Xu, C.; Lukas, H.; Shin, S.; Yang, Y.; Solomon, S. A.; Mukasa, D.; Gao, W. Skin-Interfaced Wearable Sweat Sensors for Precision Medicine. *Chemical Reviews* **2023**, 123 (8), 5049–5138. https://doi.org/10.1021/acs.chemrev.2c00823."

Broad adoption of wearable sensor devices that continuously and unobtrusively monitor physiochemical biomarkers can enable personalized healthcare through big data and predictive algorithms. Wearable sweat sensing offers an attractive means of biochemical screening among large populations as sweat is rich in biomarkers. However, sustainable powering of wearable sweat sensor devices is a challenge as autonomous sweat extraction, multiplexed biomarker detection, data processing, and data communication consume significant energy and typically require bulky lithium batteries. This section will first detail the various electronic modules in wearable sweat sensor devices that consume power (**Fig. 4-1**), then explore innovative approaches in sustainably powering these devices without relying of lithium batteries. We have designed and integrated various energy harvesting modules such as biofuel cells (BFCs), triboelectric nanogenerators (TENGs), and solar cells (SCs) into wearable platforms for battery-free analysis of sweat biomarkers.

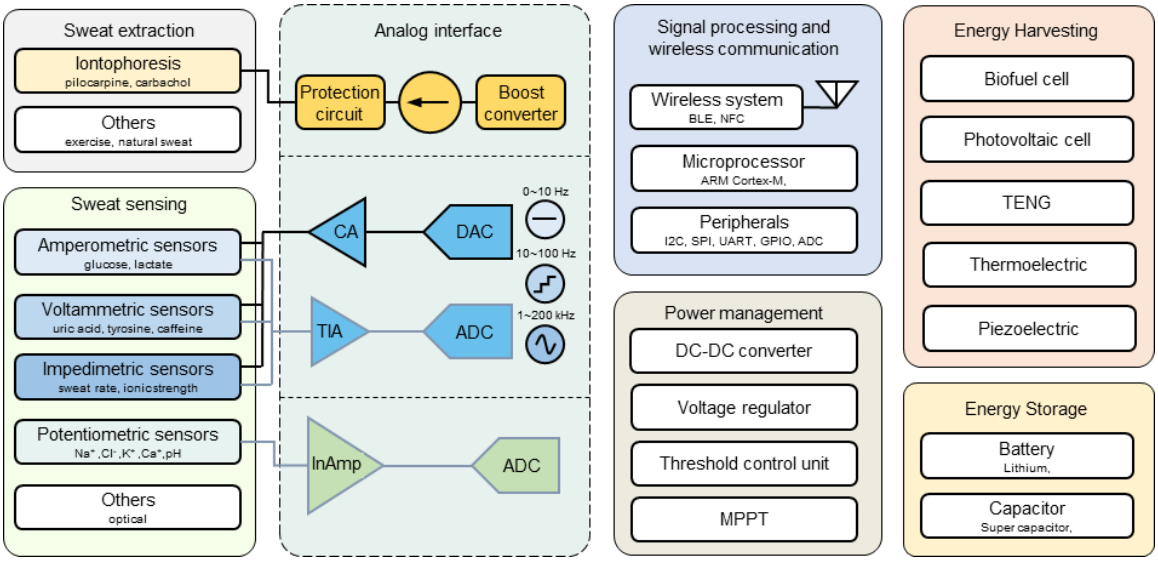

Figure 4-1. Electronic system block diagram of wearable sweat sensors. Control amplifier (CA), digital to analog converter (DAC), transimpedance amplifier (TIA), analog to digital converter (ADC), instrumentation amplifier (InAmp), serial peripheral interface (SPI), universal asynchronous receiver-transmitter (UART), general-purpose input/output (GPIO), direct current (DC).

4.1 Analog Interface

4.1.1 Iontophoretic Sweat Stimulation

The analog interface for wearable sweat sensors can be divided into two main categories: iontophoretic sweat stimulation control and electrochemical sweat analysis. For the controlled transdermal delivery of sweat inducing drugs (pilocarpine, carbachol), a high compliance voltage constant current source circuit is required. For reliable and safe sweat stimulation, a constant current density of around 1.5 mA cm^{-2} is often used, which typically requires a compliance voltage between 10 V and 40 V due to the high, dynamic, and variable impedance of the skin. As the remainder of the circuit generally operates below 5 V, a boost converter is required to generate the power supply for the current source. A variety of current source circuits have been used for wearable iontophoretic sweat stimulation: a voltage controlled current source using a differential amplifier and transistor was used for generating a variety of current waveforms[48], and a commercial three terminal current source (LM334, Texas Instruments) was used to deliver a constant current.[136] Simple constant current sources based on active transistors or linear regulators could also be explored for generating constant currents independent of the load. While skin impedance is initially high, delivery of an iontophoretic current increases skin permeability and rapidly decreases skin impedance until it levels off to a value dependent upon applied current density.[137] With a limited compliance voltage, it often takes some time for the skin impedance to decrease and applied current to reach a desired level. With poor electrode contact, the current may never reach the desired value. Therefore, it is important to monitor the applied current using a current shunt monitor or a transimpedance amplifier (TIA). Finally, a protection circuit including a current limiter and switch should be employed for user safety and to isolate the iontophoresis circuit from the measurement circuit during sweat analysis.

4.1.2 Sweat Analysis

Various electrochemical measurement techniques have been utilized for quantifying biomarker levels in sweat. A potentiostatic circuit is required for amperometric and voltammetric measurements, where the current across the reference and working electrodes

is measured in response to the application of a controlled potential across the reference and working electrodes of a three-electrode electrochemical system. Amperometric measurements are often paired with enzymatic electrodes for the detection of sweat metabolites such as glucose and lactate, whereas voltammetric measurements are often used for the direct detection of redox active biomarkers such as uric acid and tyrosine. Generally, two low input bias operational amplifiers (op-amps) are used to construct a potentiostat circuit to minimize undesired current flow into the reference electrode, including a control amplifier and a TIA. The control amplifier utilizes digital to analog converter (DAC) generated voltages to bias the reference electrode with respect to the working electrode, and the TIA converts the resultant current flowing through the counter and working electrodes into a potential that is acquired by an analog to digital converter (ADC). A constant potential is applied across the reference and working electrodes for amperometric measurements, whereas dynamic potential waveforms of various frequencies are applied for voltammetric measurements. Typically, the voltage sweep rate for voltammetric techniques is up to 50 mV/s for DPV, up to 500 mV/s for cyclic voltammetry (CV), up to 5 V/s for SWV, and up to 500 V/s for FSCV. Thus, while amperometric measurements can operate with low bandwidth operational amplifiers and long ADC measurement intervals to achieve a low power consumption, voltammetric measurements with higher frequency signals require higher bandwidth operational amplifiers and shorter ADC measurement intervals, which correlates to an increased power consumption.

Impedance measurements have been commonly used for sweat rate and sweat ionic strength sensors. Like potentiostatic circuits, impedance measurement circuits apply an alternating current (AC) voltage signal across the sensor electrodes, and then measure the resulting current waveform to compute the magnitude and phase angle of the impedance. However, impedance measurements can require the handling of AC signals with frequencies as high as 200 kHz, and therefore require a circuit with significantly higher bandwidth and complexity, as well as quick and frequent ADC conversions. In addition, due to the difficulty of transmitting large amounts of resulting ADC data, impedance measurement circuits often

incorporate a discrete Fourier transform (DFT) engine for the hardware-based processing of impedance data.

Open circuit potentiometry (OCPT) is one of the most commonly used electrochemical techniques for wearable sweat sensors due to its simplicity and low power consumption. Typically used for the selective detection of sweat electrolytes, OCPT requires a high-impedance voltmeter for measuring the potential between the reference electrode and a working electrode (ISE). As the source impedance of potentiometric sensors can be high, they must be interfaced with a high input impedance voltage buffer to minimize current flow through the electrodes. Typically, a buffered reference voltage sets the potential of the reference electrode, and an instrumentation amplifier is used to buffer and amplify the potential difference between the reference and working electrodes, and that potential is then acquired by an ADC. For sweat electrolyte measurements, the sensor response is generally stable and therefore a low bandwidth instrumentation amplifier and a long ADC measurement interval can suffice the requirements for continuous monitoring, enabling low power and small footprint instrumentation. For multiplexed sensors requiring simultaneous potentiometric and amperometric measurements, the control amplifier from the potentiostat circuit can be shared for biasing the shared reference and counter electrodes.[138]

4.2 Signal Processing and Wireless Communications

Wearable devices typically contain a microcontroller and a Bluetooth low energy (BLE) or near field communication (NFC) wireless system for signal processing. The microcontroller consists of a microprocessor that runs algorithms to control the rest of the electronic system through its peripherals (timers, ADC, etc.) and acquire and transmit accurate sweat sensor data while consuming the least power. For wireless communications, BLE and NFC are the most popular wireless communication protocols due to their low power and ease of integration into systems as mobile phones are often embedded with BLE and NFC capabilities. BLE devices operating at 2.4 GHz can transmit data up to ~100 m with a tiny antenna but requires a power supply to be on the device. On the other hand, NFC devices operating at 13.56 MHz can only transmit data up to ~10 cm with a larger antenna but do not

require a power supply as the power is wirelessly transferred from the NFC reader. BLE system-on-chips (SoCs) that integrate a microcontroller and BLE radio such as nRF52832 (Nordic Semiconductor), CC2540 (Texas Instruments), PSoC 4 BLE (Infineon Technologies) have been popularly used for developing wearable sweat sensor devices. These devices are typically in deep sleep mode (< 2 μA) and wake up intermittently to perform quick tasks or to transfer BLE data (5 ~ 20 mA) at connection intervals of up to 4 s, consuming an average current as low as 10 μA. BLE SoCs are also sometimes integrated with antennas into system-on-modules (SOMs) or system-in-packages (SiPs) to save costs on antenna design and Federal Communications Commission (FCC) certification fees. However, for mass production or customized circuit geometries, designing a custom antenna matching circuit with a BLE SoC may be more attractive. SoCs such as RF430FRL154H (Texas Instruments) integrating an NFC transponder with a microcontroller have also been used for the battery-free wireless transmission of wearable sweat sensor data.

4.3 Power Management

For battery-powered wearables, a power management circuit can be as simple as a single voltage regulator, or a direct current (DC)-DC converter followed by a voltage regulator depending on the battery voltage with respect to the operation voltage of the system. However, for prolonged device use and extended battery life, it is often beneficial to include charging and battery management circuits that make sure the battery safely charges and discharges within a desired temperature current, and voltage range. Energy harvesting wearables often require additional circuitry to best utilize the scavenged electricity for either charging a battery or supercapacitor, or directly powering the electronics through capacitors. Energy harvesters such as biofuel cells or solar cells that generally output low DC voltages require DC-DC boost converters with dynamic maximum power point tracking to extract maximal energy while boosting the supply voltage above the system operation voltage for charging an energy storage device. Energy harvesters that output a DC voltage significantly higher than the system operation voltage, such as solar cells connected in series, can directly charge the energy storage device. On the other hand, energy harvesters such as TENGs and

piezoelectric nanogenerators (PENGs) that output an AC voltage require a bridge rectifier for converting the AC voltage into a DC voltage that can charge the energy storage device either directly or through a boost converter depending on the magnitude of the voltage. Furthermore, energy harvesting wearables require a threshold control unit and protection circuit to regulate the charging and discharging of energy storage devices for safe and energy efficient powering of wearables. For example, the threshold control unit can allow an energy harvesting device to fully charge an energy storage device to an upper threshold voltage; then, the energy storage device can simultaneously be charged and discharged to power the electronics through a voltage regulator until the energy storage device reaches a lower threshold voltage; then, the energy storage device can stop discharging and get charged back to the upper threshold voltage. Power management integrated circuits (PMICs) that integrate these functionalities into a single chip greatly reduce system footprints and energy losses[139].

Chapter 5

HARVESTING ENERGY FROM BODY MOTIONS

Materials from this chapter appear in "Song, Y.; Min, J.; Yu, Y.; Wang, H.; Yang, Y.; Zhang, H.; Gao, W. Wireless Battery-Free Wearable Sweat Sensor Powered by Human Motion. *Science Advances* **2020**, *6* (40), eaay9842. https://doi.org/10.1126/sciadv.aay9842." and " Yu, Y.; Nassar, J.; Xu, C.; Min, J.; Yang, Y.; Dai, A.; Doshi, R.; Huang, A.; Song, Y.; Gehlhar, R.; Ames, A. D.; Gao, W. Biofuel-Powered Soft Electronic Skin with Multiplexed and Wireless Sensing for Human-Machine Interfaces. *Science Robotics.* **2020**, *5* (41), eaaz7946. https://doi.org/10.1126/scirobotics.aaz7946.", and " Min, J.; Gao, W. Battery-Free Wearable Electrochemical Sweat Sensors. In *2023 IEEE International Flexible Electronics Technology Conference (IFETC)*; IEEE: San Jose, USA, CA, USA, **2023**; pp 1–5. https://doi.org/10.1109/IFETC57334.2023.10254891."

Current wearable devices in the market are primarily powered by bulky rechargeable lithium-ion batteries that need to be charged by a universal serial bus (USB) cable or through inductive coupling every couple of days. In the short run, companies are looking for innovations to extend the battery life of wearable devices and minimize the inconveniences of frequent charging. While the increase of battery power density is slow, rapid improvements in low-power electronics and wireless communication protocols have contributed significantly to extend the battery life of wearables, and the convenience of wireless charging options has also appealed to customers. On the other hand, charging of wearable devices can be eliminated by developing wearable energy harvesting systems that can harvest energy from the body through sweat or motion. In the long term, it is also critical to devise powering systems that are biocompatible and sustainable. Currently lithium batteries are rigid and bulky, limiting wearability to applications such as wrist watches that people are already accustomed to. Furthermore, lithium batteries often contain toxic heavy metals and flammable electrolytes that can cause potential safety hazards and disposal burdens.[140] Wearable powering systems composed of energy harvesting modules and energy storage modules that are flexible, stretchable, washable, and sustainable are highly sought after. These innovations will not only serve as a convenience to everyday users of wearable sensors, but also can be life changing in emergency or military scenarios where traditional device charging is not possible.

5.1 Background

Over the past years, extensive interest and efforts have focused on developing novel sensors and improving the wearability of these platforms.[141,142] Until now, most wearable sensor prototypes relied on bulky and rigid battery packs to power the electronic circuitry for data acquisition, processing, and transmission. Flexible batteries have been proposed to enable conformal contact on skin[143,144], and incorporation of low-power electronics has substantially reduced the power requirements of wearables and enabled the use of small coin cell batteries. Despite these efforts, batteries still face limitations in that they need to be charged and replaced frequently. In addition, while unlikely, lithium ion batteries are susceptible to

explosion, posing safety concerns. Battery-free systems powered by near-field communication (NFC) are reported[145,146] but could suffer from short operation distance. As an alternative, energy can be harvested from renewable, portable, and sustainable sources such as solar light, biofluids, and human motion to power future wireless wearable electronics.[147–150]

TENG, which convert the mechanical energy created by human motion into electrical energy via coupling of inductive and triboelectric effects[151–156], offer a highly attractive energy harvesting strategy to power wearable sweat sensors during intensive physical activities as their operation is independent from uncontrollable external sources such as sunlight or wireless power transmitters. Despite the advantage, most of the existing TENG-based devices suffer from low power intensity, inefficient power management, and a lack of power continuity and longevity; thereby, the use of a TENG to continuously power a fully integrated wireless wearable molecular sensor system has not been reported.[149,157–160]

Here, we propose a battery-free, fully self-powered wearable system that consists of a highly efficient wearable freestanding-mode TENG (FTENG), low-power wireless sensor circuitry, and a microfluidic sweat sensor patch on a single FPCB platform that can dynamically monitor key sweat biomarkers (e.g., pH and Na^+) (**Fig. 5-1a**). Such an FTENG-powered wearable sweat sensor system (FWS^3) is designed and prepared to be compatible with traditional FPCB manufacturing processes, which enables mass productivity and high reliability. Our freestanding FPCB-based design, coupled with effective power management, allows efficient energy harvesting from human skin, particularly suitable for powering skin-interfaced wearables. With the aid of waterproof medical tape, the FWS^3 can be conformally laminated on the side torso to maximize the potential for energy harvesting (**Fig. 5-2b,c**). The integrated Bluetooth Low Energy (BLE) module allows sensor data to be conveniently transmitted to a mobile interface for health status tracking during exercise. This represents the first demonstration of a fully integrated battery-free triboelectrically driven wearable system for multiplexed sweat sensing.

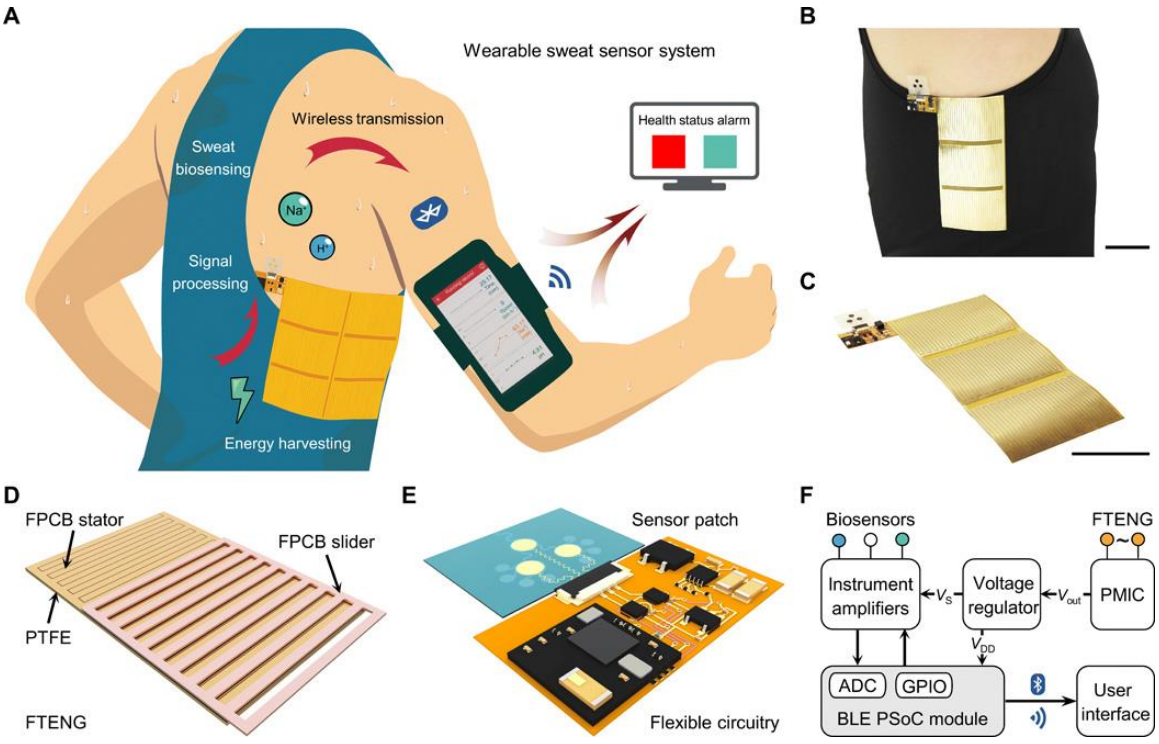

Figure 5-1. Battery-free FWS[3] for wireless and noninvasive molecular monitoring. a, Schematic illustrating the FWS[3] that integrates human motion energy harvesting, signal processing, microfluidic-based sweat biosensing, and Bluetooth-based wireless data transmission to a mobile user interface for real-time health status tracking. **b**,**c**, Optical images of an FPCB-based FWS[3], which can be worn on a human side torso. Scale bars, 4 cm. **d**, Schematic diagram of the FPCB-based FTENG with a grating slider and an interdigital stator. **e**, Schematic diagram of the FWS[3] showing a microfluidic-based sweat sensor patch interfacing with the flexible circuitry. **f**, System-level block diagram showing the power management, signal transduction, processing, and wireless transmission of the FWS[3] from the FTENG to the biosensors, then to the user interface. Photo credit: Yu Song, California Institute of Technology.

5.2 Results

5.2.1 Design of the FWS[3]

The FTENG consists of an interdigital stator and a grating-patterned slider (**Fig. 5-2d**). To obtain a strong electrification effect, polytetrafluoroethylene (PTFE) and copper are used as tribo-pairs in the flexible FTENG. The FTENG is fabricated through commercial FPCB technology (as illustrated in **Supplementary Fig. 5-1**), and the detailed dimensional parameters are shown in **Supplementary Fig. 5-2**. The inter-electrode distance was optimized through transferred charge density studies of the FTENGs (**Supplementary Fig. 5-3**). The stator and slider are patterned through photolithography as the periodically complimentary interdigital structure and the grating structure, respectively. With an electroless nickel/immersion gold (ENIG) surface finish on the electrode area, the stator is further laminated by PTFE. The reusable flexible circuitry in conjunction with a disposable microfluidic sweat sensor patch can continuously perform electrochemical measurements of key biomarkers in sweat (**Fig. 5-2e**). During exercise, the FTENG generated power is stored and released from a capacitor as controlled by the power management integrated circuit (PMIC) (**Fig. 5-2f**). When fully charged, the storage capacitor releases its stored energy, which is regulated to a stable voltage to power the BLE programmed system on a chip (PSoC) module and instrumentation amplifiers for acquisition and transmission of potentiometric measurements over BLE.

5.2.2 Characterization of the FTENG

The working mechanism of the FTENG can be explained as the coupling effect of contact electrification and in-plane sliding-induced charge transfer, as illustrated in **Fig. 5-2a**. As copper is more triboelectrically positive than PTFE, electrons accumulate on PTFE during the sliding process. In the initial state, the grating slider fully overlaps with one stator electrode and no charge flow occurs between the interdigital stator electrodes due to the electrostatic equilibrium. The unidirectional sliding process results in a charging flow between stator electrodes until the grating slider fully overlaps with the second stator electrode with reversed polarity. This working process was further validated by numerical

simulation using COMSOL Multiphysics (**Supplementary Fig. 5-4**). The detailed model of the FTENG under open-circuit and short-circuit conditions is explained in **Supplementary Fig. 5-5** and notes S1 and S2. The optical microscopic image of our proposed FPCB-based FTENG and the typical short-circuit current (I_{SC}) profiles of an FTENG at different working frequencies are shown in **Fig. 5-2b**,**c**. The FTENG operates consistently at varying frequencies of 0.5, 1.25, and 3.3 Hz, resulting in the maximum I_{SC} of 8.39, 19.11, and 42.25 μA, respectively. The open-circuit voltage (V_{OC}) attained at the frequency of 0.5 Hz is presented in **Supplementary Fig. 5-6a**, where the signal polarity of the envelope waveform oscillates rapidly along the sliding process. To evaluate the use of our FPCB-based FTENG as a power source, the voltages and powers are measured under a series of different load resistances (**Fig. 5-2d**), with a working frequency of 1.5 Hz for actuation. An increase of resistance beyond 1 megohm leads to a rapid increase of voltage. With a load resistance of 4.7 megohms, the FTENG reaches a maximum power output of 0.94 mW (corresponding to 416 mW m^{-2}).

The PTFE of the FPCB-based FTENG displays superior durability performance over conventional micro-pyramid polydimethylsiloxane (M-PDMS) and wrinkled PDMS (W-PDMS) after 20,000 working cycles, where the VOC experiences minimal decay as displayed in **Supplementary Fig. 5-6b**. The scanning electron microscopy (SEM) images in **Fig. 5-2e** and **Supplementary Fig. 5-7** reveal the morphologies of different triboelectric materials before and after the durability test: The PTFE shows great mechanical robustness without scratches, while both M-PDMS and W-PDMS suffer notable surface damage. The influence of normal force and shear force (reflected by sliding frequency) on the performance of the FTENG during regular use is demonstrated in **Supplementary Fig. 5-8**: The peak output voltage increases and then saturates with the increase of normal forces, while the output voltage remains stable under varied sliding frequencies for a given normal force. The FTENG is mechanically robust and shows similar electrical output even under a high normal force of 100 N. The FTENG's response is stable after 1000 bending cycles (radius of curvature, 5 cm) (**Supplementary Fig. 5-9**) and under varied physiological temperatures (**Supplementary Fig. 5-10**). Moreover, the FTENG could maintain high performance after

100 washing cycles, indicating superior wearable capabilities over conventional TENGs (**Supplementary Fig. 5-11** and **Supplementary Table 5-1**). In designing future TENG-powered devices, it is important to consider factors such as cost, materials, mechanical properties, and power density. TENGs commonly prepared through fabric weaving and polymer coating processes are very low cost but limited by low fabrication resolution and reproducibility. In contrast, the FPCB-based FTENG offers a high-resolution, cost-effective, and mechanically robust energy harvesting solution.

To meet the high energy demands of the wearable sensors, one, three, and six panels of the FTENGs, designed by taking consideration of the size of human side torso, were further evaluated by capacitor charging (**Fig. 5-2f**). The output of the FTENG was rectified with a full-wave rectifier. These different FTENG layouts were each actuated for 30 working cycles to charge capacitors ranging from 10 to 1000 μF (**Fig. 5-2g**). For the capacitor with 1000 μF, 0.03, 0.12, and 0.19 V could be obtained for one, three, and six panels, respectively, showing great charging capability. At a working frequency of 3.3 Hz, the six-panel FTENG showed a maximum transferred charges (σSC) of 15.73 μC during one working cycle (**Supplementary Fig. 5-12a**). Meanwhile, **Supplementary Fig. 5-12b** portrays the charging-discharging curves of different capacitors charged to 2 V with a three-panel FTENG at a working frequency of 2 Hz. The three-panel FTENG, actuated at a working frequency of 1.5 Hz, was able to repetitively charge a 47-μF capacitor over a 2-hour duration from 0 to 2 V (**Fig. 5-2h**), indicating high long-term cycling stability. The FTENGs can also be used to charge capacitors of various capacitances at different cycle lengths (**Supplementary Fig. 5-13**). Depending on the application, connecting several FTENGs in parallel can be a practical and attractive strategy to greatly increase power output.

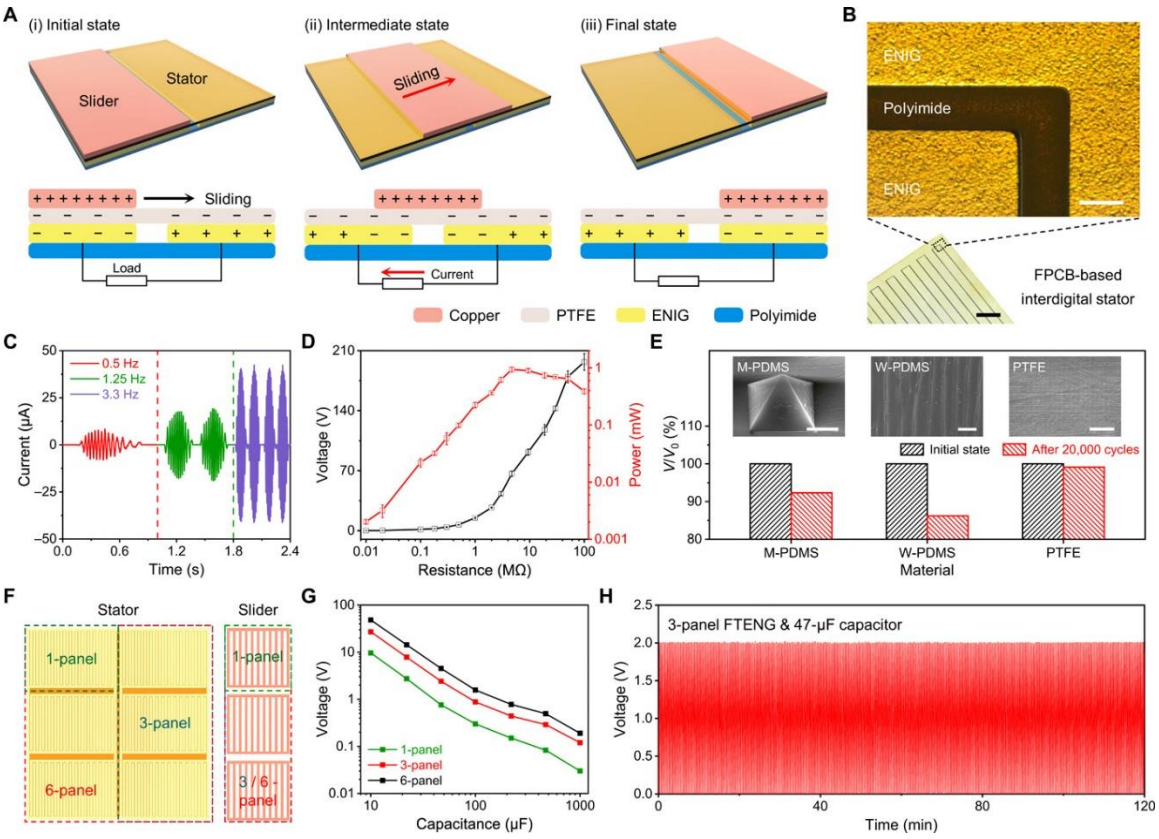

Figure 5-2. Characterization of the FTENG for energy harvesting from human motion. a, Schematic illustration of the working mechanism and charge distribution of the FTENG. **b**, Microscopic and optical images of an FPCB-based interdigital stator with an ENIG surface finish on the patterned electrode area. Scale bars, 200 μm and 5 mm. **c**, Current output of an FTENG under different working frequencies. **d**, Peak voltage and the corresponding average power of an FTENG at different external load resistances (n = 5). Working frequency, 1.5 Hz. **e**, Durability of M-PDMS–, W-PDMS–, and PTFE-based stators after 20,000 test cycles. V and V_0 represent the peak open-circuit voltage after and before the durability test. Inset images, SEM images of M-PDMS, W-PDMS, and PTFE after 20,000 test cycles. Scale bars, 5, 50, and 50 μm. **f**, Schematic of the flexible FTENG with different stator layouts (one, three, or six panels in parallel) and corresponding slider layouts. **g**, Comparison of voltages of the capacitors ranging from 10 to 1000 μF charged with one-, three-, and six-panel FTENGs for 30 cycles. **h**, Long-term stability of a three-

panel FTENG in charging a 47-μF capacitor under a working frequency of 1.5 Hz for 2 hours.

5.2.3 Design and characterization of microfluidic sweat sensor patch

Fig. 5-3a depicts the schematic of the dual biosensor array used for sweat analyte analysis based on ion-selective electrodes (ISEs). Laser-engraved microfluidic channels are assembled onto the sensing patch. Detailed fabrication procedures are listed in Materials and Methods and **Supplementary Fig. 5-14**. The Ag/AgCl reference electrode is coated with polyvinyl butyral (PVB) to sustain a steady potential for the potentiometric measurements of various electrolytes in sweat regardless of solution ionic strength. For pH analysis, the deprotonation of H^+ atoms on the surface of the electrodeposited polyaniline (PANI) layer is measured as an indicator of bulk H^+ concentration. Na^+ concentration measurements are facilitated by a thin ion-selective membrane containing a Na^+ ionophore X and a poly(3,4-ethylenedioxythiophene (PEDOT):poly(sodium 4-styrenesulfonate) (PSS) layer in between the gold electrode layer and sodium ion-selective membrane as an ion-electron transducer that can minimize the potential drift of the biosensor. As depicted in **Fig. 5-3b,c**, the pH and Na^+ sensors display near-Nernstian sensitivities of 56.28 and 58.63 mV per decade concentration, respectively, in physiologically relevant pH levels (4 to 8) and Na^+ concentrations (12.5 to 200 mM). Both sensors show excellent selectivity, reproducibility, and long-term stability (**Supplementary Figs. 5-15-17**), and their responses remain stable under different physiological temperatures (**Supplementary Fig. 5-18**), making them suitable for wearable continuous monitoring.

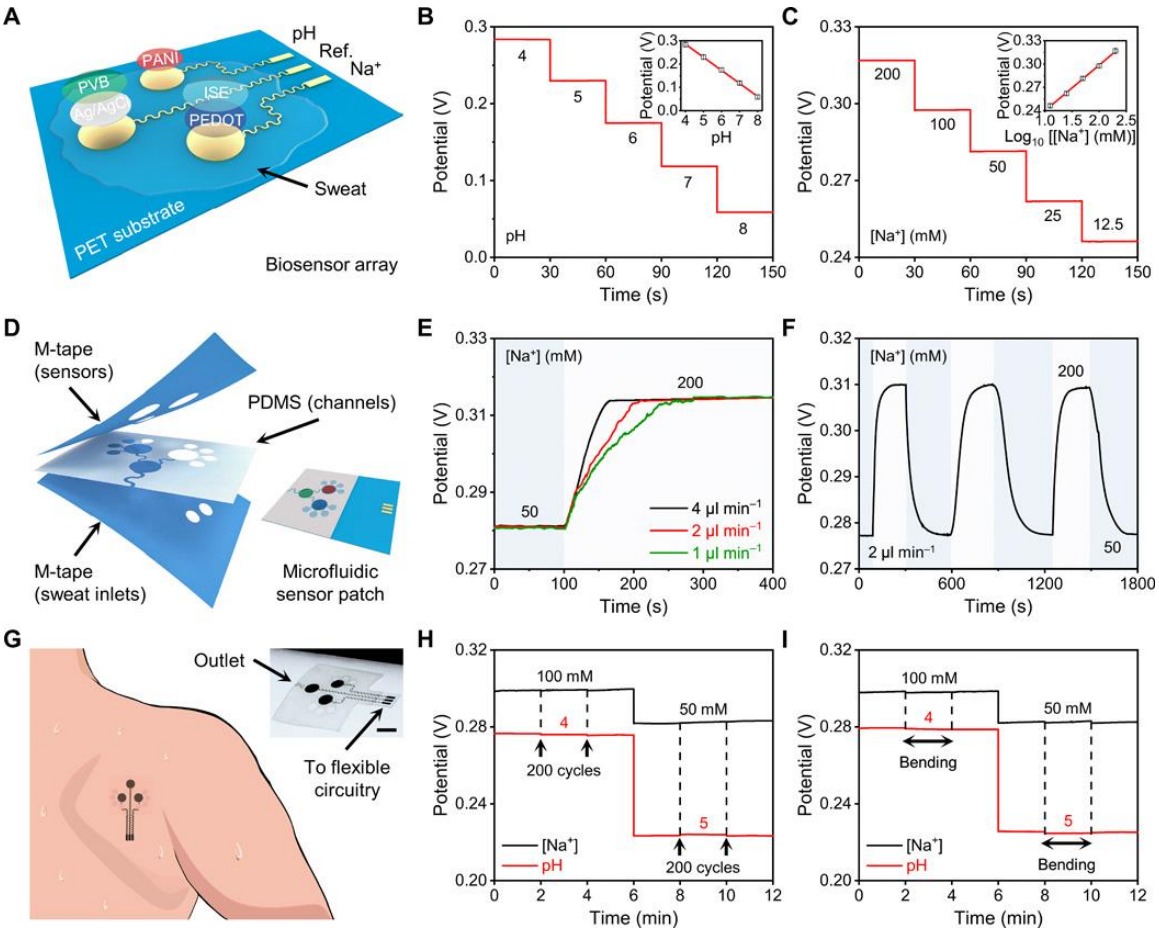

Figure 5-3. Characterization of the microfluidic-based biosensor patch in vitro. a, Schematic of a flexible biosensor array containing a pH sensor and a Na^+ sensor patterned on a flexible PET substrate. **b**,**c**, Open-circuit potential responses of a pH sensor in standard Mcllvaine's buffer solutions (**b**) and a Na^+ sensor in NaCl solutions (**c**). Insets show the corresponding calibration plots of each sensor. Error bars represent the SDs from six independent tests. (**d**) Schematic of the microfluidic design for dynamic sweat sampling. M-tape, medical tape. (**e**) Dynamic response of a Na^+ sensor under different flow rates upon switching the solution concentrations. (**f**) Repeatability of dynamic response of a Na^+ sensor by continuously switching the inflow solutions at a flow rate of 2 μl min^{-1}. (**g**) Schematic of microfluidic sensor patch conformally attached to human skin. Inset image, optical image of a microfluidic sensor patch under mechanical deformation. Scale bar, 5 mm. **h**,**i**, Responses of a Na^+ and pH sensor array after 0, 200, and 400 cycles of bending

(**h**) and during bending states (**i**) (radius of curvature, 2 cm). Data recording was paused for 30 s to change the conditions and settings. Photo credit: Yu Song, California Institute of Technology.

Laser patterned microfluidic layers were attached onto a polyethylene terephthalate (PET) sensor substrate in a sandwich structure (medical-tape/PDMS/medical-tape) for controlled and automated on-body sweat sampling (**Fig. 5-3d** and **Supplementary Fig. 5-19**). To validate the performance of the microfluidic system, dynamic biosensing was performed during continuous flow injection of Na+ solutions at varying physiologically relevant sweat rates (1, 2, and 4 μl min−1) (**Fig. 5-3e**). When the Na+ concentration was switched from 50 to 200 mM at a flow rate of 2 μl min−1, the Na+ sensor took ~2 min to reach new stable readings. The high temporal resolution is repeatable over multiple concentration change cycles (**Fig. 5-3f**). The flexible microfluidic sensor patch can conformally adhere to human skin (**Fig. 5-3g**) and shows excellent mechanical stability through rigorous bending tests (radius of curvature, 2 cm), indicating their potential for wearable applications in various physical activities (**Fig. 5-3h,i**).

5.2.4 System-level integration for energy management and low-power biosensing

As aforementioned, the FWS^3 consists of an interdigital FENG stator, a PMIC, a low-dropout voltage regulator, two low-power instrumentation amplifiers, and a BLE PSoC module seamlessly integrated onto a polyimide-based FPCB. In addition, the full platform requires a grating-patterned FTENG slider and a microfluidic sensor patch. For design compatibility and flexibility, the FTENG and electronic circuitry were designed on a single PCB design software. The detailed part list and circuit diagram for the flexible circuitry are shown in **Supplementary Figs. 5-20 and 5-21**, respectively. A block diagram illustrating the electrical connections between the modules is shown in **Fig. 5-4a**. For optimal power management, a commercial energy harvesting PMIC was adopted to manage power generated by the FTENG with minimal power waste. With the aid of a bridge rectifier that converts the high voltage AC signal generated by the FTENG into a DC signal, the PMIC stores the FTENG generated power in two capacitors in parallel (220 and 22 μF). The three SET_V_{OUT} resistors

set the programmable threshold and hysteresis voltages such that the stored power is released only when absolutely necessary through built-in switch control logic. When the voltage of the storage capacitors (V_{STORE}) reaches 3.5 V, the capacitors supply energy to the load/output (V_{OUT}) until V_{STORE} decreases to 2.2 V. At 2.2 V, the PMIC's control unit disconnects the storage capacitors from the load/output until the storage capacitors are charged back to 3.5 V. When supplied by the storage capacitors, the load/output voltage is regulated to 2.2 V by a voltage regulator to provide a stable voltage for the precise measurement circuitry.

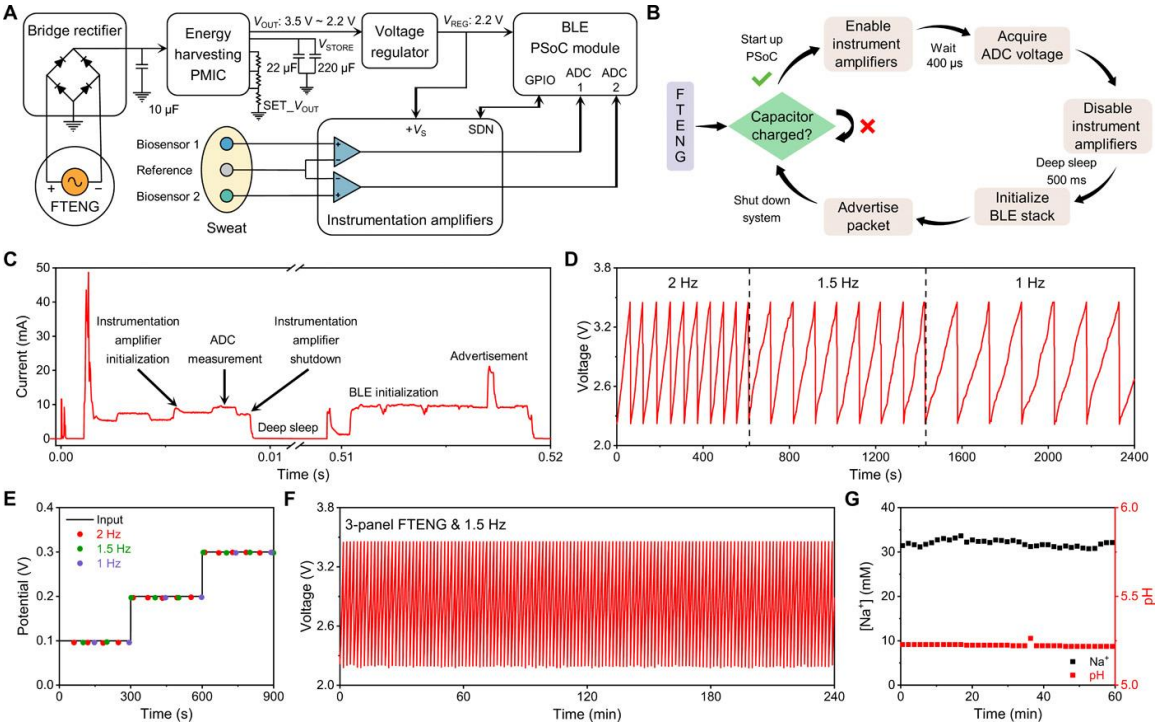

Figure 5-4. System-level integration and evaluation of the FWS³. a, Schematic diagram of the battery-free FWS³ consisting of an FTENG module, a biosensor interface, instrumentation amplifiers, an energy harvesting PMIC, a voltage regulator, and a BLE PSoC module. **b**, Operation flow of the FWS³ with signal processing and data transmission. **c**, Power consumption of the FWS³ during the operation. **d**, Real-time potential of the capacitor (242 μF) during the continuous operation of the FWS³ with a three-panel FTENG under different working frequencies. **e**, Validation of data transmission from an FWS³ with

a three-panel FTENG under different working frequencies. **f**, Long-term stability of the capacitor charging process when an FWS^3 operates under a working frequency of 1.5 Hz. **g**, Sensor responses in a collected human sweat sample when an FWS^3 operates under a working frequency of 1.5 Hz.

Efficient power management is matched with low-power measurement via low-power instrumentation amplifiers with shutdown modes, and low-power data transmission via connectionless BLE advertisements to enable FTENG-powered wearable and wireless sweat analysis. Every time the storage capacitor is charged to 3.5 V, the BLE PSoC module initiates one ~510-ms operation cycle as portrayed in the flow diagram (**Fig. 5-4b**). After startup of the main processor, the PSoC pulls a general-purpose input/output (GPIO) pin high to wake up the two instrumentation amplifiers from shutdown. After initialization of the instrumentation amplifiers, the PSoC's embedded 12-bit ADC samples and averages 32 potentiometric measurements acquired through the instrumentation amplifiers. After ADC measurements, the instrumentation amplifiers are shut down to minimize power consumption. The BLE submodule of the PSoC requires the 32-kHz watch crystal oscillator (WCO) for accurate operation, which has a maximum startup time specification of 500 ms. Therefore, after the ADC measurements, the main processor of the PSoC starts the WCO and goes into deep sleep for 500 ms where it consumes ~2 μA. Then, the BLE stack initializes and the ADC measurements are advertised to a nearby BLE observer user device. The detailed power consumption breakdown of the circuit including the voltage regulator, BLE PSoC module, and two instrumentation amplifiers is shown in **Fig. 5-4c**. When supplied with 2.2 V, the circuit consumes an average of 330 μA during ~510 ms (168 μC).

Several studies were performed to validate the robust operation of the fully integrated system. The three-panel FTENGs were activated via sliding motion at frequencies ranging from 2 to 1 Hz to simulate human arm swing during exercise.[161] The resultant charging and discharging cycles of the storage capacitors are shown in **Fig. 5-4d**. Furthermore, to validate the operation of the low-power wireless sensor circuitry, the potentiometric inputs were simulated by using a DC power supply to apply voltages ranging from 100 to 300 mV (charged every 300 s)

across the reference and working electrode pins (**Fig. 5-4e**). These simulated sensor inputs were accurately measured and transmitted by the FPCB platform while being powered by a three-panel FTENG actuated at various working frequencies. The long-term stability of the whole FWS^3 system is demonstrated by using the FTENG to power the FPCB for more than 4 hours, during which pH and Na^+ concentrations in collected human sweat were measured for an hour (**Fig. 5-4f,g**). Furthermore, the long-term durability of the FPCB-based FTENG was tested by comparing its ability to power the whole platform after 1 month of its initial use (**Supplementary Fig. 5-22**). Improvements in wireless data transmission in terms of transmission interval can be attained by further advancing the power density and efficiency of the FTENG.

5.2.5 On-body evaluation of the FWS^3 in prolonged physical activities

Common cardiovascular exercises such as running, rowing, and elliptical training induce a sliding motion between the side of the torso and the inner arm. Taking advantage of this mechanical motion, the stator of FTENG can be fixed on the side torso, and the slider of FTENG can be attached to the inner part of the arm. For on-body evaluation, a six-panel stator FTENG-based FWS^3 was used for increased power output (as illustrated in **Supplementary Fig. 5-23**). The FTENG power output waveforms during various exercises are shown in **Fig. 5-5a**. Treadmill running was chosen as the exercise to perform on-body validation experiments for the entire system. The FPCB's storage capacitor charging and discharging curve during a 60-min constant speed running session shows that up to 18 operation cycles can be achieved (**Fig. 5-5b**). The length of charging/discharging cycle ranges from 2.1 to 3.7 min (**Fig. 5-5c**). It should be noted that the system generates power when the stator and slider physically rub against each other; the charge in the capacitor will accumulate without discharge whenever there is rubbing motion; when the capacitor is charged to a threshold voltage, the capacitor will discharge and power a single measurement event. Despite duration variations in capacitor charging/discharging cycles caused by varied rubbing area, forces, and frequencies, the FWS^3 system proved itself to be fully functional during normal physical exercises (**Supplementary Fig. 5-24**). On-body performance of the entire FWS^3 was evaluated on a healthy subject through treadmill running at a constant speed

of 9 km hour^{-1}. Two wearable systems, charged by the FTENG and the battery, were placed on the back of the subject. The physiological information collected by both systems were wireless-transmitted to a user interface through BLE for further analysis (**Fig. 5-5d**). Five measurements were recorded from the FWS^3 during the 30-min exercise; stable pH levels and increased Na^+ levels were observed from both systems (**Fig. 5-5e**), confirming the accuracy of the battery-free FWS^3 for on-body sensing. The noise contribution during various exercises performed by the subjects wearing an FWS^3 is insignificant in comparison to the sensor signal of interest (**Supplementary Fig. 5-25**). These data demonstrate the potential of the self-powered wearable platform for continuous monitoring of various physiological biomarkers in sweat during exercise.

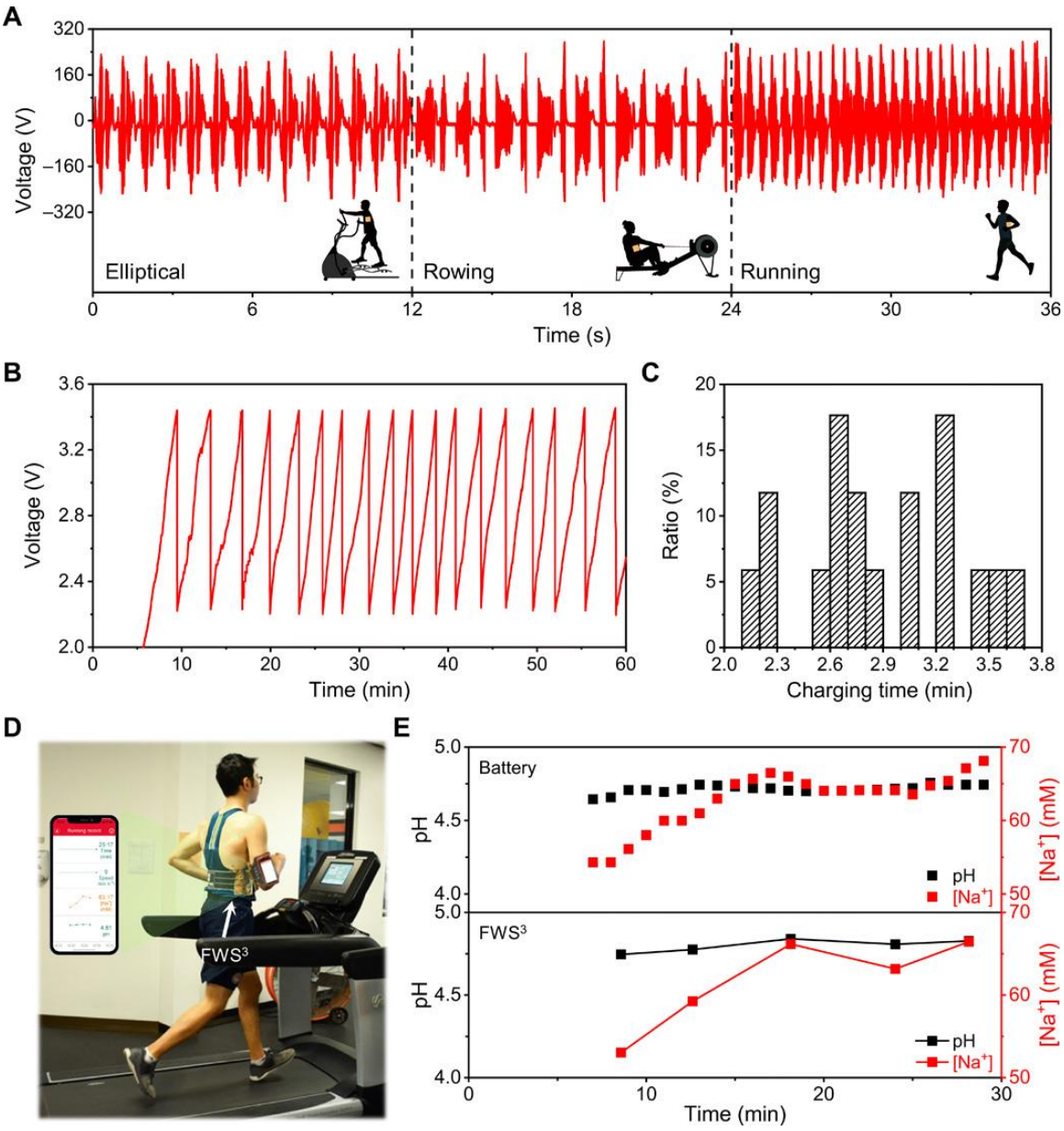

Figure 5-5. On-body evaluation of the FWS³ for wireless, dynamic perspiration analysis. a, Output waveforms of a six-panel FPCB-based FTENG during various exercises. **b**,**c**, Real-time potential of the capacitor charged by an FTENG (**b**) and the average charging time for each package transmission (**c**) when a subject is running on a treadmill for 1 hour at a constant speed of 9 km hour^{-1}. The ratio in **c** represents the percentage of charging cycles (with charging duration within a given time range) out of all the charging cycles. When the potential reaches 3.3 V, the capacitor is discharged due to

the BLE data transmission. **d**, Optical image of a subject on a treadmill wearing an FWS[3] and a mobile phone. **e**, Real-time sweat pH and Na^+ levels wirelessly obtained from the wearable systems charged by a lithium battery and by an FTENG during constant speed running. Photo credit: Yu Song, California Institute of Technology.

5.3 Discussion

The emerging wearable technologies have enabled numerous personalized medical applications. Wearable sweat analysis has the potential to achieve noninvasive and continuous monitoring of an individual's health status at molecular levels. Owing to the multifunctioning and multitasking requirements, wearable sweat biosensors usually have high power consumption. Batteries are the primary power source of most of the wireless e-skin systems but usually suffer from limited usability, especially when there is limited electricity availability. Given that a major application of sweat sensing is health and fitness tracking during vigorous exercise, energy harvesting from the human body is a promising approach for powering future wearable sweat sensors, particularly the ones that can convert biomechanical energies from human motion into electricity.

The advent of TENG technology sparked great excitement due to its potential application in self-powered systems, particularly for wearable and implantable electronics. As a newly emerging technique for energy conversion, TENGs face major challenges that need to be addressed for practical applications. First, TENG signals are essentially high-voltage pulses and insufficient to meet real-time energy consumption for wearable electronics; second, for wearable continuous use, the longevity of TENGs needs to be improved due to the stability limitations of organic polymeric materials used for device fabrication. Last but not least, system integration of TENGs in wearable devices and demonstrations of their usability in practical applications are significantly underdeveloped.

Here, we addressed these challenges by proposing a highly robust, mass-producible, fully self-powered battery-free wearable system that can efficiently and reliably harvest energy from human motion during vigorous exercises through an FPCB-enabled FTENG. As

compared to traditional TENGs, the fabricated FTENG using commercial FPCB fabrication procedures shows remarkable mechanical and electrical stability even after intensive mechanical deformations and repeated washing cycles. Through seamless system integration and efficient power management, this fully flexible system is able to power multiplexed sweat biosensors and wirelessly send data to the user interfaces through Bluetooth during on-body human trials. Compared to previously reported TENG-based wireless sensor systems (**Supplementary Table 5-2**) that either are not wearable or require ultralong charging periods to perform measurements, the FWS^3 represents a breakthrough in terms of practicality for wearable applications. We envision that, with further development, this technology could serve as a highly attractive approach toward self-powered wireless personalized health monitoring during people's daily activities; it will also find numerous applications in environmental and defense areas.

5.4 Methods

5.4.1 Design and fabrication of the FPCB module

The FPCB module for the FTENG and electronic circuit was designed using Eagle CAD (Autodesk). The BLE PSoC module was programmed in the PSoC Creator Integrated Design Environment (Cypress Semiconductor). A full list of components for the circuit design provided in **Supplementary Fig. 5-20** includes power management units (MB10S-13, Diodes Incorporated; S6AE101A, Cypress Semiconductor; TPS7A05, Texas Instruments), a BLE PSoC module (CYBLE-022001-00, Cypress Semiconductor), potentiometric sensing units (AD8235, Analog Devices), and passive components. A detailed circuit diagram is shown in **Supplementary Fig. 5-21**.

The flexible circuitry and FTENG were fabricated by a commercial FPCB manufacturer (detailed fabrication process shown in **Supplementary Fig. 5-1**). Two sheets of commercial flexible copper clad laminates (120 μm thick; JingHuang Electronics Co.), consisting of a flexible polyimide substrate and a copper film, sandwich a thin layer of epoxy adhesive. The copper films were patterned by photolithography and etched by a $FeCl_3$ solution to fabricate the circuit elements and interdigital electrode of the stator, and complementary grating

structures of the slider. An ENIG layer was deposited to protect the stator electrode. Last, a layer of PTFE was laminated on the interdigital electrode of the stator to induce electrification. The total size of one-panel stator of the FTENG is 22.6 cm^2 (length, 5.78 cm; width, 3.78 cm). The weight of one-panel stator of the FTENG is 0.586 (without PTFE coated) and 0.782 g (with PTFE coated). The total size and weight of one-panel slider of the FTENG are 18.22 cm^2 (length, 4.36 cm; width, 4.18 cm) and 0.396 g, respectively.

5.4.2 Fabrication of microfluidic sensor patch

The fabrication of the electrode array is demonstrated in **Supplementary Fig. 5-14**. After pretreatment of the PET substrate, E-beam evaporation was used to deposit 20 nm of Cr and then 100 nm of Au onto a PET substrate to form the 3-mm-diameter gold electrodes. The electrode arrays were additionally coated with 1 μm of Parylene C (ParaTech LabTop 3000 Parylene coater) and patterned through photolithography. The fabricated array was further etched with O_2 plasma via reactive ion etching (Oxford III-V System 100 ICP/RIE) to remove the parylene layer at the designated sensing area. Then, the electrodes were modified and deposited with different functional materials to form the Na^+ and pH working electrodes with a shared Ag/AgCl reference electrode. A CO_2 laser cutter was used to pattern the microfluidic layers. A waterproof double-sided medical tape layer patterned with 3-mm-diameter chambers was first attached to the PET sensor substrate. Then, a PDMS layer (100 μm thick) patterned with 3-mm-diameter reservoirs, inlets, an outlet, and fluidic connections was adhered onto the medical tape. Last, another medical tape layer patterned with inlets was attached on the PDMS layer.

5.4.3 Preparation of biosensors

An electrochemical workstation (CHI 860, CH Instruments) was used for electrochemical deposition and sensor characterization. For the Ag/AgCl reference electrode, an Ag deposition solution (0.25 M $AgNO_3$, 0.75 M $Na_2S_2O_3$, and 0.43 M $NaHSO_3$) was used to deposit Ag on the Au electrode through constant voltage electrodeposition (−0.25 V for 600 s). Next, 0.1 M $FeCl_3$ was drop-casted onto the Ag for 30 s to form Ag/AgCl. A total of 6.6 μl of the PVB reference cocktail (79.1 mg of PVB, 50 mg of NaCl, 1 mg of F127, and 0.2

mg of MWCNT in 1 ml of methanol) was drop-casted on the Ag/AgCl electrode and left overnight to dry. The pH ISE was first modified by depositing Au (50 mM $HAuCl_4$ and 50 mM HCl) at 0 V for 30 s, followed by electropolymerizing PANI on the Au electrode in a bath (0.1 M aniline and 0.1 M HCl) through 50 cycles of cyclic voltammetry (−0.2 to 1 V at a scan rate of 50 mV s^{-1}). For the Na^+ ISE, constant current electrodeposition (14 μA for 740 s) in a solution containing 0.01 M EDOT and 0.1 M NaPSS was used to deposit PEDOT:PSS on one Au electrode. Then, 15 μl of Na^+ selective membrane cocktail was drop-coasted onto the PEDOT:PSS layer and dried overnight. To prepare the cocktail, 100 mg of a mixture containing Na ionophore X (1%, w/w), Na-TFPB (0.55%, w/w), PVC (33%, w/w), and DOS (65.45%, w/w) was dissolved in 660 μl of THF.

5.4.4 On-body evaluation of the FWS^3

The validation and evaluation of the FWS^3 were performed with human subjects at the gymnasium in compliance with all the ethical regulations under a protocol (ID 19-0892) that was approved by the Institutional Review Board at the California Institute of Technology. The participating healthy subjects, ages 20 to 35, were recruited from the California Institute of Technology. All subjects gave written, informed consent before participating in the study.

Subjects performed cardiovascular exercises using a running machine (Aeon), an elliptical machine (Precor), and a rowing machine (Stamina). Before exercise, the subject's upper back was wiped and cleaned with alcohol swabs and gauzes. Then, waterproof double-sided medical tape was used to adhere the FWS^3 onto the subjects. The system including the FTENG stator was adhered to the side torso, and the FTENG slider was fixed onto the inner arm. To ensure accurate data, a new microfluidic sensor patch was used for each human trial. To evaluate the power output of the FTENG during the exercise, the output of the FTENG or the voltage across the storage capacitor was connected to an oscilloscope. When evaluating the entire system including the microfluidic sensor patch, the subjects were asked to run on a treadmill at a constant speed of 9 km $hour^{-1}$ for 30 min (to obtain sensor data regularly every several minutes); the BLE data were retrieved from a mobile phone or a personal computer. In addition, sweat samples were collected periodically from the forehead

of the subjects and pipetted into centrifuge tubes to be centrifuged at 6000 rpm for 15 min. The sweat samples were then frozen at −20°C for further testing.

5.5 Supporting Information

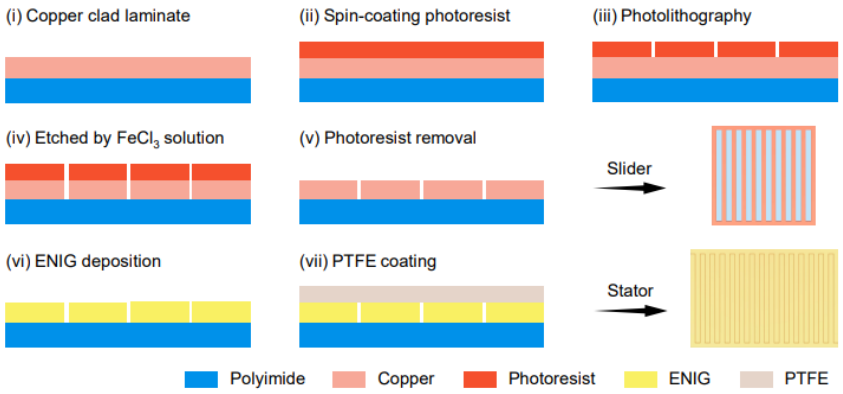

Supplementary Figure 5-1. Fabrication process of the slider and the stator of the FTENG. Steps (i-vi) are compatible to the commercial FPCB fabrication process.

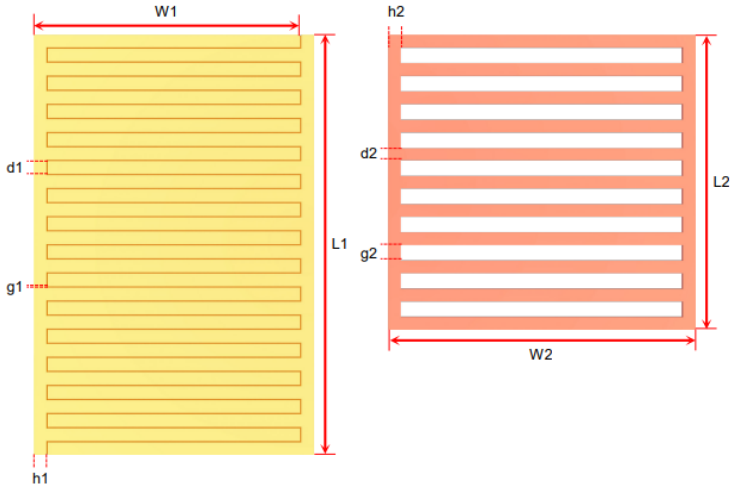

Dimension of FTENG

Stator	Length (mm)	Slider	Length (mm)
W1	37.8	W2	43.6
L1	59.8	L2	41.8
d1	1.8	d2	1.8
g1	0.2	g2	2.2
h1	1.8	h2	1.8

Supplementary Figure 5-2. Structure and parameters of the FPCB-based FTENG with an interdigital stator and a grating slider.

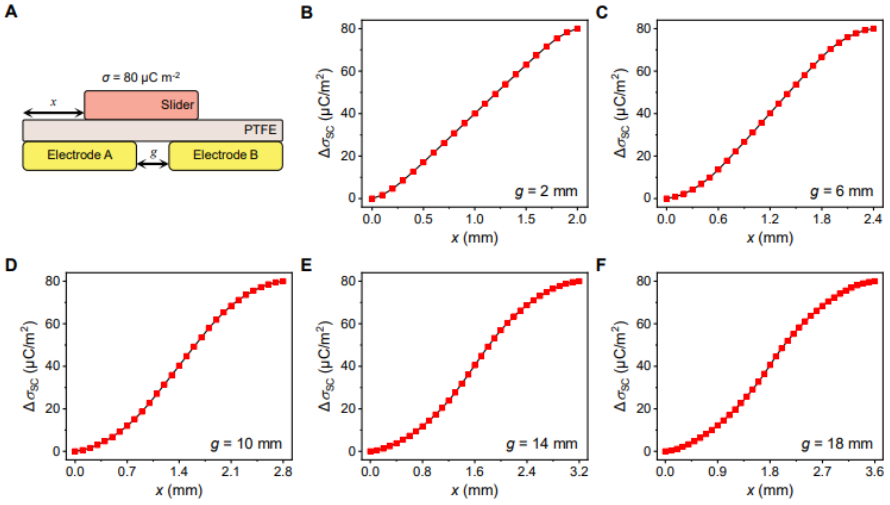

Supplementary Figure 5-3. Theoretical model and transferred charge density studies of FTENGs. a, The theoretical model of FTENG. **b-f,** The simulated transferred charge densities at different sliding displacements of 5 FTENGs with varied inter-electrode distances.

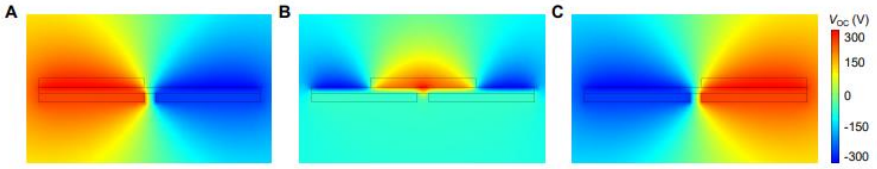

Supplementary Figure 5-4. Potential distribution across the interdigital electrodes of the FTENG under opencircuit condition. a-c, The potential distributions at initial state (**a**), intermediate state (**b**), and final state (**c**), respectively, as simulated by COMSOL.

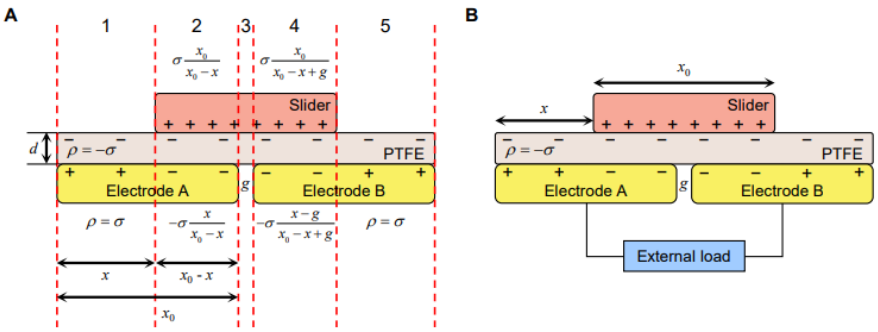

Supplementary Figure 5-5. Model and theoretical analysis of the FTENG. a,**b**, Schematic illustration of FTENG under open-circuit condition (**a**) and short-circuit condition (**b**).

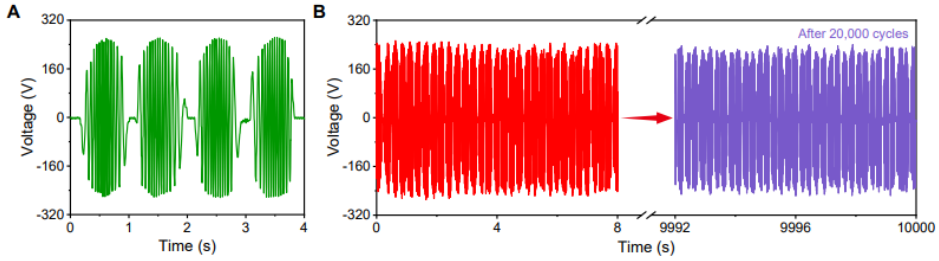

Supplementary Figure 5-6. Output performance of the FTENG. a, Waveforms of output voltages of an FTENG under a working frequency of 0.5 Hz. **b**, Cycling stability of output performance of a FTENG after 20,000 cycles under a working frequency of 2 Hz.

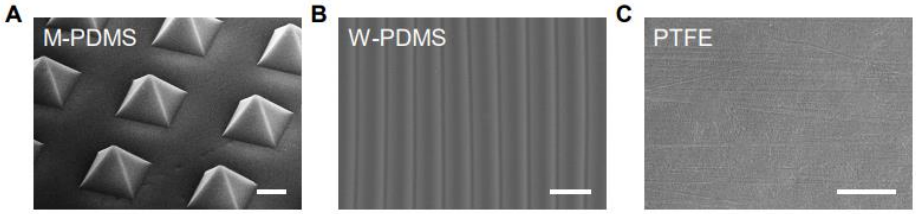

Supplementary Figure 5-7. Morphologies of different triboelectric materials before durability test. a-c, Scanning electron microscopy (SEM) images of conventional micro-pyramid PDMS (M-PDMS) (**a**), wrinkled PDMS (W-PDMS) (**b**) and PTFE (**c**), respectively. Scale bars, 50 μm, 5 μm, and 50 μm, respectively.

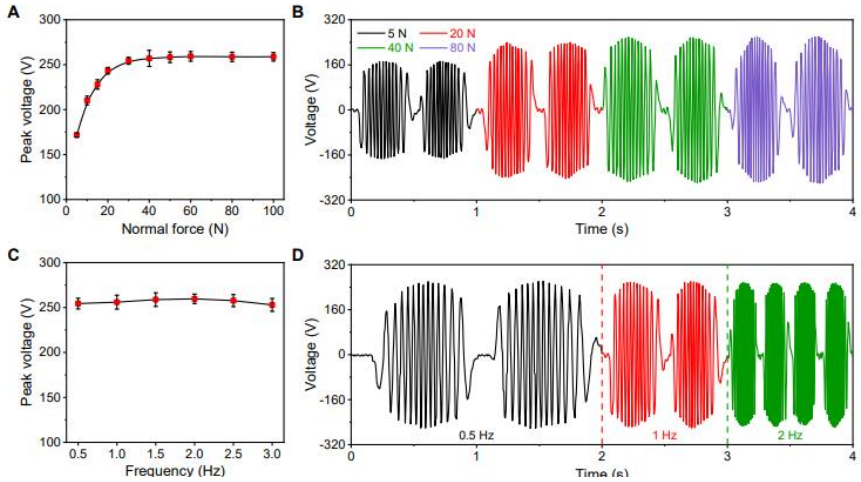

Supplementary Figure 5-8. Force-influenced performance of the FTENG. a-d, The peak open-circuit voltage of the FTENG under different normal forces at a fixed working frequency of 1 Hz (**a** and **b**) and at varied working frequencies (**c** and **d**). The normal force acting on the FTENG was kept at 30 N for **c** and **d**. Error bars represent the standard deviations dof the peak voltages measured from 10 working cycles.

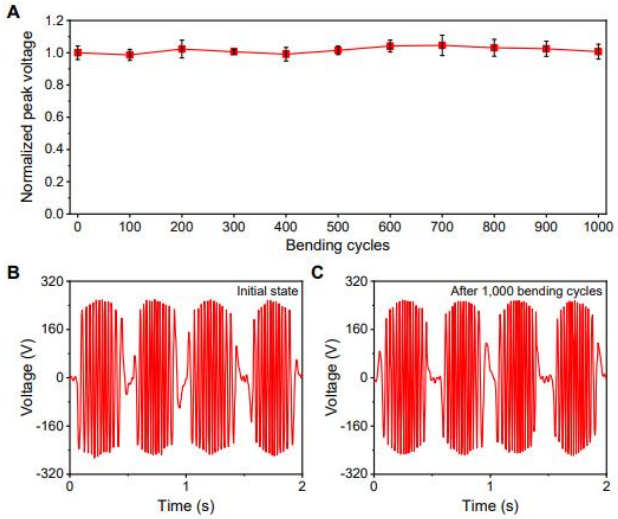

Supplementary Figure 5-9. Mechanical stability of the FTENG. a, The normalized peak open-circuit voltage of an FTENG after hundreds of bending cycles at a working frequency of 1 Hz. **b**,**c**, The output performance of an FTENG at initial state (**b**) and after 1,000

bending cycles (**c**) during the test. Error bar represents the standard deviations of the normalized peak voltages measured from 10 working cycles.

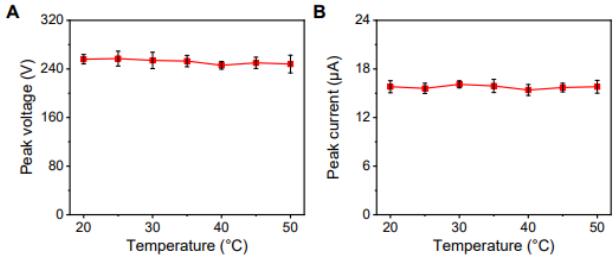

Supplementary Figure 5-10. Dependence of FTENG output on temperature. a,**b**, Peak open-circuit voltage (**a**) and peak short-circuit current (**b**) of FTENG under different temperatures at a working frequency of 1 Hz. Error bars represent the standard deviations of the peak amplitudes measured from 10 working cycles.

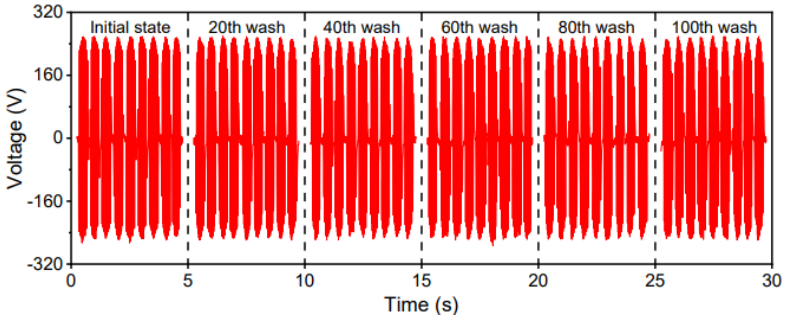

Supplementary Figure 5-11. Washing durability of the FTENG with 100 washing cycles at a working frequency of 1 Hz.

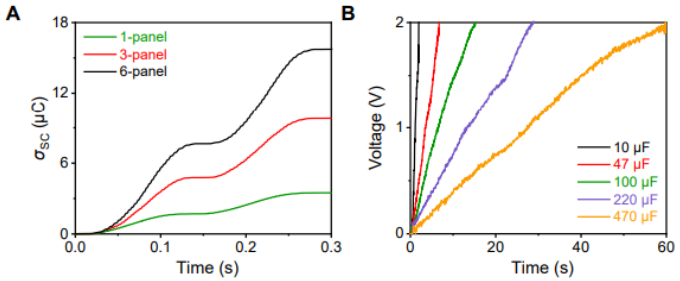

Supplementary Figure 5-12. Output performance of the FTENG with different panels. a, Transferred charges of an FTENG with different panels during sliding process at a frequency of 3.3 Hz. **b**, Charging curves of different capacitors charged to 2 V with a 3-panel FTENG through a rectifier at a working frequency of 2 Hz.

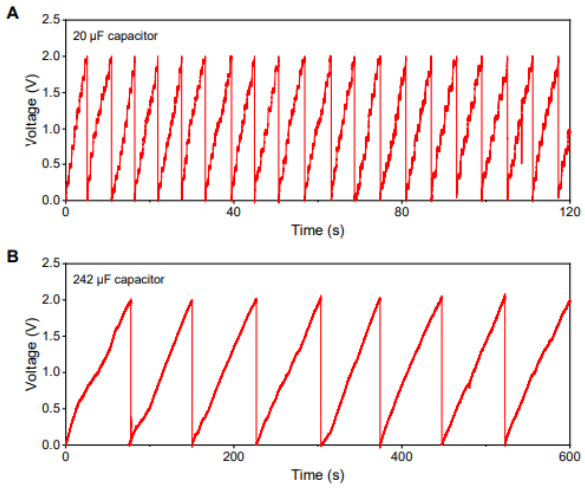

Supplementary Figure 5-13. Charging stability of the FTENG on different capacitors. a,**b**, Charging curves of a 3-panel FTENG in charging a 20 μF (**a**) and 242 μF (**b**) capacitor under a working frequency of 1.5 Hz.

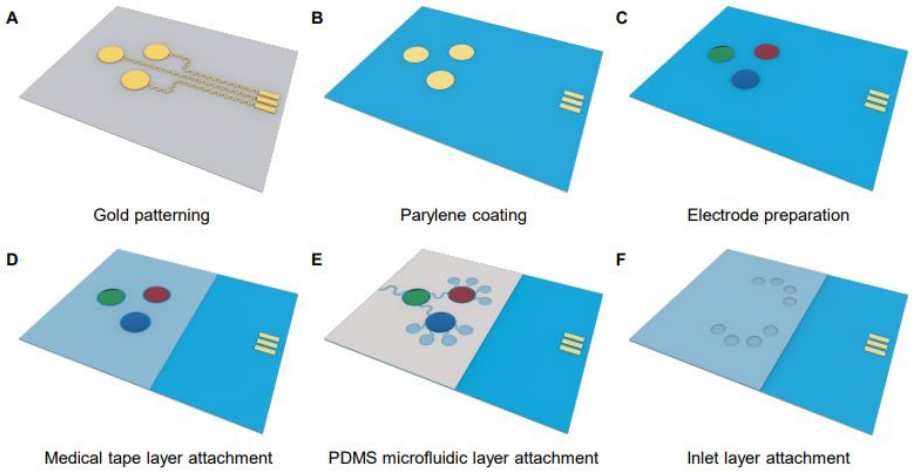

Supplementary Figure 5-14. Fabrication process of the microfluidic sensor patch. **a**, Patterning of Au/Cr electrodes using photolithography, electron-beam evaporation and lift-off process on a PET substrate. **b**, Patterning insulating layer via Parylene C deposition, photolithography and oxygen plasma etching. **c**, Modifying working electrode and reference electrode through electrodeposition and drop casting. **d**, Patterning laser-patterned medical tape. **e**, Patterning the microfluidic channels in the PDMS layer. **f**, Assembling medical tape with fluid inlets to form the microfluidic sensor patch.

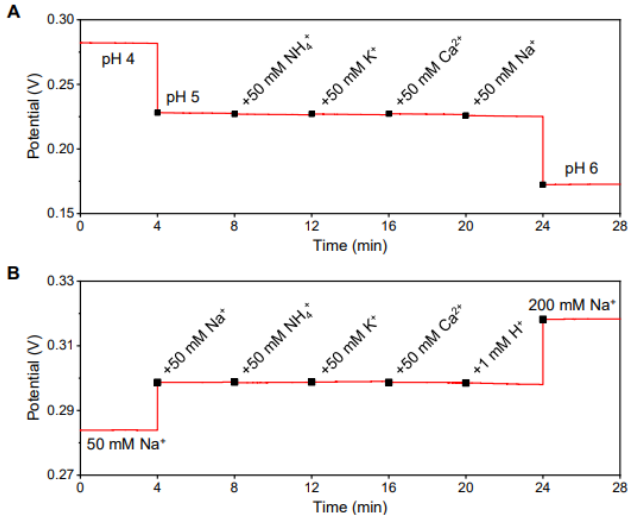

Supplementary Figure 5-15. Selectivity study of the biosensor array. a,**b**, Selectivity study of a pH sensor (**a**) and a Na+ sensor (**b**) against other major electrolytes in human sweat. Data recording was paused while changing solutions with 30 s waiting period.

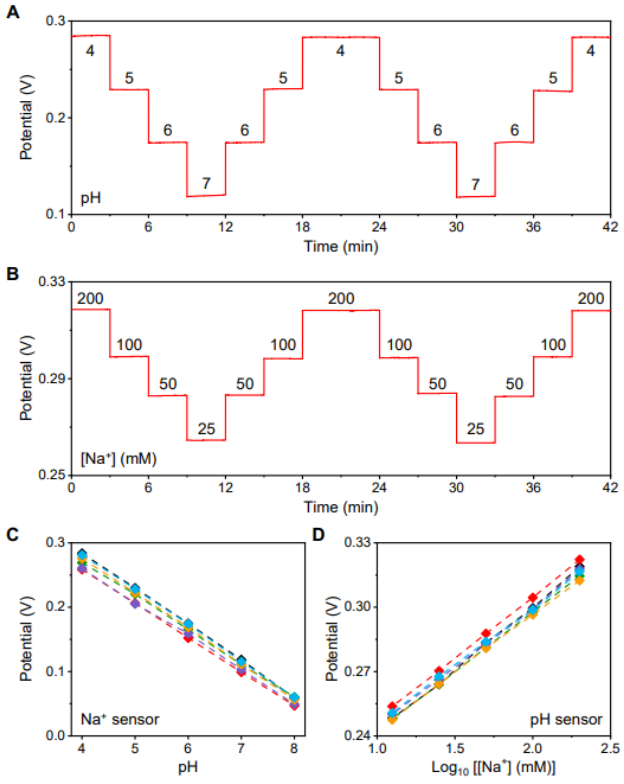

Supplementary Figure 5-16. Repeatability and reproducibility of the biosensor array. **a**,**b**, Repeatability of a pH sensor in McIlvaine's Buffer solutions (**a**) and a Na+ sensor in NaCl solutions (**b**). **c**,**d**, Reproducibility of pH sensors (**c**) and Na+ sensors (**d**) (n=6).

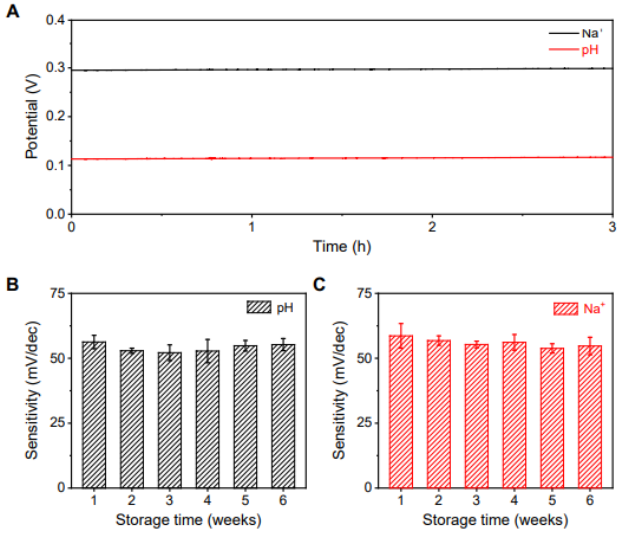

Supplementary Figure 5-17. Stability of the biosensor array. a, Response stability of a pH sensor and a Na+ sensor in a 100 mM NaCl solution for 3 h. **b**,**c**, Long-term stability of pH sensors (**b**) and Na+ sensors (**c**) after 6 weeks of storage. Error bars represent the standard deviation from 6 sensors.

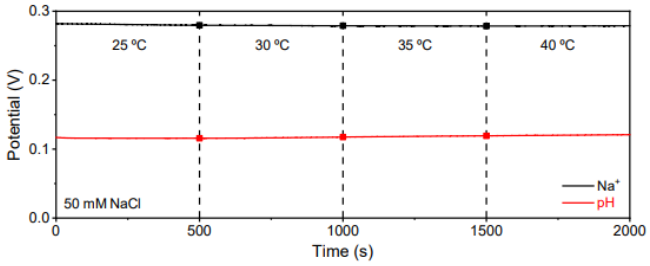

Supplementary Figure 5-18. Dependence of biosensor array on temperature.

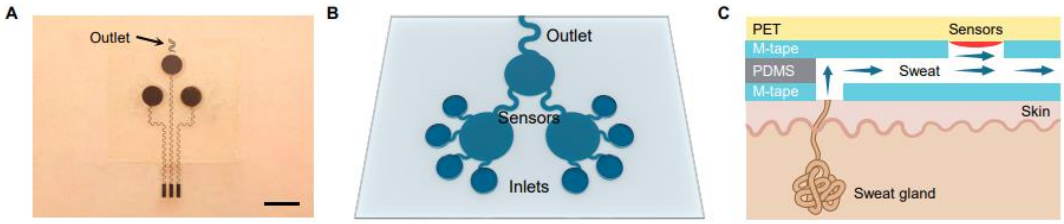

Supplementary Figure 5-19. Schematic of microfluidic design. a, Optical image of a microfluidic sweat sensor patch. Scale bar, 5 mm. **b**, Sweat flow in laser-engraved microfluidic channels. **c**, Cross-section view of layout and operation of microfluidic sweat sensor patch. M-tape, medical tape. Photo credit: Yu Song, California Institute of Technology.

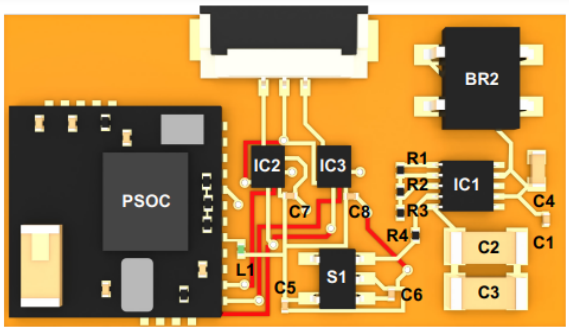

List of components

Components	Value and series number	Description
BR2	MB10S-13	Bridge Rectifier
C1	0.1 µF	0201 Capacitor
C2	220 µF	1206 Capacitor
C3	22 µF	1206 Capacitor
C4	10 µF	0402 Capacitor
C5	1 µF	0201 Capacitor
C6	1 µF	0201 Capacitor
C7	0.1 µF	0201 Capacitor
C8	0.1 µF	0201 Capacitor
L1	BKP0603HS121-T	0201 Ferrite Bead
IC1	S6AE101A	Energy Harvesting PMIC
IC2	AD8235ACBZ	Instrumentation Amplifier
IC3	AD8235ACBZ	Instrumentation Amplifier
PSOC	CYBLE-022001-00	EZ-BLE Module
S1	TPS7A0522PDBVT	LDO Regulator
R1	5.6 MΩ	0201 Resistor
R2	4.3 MΩ	0201 Resistor
R3	7.5 MΩ	0201 Resistor
R4	10 Ω	0201 Resistor

Supplementary Figure 5-20. Schematic and list of components of the flexible circuitry.

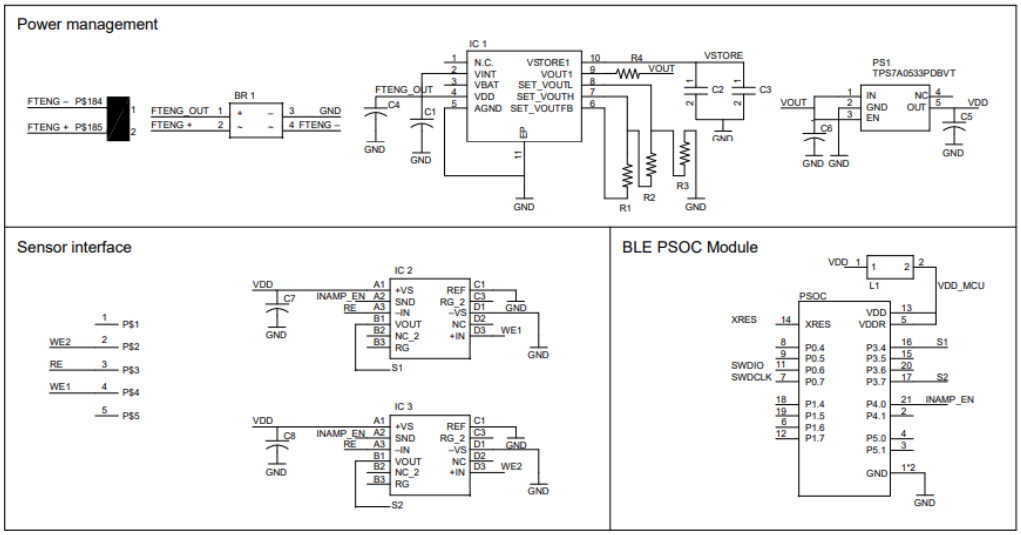

Supplementary Figure 5-21. Circuit diagram of power management, sensor interface, and BLE PSoC modules.

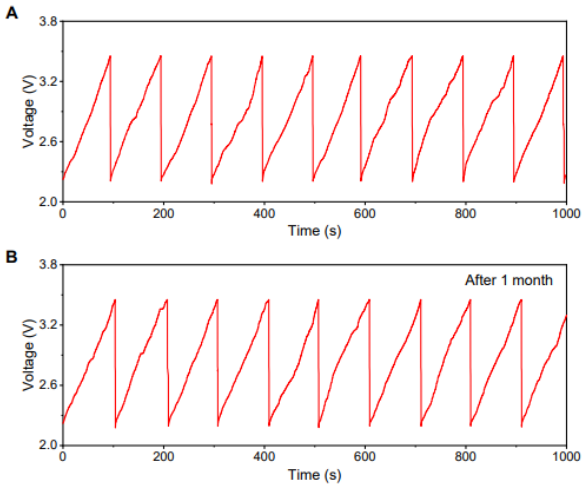

Supplementary Figure 5-22. Long-term stability of FWS3. a,b, Charging curves of the capacitor when an FWS3 operates under a working frequency of 1.5 Hz before (a) and after 1 month (b).

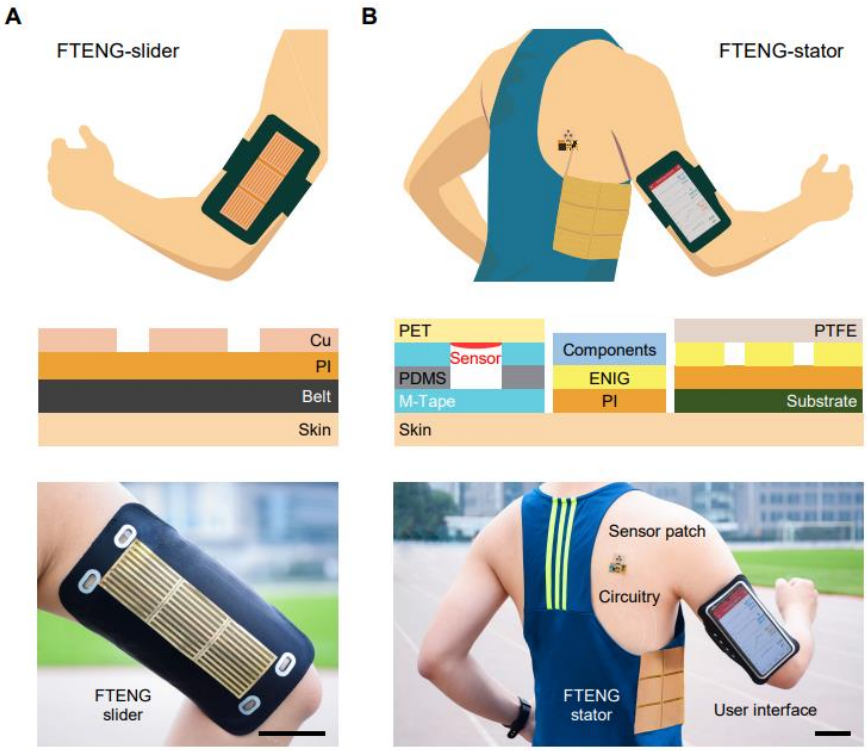

Supplementary Figure 5-23. Schematic and optical images of an FTENG worn on body. a,**b**, Schematic, cross-section view and real photos of FTENG slider (**a**) and FTENG stator (**b**) worn on body. Scale bars, 5 cm. Photo credit: Yu Song, California Institute of Technology.

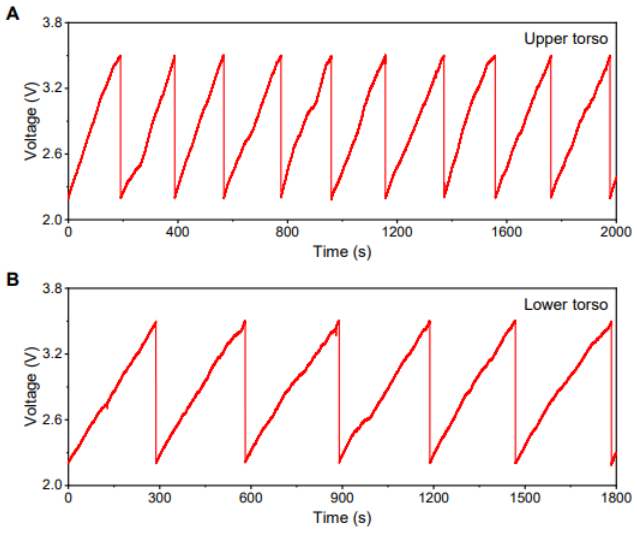

Supplementary Figure 5-24. Real-time potential of the circuitry capacitor charged by an FTENG. a,**b**, The circuitry capacitor charged by an FTENG at different positions (**a**) and different contact modes (**b**) during a regular running of a healthy subject.

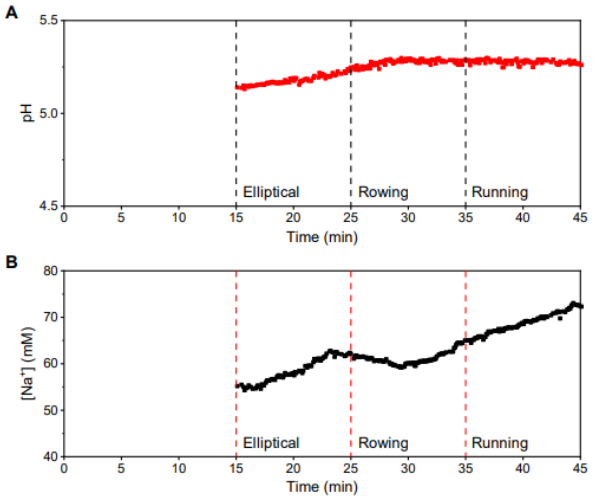

Supplementary Figure 5-25. Real-time sweat pH and Na+ level wirelessly obtained from an FWS3 during different physical exercises. In this experiment, the FWS3 system was charged by a battery instead to collect continuous data points for better noise characterization.

Supplementary Table 5-1. Comparison of currently reported wearable TENGs.

Working Mode	Size (cm^2)	Material preparation	Position	Output	Power density	Sampling rate	Durability	Washability	Ref.
Contact-separation	4 * 4	Weaving process	Wrist	150 V, 1.5μA	85 mW m^{-2}	1 – 5 Hz	50,000	Washable	41
Contact-separation	6 * 4	Weaving process	Waist	4.98 V, 37.2 μA	33.16 mW m^{-2}	0.4 Hz	1,000	Washable	42
Contact-separation	4.5 * 4	Weaving process	Arm	45 V, 9.9 μA	263.36 mW m^{-2}	0.5 – 5 Hz	1,500	Washable	43
Contact-separation	6 * 8	Weaving process	Hand	206 V, 1.5 μA	30.4 mW m^{-2}	1 Hz	10,000	Washable	44
Contact-separation	1.4	Inkjet printing	Shoe	54.8 V, 1.2 μA	126 mW m^{-2}	0.75 – 4 Hz	500	N/A	45
Lateral-sliding	2 * 5	ICP etching	Knee	24.1 V	N/A	0.7 Hz	1,000	N/A	46
Single-electrode	4.5 * 10.5	Drop coating	Arm	70 V, 28.35 μA	500 mW m^{-2}	1 – 4 Hz	3,600	N/A	47
Single-electrode	6 * 3	Blade coating	Wrist	180 V, 22.6 μA	4.06 mW m^{-2}	0.5 – 2.5 Hz	200	N/A	48
Freestanding	12 * 8	Weaving process	Side torso	118 V, 1.5 μA	N/A	1 – 5 Hz	15,000	N/A	49
Freestanding	5.78 * 3.78	FPCB technique	Side torso	248 V, 42.3 μA	415.9 mW m^{-2}	0.5 – 3.3 Hz	20,000	Washable	This work

Supplementary Table 5-2. Comparison of TENG-powered wireless sensor systems.

Power source	Working mode	Working condition	Charging period	External power	Sensing signal	Data	Wearable	Ref.
Air flow	Freestanding	100 μF, 8 V	N/A	Yes	Wind speed	Bluetooth	No	50
Air/water flow	Contact-separation	1 mF, 5 V	40 min	No	pH	Bluetooth	No	51
Air flow	Freestanding	10 mF, 3.3 V	98 s	No	Temperature	RF transmission	No	52
Water flow	Freestanding	1 mF, 3.3 V	60 min	No	Temperature	RF transmission	No	53
Air flow/light	Contact-separation	100 mAh, 2.7 V	540 s	No	Temperature	RF transmission	No	54
Human motion	Freestanding	N/A	45 min	No	Heart rate	Bluetooth	Yes	55
Human motion	Contact-separation	N/A	N/A	Yes	Ca^{2+}	RF transmission	Yes	56
Human motion	Freestanding	242 μF, 3.5 V	60 s	No	pH & Na^{2+}	Bluetooth	Yes	This work

5.6 Harvesting energy from human sweat

While TENGs are remarkable for harnessing energy through variable mechanical interactions, BFCs offer an appealing alternative for powering sweat sensors. BFCs hold an advantage in their ability to continuously output power as long as there is a supply of sweat, enabling them to generate electricity even during periods of inactivity or no motion.

BFCs offer a revolutionary technology in the realm of energy harvesting for sustainably powering wearable sweat sensors without the need for batteries. BFCs employ enzymes as catalysts to generate electricity from redox-active metabolites such as lactate and glucose. For powering sweat sensors, lactate BFCs are an ideal candidate as sweat is rich in lactate. Lactate biofuel cells comprise an anode that is immobilized with a redox mediator and LOx enzyme for oxidation of lactate into pruvate, and a complementary cathode that facilitates the reduction of oxygen into water. We developed a highly stable and efficient wearable lactate BFC that can generate up to 3.5 mW cm^{-2} from natural sweat through the monolithic integration of zero-dimensional (0D) to 3D nanomaterials (**Fig. 5-6**). This BFC was able to continuously power a battery-free electronic skin system for multiplexed biosensing and Bluetooth data transmission (**Fig. 5-7**).

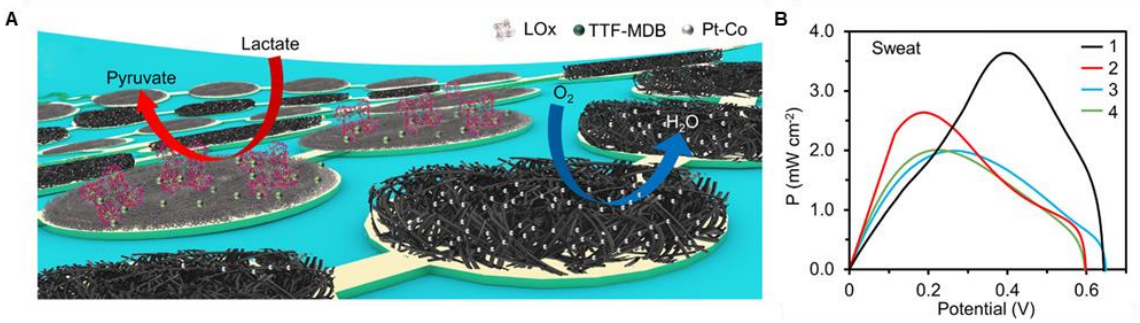

Figure 5-6. Flexible nanoengineered BFC array for efficient energy harvesting. a, Schematic of a soft BFC array consisting of LOx-modified bioanodes and Pt alloy nanoparticle–modified cathodes. **b**, Power density curves of BFCs in sweat samples from four healthy humans.

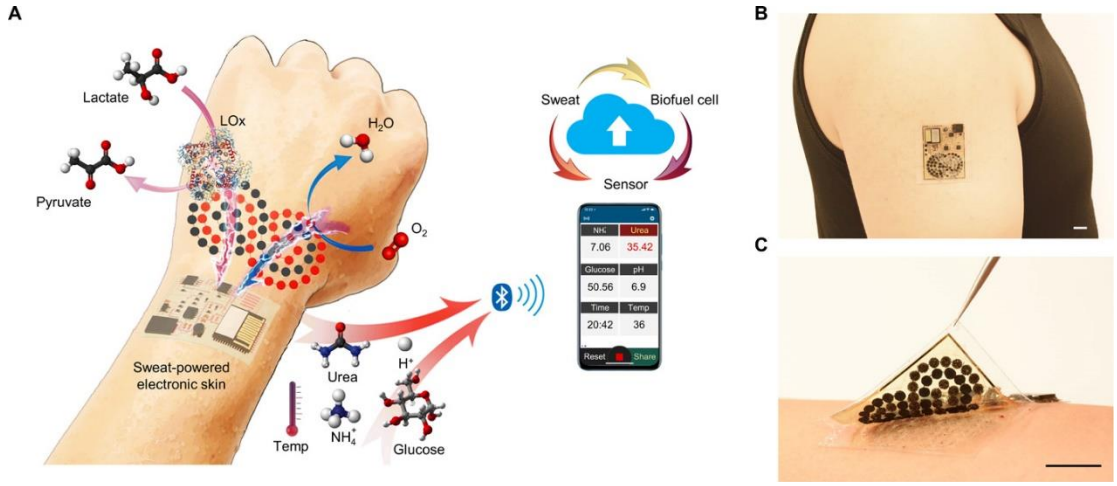

Figure 5-7. Perspiration-powered soft electronic skin (PPES) for multiplexed wireless sensing. a, Schematic of a battery-free, biofuel-powered e-skin that efficiently harvests energy from the human body, performs multiplexed biosensing, and wirelessly transmits data to a mobile user interface through Bluetooth. **b**,**c**, Photographs of a PPES on a healthy individual's arm. Scale bars, 1 cm.

As the BFC outputs a low voltage DC signal, a power management circuit was used for boost converting the BFC output with maximum power point tracking to charge an energy storage

capacitor (**Fig. 5-8a**). One the capacitor was charged to an upper threshold voltage, the electronic system was continuously powered to perform multiplexed potentiometric measurements and data transmission at a fixed interval of 15 s, as long as the capacitor didn't discharge below the lower threshold voltage (**Fig. 5-8b**). The BFC-powered e-skin system was validated through onbody biking trials, where the device was able to monitor two analytes along with skin temperature continuously and simultaneously (**Fig. 5-9**).

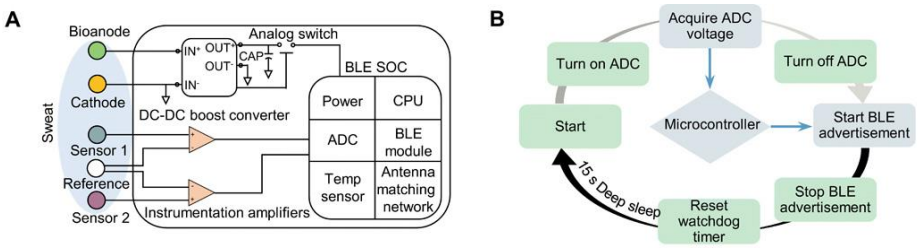

Figure 5-8. System-level integration and evaluation of the PPES. a, Schematic diagram of the PPES system including the BFC array, sensor array, boost converter, instrumentation amplifiers, and BLE module. SOC, system-on-chip; CPU, central processing unit. **b**, Operation flow of the energy control and data-transmission processes.

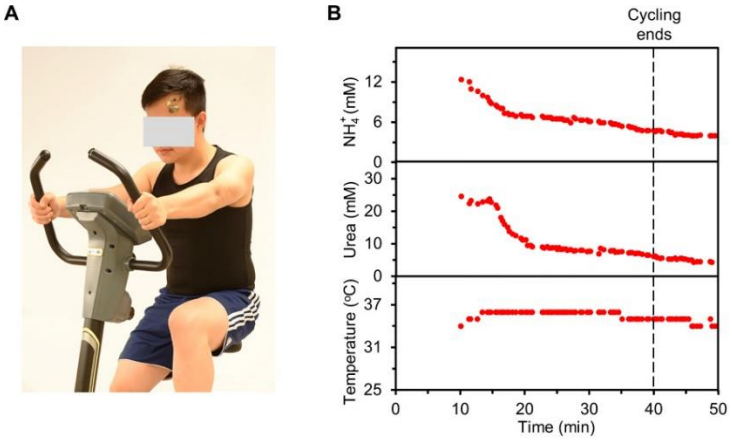

Figure 5-9. On-body evaluation of the PPES toward personalized metabolic monitoring. a, Photograph of an individual wearing a PPES during cycling exercise. **b**, Real-time multiplexed urea and $NH4^+$ analysis using a PPES on an individual's forehead.

Biofuel cells offer a sustainable and environmentally friend approach to generating electricity. Furthermore, BFC powered battery-free systems can operate continuously as long as there is exposure to sweat with sufficient lactate concentrations. However, BFCs still require significant sweat volumes produced by exercise to initiate the energy harvesting, therefore making it difficult to monitor biomarkers continuously throughout the day even while performing sedentary tasks. While BFCs scavenging energy from natural perspiration have been developed, low sweat volumes limit their power output.

Chapter 6

HARVESTING ENERGY FROM AMBIENT LIGHT

Materials from this chapter appear in " Min, J.; Demchyshyn, S.; Sempionatto, J. R.; Song, Y.; Hailegnaw, B.; Xu, C.; Yang, Y.; Solomon, S.; Putz, C.; Lehner, L. E.; Schwarz, J. F.; Schwarzinger, C.; Scharber, M. C.; Shirzaei Sani, E.; Kaltenbrunner, M.; Gao, W. An Autonomous Wearable Biosensor Powered by a Perovskite Solar Cell. *Nature Electronics* **2023**, *6* (8), 630–641. https://doi.org/10.1038/s41928-023-00996-y."

While TENG and BFC-powered wearable sweat sensor devices were able to sustainably harvest energy from body motion and body fuel, they require exercise for power generation and have limited power output. Such systems are limited to performing simple electrochemical measurements such as potentiometry during exercise, making it difficult to monitor a wide range of biomarkers while performing various activities and account for personalized factors such as sweat rate or sweat pH. Power from ambient light such as sunlight and indoor light is ubiquitous and readily accessible during daily activities. This section will detail the development of an autonomous wearable biosensor that is powered by a perovskite solar cell and can provide continuous and non-invasive metabolic monitoring.

6.1 Background

The recent shift towards personalized and remote healthcare has accelerated the development and adoption of wearable devices that can continuously monitor physical vital signs as well as biochemical markers[141,145,162–174]. Wearable biosensors can potentially be used to continuously and non-invasively analyze body fluids such as sweat, which contains a wealth of information pertinent to disease diagnostics and fitness tracking[162,168,172,175,176]. A variety of electrochemical sensing strategies, including amperometry, potentiometry, voltammetry, and impedance spectroscopy, have been used to detect sweat biomarkers (such as electrolytes, metabolites, nutrients, drugs, and hormones)[66,108,162–164,168,176] and sweat rate (which may have a close link to secreted biomarker levels)[170,171,177]. For practical health monitoring beyond that during vigorous exercise, wearable biosensors can also benefit from steady sweat extraction via iontophoresis, a localized sedentary sweat stimulation technique[178,179]. However, due to challenges related to multimodal system miniaturization and integration, the development of a wearable system capable of autonomous sweat induction and sampling, real-time sweat rate monitoring, and continuous multiplexed biomarker analysis remains limited.

High power demand also impedes the development of such multifunctional wearable sensing systems. Wearable sensors typically rely on the use of batteries: a bulky and unsustainable power source that requires an external source of electricity to recharge. Various energy

harvesting strategies — including biofuel cells and triboelectric nanogenerators — have been explored for powering battery-free wearables[148,180–185]. However, biofuel cells typically suffer from limited long-term stability due to biofouling in human sweat[180], and triboelectric nanogenerators require extensive physical activity to generate electricity[181]. Furthermore, the power densities produced by biofuel cells and triboelectric nanogenerators from casual daily activities are limited[181,182].

Ambient light, including natural sunlight and artificial indoor light, is an abundant form of energy that is readily available during daily activities. The commercially dominant photovoltaics technologies, which are based on silicon, work well for large-scale solar energy harvesting, but struggle to address the power needs of wearable devices. In particular, silicon cells are often fragile, bulky and rigid. They also provide insufficient power conversion efficiency (PCE) under low or indoor illumination, due to their narrow bandgap and preferentially trap-assisted recombination, limiting their range of applications[186]. Light harvesting technologies based on the III-V family of semiconductors can address some of the limitations of silicon, but their fabrication often requires complex processing conditions, which is reflected in their price/energy payback time and thus their potential areas of application[187,188].

Perovskite solar cells offer a number of favorable intrinsic properties including long charge carrier diffusion lengths, high absorption coefficients, solution processability, small exciton binding energies, high structural defect tolerance, tunable bandgap, and high photoluminescence quantum yields[189,190]. Such solar cells have developed quickly in the last decade due to their evolving fabrication protocols and the adaptability of the material compositions[191]. Perovskites also offer strong defect tolerance that leads to high parallel resistance (Rp), which is the key parameter of solar cell performance under low light conditions. This results in increased fill factor (FF) and reduced open circuit voltage (Voc) losses at low light conditions, which in combination with the matching of perovskite solar cell spectral response to common indoor lighting emission spectrum, yields high PCE under indoor illumination[186,192].

In this Article, we report an autonomous wearable biosensor that is powered by a flexible perovskite solar cell (FPSC) and can provide continuous and non-invasive metabolic monitoring (**Fig. 6-1a**). Our multifunctional wearable device offers autonomous sweat extraction via iontophoresis, dynamic microfluidic sweat sampling, multiplexed monitoring of sweat biomarkers using different electrochemical detection techniques, impedance-based sweat rate analysis, and Bluetooth-based wireless data transmission. The wearable device operates under a wide range of illumination conditions ranging from full sunlight to indoor lighting. It is powered by an efficient 2 cm^2 active area lightweight quasi-2D FPSC energy harvesting module with a PCE of 14% under air mass global 1.5 (AM1.5) illumination, and 29.64% under 600 lx indoor illumination with a white light LED light bulb. The sensing platform can be used to continuously collect multimodal physicochemical data (glucose, pH, Na^+, sweat rate, and temperature) across indoor and outdoor physical activities for over 12 hours, and without the need for batteries or vigorous exercise.

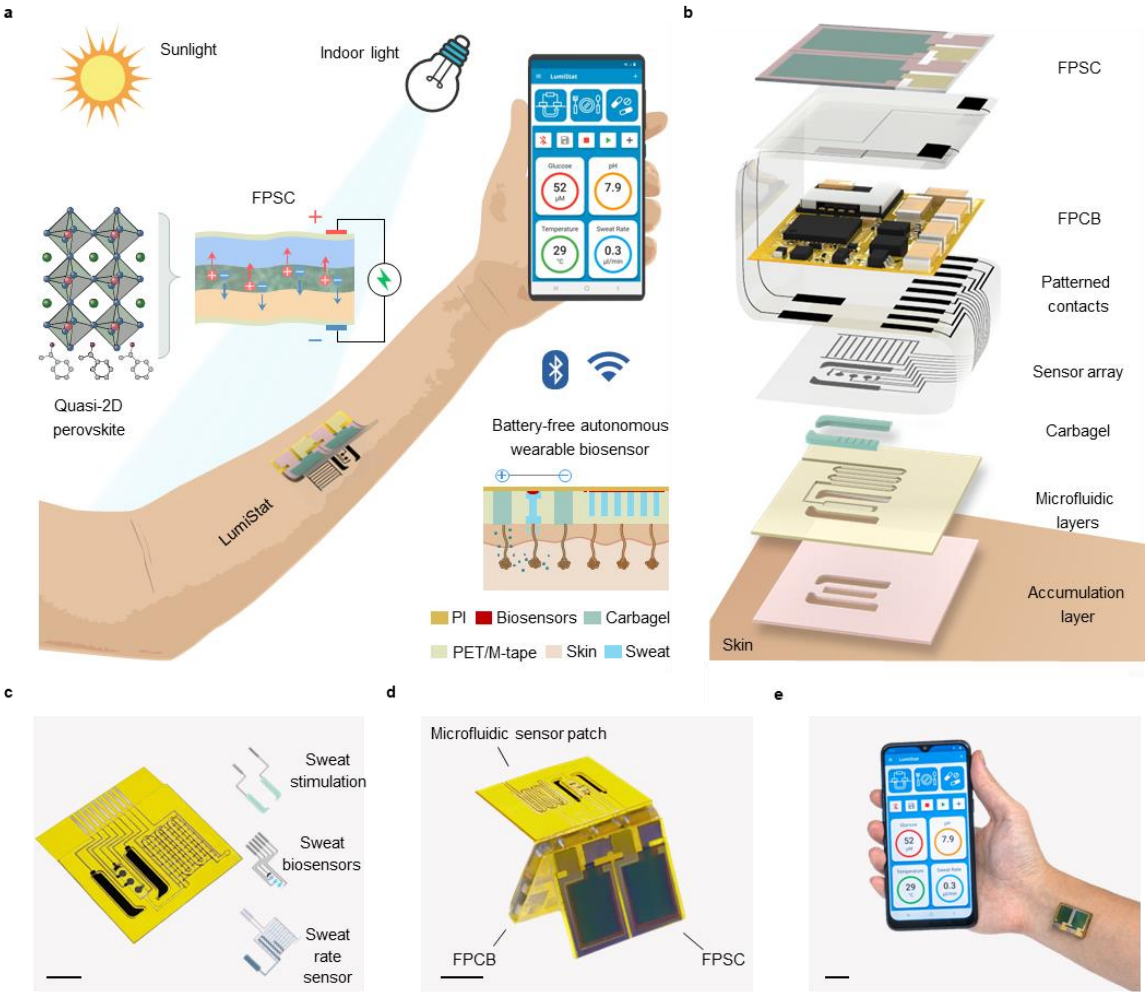

Figure 6-1. **Schematics and images of the ambient light-powered battery-free lab on the skin. a**, Illustration of the energy autonomous wearable device that is powered from both outdoor and indoor illumination *via* a quasi-2D flexible perovskite solar cell (FPSC) and perform multiplexed wireless biomolecular analysis across a wide range of activities. Carbagel, carbachol hydrogel; M-tape, medical tape; PET, polyethylene terephthalate; PI, polyimide. **b**, Exploded 3D model of the layer assembly of the wearable device. **c**, Photo of an inkjet-printed disposable microfluidic sensor patch that contains an iontophoretic module for autonomous sweat stimulation, microfluidics for sweat sampling, multiplexed electrochemical biosensors for perspiration analysis, and an impedimetric sweat rate sensor. Scale bar, 0.5 cm. **d**, Photo of the wearable device assembled in origami-style. Scale

bar, 1 cm. e, Photo of the wearable device worn on the ventral forearm and wirelessly connected to a custom developed mobile app over BLE. Scale bar, 2 cm.

6.2 Results

6.2.1 Wearable device design for autonomous biomarker analysis

The wearable device consists of disposable and reusable modules assembled in an origami-like fashion (**Fig. 6-1b** and **Supplementary Figs. 6-1,2**). Among the reusable parts is the highly efficient quasi-2D FPSC module that converts ambient light into electrical power and the energy-efficient FPCB for electrochemical instrumentation, signal processing, and Bluetooth wireless communication. A daily disposable flexible patch contains a pair of carbachol hydrogel (carbagel) coated iontophoresis electrodes for sweat stimulation, a laser-engraved microfluidic module integrated with interdigitated electrodes for sweat sampling and sweat rate monitoring, and a multiplexed electrochemical sweat biosensor array for molecular analysis (**Fig. 6-1c**). Compared to traditionally used pilocarpine gels, carbachol gels were selected for iontophoresis as they allow for efficient and long-lasting sudomotor axon reflex sweat secretion from the surrounding sweat glands, ideally suiTable 6-for microfluidic sweat sampling[178]. Inkjet printing was used to fabricate all flexible biosensing electrodes and interconnects at a large scale and low cost. Considering that chemical sensors usually suffer from signal drift during long-term use, their capacity for mass-production allows disposable use on a daily or multi-day basis for reliable wearable health monitoring. Potentiometric, amperometric, voltammetric, and impedimetric techniques can all be performed using the wearable device to analyze a broad spectrum of sweat biomarkers ranging from metabolites, electrolytes, nutrients, to substances and drugs. The fully assembled wearable device is 20 mm × 27 mm × 4 mm in size and can comfortably adhere to the skin (**Fig. 6-1d,e**). The custom embedded algorithm and mobile application enable an energy-saving adaptive power consumption scheme such that the wearable device can extract and analyze sweat across various activities and illumination conditions in a prolonged and efficient fashion. All calibrated biomarker information can be wirelessly transmitted and displayed on a custom mobile app (**Fig. 6-1e**, **Supplementary Fig. 6-3**).

6.2.2 FPSC design and characterization for wearable use

To effectively and sustainably power the wearable device, an FPSC module (**Fig. 6-2a**) is designed to have a high power density and PCE for energy harvesting under diverse lighting conditions, flexibility to endure the mechanical stresses common for on-body wear, and sTable 6-performance with reliable encapsulation against sweat exposure. The FPSC device utilizes a p-i-n architecture and comprises of flexible polyethylene terephthalate (PET) coated with indium tin oxide (ITO), Cr/Au busbars, a poly(3,4-ethylenedioxythiophene)-poly(styrenesulfonate)(PEDOT:PSS) hole transport layer, quasi-2D perovskite photoactive layer, [6,6]−phenyl-C61-butyric acid methyl-ester (PCBM) electron transport layer, TiO_x interlayer, Cr/Au contacts, and an epoxy/PVC/PCTFE encapsulation (**Fig. 6-2b**). The perovskite absorber layer (ca. 450 nm thick) with an empirical formula of $(MBA)_2(Cs_{0.12}MA_{0.88})_6Pb_7(I_xCl_{1-x})_{22}$ is at the heart of the device (**Fig. 6-2c**). A large organic spacer, α-methylbenzylamine (MBA), facilitates the formation of a quasi-2D perovskite structure with large grain size and improved defect passivation, resulting in an excellent device performance (**Supplementary Fig. 6-4**). Under simulated solar illumination (AM1.5) quasi-2D FPSC with a small active area (0.165 cm^2) achieve PCE of up to 18.1 %, which remains as high as 16.5 % for large area device (1 cm^2), and 14.0% for modules consisting of two large cells joined in series (total active area 2 cm^2) (**Supplementary Fig. 6-5, Supplementary Table 6-1**).

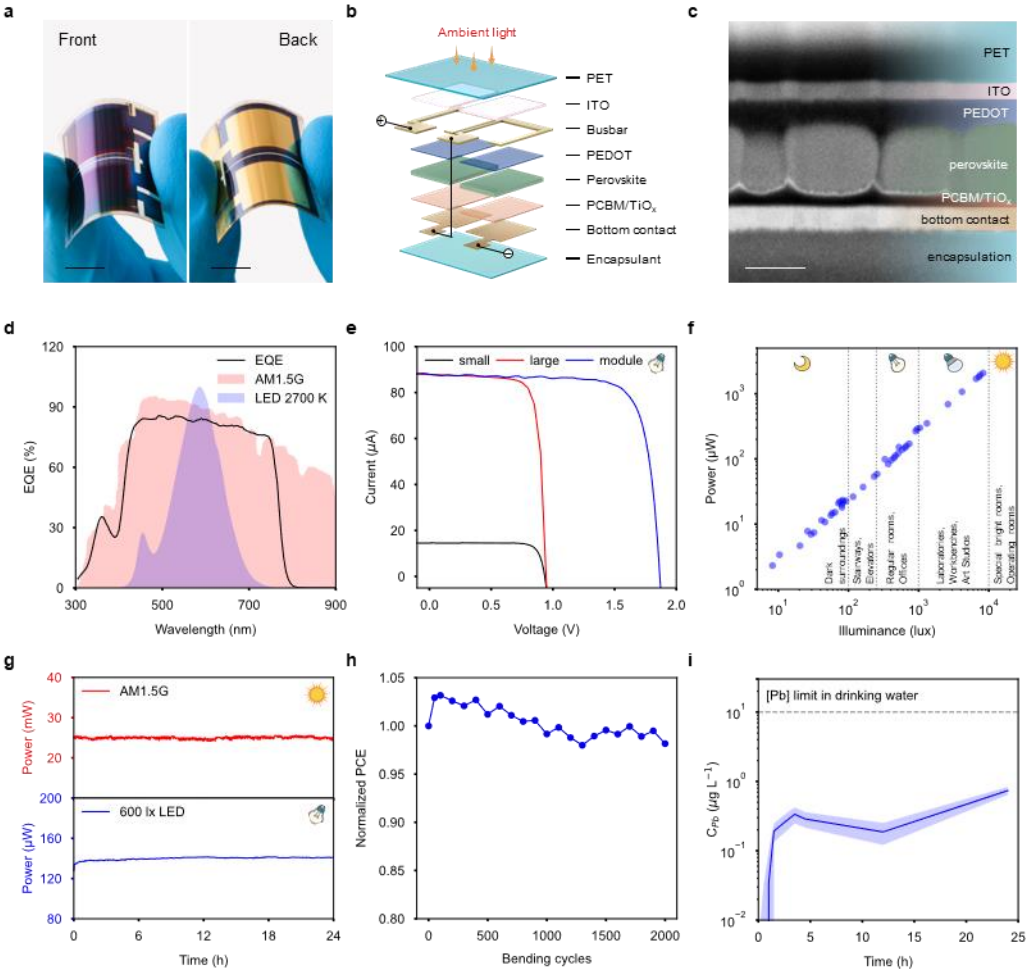

Figure 6-2. **Design and characterization of the flexible perovskite solar cell. a**, Photograph of an FPSC. Scale bar, 1 cm. **b**, 3D model of FPSC module architecture consisting of 2 individual 1 cm^2 active area solar cells connected in series. **c**, Cross-sectional transmission electron microscopy (SEM) image of the FPSC. Scale bar, 400 nm. Experiments were repeated five times independently with similar results. **d**, External quantum efficiency (EQE) of FPSC superimposed with normalized emission spectrum of standard reference AM1.5G tilt sun illumination and room-light (2700 K) LED light bulb spectrum. **e**, IV curves of small (0.165 cm^2), large (1 cm^2), and module (2 cm^2) FPSCs recorded room-light LED light bulb illumination (2700 K, 600 lx). **f**, The power output of a FPSC module as a function of illuminance. R^2, coefficient of determination of the linear regression. **g**, Maximum power point tracking of FPSC module under full sunlight AM1.5G

and indoor warm light LED 600 lx illumination over 24 hours. **h**, Normalized PCE of FPSC module as a function of 2000 bending cycles (5 cm bending radius). **i**, Results of lead release test from FPSC module when submerged in a synthetic sweat solution and operated for 24 hours.

The main advantage of our quasi-2D FPSC energy harvesting module is its ability to operate at high efficiency even under indoor and low light illumination conditions. Common indoor lighting sources, like LEDs, have a narrower emission spectrum that closely matches the external quantum efficiency (EQE) of our quasi-2D FPSC, and a lower photon flux density, when compared to sunlight (**Fig. 6-2d**). This results in an increased PCE due to reduced sub-bandgap relaxation and recombination losses, as well as passivation of trap states and grain boundaries via MBA incorporation. Thus, quasi-2D FPSC practically double their efficiency under 600 lx (215 $\mu W\ cm^{-2}$) LED indoor illumination, achieving a PCE as high as 31.2 % in small area devices, scaling up efficiently to large area with a PCE of up to 29.9 %, and reaching 29.6 % in module configuration (**Fig. 6-2e, Supplementary Table 6-2**). These are the highest reported PCE values among indoor flexible solar cells, outperforming not only perovskite but also other PV technologies in this field (**Supplementary Table 6-3**). Furthermore, the power output of the quasi-2D FPSC module reliably extends over a broad range of indoor illuminance ranging from very bright (10k lx), common for special environments like surgery rooms, down to dimly lit surroundings (20 lx) (**Fig. 6-2f, Supplementary Figs. 6-6** and **6-7**).

In order to acquire light-source-independent performance values, we also measured PCE using a monochromatic light source (continuous laser, $\lambda = 637$ nm) over a range of indoor and low light irradiances ($0.07 < P_{in} < 18\ mW\ cm^{-2}$) (**Supplementary Fig. 6-8**). We achieved a record breaking PCE of 41.4±0.1% measured at $P_{in} = 12.23\ mW\ cm^{-2}$ for the small area devices, and a PCE of 30.4±0.2% at $P_{in} = 6.08\ mW\ cm^{-2}$ for large area devices (**Supplementary Table 6-4, Supplementary Note 1**).

The quasi-2D FPSC modules show steady power output with no loss in performance after continuous 24 hours operation under both AM1.5 and indoor illumination conditions (**Fig.**

6-2g, Supplementary Fig. 6-9). Additionally, the module mechanical stability was confirmed to withstand 2000 bending cycles (bending radius 5 cm) with only negligible reduction in performance that can be attributed to decrease in ITO electrode resistance (**Fig. 6-2h, Supplementary Figs. 6-10** and **6-11**).

Considering the concern of possible lead leakage while using perovskite solar cells, a set of Pb-release tests were performed in deionized water (**Supplementary Fig. 6-12**), as well as in a standard synthetic sweat solution[193,194] on a fully-encapsulated quasi-2D FPSC module (**Fig. 6-2i**). Continuous operation of the FPSC module under AM1.5 for 24 hours while fully immersed in simulated sweat solution resulted in a lead concentration that remained more than one order of magnitude below the maximum allowable level in drinking water as per the Joint Food and Agriculture Organization/World Health Organization (FAO/WHO) Expert Committee on Food Additives (JECFA)[195] (**Fig. 6-2i**), indicating the encapsulation robustness and module safety even under conditions that far exceed the expected operational conditions of the wearable device. Furthermore, the encapsulated FPSC maintained high biocompatibility even after vigorous mechanical bending tests as evidenced by low Pb-leakage as well as high cell viability and metabolic activity of the cells seeded on the FPSCs (**Supplementary Figs. 6-13** and **6-14**).

6.2.3 System-level integration and operation of wearable device

Composed of off-the-shelf electronic components, the judiciously designed wearable electrochemical instrumentation system of the wearable device is more powerful in functionality and power-efficient than any other reported wearable sweat analyzer. The battery-free electronic system interfaces with the skin via an inkjet-printed disposable sweat patch that contains two gel-loaded iontophoretic electrodes, three electrochemical sweat biosensors, and one sweat rate sensor embedded in the microfluidics (**Fig. 6-3a**). The system performs constant-current iontophoresis for sweat induction; amperometry, potentiometry, and voltammetry for continuous analysis of a variety of sweat biomolecular markers; impedance measurements for sweat rate monitoring; and Bluetooth data communication with the user interface (**Fig. 6-3b,c**, **Supplementary Figs. 6-15 and 6-16**).

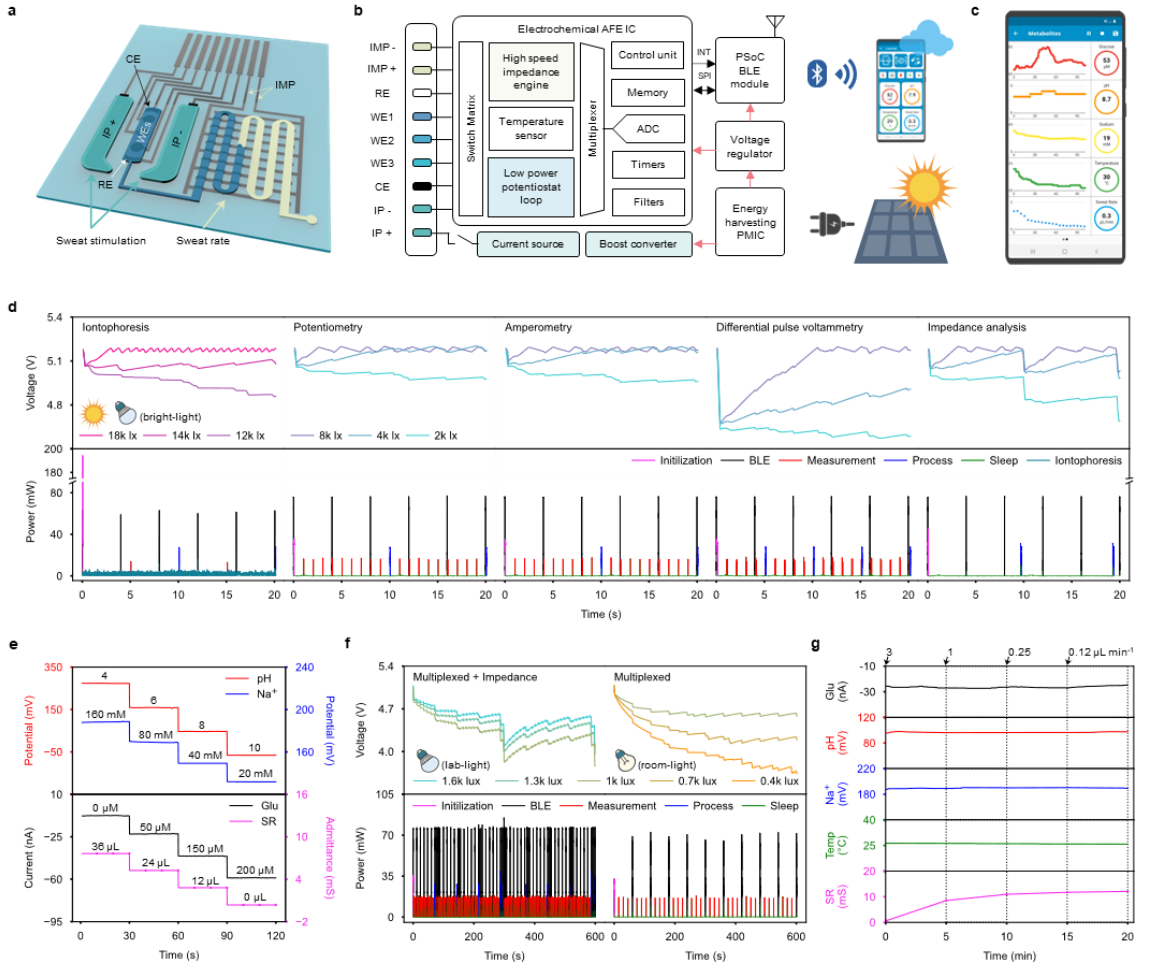

Figure 6-3. **System design and characterization of the wearable device for energy harvesting and autonomous multimodal biosensing. a**, Schematic of the disposable microfluidic sweat patch for sweat induction and sampling. IMP, impedance; CE, counter electrode; WE, working electrode; RE, reference electrode; IP, iontophoresis. **b**, System-level block diagram of the wearable device. **c**, Custom mobile application for the wearable device. ADC, analog to digital converter; AFE IC, analog front end integrated circuit; PsoC, programmable system on chip; INT, interrupt; SPI, serial peripheral interface. **d**, Power consumption profile (bottom) and corresponding capacitor charging-discharging curves (top) of various operation modes under varying light intensities. **e**, Responses of the Na^+, pH, glucose (Glu), and sweat rate (SR) sensors obtained by the wearable device. **f**, Power consumption profile (bottom) and corresponding capacitor charging-discharging

curves (top) during multiplexed measurements under indoor lab-light (left) and room-light (right) illumination conditions. **g**, Multiplexed and multimodal sensing response under varying flow rates (0.12–3 μL min^{-1}) and lab-light illumination (1200 lx). Temp, temperature.

More specifically, the wearable device's electronic system consist of: 1) an energy harvesting power management integrated circuit (PMIC) that efficiently boost converts and manages the output from the quasi-2D FPSC, 2) a compact programmable system-on-chip (PSoC) Bluetooth low energy (BLE) module that integrates a microcontroller (MCU) and BLE radio, 3) an electrochemical analog front-end (AFE) that integrates various configurable blocks necessary for electrochemical detection, and 4) a high compliance-voltage current source with an overcurrent protection switch for iontophoresis (**Fig. 6-3b** and **Supplementary Fig. 6-17a,b**). Under illumination, the PMIC charges the 5 mF solar energy storage capacitor up to ~5 V to continuously power the wearable device. Our custom-developed embedded algorithm ensures that each block of the system operates at its lowest viable power mode, enabling ultra-low-power multiplexed electrochemical measurements consuming below 60 μW (**Supplementary Fig. 6-17c** and **Supplementary Fig. 6-17**). During operation, the wearable device stays in deep-sleep (33 μW during standby) or sleep (47 μW during potentiostat operations) modes and wakes up intermittently to either wirelessly communicate with the host software, perform an electrochemical measurement, or process measurement data (**Supplementary Fig. 6-19**). Depending on the illumination conditions and the quasi-2D FPSC's power output, the wearable device adapts its operation mode (e.g., parameters such as BLE communication interval and sensor data acquisition interval to mediate power consumption) (**Supplementary Note 2**). The power consumption profiles for each electrochemical operation and the corresponding capacitor charging/discharging curves of the solar energy storage capacitor when powered by a quasi-2D FPSC module under various illumination conditions (2k–18k lx) are highlighted in **Fig. 6-3d** as well as **Supplementary Fig. 6-20** and **Supplementary Table 6-5**. The electrochemical instrumentation performance

of the wearable device was successfully validated by comparing its potentiometric, amperometric, and voltammetric responses to those of a commercial potentiostat (**Supplementary Fig. 6-21**).

6.2.4 Characterization of device for multimodal biosensing

An iontophoretic sweat induction microfluidic module was carefully designed and optimized for minimal power consumption and prolonged use. Unlike standard pilocarpine gels that can only stimulate local sweat glands directly beneath the agonist gel for a short duration and lead to low sensing accuracy due to the mixing of sweat and gel fluid[174,175], carbagels stimulate local and neighboring sweat glands steadily for extended durations[178,179]. This property enables the use of miniaturized carbagels for prolonged sweat induction and microfluidic neighboring sweat collection on a single patch design. The dimensions and layout of the carbagels with respect to the sweat accumulation reservoir were optimized for minimal size, applied current, and maximal sweat extraction efficiency (**Supplementary Note 3**). The reusable carbagel, capable of stimulating sweat continuously throughout the day, is a part of the mass-producible and disposable microfluidic sensor patch that can be replaced for daily use. To demonstrate the device's wearable use, the sweat processing system was paired with a sensor array consisting of an amperometric enzymatic glucose sensor, potentiometric ion-selective pH and Na^+ sensors, and an impedimetric sweat rate sensor. The individual current, potential, and admittance responses of each sensor were recorded by the wearable device under physiologically relevant target analyte concentrations and/or sweat rates (**Fig. 6-3e, Supplementary Fig. 6-22**); linear responses were observed between the measured electrochemical signals and target concentrations (for glucose sensor), logarithm target concentrations (for pH and Na^+ sensors), and reciprocal flow rate (for sweat rate sensor). While sweat Na^+ and pH levels can individually serve as a potent biomarker for various health conditions, they could synergistically aid in calibrating the sweat rate and glucose sensors, respectively (**Supplementary Fig. 6-23**). In addition, temperature information recorded by the built-in temperature sensor in the AFE of the wearable device aids in more accurate sensor calibrations during wearable use (**Supplementary Fig. 6-24**).

Moreover, the sweat rate sensor can be reconfigured with different volumetric capacities for desired operation duration (**Supplementary Fig. 6-25**).

When powered by the quasi-2D FPSC module, the wearable device performs multiplexed on-body measurement sequences under a wide range of indoor illumination conditions. With indoor LED illumination with a brightness as low as 1k lx, the wearable device simultaneously monitors glucose, pH, Na^+, and temperature, along with the periodic impedimetric measurement of sweat rate; when less light as low as 400 lx is available, the wearable device's custom algorithm adapts to decrease the multiplexed measurement frequency and transmits data over BLE advertisements (**Fig. 6-3f**). With a larger area wearable solar cell (8.9 cm x 7.4 cm), the wearable device performs the same multiplexed on-body measurement sequences under even darker illumination conditions (100-300 lx) (**Supplementary Fig. 6-26**).

In vitro multimodal analysis of glucose, pH, Na^+, temperature, and flow rate through the assembled microfluidic sensor patch was performed in a phosphate-buffered saline (PBS) solution containing 100 μM glucose under varying flow rates (0.12–3 μL min^{-1}) and under lab-light illumination (1200 lx) (**Fig. 6-3g**). The glucose, pH, and Na^+ biosensors maintained sTable 6-and accurate responses even at a flow rate as low as 0.12 μL min^{-1}, while the sweat rate sensor responded accurately according to the increasing volume. This indicates that while the integrated biosensors will respond to physiologically-induced analyte level changes during the on-body tests, their performance will not be substantially affected by changes in sweat rates. The long-term stability of the wearable device for continuous energy harvesting and multiplexed biosensing was further validated in a long-term study with a constant flow rate of 1 μL min^{-1} for 100 min under varying indoor illumination conditions (**Supplementary Fig. 6-27**).

6.2.5 On-body device evaluation for multimodal sweat monitoring

The compact design of the wearable device enables the comforTable 6-and strong adhesion of the device to different body parts with access to ambient light (**Fig. 6-4a**). When worn on body under various outdoor and indoor illumination conditions, the wearable device harvests

energy sufficient to enable iontophoresis and multiplexed sweat biosensing sequences; additionally, the light-powered iontophoresis results in efficient and prolonged sweat extraction to allow dynamic sweat biomarker analysis (**Fig. 6-4b**, **Supplementary Fig. 6-28**). The accuracy of the device's interdigitated electrode-enabled sweat rate sensor during wearable use was successfully validated with image-based colorimetric sweat rate analysis (enabled by filling a color dye in the microfluidic sweat inlet before the on-body test) (**Supplementary Fig. 6-29a**). Autonomous periodical sweat induction allows prolonged continuous sweat extraction: our pilot studies show that a single sweat induction event was on average able to extract ~52 μL over a duration of 3 hours, while sustaining a steady sweat rate over 0.1 μL min^{-1} (**Supplementary Fig. 6-29b,c**).

The wearable device's efficient light energy harvesting capability and powerful sweat processing system enable continuous and non-invasive physiochemical monitoring under laboratory illumination conditions. The evaluation of the wearable device for cardiometabolic monitoring was performed by continuously monitoring sweat glucose, pH, Na^+, and sweat rate levels along with the skin temperature of human subjects in both sedentary and exercise trials (**Fig. 6-4c–f** and **Supplementary Figs. 6-30 and 6-31**). In the sedentary studies, light-powered iontophoretic sweat extraction was followed by the continuous monitoring of key biomarkers. In the fasting studies, sweat glucose, pH, Na^+, and skin temperature remained sTable 6-while sweat rate rapidly increased in the first 30 min and then gradually decreased (**Fig. 6-4c**). In the oral glucose intake studies, a substantial increase in sweat glucose was observed through the first hour (**Fig. 6-4d**). Sedentary fasting and glucose intake studies were repeated twice for two additional subjects (**Supplementary Figs. 6-30** and **31**). From the sedentary oral glucose intake studies performed across 3 subjects, a high correlation was observed between blood glucose levels and sweat glucose levels (**Supplementary Fig. 6-32**). Similarly, in the exercise studies, sweat glucose remained relatively sTable 6-or slightly decreased during fasting, while clearly elevated glucose levels were observed after oral glucose intake followed by a quick decrease after 30 min (**Fig. 6-4e,f**). We also noticed a conspicuous discrepancy between pH levels of carbachol iontophoresis-induced sweat (~pH 9) and exercise-induced sweat (~pH 5), indicating the

importance of sweat induction approaches and pH calibrations on personalized metabolic monitoring (**Supplementary Fig. 6-33**). In all sedentary and exercise studies, positive correlations between the real-time calibrated sweat glucose and blood glucose levels were obtained, indicating the high potential of realizing non-invasive glucose monitoring using the wearable device. Potential noise due to motion artifacts during on-body sensing was mitigated by tightly packing and adhering the miniaturized wearable system onto the skin, where electrochemical sensing was performed in a bound microfluidic reservoir to prevent direct skin-sensor contact. Noise was further reduced by hardware filters integrated on-board as well as smoothing algorithms implemented in the custom app.

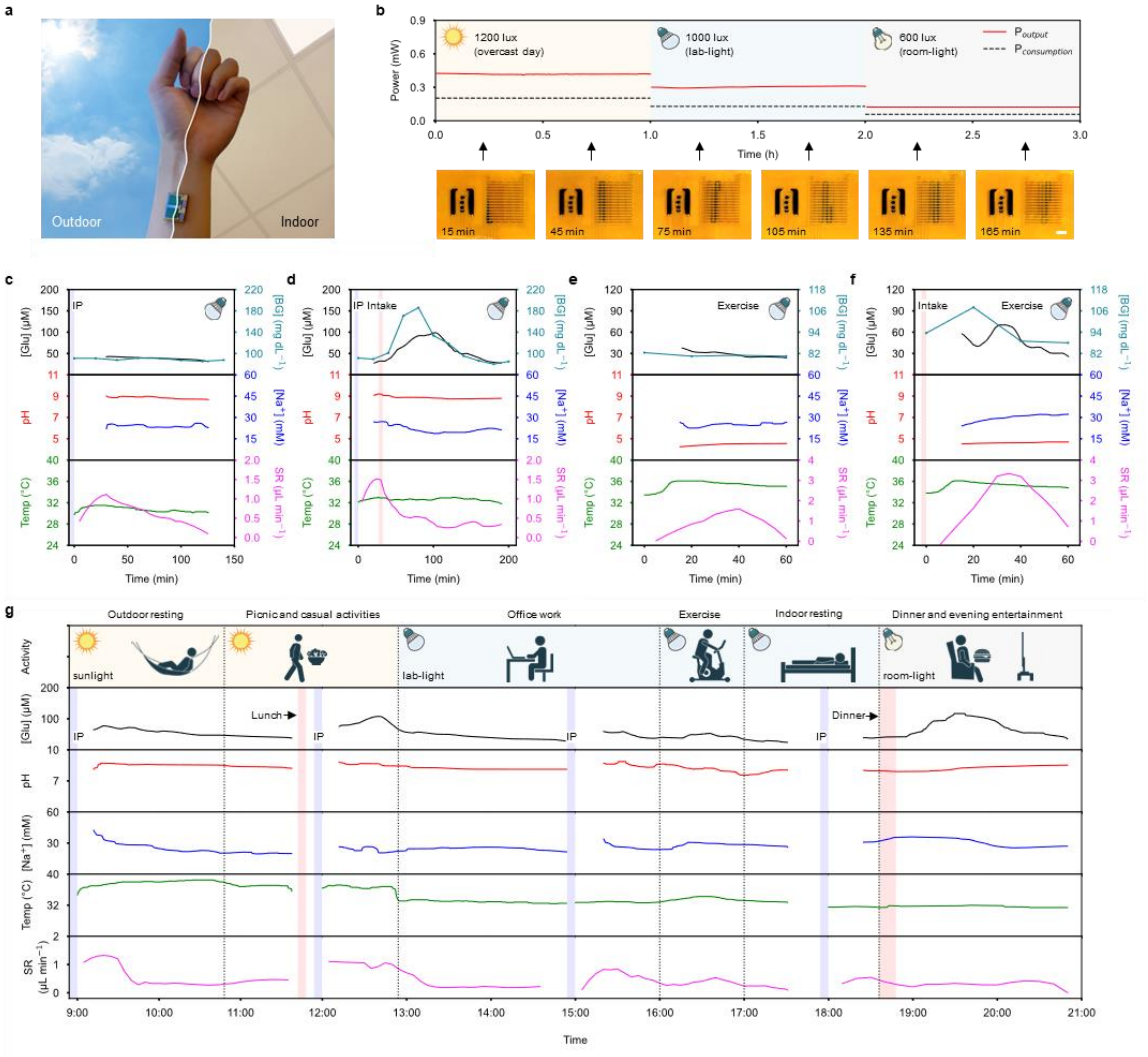

Figure 6-4. **On-body evaluation of the wearable device for prolonged and cross-activity perspiration analysis. a**, Photo of a wearable device worn on-body. **b**, Power output of wearable device's quasi-2D FPSC module and power consumption of the wearable device electronics when performing multiplexed sweat biosensing under various illumination conditions. Inset photos below show the corresponding microfluidic sweat sampling after a single iontophoresis sweat induction event. Scale bar, 3 mm. **c**,**d**, Wearable device-enabled autonomous multiplexed physiological monitoring at a fasting state (**c**) and after a glucose tolerance test (**d**) on a healthy subject under lab-light illumination. IP, iontophoresis. **e**,**f**, Wearable device-enabled multiplexed physiological monitoring during vigorous exercise at a fasting state (**e**) and after a dietary intake (**f**) under lab-light illumination. g, Full-day cross-activity physicochemical monitoring with the wearable device under different light conditions.

Prolonged cross-activity multimodal monitoring of sweat biomarkers in real-life scenarios was enabled by the wearable device as illustrated in **Fig. 6-4g**. Throughout the day, over a 12-hour time span, the subject performed various physical activities under various lighting environments. During this time, the wearable device performed iontophoresis intermittently to ensure that a sufficient sweat rate could be maintained for sweat refreshing and continuous sensor measurements throughout the day. Depending on the available illumination, the wearable device switched its on-body measurement sequence to adjust its power consumption while trading off for measurement intervals. While the multiplexed data interval varied from 8 s to 60 s throughout the day, the wearable device was able to collect, process, and calibrate sensor data continuously in all scenarios. The glucose trend throughout the day shows that the larger meal during dinner results in a higher and longer sweat glucose spike than the lighter lunch. In addition, the average sweat rate during outdoor sedentary activities was higher than the average sweat rate during indoor sedentary activities while vigorous exercise leads to a substantial increase in sweat rate. Considering that the battery-free version of the wearable device requires access to light for long-term operation,

integrating a small battery into the wearable device could realize 24-hour operation (even during sleep) (**Supplementary Figs. 6-34** and **6-35**).

6.3 Discussion

We have reported a wearable biosensor platform that is powered by a quasi-2D FPSC. The wearable device can persistently extract sweat and simultaneously monitor physicochemical markers (glucose, pH, Na^+, sweat rate, and skin temperature) via a spectrum of electrochemical techniques (potentiometry, amperometry, voltammetry, and impedimetry). It can achieve this under various illumination conditions (strong outdoor sunlight to dim indoor LED light) and across various activities (sleep to vigorous exercise).

Our quasi-2D FPSC is uniquely suiTable 6-for powering wearable technologies. The solar harvesting technology offers high efficiency under indoor and low light illumination conditions, maintains high power conversion efficiency and power output across a wide range of illumination conditions, withstands mechanical stress common for on-body wear during vigorous exercise, and remains safe through proper encapsulation. The wearable solar cell is paired with a compact, wireless, and low-power wearable multichannel electrochemical workstation that dynamically adjusts its power consumption to continuously operate without a battery under varying illumination conditions. The modular design of the wearable device is readily scalable; if required, additional energy harvesting modules can be incorporated.

The microfluidic iontophoretic sweat processing module enables prolonged flow rate-monitored sweat extraction. This allows sweat biosensing to be applied beyond situations where vigorous exercise is required — that is, normal everyday activity — as well as use for patients with mobility impairments. The rate-monitored persistent sweat flow continuously refreshes the sensor reservoir for accurate biomarker measurements; the sensor responses are calibrated in real-time by personalized factors such as skin temperature, sweat pH, and sweat Na^+ to further improve measurement accuracy.

Future work for the technology will involve improving the long-term stability of the sensor patch and investigating the correlation between sweat/blood biomarker levels in large-scale human trials. The wearable device can also be paired with different biosensors based on a wide array of electrochemical detection mechanisms (potentiometry, amperometry, voltammetry, and impedimetry) for the identification of an endless number of target biomarkers. Potential fields of application including sport science and daily tracking, as well care for people with health conditions or impairments.

6.4 Methods

6.4.1 Solar cell fabrication and characterization

Glass substrates (1 × 1 inch, 1 mm thick) were cut and cleaned in an ultrasonic bath for 30 min each in 2 v/v% Hellmanex in DI water solution, 2 × DI water solution, acetone, and isopropanol, and dried using N_2 stream. Flexible ITO-covered PET substrates were patterned using insulating tape for masking and etched using concentrated HCl for 10 min. After that they were also cut to 1 × 1 inch size and washed using the same procedure as for glass. PDMS solution was spin-coated onto glass at 4000 rpm for 30 s and placed on a heat plate at 105 °C for 1 min. After that, flexible substrates were placed on to the PDMS-covered glass, carefully avoiding any trapped air underneath. Finally, the whole substrate was annealed for 15–20 min at 105 °C. Cr-Au bus bars were deposited via thermal evaporation using a shadow mask (base pressure 3×10^{-6} mbar).

The PEDOT:PSS solution was prepared by mixing Clevios PH1000 stock solution with 7 vol% DMSO and 0.7 vol% Zonyl FS-300. The PEDOT:PSS solution was stirred at room temperature for an hour, then kept at 4 °C overnight. Right after filtering through Minisart RC25 Syringe filter 0.45 µm regenerated cellulose, the PEDOT:PSS solution was spin-coated on the substrates with busbars at 1500 rpm for 45 s (ramp 2 s) followed by 1000 rpm for 2 s (ramp 1 s) and annealed at 120 °C for 15 min. Then the film was washed by spin-coating isopropanol at 1000 rpm for 4 s followed by 4000 rpm for 12 s and annealed again at 120 °C for 15 min.

Perovskite solution ($(MBA)_2(Cs_{0.12}MA_{0.88})_6Pb_7(I_xCl_{1-x})_{22}$) was prepared by mixing PbI_2 (322.4 mg,), $PbCl_2$ (83.5 mg,), (R)-(+)-α-methylbenzylamine iodide (MBAI) (74.7 mg,), and Methylamonium iodide (MAI) (187.7 mg,) in DMF containing 10 vol% acetylacetone and stirred for 1 h at 55 °C. MBAI was synthesized from (R)-(+)-α-methylbenzylamine and hydroiodic acid and purified using diethylether (VWR) and absolute ethanol (Merck Millipore) using a procedure previously described in the literature[196]. MAI was synthesized using an analogous procedure. Afterwards, CsI (~0.12 mmol, from 1.5 M stock solution in DMSO) was added to the mixture and stirred overnight. The solution was filtered using polytetrafluoroethylene (PTFE) syringe filters (0.45 μm; Whatman) before spin-coating. Perovskite solution was then deposited using an anti-solvent procedure inside of the nitrogen (N_2) glovebox. The solution was spin-coated in two steps at 1000 rpm for 5 s with ramp 200 rpm s^{-1} followed by 4000 rpm for 25 s with ramp 2000 rpm s^{-1}. Approximately ~0.2 mL of chlorobenzene (anti-solvent) was dropped at 15th second for about 3 s. Then the film was annealed at 100 °C for 1 h.

After the film cooled down to room temperature PCBM solution was spin-coated onto the sample at 1500 rpm for 16 s (ramp 2 s) followed by 2000 rpm for 15 s (ramp 2 s). PCBM solution was prepared by dissolving 2 wt% PCBM in chlorobenzene and chloroform (1:1 volume ratio). TiOx solgel was prepared based on procedure reported by Heilgenaw et al[196]. TiO_x was spin-coated at 4000 rpm 30 s (ramp 2 s) and annealed at 110 °C for about 5 min in an ambient atmosphere. Cr/Au contacts were evaporated at rate of 0.01-0.5 nm s^{-1} and base pressure 3×10^{-6} mbar. Finally, the devices were encapsulated using UV curable flexible epoxy and PVC/PCTFE protective films. Absorbance spectra were recorded using LAMBDA 1050 UV/Vis Spectrophotometer, Perkin Elmer, U.S.A. Photoluminescence spectra were recorded on a photomultiplier tube–equipped double-grating input and output fluorometer (Photon Technology International).

Current density-voltage (J-V) characteristics of solar cells under sunlight illumination were recorded under simulated AM1.5 global spectrum irradiation from a 150 W xenon light source using Keithley 2400 source meter and a custom Lab-View program. The intensity of

the solar simulator was adjusted using a commercial Si reference diode (Si-01TC, Ingenieurburo Mencke & Tegtmeyer, Germany). The performance of the solar cells under indoor lighting was tested using a set of commercial off-the-shelf warm light LED light bulbs (Philips, 2700 K, 4.3 W, 470 lm; Philips, 2700 K, 7 W, 806 lm; Osram, 2700 K, 21 W, 2451 lm). The measurement was performed inside of a light-tight black cloth-covered characterization chamber with the cell tightly wrapped with black tape, allowing only the active area to be exposed to the light, thus reducing the influence of reflections or stray light. A broad range of intermediate illuminance levels was achieved by utilizing a set of neutral density filters placed directly on the device. The emission spectrum of the light bulbs was measured using a fiber spectrometer (Avantes, AvaSpec-2048-USB2) (**Supplementary Fig. 6-6**) Illuminance of the LED light sources was measured using ISO calibrated lux meter (Voltcraft MS-1300). Spectral incident power intensity of the LED light bulbs was calculated as reported in literature[197]. Additionally, reference PCE under low light conditions was calculated from a JV curve measured under a monochromatic light source (637 nm laser, Coherent OBIS 637 nm, 140 mW), with the incident power intensity calculated using a calibrated Si diode (Hamamatsu S2281).

Surface SEM measurements were made using the Zeiss 1540 XB CrossBeam SEM (acceleration voltage 5 keV). A cross-section image was prepared by prepared using a standard focus ion beam cutting approach. Images of the cross-section were performed under the same conditions as surface SEM measurements.

Maximum Power Point (MPP) tracking was performed using an in-house written Python script utilizing a common Perturb-and-Observe algorithm. Starting voltage for the measurements was $V_{oc} \cdot FF$, with a step size of 50 mV and 15 s waiting time between voltage perturbations.

Lead release test was performed using standard artificial sweat solution (containing sodium chloride 0.5 % w/w, lactic acid 0.1 % w/w, and urea 0.1 % w/w in deionized water) as described in European Standard EN 1811:1998. Encapsulated solar cell modules were immersed into 100 mL freshly prepared synthetic sweat buffer and placed at about 20 cm

under a xenon lamp solar simulator with AM1.5G spectrum (distance adjusted so to achieve approximately 1 Sun illumination). The buffer was continuously stirred with a magnetic stirrer and 1 mL extract samples were collected periodically and stored in the fridge at 4 °C until the next day when they were analyzed using inductively coupled plasma mass spectrometry (ICP-MS). Alternatively the lead tests were also performed with just deionized water, following the same procedure described above.

Each ICP-MS sample was extracted with 18.2 MOhm water. The extracts were measured without further dilution on an XSeries 2, Thermo Scientific ICP-MS instrument equipped with a MiraMist nebulizer. Calibration was performed with a Certipur multielement standard XXI.

6.4.2 In vitro cell studies

Normal Adult human dermal fibroblast cells (HDFs, Lonza) were cultured in manufacturer's recommended media (FGMTM-2 Growth Media) under 37 °C and 5% CO2. The cells were then passaged at 80% confluency (passage number 5) and were used for all cell studies. For in vitro cytocompatibility tests, two groups of FPSCs (before and after bending) were placed in media during the course of study to release the possible undesired toxic residuals. The HDF cells were seeded into 24 well plates (1 × 105 cells per well) and were treated with appropriate media and incubated under 37 ºC and 5% CO2 for up to 7 days. For the control, cells were treated with fresh media without contact with FPSCs. Cell viability was evaluated by using a commercial calcein AM/ethidium homodimer-1 live/dead kit (Invitrogen) on day 1 and 7 post culture. The samples were then visualized by using an Axio Observer inverted microscope (ZEISS) and cell viability was calculated using ImageJ software and reported as the ratio of live cells to total number of cells (live + dead). A commercial PrestoBlue assay (Thermo Fisher) was also used to evaluate cell metabolic activity according to manufacturer's protocol.

6.4.3 Electronic system design and characterization

The electronic system consists of four main blocks for power management, data processing and wireless communication, electrochemical instrumentation, and iontophoretic induction

(**Supplementary Fig. 6-8**). The power management block consists of an energy harvesting PMIC (BQ25504, Texas Instruments) and a voltage regulator (ADP162, Analog Devices). The PMIC utilizes maximum point power tracking (MPPT) to efficiently boost charge the solar cell output of 5 V and charge the 5mF energy storage capacitor. The threshold control unit of the PMIC enables the capacitor to power the rest of the system while the capacitor voltage stays within a threshold voltage between 3~5 V. The voltage regulator then regulates the capacitor voltage to a sTable 6-2.8 V to supply the data processing and wireless communication, and electrochemical instrumentation blocks.

Data processing and wireless communication are performed by a compact programmable system-on-chip (PSoC) BLE module (Cyble-222014, Cypress Semiconductor) that integrates a microcontroller (MCU) and BLE radio, and electrochemical instrumentation is performed by an electrochemical front-end (AD5941, Analog Devices) and voltage buffers (MAX40018, Analog Devices) that integrate various configurable blocks necessary for electrochemical detection. The PSoC BLE module communicates with the host software via BLE and controls the Electrochemical AFE via serial peripheral interface (SPI). The electrochemical AFE is the core of the platform. The electrochemical AFE's configurable amplifiers can be configured for various electrochemical measurements at multiple modes of measurement ranges and resolutions. For high bandwidth impedance measurements, the high speed loop can be configured, and for lower bandwidth measurements such as potentiometry, amperometry, and voltammetry, the low-power loop can be configured. The AFE contains multiple elements such as a sequencer, a memory block, a waveform generator, and a DFT hardware accelerator that enables independent operation of complex electrochemical procedures, minimizing the workload of the microcontroller and the overall power consumption. Furthermore, a switch matrix and multiplexer flexibly connect the sensors and analog signals to the appropriate channels.

The iontophoresis induction block generates a high compliance-voltage constant current with current monitoring to safely deliver current across the skin through a gel. A boost converter (TPS61096, Texas Instruments) boosts the energy storage capacitor voltage from the PMIC

to a high compliance-voltage, and a BJT array (BCV62C, Nexperia) is configured as a current mirror to supply a steady current through the analog switch (DG468, Vishay Intertechnology) while the iontophoresis block is actuated. Furthermore, the electrochemical AFE's switch matrix enables the iontophoresis block to flexibly connect to the electrochemical AFE's low-power current measurement channel for iontophoresis current monitoring overcurrent protection during iontophoresis.

The wearable device was powered by a custom developed quasi-2D FPSC in most experiments, The power consumption of the system was characterized using a power profiler (PPK2, Nordic Semiconductor), and the energy storage capacitor charging-discharging curves were collected using an electrochemical workstation (CHI 660E). For experiments under bright to room-light illumination conditions (>400 lx), a custom developed quasi-2D FPSC was used to power the wearable device; for experiments under dim-light illumination conditions (<300 lx), a commercial flexible solar cell was used (LL200-2.4-75, PowerFilm Inc.). To validate the performance of the wearable device for electrochemical measurements, we compared the potentiometric, amperometric, and voltammetric responses collected by the wearable device under laboratory-light mode with those collected by an electrochemical workstation (CHI 660E).

6.4.4 Microfluidic sensor patch fabrication and assembly

The PI substrates were cleaned prior to inkjet printing via O2 plasma surface treatment (Plasma Etch PE-25, 10–20 cm3 min-1 O2, 100 W, 150–200 mTorr) to remove debris and improve surface hydrophilicity. Next, an inkjet printer (DMP-2850, Fujifilm) was used for the sequential printing of silver (interconnects and connection pads, interdigitated sweat rate sensor, and reference electrode), carbon (iontophoresis, counter, and working electrodes), and PI (encapsulation). The reference and working electrodes were further modified via electrochemical deposition (CHI 660E) and drop-casting methods for selective electrochemical sensing. Meanwhile, a 50 W CO2 laser cutter (Universal Laser System) was used to pattern M-tape (3M 468MP) and PET layers to be further assembled onto the sensor patch for microfluidic sweat processing. Z-axis conductive tape (3M 9703) was used to

electrically connect the encapsulated PCBs, solar cells, and microfluidic sensor patch through the connection pads and interconnects printed on the PI substrate.

Both anode and cathode carbagels were prepared by heating DI water containing 3% w/w agarose to 250 °C under constant stirring until the mixture became homogenous. After cooling down the mixture to 165 °C, 1% w/w carbachol was added to the anode mixture, and 1% w/w KCl was added to the cathode mixture. Then, the mixtures were poured into the assembled microfluidic sensor patches' carbagel cutouts, where the hydrogels solidified.

6.4.5 Biosensor preparation and characterization

An electrochemical workstation (CHI 660E) was used for electrochemical deposition, and both the electrochemical workstation and the wearable device were used for sensor characterization.

Reference electrode: To form Ag/AgCl, 0.1 M $FeCl_3$ was drop-casted onto the inkjet-printed Ag reference electrode for 30 s. A PVB reference cocktail was prepared by dissolving 79.1 mg of PVB, 50 mg of NaCl, 1 mg of F127, and 0.2 mg of MWCNT into 1 ml of methanol. 1.66 μL of the PVB reference cocktail was drop-casted onto the Ag/AgCl reference electrode and left to dry overnight such that the reference electrode can maintain a steady potential regardless of the ionic strength of the solution.

Glucose sensor: Au nano-dendrites were modified on a carbon working electrode by applying a pulsed voltage from -0.9 V to 0.9 V at a frequency of 50 Hz in a solution containing 50 mM $HAuCl_4$ and 50 mM HCl. A Prussian blue layer was electrochemically deposited on the modified working electrode by performing cyclic voltammetry from -0.2 V to 0.6 V at a scan rate of 50 mV s^{-1} for 20 cycles in a solution containing 2mM $FeCl_3$, 2.5 mM $K_3[Fe(CN)_6]$, 0.1 M KCl, and 0.1 M HCl. Then, the electrode was further modified by performing cyclic voltammetry from 0 V to 0.8 V at a scan rate of 100 mV s^{-1} for 8 cycles in a solution containing 5 mM $NiCl_2$, 2.5 mM $K_3[Fe(CN)_6]$, 0.1 M KCl, and 0.1 M HCl. A GOx enzyme cocktail was prepared by mixing 99 uL of 1% BSA, 1 uL of 2.5 % glutaraldehyde,

and 0.25 uL of 10 mg/mL GOx. 1.66 μL of the enzyme cocktail was drop-casted onto the modified working electrode and left overnight to dry.

Sodium sensor: A carbon working electrode was modified in a solution containing 30 mg $K_4[Fe(CN)_6]\cdot 3H_2O$, 206.1 mg NaPSS, 10.7 μL EDOT in 10 mL DI water by applying a constant potential of 0.865 V for 10 min. A Na^+ selective membrane cocktail was prepared by dissolving 1 mg of Na ionophore X, 0.55 mg Na-TFPB, 33 mg PVC, and 65.45 mg DOS into 660 μL THF. 1.66 μL of the Na^+ selective membrane cocktail was drop-casted onto the modified carbon working electrode and left to dry overnight.

pH sensor: Au was deposited on a carbon working electrode by applying a constant potential of 0 V for 30 s in a solution containing 50 mM $HAuCl_4$ and 50 mM HCl. A PANI layer was electropolymerized on the Au modified working electrode by performing cyclic voltammetry from -0.2 V to 1 V at a scan rate of 50 mV s^{-1} for 50 cycles.

Biosensor characterization: For in vitro characterizations for the Na^+ and sweat rate sensors, NaCl solutions (12.5–200 mM) were prepared in DI water. For characterization of the pH sensors, Mcllvaine's buffers with pH values ranging from 4 to 8, and HCl-mediated Mcllvaine's buffer with a pH of 10 were used. For characterization of the glucose sensors, glucose solutions (0–200 μM) were prepared in PBS buffers with pH ranging from 4 to 10. For characterization of the sensors' dependence on temperature, a ceramic hot plate (Thermo Fisher Scientific) was used. For in vitro flow tests, a syringe pump (78-01001, Thermo Fisher Scientific) was used to inject various fluids through the microfluidic sensor patch at flow rates varying form (0.12–3 μL min^{-1}).

6.4.6 On-body evaluation of the wearable device

The validation and evaluation of the wearable device were performed using human subjects in compliance with the ethical regulations under protocols (ID 19-0892 and 21-1079) that were approved by the Institutional Review Board (IRB) at the California Institute of Technology (Caltech). Participating subjects between the ages of 18 and 65 were recruited from the Caltech campus and neighboring communities through advertisement by posted

notices, word of mouth, and email distribution. All subjects gave written informed consent before participation in the study. For all human studies, subjects cleaned their skin with water and alcohol swabs before applying the wearable device on the skin.

System evaluation conditions: For chemical sweat induction, the subjects were illuminated under bright-light conditions for 10 min to enable light-powered iontophoresis (55 μA, 10 min). Following iontophoretic stimulation, the subjects were illuminated under either bright-light (14k lx), laboratory-light (1200 lx), or room-light (600 lx) illumination conditions to enable continuous biomarker detection for the remainder of the study. Sweat rate was measured periodically either with the impedimetric sweat rate sensor, visually, or by both ways.

System evaluation with sugar intake: For fasting and intake studies, subjects reported to the laboratory after fasting overnight. For the iontophoresis-based studies, the wearable device was applied to the ventral forearm region and the subject was illuminated under bright-light (14k lx) conditions for the first 10 minutes to power iontophoresis. For the remainder of the study, the subject was illuminated under lab-light (1200 lx) conditions at rest, while the wearable device performed wireless multimodal monitoring of sweat biomarkers with multiplexed glucose, pH, sodium, and temperature measurements occurring at 8 s intervals, and sweat rate measurements occurring at 5 min intervals. The data was wirelessly transmitted in real-time via BLE indications. For the iontophoresis intake study, the subject was provided a soft drink containing 55 g of sugars. For the exercise-based studies, the wearable device was applied to the forehead region, and the subject was illuminated under lab-light (1200 lx) conditions throughout the entire study, wherein subjects performed constant-load cycling (50 rpm) on a stationary exercise bike (Kettler Axos Cycle M-LA) for 60 minutes. For the exercise intake study, the subject was provided a soft drink containing 55 g of sugars.

System evaluation during daily activities: For the full day study spanning from 9 AM to 9 PM, the subject was iontophoretically stimulated *via* the wearable device for 10 min at 9 AM, 12 PM, 3 PM, and 6 PM. The microfluidics was reset before each iontophoresis section

to obtain continuous sweat rate reading. From 9 AM to 1 PM, the subject was outdoors under the sun (100k lx); from 1 PM to 6 PM, the subject was under lab-light (1200 lx) conditions; and from 6 PM to 9 PM, the subject was in room-light (600 lx) conditions. From 9 AM to 6 PM, the wearable device performed multiplexed glucose, pH, Na^+, and temperature measurements occurring at 8 s intervals, and sweat rate measurements occurring at 5 min intervals. The data was wirelessly transmitted *via* BLE indications. From 6 PM to 9 PM, the wearable device performed multiplexed glucose, pH, sodium, and temperature measurements occurring at 60 s intervals and transmitted the data wirelessly *via* BLE advertisements, while sweat rate was evaluated optically every 10 min.

6.5 Supporting Information

Supplementary Note 1. Design and considerations of monochromatic light source PCE measurement approach for indoor and low light PV.

Solar cells behave considerably different under high and low light illumination conditions, with the major change emerging form R_p, R_s, and charge carrier concentration[192,198]. Solar cells under low light illuminations perform better with increasing R_p (higher R_p correlates with increased FF and V_{oc}). On the other hand, R_s, which greatly influences the device performance under AM1.5G conditions (higher R_s leads to decrease in FF and J_{sc}), tends to have little effect on low light device performance. Additionally, fewer incoming photons under low light illumination as well as good spectral matching of the indoor light source to the spectral response characteristics of perovskite solar cells result in less recombination and thus contribute to increase in performance.

Since incoming light is determined by the environmental conditions and J_{sc} scales linearly with the light intensity, the behavior of V_{oc} and FF become the deciding factor that determine solar cell low light performance. V_{oc} decreases as a function of decreasing light intensity, with the rate of decrease becoming stronger after a certain critical illuminance. On the other hand, FF increases as the light intensity decreases and then starts to decrease also after certain critical illuminance is reached. Thus keeping both V_{oc} and FF high (through trap passivation

and judicious perovskite composition engineering) as light intensity decreases is the key to achieving high efficiency under low light illumination[186].

Shockley-Queisser PCE limit of a solar cell with an optimal bandgap (1.82–1.96 eV) under indoor illuminance levels (100-1000 lx) using a common LED light source has been calculated to be between 51 and 57 %, which is considerably higher than that of the corresponding 33 % at 1 Sun AM1.5G irradiation.[199] Nevertheless, a consensus on standardized PCE measurement conditions, like the well-established outdoor PV method, is yet to emerge[200]. As a result, several different light sources, illuminance levels, measurement set-ups, and protocols have been reported in literature which can have a noticeable effect on PCE even when measured on the same device under the same illuminance[201].

Therefore, in this study we use monochromatic (laser) measurement, as a complementary technique that offers a unique way to assess PCE value of our quasi-2D FPSC, independent of the light source. It presents a so-called "best-case scenario" performance of a given device, with reduced influence of sub-bandgap and relaxation losses. For this purpose, a laser wavelength (λ = 637 nm) was chosen to be sufficiently close to the spectral response cut-off and have sufficiently high EQE in that region of measurement. Additionally, measuring the cell performance over a range of irradiances reveals the incident power range, where the device is best at converting light into electricity, while also bringing forward insights about device physics based on the trends of cell parameters (V_{oc}, J_{sc}, FF) as the function of light intensity. Nevertheless, the calculated values need to be used with caution and consideration, when trying to extrapolate them to real world situations, where either one or multiple light sources with various spectral shapes and intensities illuminate the device.

Supplementary Note 2. Optimization and characterization of electronic system power consumption

The wearable device can perform various operations including but not limited to current-monitored iontophoresis, potentiometry, amperometry, voltammetry, impedance analysis, multiplexed measurements (up to four voltage/current measurement channels), and on-body measurement sequences (multiplexed measurements with periodic impedance measurements). In a typical workflow, the programmable system-on-chip (PSoC) Bluetooth low energy (BLE) module acts as a data bridge between the electrochemical analog front-end (AFE) and a host software (mobile phone or PC), wherein it encodes and writes measurement instructions to the electrochemical AFE, then decodes and transmits the AFE's measurement data to a host software via BLE (**Supplementary Fig. 6-S13c**). The electrochemical AFE, on the other hand, sequentially performs tasks as instructed by the PSoC BLE module and saves all measurement data in its internal memory, while periodically interrupting the PSoC BLE module to fetch the saved measurement data. Firmware can be optimized to balance tradeoffs between measurement intervals and overall power consumption.

The power output of the solar cell can vary as the lighting conditions change, and while it is possible to maximize the electrochemical measurement, data processing, and wireless communication intervals (~ 30 s, ~ 300 s, and ~ 300 s respectively) such that the wearable device can always operate at its lowest possible power consumption mode, a higher sampling and data transmission rate improves data continuity and user experience. Therefore, the wearable device dynamically adapts the operation parameters such that it can sample, process, and transmit data as frequently as the solar cell power output permits.

To accurately configure the operation parameters, it is necessary to be able to calculate the power consumption of the system based on the operation parameters. Each operation consists of the combination of several passive tasks (hibernate, sleep, and iontophoresis) and active tasks (measurement, process, and BLE). During hibernation, most blocks of the electronic system are inactive; during sleep, most blocks of the electronic system are inactive except

the low power potentiostat loop; and during iontophoresis, most blocks of the electronic system are inactive except the iontophoresis block and the low power potentiostat loop. During a measurement task, the electrochemical AFE performs an ADC measurement; during a processing task, the AFE performs an ADC measurement and then the PSoC BLE module fetches varying amounts of ADC measurement data stored in the AFE's internal memory and processes them; during a BLE task, varying amounts of processed data can be transmitted as BLE indications (BLE connection) or as BLE advertisements (no BLE connection). Each of these tasks consumes different amounts of power. In addition, due to the dynamic conversion efficiency of the voltage regulator and boost converter, the power consumption of the system varies depending on the voltage level supplied by the energy storage capacitor. The power/energy consumption of each task when powered at varying supply voltages is shown in **Supplementary Fig. 6-15**.

For each operation, we varied the operation parameters and measured the average power consumption when supplied at 3 V. **Supplementary Fig. 6-16** displays the power consumption profiles for various operations performed at varying operation parameters measured over a 20 s timespan. Most power consumption profiles were collected at a sampling rate of 10 kHz, but the power consumption profile for iontophoresis was collected at a sampling rate of 1 kHz because the transient spikes in power consumption caused by the boost converter for iontophoresis would obscure the plot visually at high sampling rates. However, sampling rates from 1 kHz to 100 kHz all yielded accurate values for average power consumption. Furthermore, **Supplementary Fig. 6-22** shows expanded (10 min) power consumption profiles of on-body measurement sequences that were used for in vitro validation flow tests and on-body experiments shown in **Fig. 6-3f**. **Supplementary Table 6-4** shows the average power consumption of all operations performed at varying operation parameters. Operation parameters chosen for use during experiments are highlighted in yellow and green.

Supplementary Note 3. Design considerations and optimization of microfluidic sweat processing system

The design goal for the microfluidic sweat processing system was to develop a system that can induce and extract the sweat for prolonged durations above a minimal threshold flow rate while consuming minimal amounts of power. Trade-offs between power consumption for iontophoresis and the size of the carbagels, geometric location and orientation of the gels with respect to the sweat accumulation reservoir, and distance between the gels and sweat accumulation reservoir were considered. The power consumption of the iontophoresis circuit is positively correlated to the total current applied and the compliance voltage of the constant current source. As iontophoretic current density is positively correlated with regional sweat rate, power consumption could be minimized by minimizing the area of the carbagel. On the other hand, while carbachol can stimulate neighboring sweat glands, if the carbagel is too small, the sweat gland density around the gel can be low, generating low sweat volume. The next factor considered was the orientation of the gels with respect to the sweat accumulation reservoir. We found that locating the sweat accumulation reservoir between the anode and cathode can maximize extraction efficiency as the majority of the drug is delivered across the anode and cathode. Another factor considered was the distance between the gels. If the anode and cathode are too close, the drug delivery area may be too small and it is possible that not enough sweat glands are activated. However, increasing the inter-gel distance above a certain extent does not increase sweat gland activation and only increases the impedance between the two carbagels, which necessitates a higher compliance voltage and power consumption for the iontophoresis circuit. Regarding the distance between the carbagels and the sweat accumulation reservoir, sweat extraction improved when the sweat accumulation reservoir was closer to the anodic carbagel (where the drug is loaded). However, if the distance between the gel and accumulation reservoir was closer than 1 mm, the adhesive would have difficulty maintaining the sweat within the sweat accumulation reservoir and sweat would leak at times. With all these considerations in mind, our final carbagel area was 15 mm^2 per electrode, distance between the carbagels was 4 mm, and the distance between the carbagel and the sweat accumulation reservoir was 1.2 mm. A current of 55 μA was delivered for iontophoretic stimulation as lower currents did not result in sufficient sweat

output, and higher currents lead to an increased power consumption and did not necessarily result in a longer stimulation duration.

The final microfluidic sweat processing system consists of three main layers, the sweat accumulation layer, the channel layer, and the reservoir layer (**Supplementary Fig. 6-1**). All layers of the microfluidic system contain two large cutouts for holding the carbagels. In addition to these cutouts, the accumulation layer (0.13 mm) contains a well (same dimensions as the sensor reservoir) for sweat accumulation; the channel layer (0.64 mm) contains a sweat rate channel (36 μL or 95 μL capacity) for processing high volumes of sweat and a counter electrode-shaped inlet to transport the accumulated sweat into the sensor reservoir; and the reservoir layer (0.13 mm) contains a compact sensor reservoir (1.1 μL capacity) to enable rapid refreshing of sweat and a microfluidic channel to flush out the sweat through the sweat rate channel.

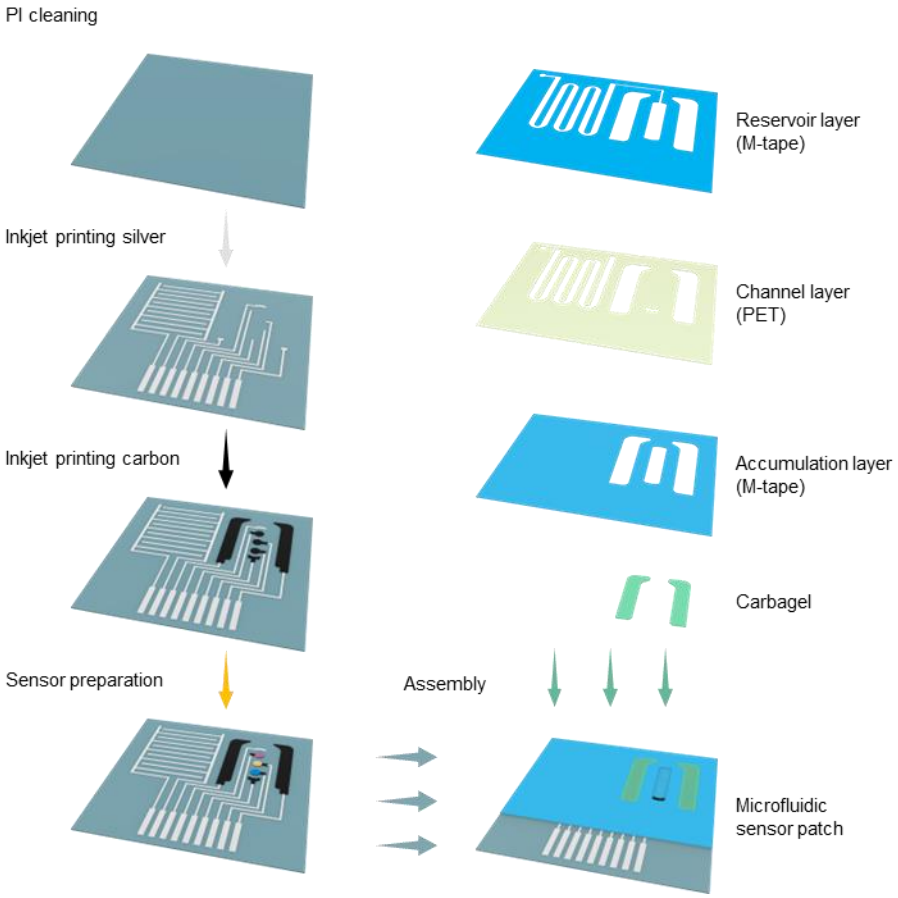

Supplementary Figure 6-1. Schematic depicting the fabrication process of the microfluidic sensor patch. For the preparation of sensors, the PI substrate was cleaned *via* O_2 plasma surface treatment, followed by the sequential inkjet printing of silver and carbon electrodes, which were further modified for electrochemical detection. The microfluidic layers consisting of medical tapes and PET films were patterned using a CO_2 laser cutter, then assembled onto the sensor patch along with the carbagels.

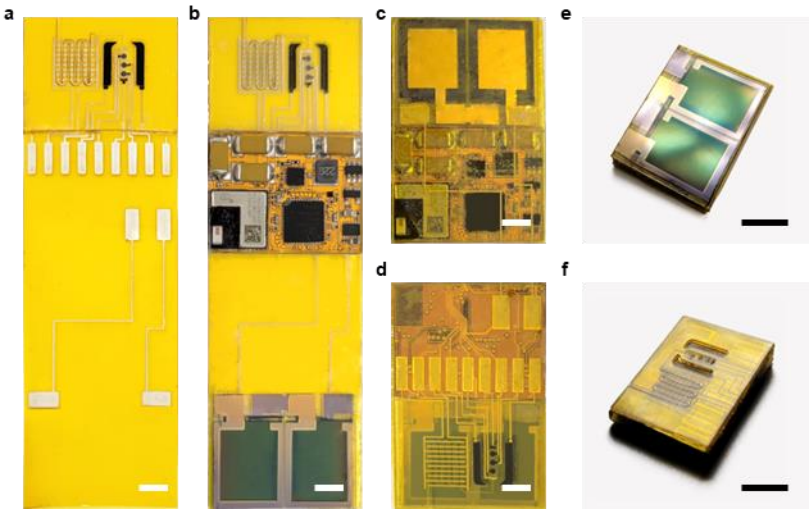

Supplementary Figure 6-2. Photos showing the assembly process of the wearable device. a–**d**, The FPSC, electronics, and microfluidic sensor patch are assembled in an origami style. Scale bars, 5 mm. e,f, The top view of the fully assembled wearable device with the solar cell facing up (**e**), and the bottom view of the fully assembled wearable device with the microfluidic sensor patch facing up (**f**). Scale bars, 1 cm.

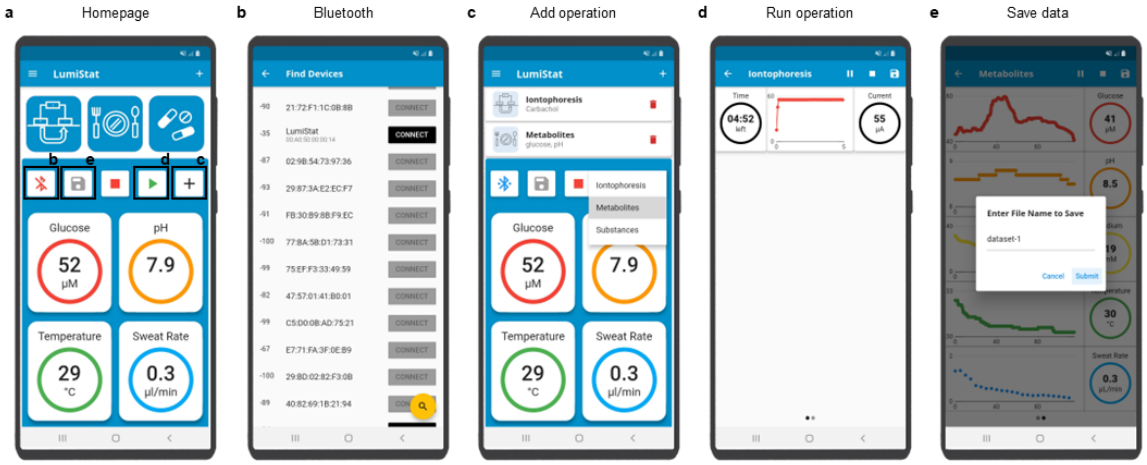

Supplementary Figure 6-3. Operation manual for the solar cell-powered wearable sweat analysis mobile application. a, Homepage of the Wearable Sweat Sensor App displaying the most recent sensor readings on a scrollable grid view. **b–e**, Above the sensor readings, there is a list of command buttons such that the app can connect to the wearable device over BLE (**b**), serially add operation sequences (e.g., iontophoretic sweat stimulation and multimodal metabolite monitoring) (**c**), serially run all the added operations and display the real time data (**d**), save acquired data to the phone (**e**), and stop all operations.

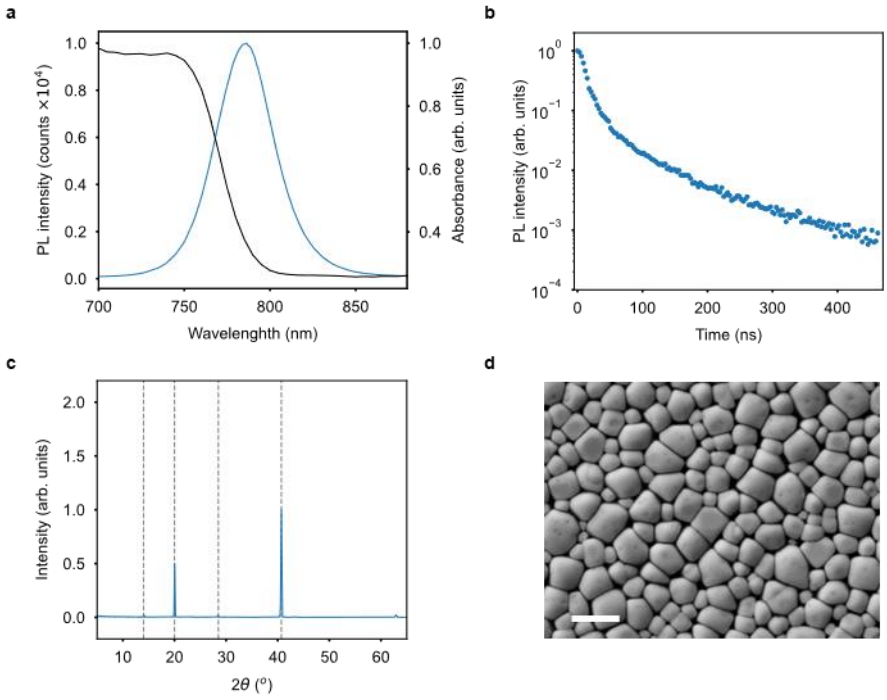

Supplementary Figure 6-4. Quasi-2D perovskite $(MBA)_2(Cs_{0.12}MA_{0.88})_6Pb_7(I_xCl_{1-x})_{22}$ material characterization. a, Photoluminescence spectrum with the peak at 786 nm and corresponding UV/Vis absorption spectrum. **b**, Transient photoluminescence measurement with triexponential fit ($i = A_1 \exp(-t/\tau_1) + A_2 \exp(-t/\tau_2) + A_3 \exp(-t/\tau_3)$) used to calculate fast (τ_1 = 13 ns), intermediate (τ_2 = 118 ns), and slow (τ_3 = 153 ns) time decay constants. **c**, XRD diffraction pattern showing sharp and narrow peaks at 14°, 20°, 28.5°, and 40.7° corresponding to (100), (112), (220), and (224) planes of tetragonal perovskite structure[202]. **d**, SEM of the perovskite film with individual grains reaching the size of above 1 μm. Scale bar 1, μm. Experiments were repeated five times independently with similar results.

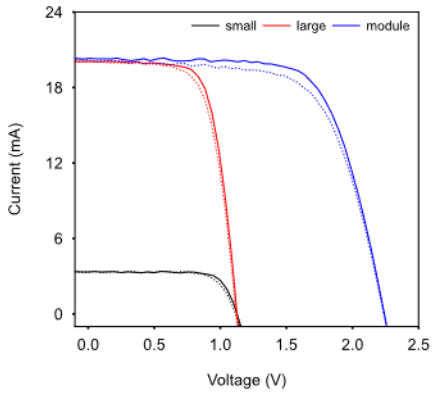

Supplementary Figure 6-5. Performance of quasi-2D FPSC under simulated sunlight illumination (AM1.5G). Example IV curves of small area (black), large area (red), as well as the module (blue) solar cells, measured in forward (dashed) and reverse (solid) scan directions.

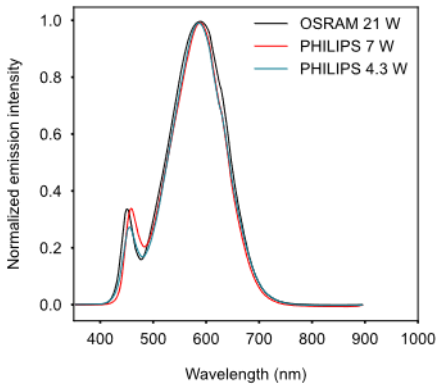

Supplementary Figure 6-6. The emission spectra of light bulbs used in indoor lighting solar cell performance testing. Room-light LED (2700 K) light bulbs of various brightness used to evaluate the performance of the quasi-2D FPSC over a broad range of illuminance. Osram 21 W (black), Philips 7 W (red), and Philips 4.3 W (red).

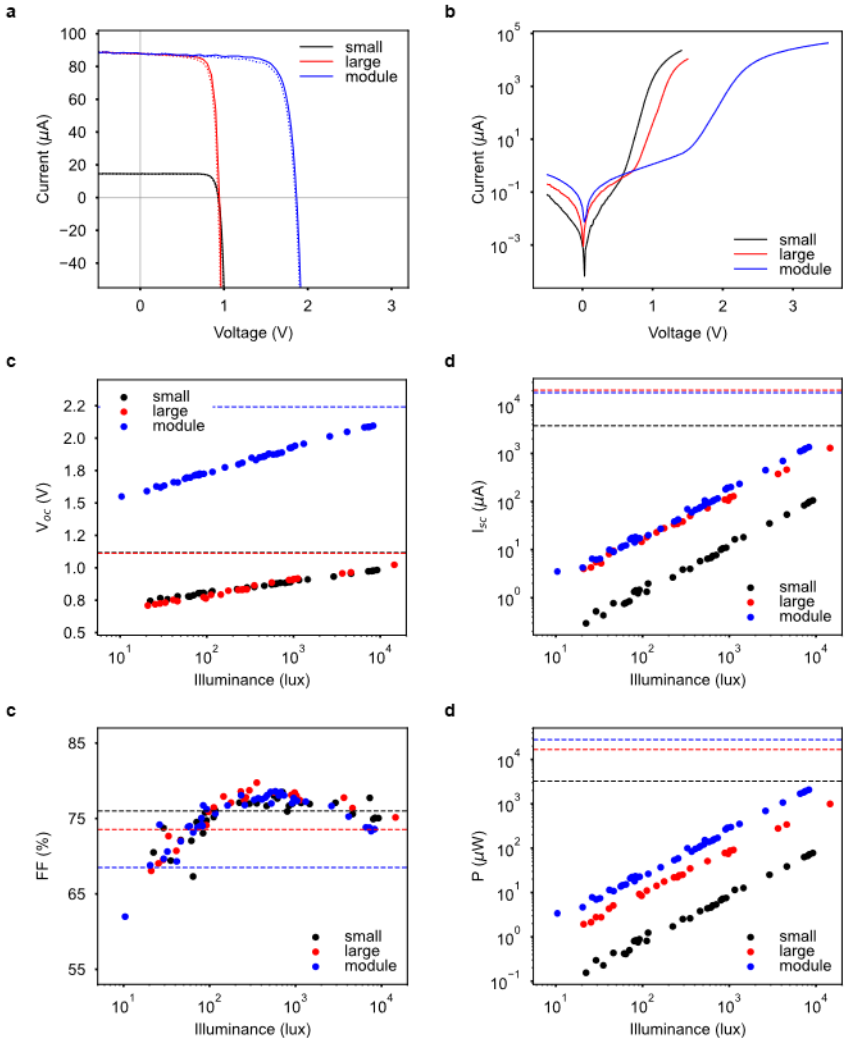

Supplementary Figure 6-7. Performance of quasi 2D FPSC under indoor lighting. Measurements were performed on devices with small (0.165 cm^2, black), and large (1 cm^2, red) areas as well as modules [2 individual 1 cm^2 cells connected in series] (2 cm^2, blue). **a**, IV curves recorded under indoor 600 lux illumination using a 2700K household LED light bulb. **b**, Dark IV curves of the corresponding devices. **c**, Open circuit voltage as a function of light intensity. Solid lines show the linear fit used for estimation of ideality factor (n) in two regions below (*low*) and above (*high*) 200 lx. For small area devices n_{high} = 1.50 and n_{low} = 1.53, which suggests an overall superposition of bimolecular and monomolecular (trap-assisted recombination) nonradiative recombination processes in these two regions. Large-area devices have n_{high} = 1.61 and n_{low} = 1.88, both larger than in

their small area counterparts, suggesting higher probability of defects occurring in these devices. Additionally, $n_{low} > n_{low}$ suggests that trap-assisted recombination will be the limiting the performance in this low light intensity region (<200 lx). Corresponding V_{oc} values measured at AM1.5G are highlighted with a dashed line (V_{oc} (small) = 1.106 V, V_{oc} (large) = 1.109 V, V_{oc} (module) = 2.241 V). **d**, Short circuit current as a function of light intensity, with all three example showing a linear relationship with illuminance. Corresponding I_{sc} values measured at AM1.5G are highlighted with a dashed line (I_{sc} (small) = 3.58 mA, I_{sc} (large) = 20.54 mA, I_{sc} (module) = 18.26 mA). **e**, The plot of fill factor as a function of light intensity. In all three cases the cells show increase in value when compared to AM1.5 conditions. The initial decrease of FF down to 200 lx suggests predominantly bimolecular recombination mechanism, and the following decrease below 200 lx indicates primarily trap-assisted recombination in that illuminance region. Corresponding FF values calculated at AM1.5G are highlighted with a dashed line (FF (small) = 75.02 %, FF (large) = 72.54 %, FF (module) = 68.50 %). **f**, Power density as a function of illuminance. Corresponding values calculated at AM1.5G are highlighted with a dashed line (P (small) = 2.8×10^3 μW, P (large) = 1.7×10^4 μW, P (module) = 2.8×10^4 μW).

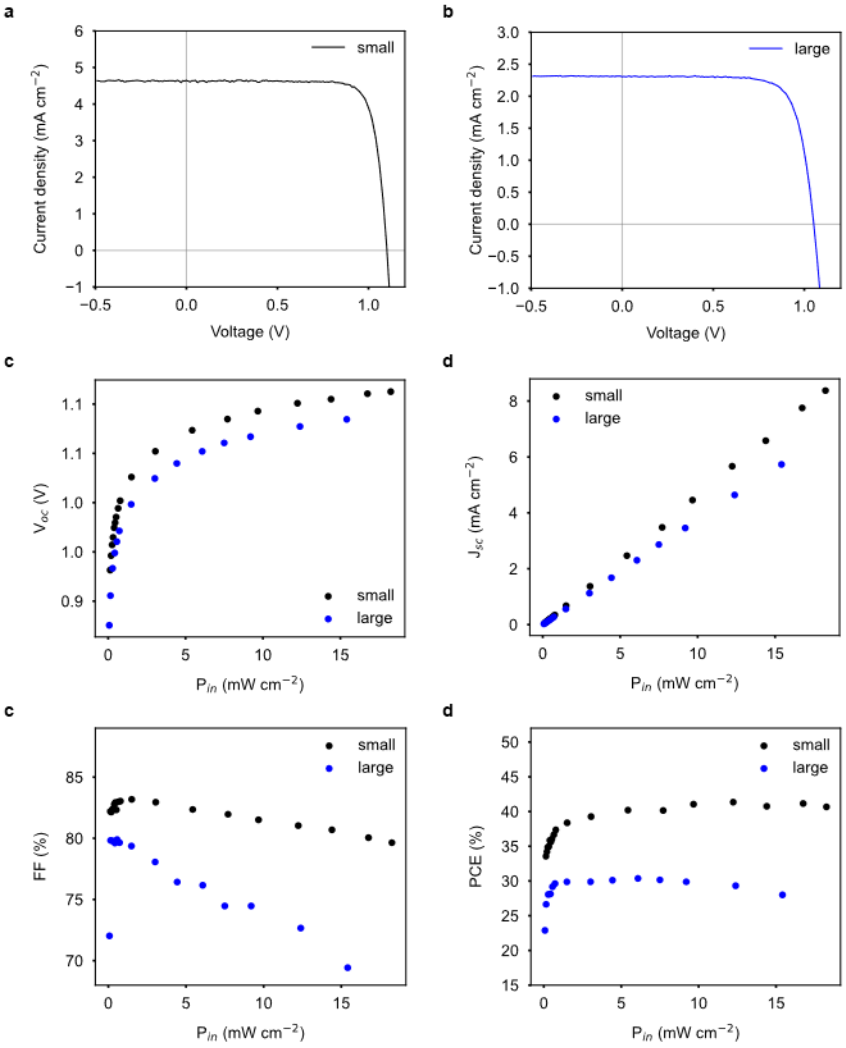

Supplementary Figure 6-8. Monochromatic (laser) PCE measurement of FPSC in the low light region. a,**b**, Examples of highest efficiency IV curves measured for small (PCE = 41.3 % at 12.23 mW cm^{-2}, black) (**a**) and large area (PCE = 30.4 % at 5.43 mW cm^{-2}, blue) (**b**) solar cells. **c**, Open circuit voltage as a function of incident power (irradiance). **d**, Short circuit current density of both small and large devices scales up linearly with increasing irradiance. **e**, FF of both types of active area devices increases at different rates up until 1-2 mW cm^{-2}. The sharp decrease in FF at values below 1-2 mW cm^{-2} could be evidence of increasing role of trap-assisted recombination under very low illumination conditions. **f**, PCE as a function of incident power shows a broad region of high performance at low light conditions for both small and large area FPSC.

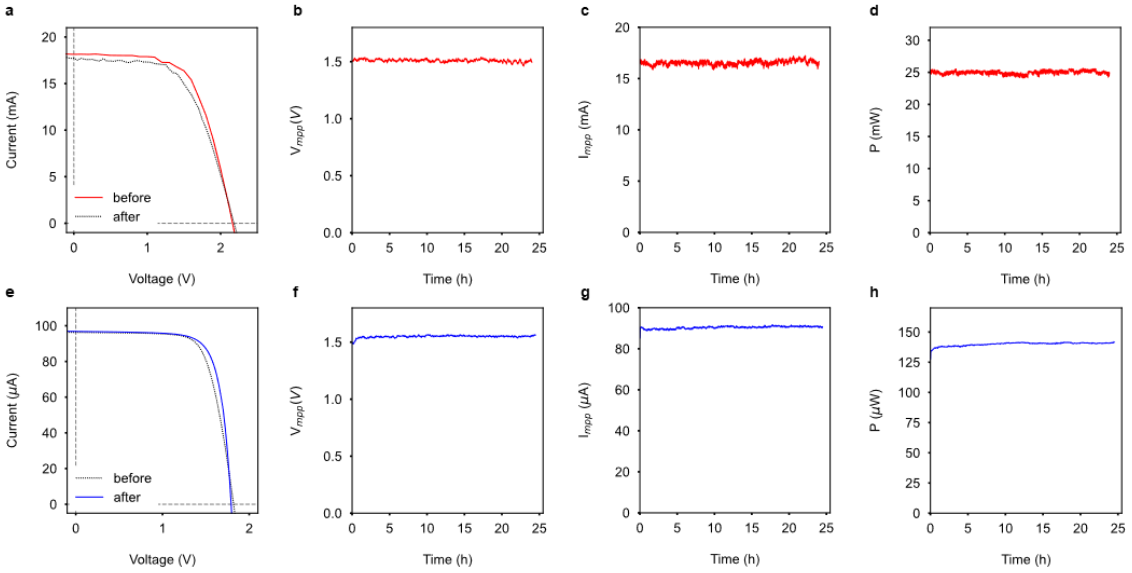

Supplementary Figure 6-9. Operational stability of quasi-2D FPSC module. a, IV curves before (black) and after (red) maximum power point (MPP) tracking for 24 hour under simulated sunlight (AM1.5). **b-d**, Corresponding maximum power point voltage (V_{mpp}) (**b**), maximum power point current (I_{mpp}) (**c**), and power output (P) (**d**) during the tracking. **e-g**, IV curves V_{mpp} (**e**), I_{mpp} (**f**), and P (**g**) of the same module operating under indoor 600 lx LED room-light illumination conditions for 24 hours.

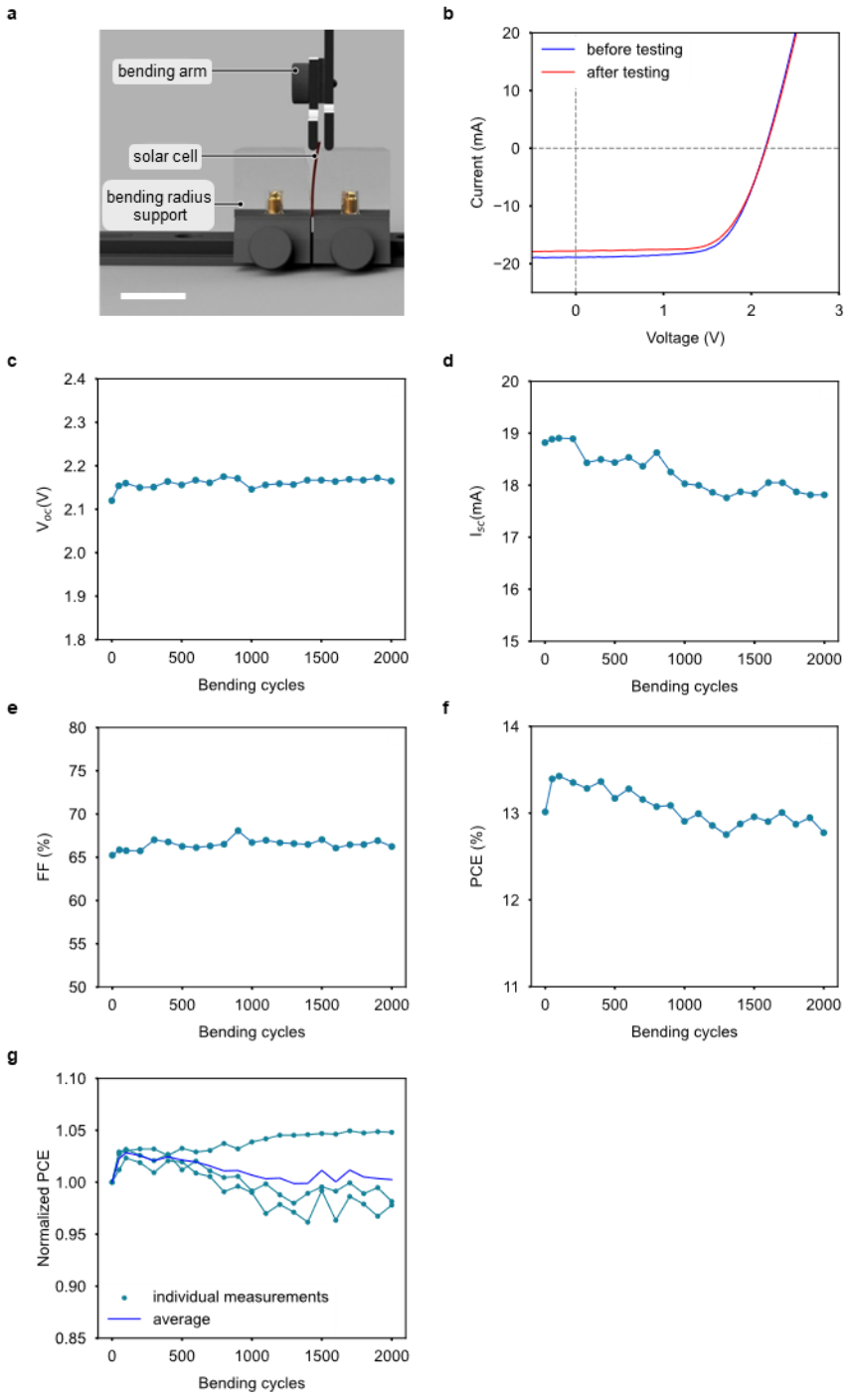

Supplementary Figure 6-10. Mechanical stability of large FPSC cells. a, Diagram of the setup used to perform mechanical stability test. Scale bar, 1 cm. **b**, JV curves of the large solar cell before and after mechanical testing. **c–f**, Open-circuit voltage (V_{oc}) (**c**), short circuit current density (J_{sc}) (**d**), fill factor (FF) (**e**), and PCE as extracted from

measured JV curves (AM1.5) (**f**) during the mechanical test. **g**, Comparison of normalized PCE of several FPSC module bending tests (5 cm bending radius), as well as their average.

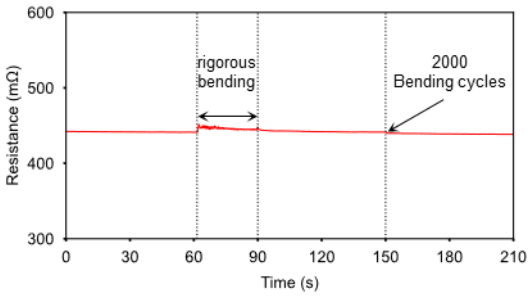

Supplementary Figure 6-11. Mechanical stability of z-axis conductive tape-based interconnects. Silver interconnects inkjet-printed on a PI substrate were electrically connected to the contact pads of the FPCB v*ia* a z-axis conductive tape. The resistance across the connection was measured before, during, and after rigorous bending, as well as after 2000 controlled bending cycles (bending radius 5 cm).

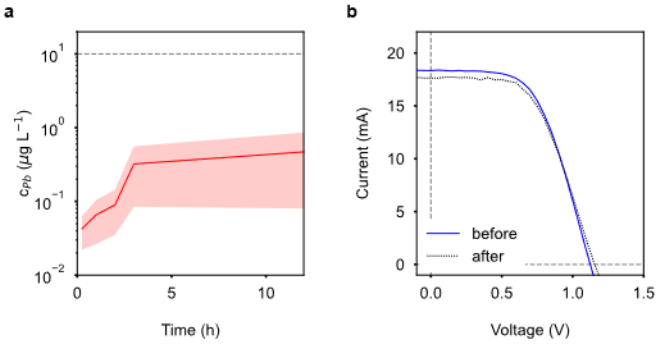

Supplementary Figure 6-12. Results of FPSC Pb-release tests conducted in deionized water under full sun illumination for intact FPSCs. a, Lead release over a period of 12 hours from a FPSC immersed in DI water under constant AM1.5 illumination. Error band corresponds to confidence interval (n = 9 independent measurements). The gray dashed line highlights the maximum allowable lead concentration in drinking water as per the Joint FAO/WHO Expert Committee on Food Additives (JECFA). **b**, Corresponding IV curves before and after the DI water Pb-release test, showing no significant change in device performance.

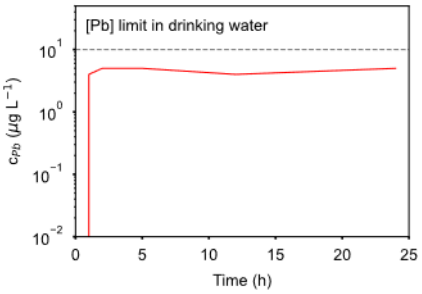

Supplementary Figure 6-13. Results of lead leakage tests performed in artificial human sweat solution under full sun illumination for bent FSPCs. The bending test was performed for total 2000 bending cycles under 5 cm bending radius. The gray dashed line highlights the maximum allowable lead concentration in drinking water as per the Joint FAO/WHO Expert Committee on Food Additives (JECFA).

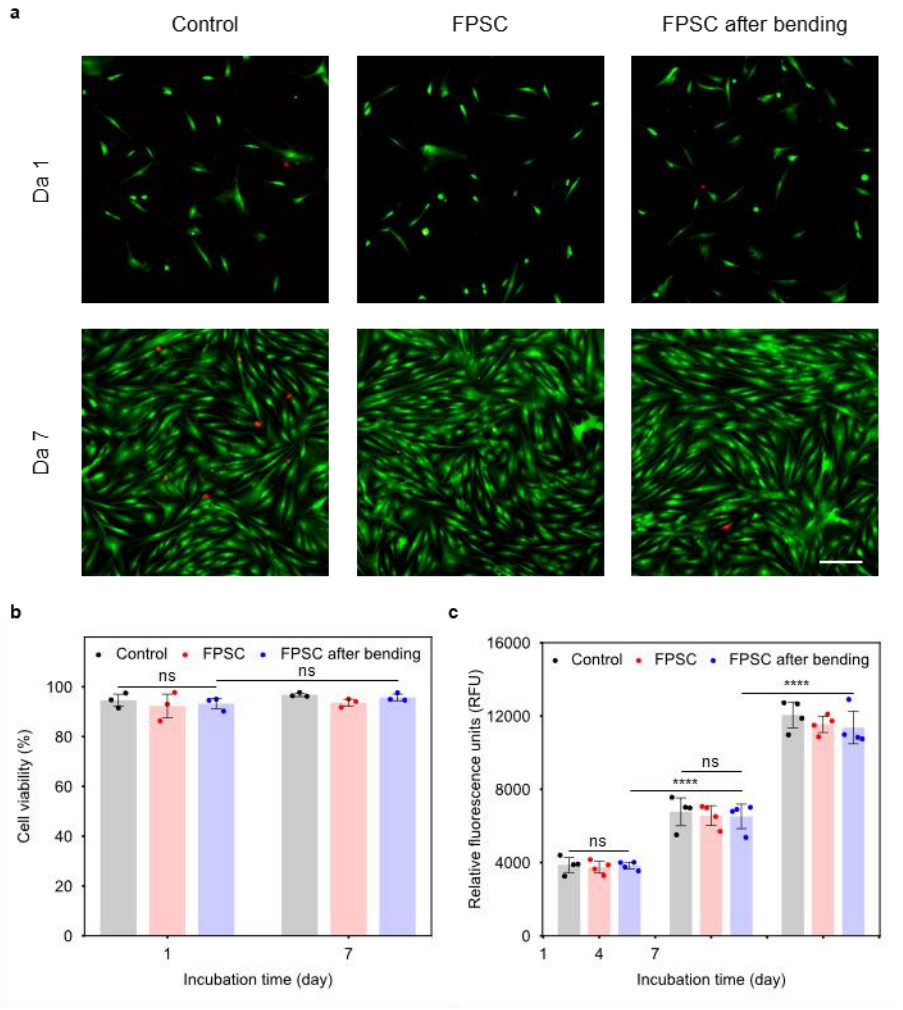

Supplementary Figure 6-14. Biocompatibility assay on the packaged FPSC. a,**b**, Fluorescent images (**a**) and bar plot (**b**) of cell viability of human dermal fibroblast (HDF) cells in the presence of FPSC before and after 2000 bending cycles (5 cm bending radius). Scale bar, 200 μm. Data are presented as mean ± SD (n = 3 biologically independent samples). c, Bar plot of metabolic activity of human dermal fibroblast (HDF) cells in the presence of FPSC before and after 2000 bending cycles (5 cm bending radius). Data are analyzed using a two-way ANOVA test (Tukey's multiple comparisons) and are presented as mean ± SD (****$p < 0.0001$, n = 4 biologically independent samples).

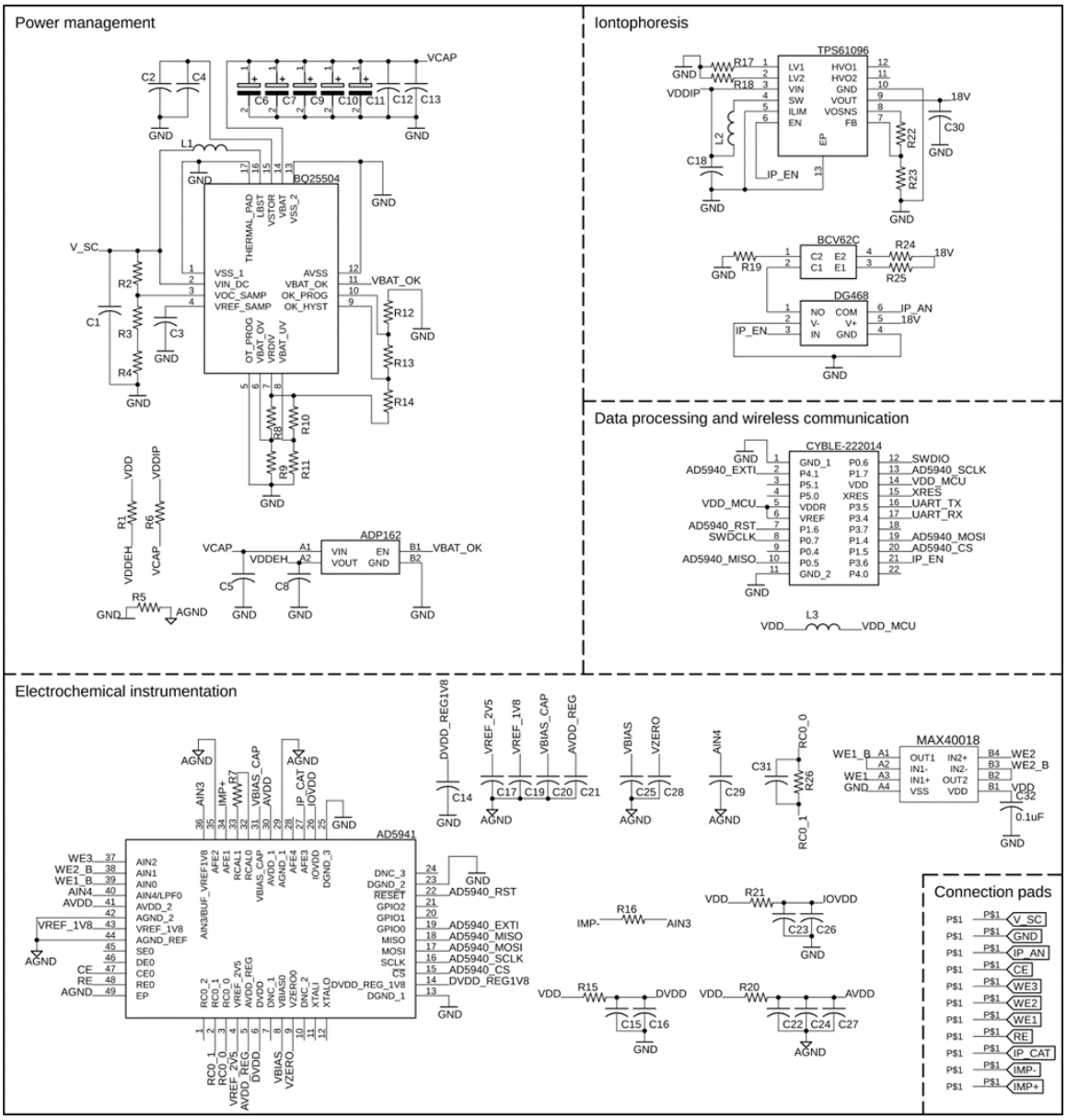

Supplementary Figure 6-15. Circuit schematic of the wearable electronic system. Schematic is divided into 4 main blocks for: power management, iontophoresis, data processing and wireless communication, and electrochemical instrumentation.

Discrete Components	Value	Package
R1, R5, R6, R16, R21	0 Ω	R0201
R2	3.4 MΩ	R0402
R3	10 MΩ	R0201
R4	6.65 MΩ	R0402
R7	470 Ω	R0201
R8, R11	6.2 MΩ	R0201
R9, R10, R13	3.6 MΩ	R0201
R12	2.49 MΩ	R0201
R14	3.9 MΩ	R0201
R15, R20	2.2 Ω	R0201
R17, R18	1 MΩ	R0201
R19, R24, R25	300 kΩ	R0201
R22	169 kΩ	R0201
R23	10 kΩ	R0201
R26	1.5 MΩ	R0201
C1, C2	4.7 μF	C0201
C3, C4	0.1 μF	C0201
C5, C8	1 μF	C0201
C6, C7, C9, C10, C11	1 mF	C2812
C12, C18, C19	4.7 μF	C0201
C13, C16, C24, C25, C26, C27, C29, C31, C32	0.1 μF	C0201
C14, C17, C20, C21	0.47 μF	C0201
C15, C22, C23	10 μF	C0402
C28	1 μF	C0201
C30	10 μF	C0603

Supplementary Figure 6-16. List of discrete components used in the wearable electronic system.

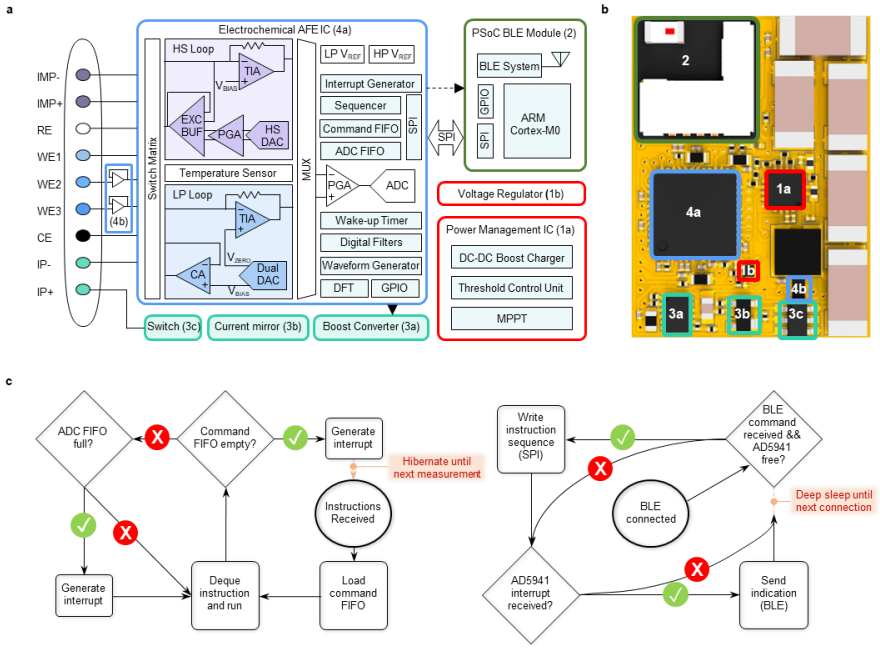

Supplementary Figure 6-17. Electronic system design. a, A detailed block diagram of the wearable device numerically labeled according to functional blocks: (1) power management, (2) data processing and wireless communication, (3) iontophoresis, and (4) electrochemical instrumentation. TIA, transimpedance amplifier; EXC BUF, excitation buffer; PGA, programmable gain amplifier; DAC, digital to analog converter; CA, control amplifier; HP, high power; FIFO, first in first out; DFT, discrete Fourier transform; GPIO, general purpose input output; DC, direct current; MPPT, maximum power point tracking. **b**, Top view of the FPCB with major components numerically labeled according to their function. **c**, Flow diagram of the low power embedded system algorithm composed of the electrochemical AFE (left) and PSoC BLE module (right).

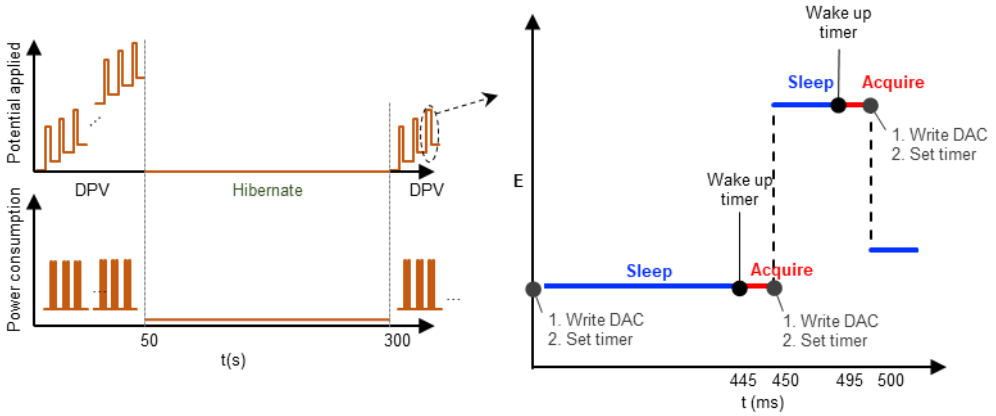

Supplementary Figure 6-18. Illustration showing how the electrochemical AFE operates during a DPV measurement. During DPV, the AFE applies a dynamic pulsed staircase waveform across the electrochemical cell and briefly samples the current periodically. In each step of the staircase waveform, the AFE sets the DAC to apply a baseline potential, sets the timer such that the AFE can sleep for a specified duration (pulse period – pulse width – acquire period), then acquires current data once woken up. Next, the AFE sets the DAC to apply a pulsed potential (baseline potential + pulsed amplitude), sets the timer such that the AFE can sleep for a specified duration (pulse width – acquire period), then acquires current data once woken up. After this cycle, the AFE sets the DAC to apply the new baseline potential (baseline potential + step potential) and repeats the cycle until the end of the measurement.

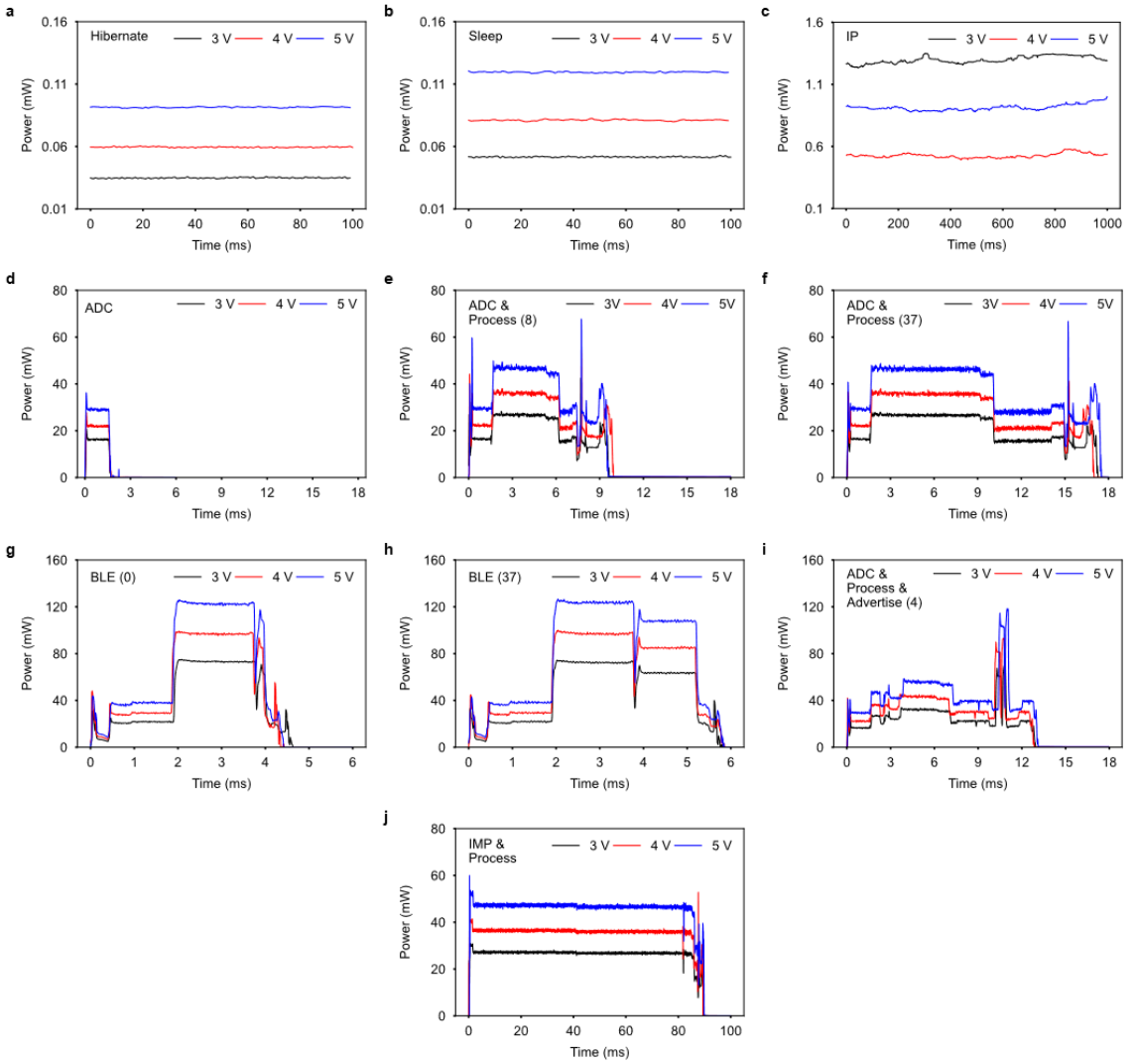

Supplementary Figure 6-19. Instantaneous power consumption of the electronic system while performing various tasks while powered under varying supply voltages. **a–j**, The performed tasks include: hibernation (**a**), sleep (**b**), iontophoresis (**c**), an ADC measurement (**d**), an ADC measurement followed by the processing of 8 and 37 measurement data sets (**e**,**f**), a BLE connection event with no measurement data and 37 measurement data to transmit (**g**,**h**), an ADC measurement followed by the processing and transmission (BLE advertisement) of 4 measurement data (**i**), and the acquisition and processing of an impedance measurement (**j**).

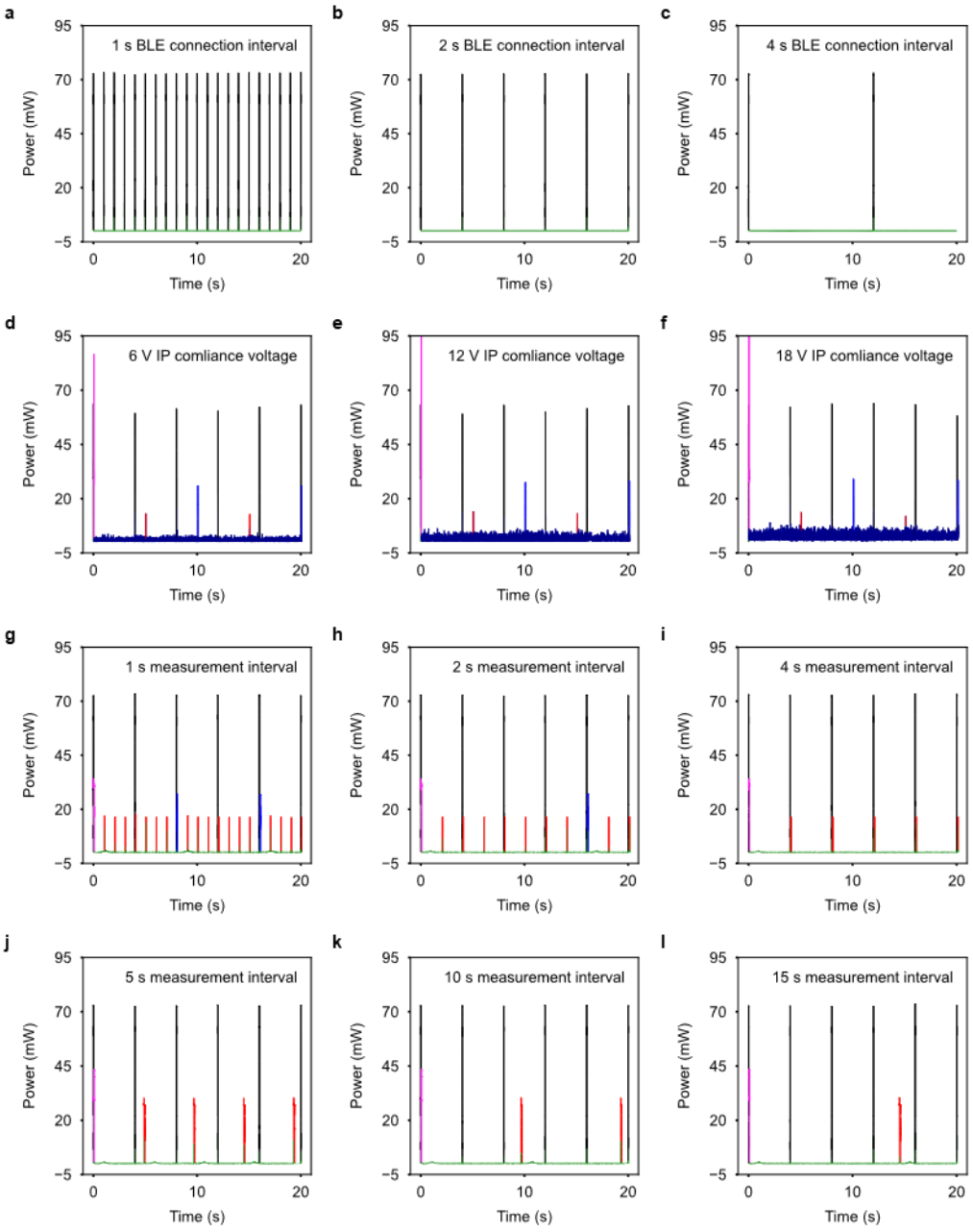

Supplementary Figure 6-20. Power consumption of electronic system supplied at 3 V when performing various operations under varying operation parameters. a–l, Operations include: standby with a 1 s (**a**), 4 s (**b**), and 12 s (**c**) BLE connection interval; current monitored iontophoresis with a compliance voltage of 6 V (**d**), 12 V (**e**), and 18 V (**f**); multiplexed measurements (1 amperometric, 2 potentiometric, 1 temperature) with a

ADC interval of 1 s (**g**), 2 s (**h**), and 4 s (**i**); and impedance measurements with a measurement interval of 5 s (**j**), 10 s (**k**), and 15 s (**l**).

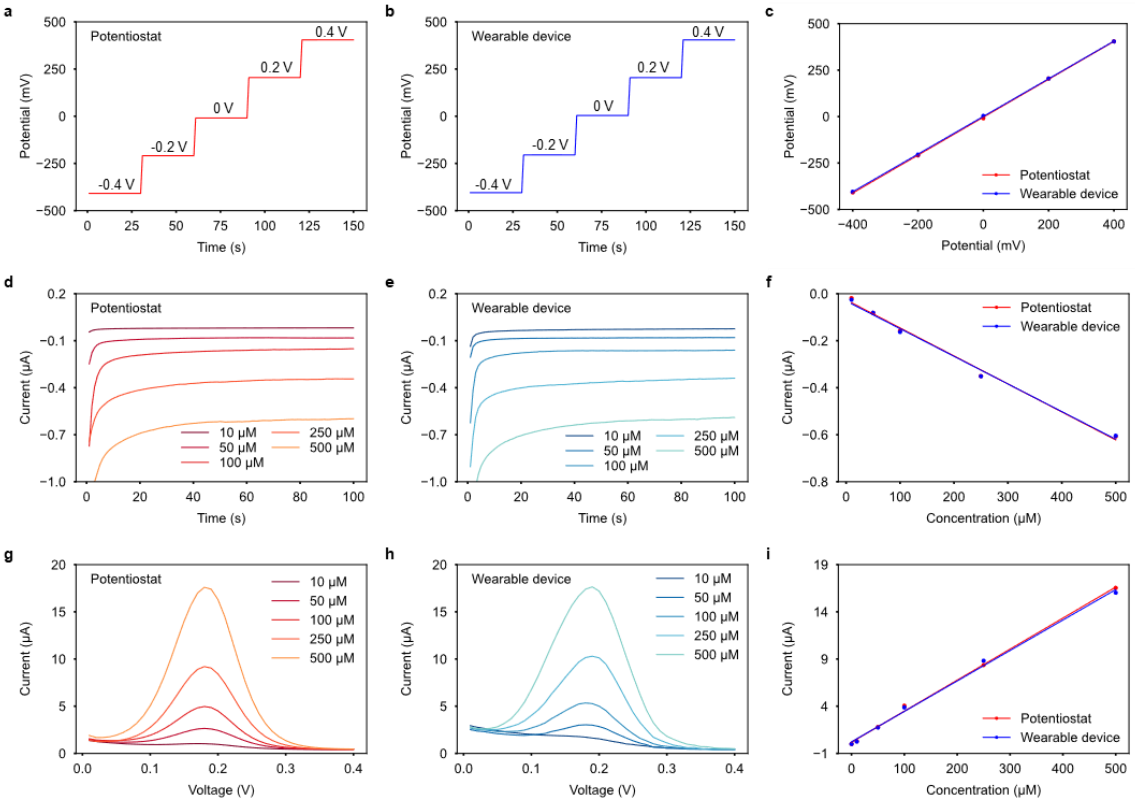

Supplementary Figure 6-21. Validation of the wearable device for electrochemical measurements. a–c, OCP response (1 s sampling interval) to power supply produced voltage signals recorded by a benchtop potentiostat (**a**), and by the wearable device (**b**), and their overlayed calibration curves (**c**). d-f, Chronoamperometric response (1 s sampling interval) to a hydrogen peroxide solution (10–500 μM H_2O_2 in 1x PBS) on a Prussian blue modified carbon electrode recorded by a benchtop potentiostat (**d**), and by the wearable device (**e**), and their overlayed calibration curves (**f**). g-i, DPV response (500 ms pulse period, 50 ms pulse width, 10 mV step potential, 50 mV pulse amplitude) to ferricyanide solutions (10–500 μM $K_3Fe(CN)_6$ in 0.2 M KCl) on an LEG recorded by a benchtop potentiostat (**g**), and by the wearable device (**h**), and their overlayed calibration curves of the oxidation peak current heights (**i**).

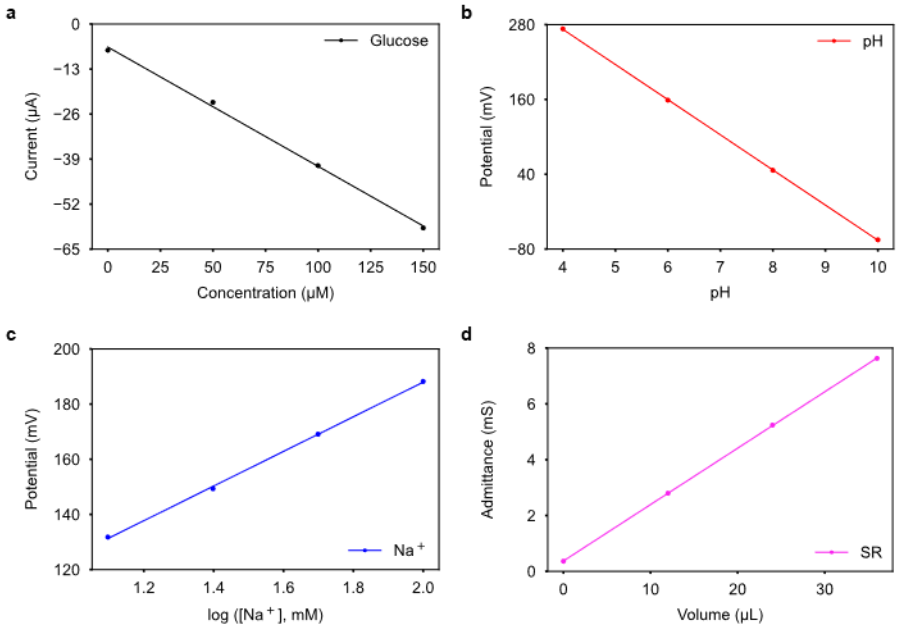

Supplementary Figure 6-22. Calibration plots of biosensors in physiological biomarker levels. a-d, Characterized sensors include: the glucose sensor (**a**), pH sensor (**b**), Na^+ sensor (**c**), and sweat rate (SR) sensor (**d**).

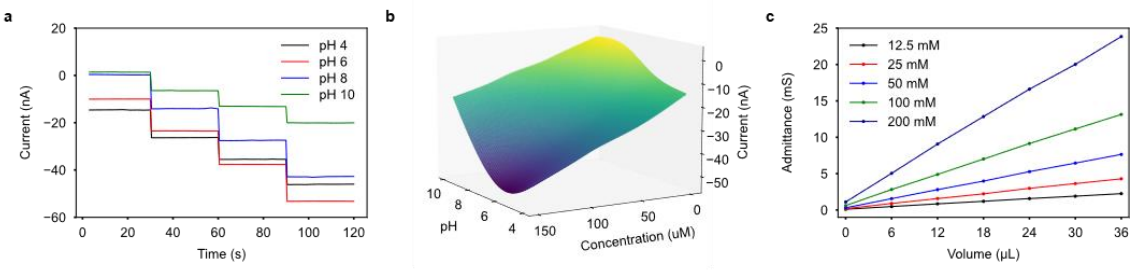

Supplementary Figure 6-23. Dependence of the glucose sensor on pH, and the sweat rate sensor on Na^+. a,**b**, Current response of the glucose sensor in 0–150 µM glucose with varying pH levels (**a**), and the corresponding 3D calibration plot (**b**). **c**, Admittance response of the sweat rate sensor while NaCl solutions fill up the sweat rate sensor reservoir.

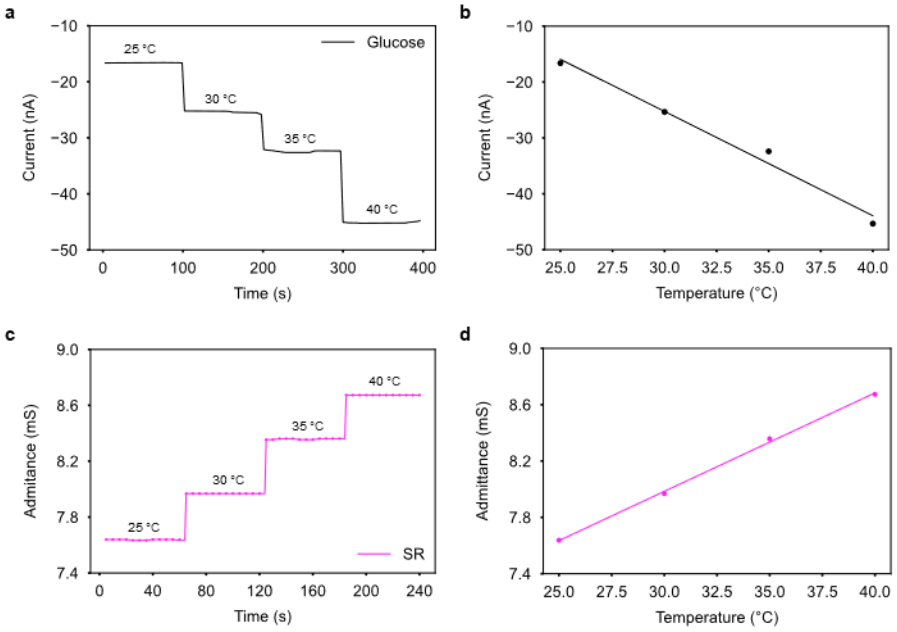

Supplementary Figure 6-24. Dependence of sensors on temperature. a,**b**, Glucose sensor response (50 μM glucose) under varying temperatures (**a**) and the corresponding calibration plot (**b**). **c**,**d**, Sweat rate sensor response under varying temperatures (**c**) and the corresponding calibration plot (**d**).

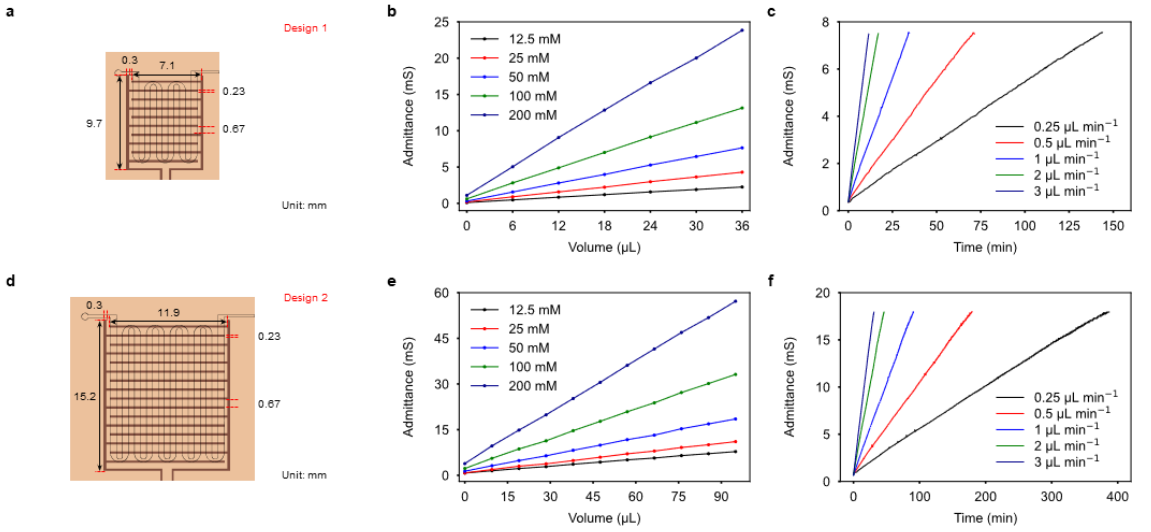

Supplementary Figure 6-25. Characterization of sweat rate sensors with different volumetric capacities. a,**b**, Schematic of the microfluidic sweat rate sensor with a 36 μL volumetric capacity (**a**), and the admittance response of the sweat rate sensor measured by the wearable device as NaCl solutions (12.5 mM ~ 200 mM NaCl in DI) fill up the reservoir (**b**). **c**, Response of the sweat rate sensor measured by the wearable device while a 50 mM NaCl solution fills the reservoir at varying flow rates. **d–f**, Repeated characterization for microfluidic sweat rate sensor with a 96 μL volumetric capacity.

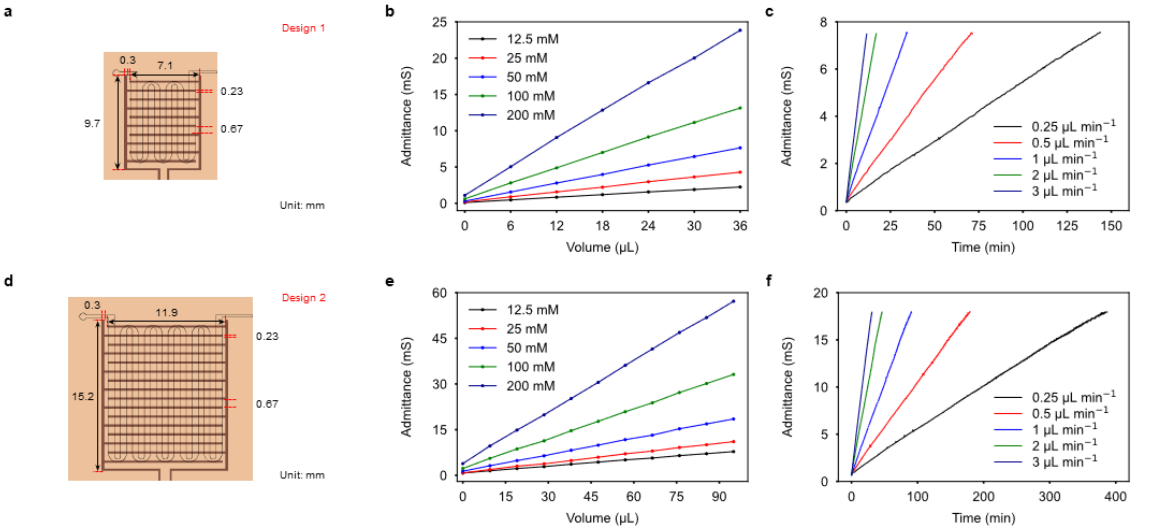

Supplementary Figure 6-26. Characterization of the wearable device performing multiplexed on-body measurement sequences while powered by a commercial flexible solar cell (8.9 cm x 7.4 cm) under dark indoor light intensities. a, Expanded view of power consumption profile of multiplexed measurements with a 2 s interval (8 s per data set), impedance measurements with a 5 min interval, and BLE connection with a connection interval of 4 s and a slave latency of 8 s (bottom); corresponding capacitor charging-discharging curve when powered at 300 and 200 lx by a LED (top). **b**, Expanded view of power consumption profile of multiplexed measurements with a 15 s interval (60 s per data set), and BLE advertisements with a transmission interval of 60 s (bottom); corresponding capacitor charging-discharging curve when powered at 200 and 100 lux by a LED (top).

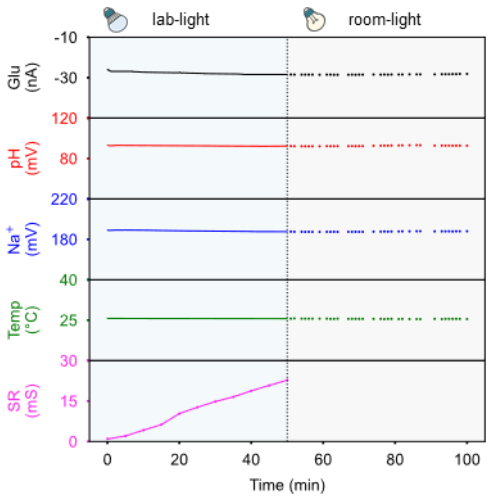

Supplementary Figure 6-27. In vitro multimodal monitoring of biomarkers in a glucose solution (100 µM glucose in pH 7.4 PBS) with a constant flow rate of 1 µL min^{-1}. The wearable device was powered by lab-light (1200 lx) for the first 50 minutes, and powered by room-light (600 lx) for the next 50 minutes.

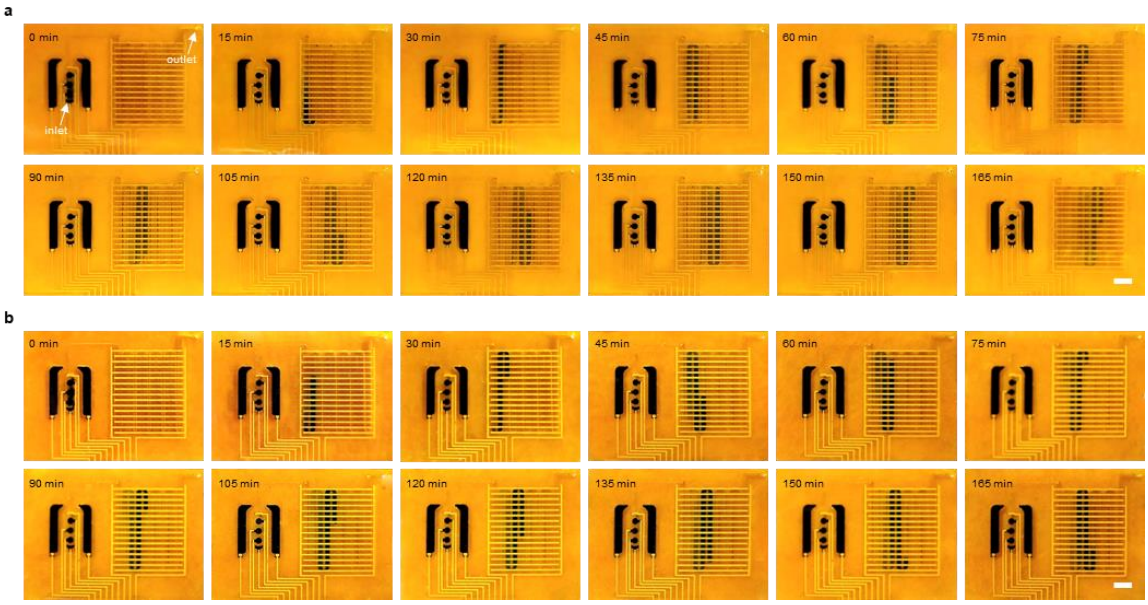

Supplementary Figure 6-28. On-body evaluation of the wearable device's light-powered iontophoresis and sweat processing system at rest. a,**b**, Time-lapsed photos in minutes after 10 minutes of iontophoresis under bright laboratory light for two subjects. Blue dye was placed on the sweat accumulation layer to visualize the sweat filling the biosensor and sweat rate sensor reservoirs at rest. Scale bars, 3 mm.

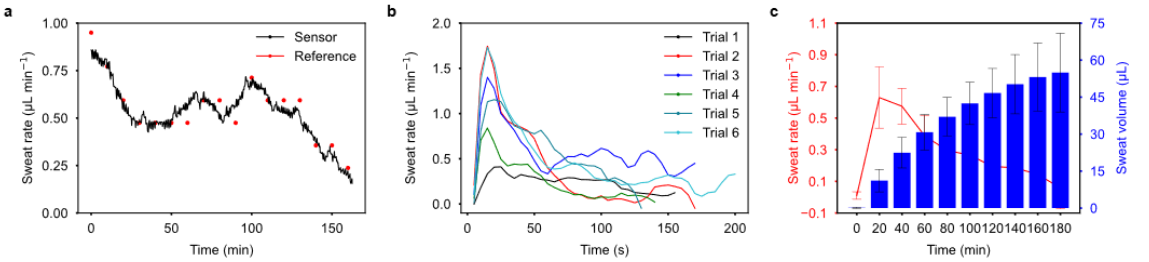

Supplementary Figure 6-29. On-body evaluations of the wearable device's iontophoresis and sweat rate monitoring system at rest. a, Iontophoresis induced on-body sweat rate sensor measurement with a 5 s impedance measurement interval validated by visually measured sweat rate. **b**, Iontophoresis induced sweat rate sensor responses from 6 subjects. **c**, Average iontophoresis induced sweat rates and accumulated sweat volumes and over 3 hours. Data are presented as mean ± SD (n = 6 subjects).

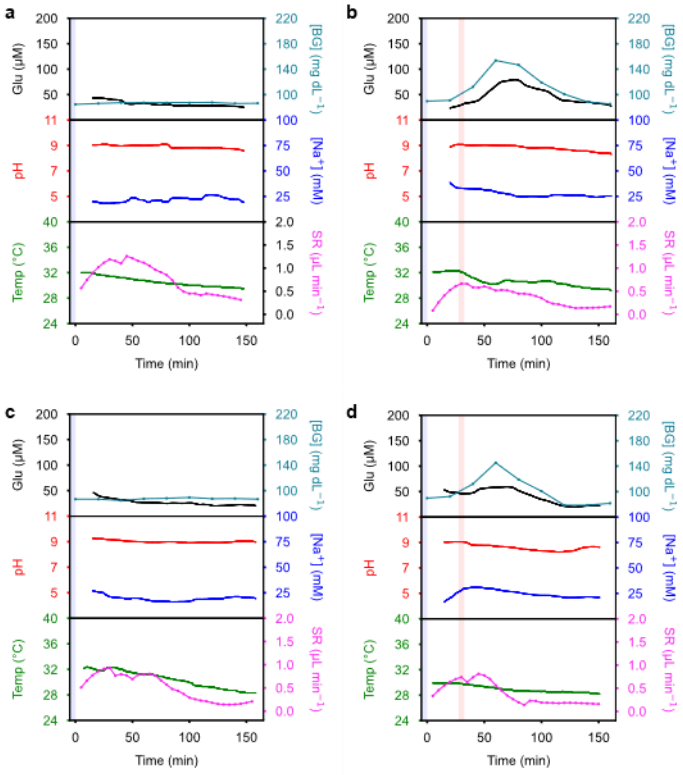

Supplementary Figure 6-30. Evaluation of the wearable device for multiplexed physiological monitoring in Subject 2. a,**b**, Wearable device-enabled autonomous multiplexed physiological monitoring at a fasting state (**a**) and after a glucose tolerance test (**b**) under lab-light illumination. **c**,**d**, Wearable device-enabled autonomous multiplexed physiological monitoring repeated on Subject 2.

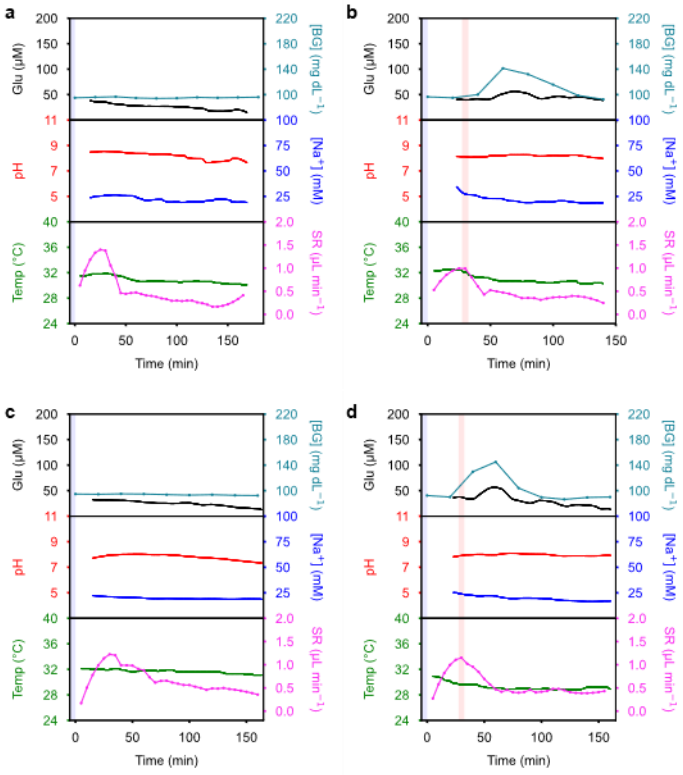

Supplementary Figure 6-31. Evaluation of the wearable device for multiplexed physiological monitoring in Subject 3. a,**b**, Wearable device-enabled autonomous multiplexed physiological monitoring at a fasting state (**a**) and after a glucose tolerance test (**b**) under lab-light illumination. **c**,**d**, Wearable device-enabled autonomous multiplexed physiological monitoring repeated on Subject 3.

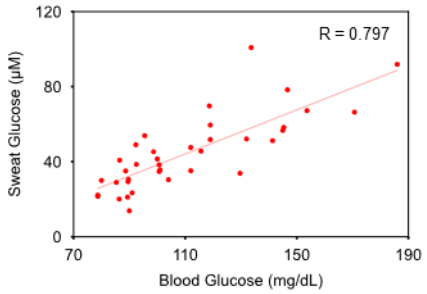

Supplementary Figure 6-32. Correlation between blood glucose levels and sweat glucose levels measured during sedentary glucose tolerance tests across 3 subjects.

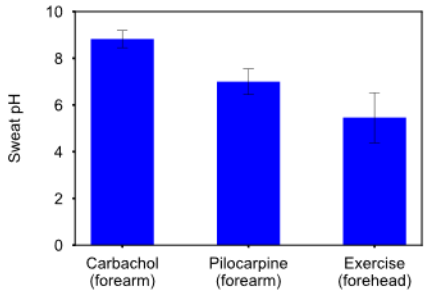

Supplementary Figure 6-33. Relationship between the sweat induction location/method and sweat pH. Data are presented as mean ± SD (n = 5 subjects).

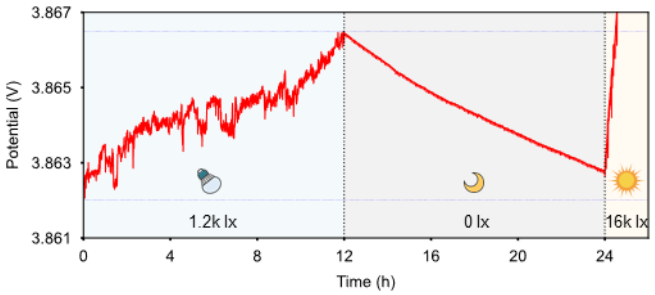

Supplementary Figure 6-34. Operation of battery-aided wearable device for over 24 hours while exposed to various illumination conditions. The potential of the 3.7 V battery was continuously monitored while the wearable device performed multiplexed measurement sequences.

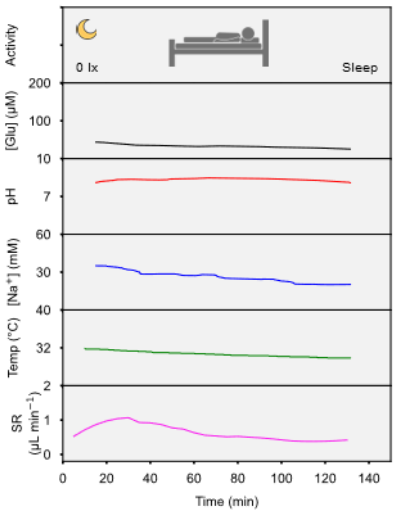

Supplementary Figure 6-35. Evaluation of the light-powered wearable device for physiological monitoring during sleep without the access to light. A 3.7 V battery was integrated into the wearable system and charged during the day with available ambient light.

Supplementary Table 6-6-1. FPSC performance under full sunlight conditions. Average solar cell performance parameters extracted from JV curves recorded under simulated sunlight illumination (AM1.5G) (mean ± SD, n = 7), with the best performance shown in square brackets. Pixel size "small" corresponds to 0.165 cm^2, "large" to 1 cm^2, and "module" to 2 individual 1cm^2 cells connected in series.

Pixel size	**Scan direction**	**V_{oc}** (V)	**J_{sc}** (mA cm^{-2})	**FF** (%)	**PCE** (%)
small	Forward	1.102±0.005 [1.107]	20.1±1.3 [21.4]	74.2±0.5 [74.8]	16.4±1.3 [17.7]
small	Reverse	1.106±0.008 [1.115]	20.2±1.3 [21.7]	74.3±0.5 [75.0]	16.6±1.5 [18.1]
large	Forward	1.075±0.028 [1.107]	20.0±0.5 [20.6]	66.9±0.6 [67.6]	14.7±0.7 [15.4]
large	Reverse	1.081±0.024 [1.109]	20.1±0.5 [20.5]	71.8±0.7 [72.5]	15.6±0.7 [16.5]
module	Forward	2.149±0.060 [2.237]	8.8±0.2 [9.0]	64.9±0.7 [65.6]	12.3±0.7 [13.3]
module	Reverse	2.184±0.056 [2.241]	8.8±0.2 [9.1]	67.8±0.7 [68.5]	13.1±0.6 [14.0]

Supplementary Table 6-6-2. FPSC performance under LED illumination. Photovoltaic parameters extracted from JV curves recorded under 600 lx (215 μW cm^{-2}) indoor illumination using a white light LED, 2700 K (mean ± SD, n = 7), with the best performance shown in square brackets. Pixel size "small" corresponds to 0.165 cm^2, "large" to 1 cm^2, and "module" to 2 individual 1cm^2 cells connected in series.

Pixel size	**Scan direction**	**V_{oc}** (V)	**J_{sc}** (μA cm^{-2})	**FF (%)**	**P_{max}** (μW cm^{-2})	**PCE** (%)
small	Forward	0.929±0.003 [0.936]	87.28±0.06 [87.35]	79.9±0.8 [80.8]	64.8±1.2 [66.1]	30.1±0.5 [30.8]
small	Reverse	0.940±0.004 [0.948]	88.11 ±0.06 [88.11]	79.3±0.8 [80.2]	65.7±1.2 [67.1]	30.6±0.5 [31.2]
large	Forward	0.918±0.007 [0.936]	85.82±0.04 [85.87]	76.6±0.9 [77.6]	60.4±1.3 [61.8]	28.1±0.6 [28.7]
large	Reverse	0.935±0.006 [1.853]	86.03±0.03 [86.07]	78.0±0.9 [78.9]	62.9±1.2 [64.2]	29.2±0.5 [29.9]
module	Forward	1.842±0.009 [1.853]	47.70±0.02 [43.76]	75.1±1.0 [76.2]	60.5±1.2 [61.8]	28.1±0.6 [28.7]
module	Reverse	1.857 ±0.007 [1.866]	43.92±0.03 [43.96]	76.7±1.0 [77.7]	62.5±1.2 [63.7]	29.1±0.6 [29.6]

Supplementary Table 6-6-3. List of the best performing indoor flexible solar cells among different PV technologies. a-Si – amorphous silicon, III-V - , CIGS - , DSSC – dye sensitized solar cells, OPV – organic photovoltaics, PVSK – perovskite solar cells[203–209].

Material	**Light source**	**Illuminance** (lx)	**PCE** (%)	**Reference**
a-Si	Fluorescent	300	8.7	[8]
III-V	Fluorescent	1000	21	[9]
CIGS	Incadescent	3000	5.3	[10]
OPV	Fluorescent	800	13.5	[11]
DSSC	Fluorescent	1000	28.9	[9]
PVSK	LED	400	22.6	[12]
PVSK	LED 6400K	400	23.3	[13]
PVSK	LED 6400K	600	25.3	[13]
PVSK	LED 6400K	1000	25.7	[13]
PVSK	LED 2700K	400	13.3	[14]
PVSK	LED 6400K	600	31.2	This work

Supplementary Table 6-6-4. Performance of quasi-2D FPSC under laser illumination. Photovoltaic parameters extracted from selected JV curves recorded under monochromatic laser light (λ = 637 nm), with values recorded at AM1.5 and 600 lx LED 2700K included for comparison. Pixel size "small" corresponds to 0.165 cm^2, "large" to 1 cm^2, and "module" to 2 individual 1cm^2 cells connected in series. R_s and R_p values were calculated from slope near V_{oc} and J_{sc}, respectively.

Pixel size	**Light source**	**V_{oc}** (V)	**J_{sc}** (mA cm^{-2})	**FF** (%)	**PCE** (%)	**R_s** (Ω cm^2)	**R_p** (kΩ cm^2)
small	AM1.5	1.115	21.7	75.0	18.1	4.5	3.9
	Laser (12.23 mW cm^{-2})	1.102	5.7	80.9	41.3	15	28
	Laser (5.43 mW cm^{-2})	1.074	2.5	82.5	40.2	29	124
	Laser (0.194 mW cm^{-2})	0.947	0.070	82.6	34.5	383	535
	LED 600lx (0.215 mW cm^{-2})	0.948	0.088	80.2	31.2	306	500
large	AM1.5	1.109	20.5	72.5	16.5	8.3	7.5
	Laser (12.23 mW cm^{-2})	1.080	4.7	73.7	29.4	25	126
	Laser (5.43 mW cm^{-2})	1.050	2.3	76.0	30.4	34	259
	Laser (0.286 mW cm^{-2})	0.948	0.108	79.3	28.4	329	390
	LED 600lx (0.215 mW cm^{-2})	0.945	0.086	78.9	29.9	389	437
module	AM1.5	2.241	9.1	68.5	14.0	21.1	10.7
	LED 600lx (0.215 mW cm^{-2})	1.866	0.044	77.7	29.6	1014	795

Supplementary Table 6-6-5. Average power consumption of electronic system supplied at 3 V while performing various operations under varying operation parameters. Blocks highlighted in yellow represent average power consumptions of power consumption profiles shown in **Fig. 6-3d**, and blocks highlighted in green represent average power consumptions of power consumption profiles shown in **Fig. 6-6-3f**.

Operation	**Operation parameters**		**Power consumption (μW)**
Standby	BLE connection interval	1 s	127
		4 s	82
		12 s	72
Iontophoresis	Compliance voltage	6 V	719
		12 V	1604
		18 V	2589
Potentiometry	Measurement interval	1 s	147
		2 s	119
		4 s	103
Amperometry	Measurement interval	1 s	161
		2 s	129
		4 s	111
Differential pulse voltammetry	Pulse period	0.25 s	334
		0.5 s	211
		1 s	142
Impedance analysis	Measurement interval	5 s	600
		10 s	343
		15 s	252
Multiplexed measurement (1 amperometry, 2 potentiometry, 1 temperature)	Measurement interval	1 s	170
		2 s	132
		4 s	110
			203

On-body measurement sequence	Multiplexed (1 s interval) + impedance (5 min interval) + BLE connection (4 s interval)	
	Multiplexed (2 s interval) + impedance (5 min interval) + BLE connection (4 s interval with slave latency of 2)	129
	Multiplexed (15 s interval) + BLE advertisement (60 s interval)	58

Chapter 7

INGESTIBLE SENSORS FOR EXPLORING THE GUT

The GI tract, integral to essential physiological processes, harbors a wealth of chemical information crucial for deciphering the health and functionality of the digestive and nervous systems. Traditional methods, such as fecal analyses and biopsies, despite being informative, are invasive, costly, and incapable of providing real-time metabolic and neurotransmitter profiling across the entire GI tract, thus limiting their utility for comprehensive and ongoing health monitoring. Conversely, commercially available ingestible capsule sensors, albeit non-invasive and capable of real-time data transmission, merely monitor basic markers like pH and pressure, neglecting a detailed chemical analysis. Addressing these challenges, we developed a multiplexed ingestible sensor platform designed for simultaneous detection of a broad spectrum of biochemical markers, including electrolytes, metabolites, and neurotransmitters. Our innovative capsule, measuring a mere 7 mm in diameter and 25 mm in length, encloses a miniaturized wireless electrochemical workstation capable of executing a suite of electrochemical measurement techniques—potentiometry, amperometry, voltammetry, and impedimetry—interfaced with a variety of electrochemical sensors to meticulously explore the GI tract's chemical landscape. Validating our approach in animal studies, we utilized an array of sensors, namely glucose, serotonin, pH, ionic strength, and temperature, to monitor the dynamic profile of these crucial biomarkers and their responsiveness to different dietary intakes.

7.1 Background

The GI tract plays dual, pivotal roles: it serves as a vital conduit for nutrient absorption and waste expulsion, and as a complex interface that links our overall health to the inner workings of our physiological depths[210,211]. This multifaceted system, woven through with various compartments, hosts the gut microbiota, which, alongside the central and enteric nervous systems, regulates myriad processes. These include the scrupulous breakdown and selective absorption of nutrients, as well as exerting an unexpected influence over our emotional and cognitive states[212]. Such influence can materialize directly through neurotransmitter production or indirectly by triggering brain signals through the production of metabolites or stimulating immune cells to release cytokines[213,214].

Dysbiosis, a perturbation of the delicate ecosystem within the GI tract, is intertwined with a diverse array of disorders, not merely confined to GI issues like Irritable Bowel Syndrome (IBS) and Inflammatory Bowel Disease (IBD), but also extending into Central Nervous System (CNS) disorders, such as autism, anxiety, depression, and Parkinson's disease. A particular point of intrigue lies in the intersection between gut dysbiosis and IBDs, such as ulcerative colitis and Crohn's disease, which can illuminate associations with factors like oxidative stress and imbalances in microbial metabolites within the intestines[215,216]. Disruptions in this delicate balance can incite a cascade of adverse effects, fostering inflammation and further unsettling the stability of the GI's homeostatic state.

Monitoring glucose and serotonin levels in the GI tract, especially during postprandial phases, provides a distinct perspective for examining metabolic health and digestive efficacy. The detailed interplay between dietary intake, glucose fluctuations, and serotonin release is essential not only for understanding metabolic health but also for predicting potential metabolic disorders. Serotonin, of which a substantial 95% is synthesized within the GI tract, is not merely a regulator of GI motility but also a significant player within the gut-brain axis, impacting mood, appetite, and cognitive functionality. Variations in serotonin, particularly post-consumption, can thus shed light on the multifaceted dialogues occurring within our physiology, acting as a barometer for both GI and CNS health.

However, there is a lack of bioelectronic platforms for the multiplexed detection of various chemicals in vivo. Currently, biochemical analyses of such target analytes in the gut primarily rely on biopsies or fecal analyses, which necessitate separate and costly sample collection and molecular screening procedures. Commercial ingestible technologies, such as capsule endoscopes and pH/pressure sensing capsules for motility testing, are designed to detect the optical and physical alterations of the GI tract due to underlying GI disorders, often resulting from deviations from gut homeostasis[210,211]. While such physical biomarkers aid in diagnosing disease symptoms, they frequently fail to reveal early signs or ascertain the underlying cause of the disease. Additionally, current technologies for in-vivo detection of basal neurotransmitter levels, including serotonin, are limited. While methods using fast-scan

cyclic voltammetry (FSCV) with carbon fiber electrodes via direct oxidation offer high temporal resolution and sensitivity in clear media like cerebrospinal fluids, they falter in providing information on basal neurotransmitter concentrations and may lack selectivity in complex fluids like GI fluids due to possible interferents[217].

In response to these challenges, and to adeptly navigate the intricacies of GI tract biochemistry, we introduce PillTrek: an integrated smart capsule platform designed for real-time, continuous, and multiplexed monitoring of various parameters in GI fluids—including pH, glucose, serotonin, ionic strength, and temperature (**Fig. 7-1**). PillTrek, with a compact form under 1cm^3 in volume, can perform potentiometric, amperometric, voltammetric, and impedimetric techniques, providing a versatile platform where diverse electrochemical sensors can be interfaced to detect additional parameters of interest. This innovative ingestible platform aspires to render a nuanced biochemical portrait of the GI tract, illuminating the intricate and often obscured chemical activities related to the gut-brain axis, and thereby facilitating the development of personalized and targeted therapies for safeguarding GI and CNS health.

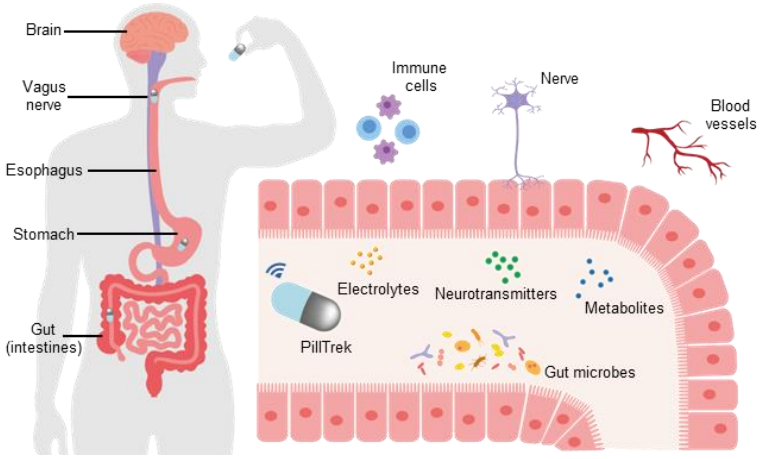

Figure 7-1. PillTrek, an ingestible electrochemical platform for continuous, multiplexed gastrointestinal fluid analysis.

7.2 Sensor Array for Multiplexed Monitoring of GI Biomarkers

7.2.1 Results

A custom-developed sensor array has been fabricated for the real-time, multiplexed monitoring of key biomarkers in GI fluids, with potential packaging in an ingestible capsule for authentic in vivo analysis. The sensor array is constructed on a PET substrate, featuring mass-producible inkjet-printed electrodes, ensuring a combination of adaptability and precision in the detection processes (**Fig. 7-2a,b**). The modified electrode array in conjunction with the ingestible electronic system can detect a wide range of key biomarkers in GI fluids such as serotonin, glucose, pH, and ionic strength (**Fig. 7-2c**).

Each individual sensor within the array has been meticulously optimized for the robust detection of specific biomarkers in GI fluids. These include neurotransmitters such as serotonin, metabolites like glucose, pH levels, and ionic strength, supplemented with an embedded temperature sensor. For serotonin detection, the sensor is integrated with specially prepared aptamers tagged with methylene blue (MB), enabling the monitoring of target-induced conformational changes. These alterations influence the efficiency of electron transfer between the MB redox molecule and the electrode surface, thereby allowing for a nuanced detection of varying serotonin concentrations using square wave voltammetry (SWV) (**Fig. 7-2d**). In the case of glucose sensing, the array employs a sophisticated enzymatic sensor, where a hydrophilic porous matrix immobilizes selective and sensitive enzymes on the electrode surface. This specialized construction allows for the sensitive detection of glucose concentrations through amperometry, leveraging a synthesized mediator to facilitate electron shuttling from glucose oxidase to the electrode (**Fig. 7-2e**). The pH sensor within the array operates through a streamlined approach. It features an electrodeposited polyaniline (PANI) layer, effectively utilizing the deprotonation of H^+ atoms as a metric to accurately gauge the prevailing pH levels within the GI environment (**Fig. 7-2f**). Impedance between two bare carbon electrodes is measured to quantify the ionic strength of the target solutions (**Fig. 7-2g**). Demonstrating their efficacy, the pH sensor shows a consistent linear response from pH 4-8, the glucose sensor from 0 mM to 50 mM, serotonin

detection is log-linear from 0 to 25 µM, and ionic strength from 0.1x to 2x simulated intestinal fluid (SIF)[218] (with 1x SIF approximating 140 mM) (**Fig. 7-2h-k**).

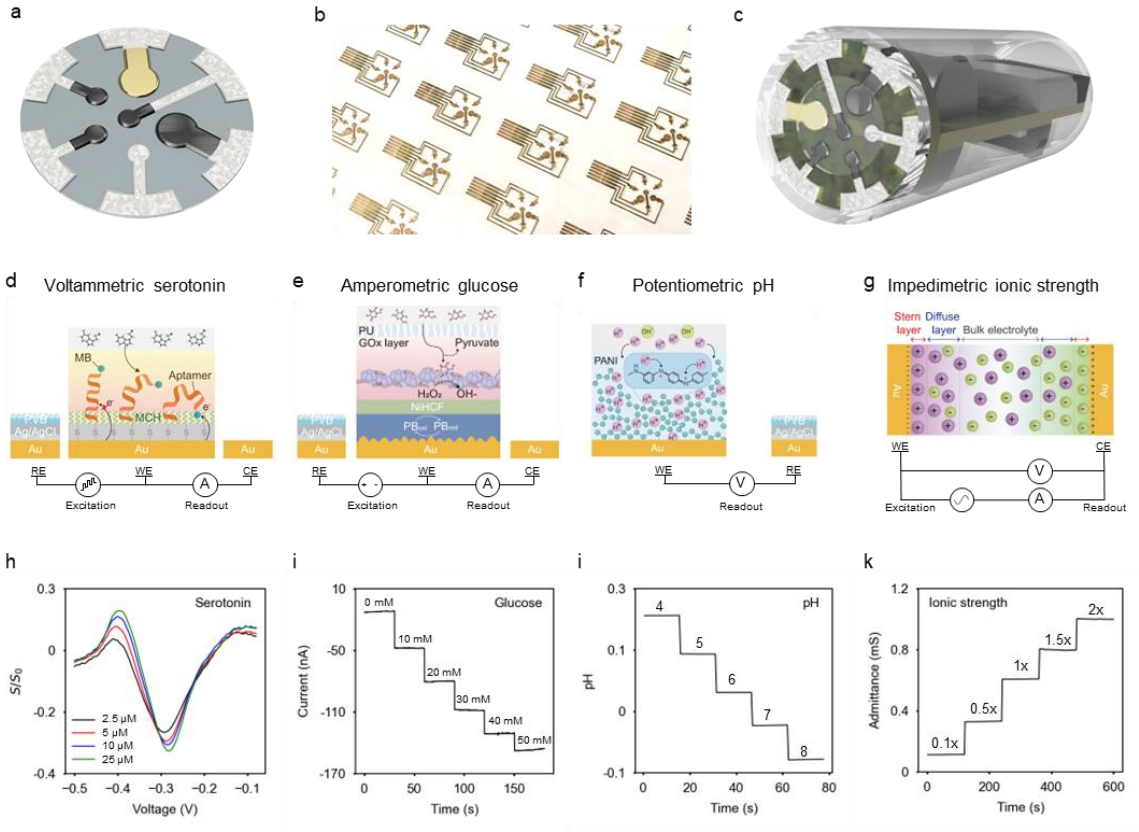

Figure 7-2. Ingestible sensor array for multiplexed detection of gastrointestinal biomarkers. a, Schematic of multiplexed sensor array electrodes inkjet-printed on a PET substrate. **b**, Photo of a batch of sensor arrays inkjet-printed on a PET substrate. **c**, Schematic of the sensor array integrated into the ingestible capsule system. (**d-k**) Schematic of the electrochemical transduction mechanisms for the voltametric serotonin (**d**), amperometric glucose (**e**), potentiometric pH (**f**), and impedimetric ionic strength (**g**) sensors and their corresponding electrochemical responses (**h-k**) in SIF.

Modification strategies have been applied to enhance sensor performance within the GI's complex fluid environment. A notable adaptation includes the application of a polyurethane

(PU) coating on the glucose sensor, enhancing its operational range, antibiofouling capabilities, and overall measurement accuracy in the real intestinal fluid of rats.

7.2.2 Methods

An electrochemical workstation (CHI660E) was utilized for the electrode preparation processes, encompassing electrochemical deposition and characterization steps. Both the electrochemical workstation and an ingestible device were applied in the sensor characterization procedures.

Serotonin sensor: Aptamers were prepared by dissolving them to a concentration of 100 µM in 1X Tris-EDTA buffer, and were then frozen in individual aliquots at 20°C. The electrode was subjected to cleaning through cyclic voltammetry in 0.5 M NaOH, executing 50 cycles from -1 to -1.6 V at a scan rate of 1 V/s. Subsequently, a TCEP reduction was carried out by mixing 5 µl of a 10 µM DNA aliquot and 5 µl of 1 mM TCEP, incubating the mixture at room temperature in the dark for one hour. The prepared aptamers were then bound to the cleaned electrode to finalize the serotonin sensor.

Glucose sensor: A nanostructured Au film was electrodeposited on the Au electrodes to increase the electrode surface area, involving multi-potential deposition in a solution of 50 mM chloroauric acid and 0.1 M HCl, undergoing 1500 cycles. A layering process followed where Prussian blue and Nickel layers were deposited, and then an enzyme layer was applied which consisted of a mixed solution of chitosan/CNTs and enzyme. A final polyurethane (PU) layer was then prepared and left to air-dry overnight at 4°C.

pH sensor: The electrode was initially cleaned using 0.5 M HCl, and cyclic voltammetry was performed from -0.1 to 0.9 V across 10 cycles. A polyaniline (PANI) deposition was conducted within a 0.1 M aniline solution in 1 M HCl by applying cyclic voltammetry across two sets of 12 cycles each to ensure the effective functionality of the pH sensor.

7.3 System Level Integration of Bioelectronic System

7.3.1 Results

In the creation of an advanced ingestible electronic system, paramount considerations were directed towards its size, power efficiency, and wireless transmission capabilities to facilitate accurate measurements within the GI tract. Emphasizing miniaturization, the meticulously crafted device boasts a compact form, occupying a volume just under 1cm^3, ensuring optimized ingestibility and maneuverability through the GI transit pathways (**Fig. 7-3**).

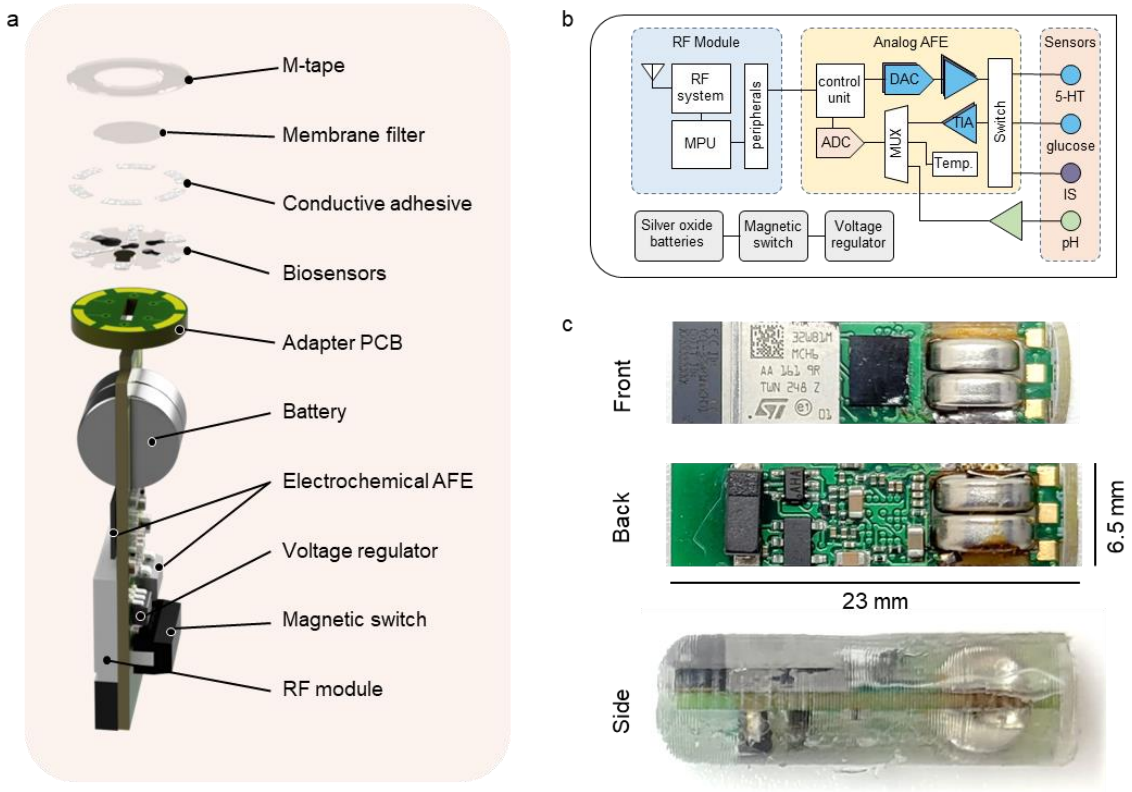

Figure 7-3. Compact ingestible electronic system for prolonged wireless operation in GI tract. a, Exploded diagram showing the key compartments of PillTrek. **b**, Block diagram illustrating key electronic modules in PillTrek. **c**, Photos of the electronic system from the top and bottom view before encapsulation, and from the side after encapsulation.

The operational architecture of the device is ingeniously formulated. At its core, the main Printed Circuit Board (PCB) (0.65 cm x 2.3 cm) integrates essential components such as silver oxide batteries, an RF module, and an Electrochemical Analog Front-End (AFE), amongst others. An innovative approach has been adopted with a perpendicularly interfaced secondary adapter PCB, augmenting the connection to the sensor array and enabling a comprehensive suite of electrochemical measurements including potentiometry, amperometry, square wave voltammetry, and impedance measurements with notable precision.

Power management is a crucial facet of the design strategy, aimed at promoting operational longevity. Fueled by two silver oxide batteries (3.1V, 16mAh) in series, the system exhibits a consummate power economy, operating below 300 μW, which substantiates continuous, unhindered functionality aligned with the GI transit durations. The prowess of the device is further manifested through its robust wireless communication abilities, facilitating the meticulous execution of measurement commands, data acquisition, and secure wireless transmission, all of which underpin its readiness and efficacy for imminent in-vivo applications and trials.

7.3.2 Methods

A sophisticated electronic system is integrated into a highly compact 4-layer PCB, having dimensions of a mere 23 mm x 6.5 mm, meticulously crafted using Eagle CAD. The system's energy is harnessed from two series-connected silver oxide batteries (SR521SW; Energizer), delivering a combined voltage of 3.1 V with a capacity of 16 mAh. Power management within the system is diligently administered through a magnetic reed switch (MK24-B-3-OE; Standex-Meder Electronics) and a voltage regulator (ADP162; Analog Devices), ensuring consistent and stable power output. Wireless communication and control processes are managed by an adept RF module (STM32WB1MMC; STMicroelectronics), responsible for wireless data transmission, signal processing, and overseeing the electrochemical instrumentation system, which operates principally through the AD5940 (Analog Devices), and is complemented by a voltage buffer (LPV521; Texas Instruments). The electronic

system is proficient in continuous measurement operations, maintaining a power consumption below 300 μW, thereby theoretically allowing for sustained operational for nearly 7 days.

7.4 Future Work and Outlook

Moving forward, there is a cascade of essential explorations and validations that are imperative to advance the practical functionality and reliability of the PillTrek system. Initial endeavors will prioritize the meticulous characterization of the sensors and the entire electronic system. A pivotal focus will be on ensuring that the sensors operate with remarkable stability and precision across a diverse spectrum of real intestinal fluids, extracted from rats, aligning with the physiological variations encountered during actual GI transit.

Moreover, emphasis will be placed on executing comprehensive in vitro studies, leveraging diverse dietary inputs to discern their impacts on GI biomarkers. This inquiry aims to unravel the intricate interplay between various consumed foods and the subtle shifts in GI biomarkers, thus enhancing our understanding of dietary influences on GI health. Concurrently, the encapsulated system will undergo rigorous testing in simulated fluids and authentic biological environments, fortifying its readiness for subsequent in vivo applications.

The envisioned trajectory also includes the translation of the system into practical, living models, such as rabbits. In these in vivo scenarios, the PillTrek capsule will be employed to ascertain real-time intestinal biomarkers, exploring the underlying dynamism and modulations within the GI environment in response to dietary variables. Such explorations promise novel insights into the gut-brain axis, potentially uncovering the nuanced influences of gut activities on broader physiological and behavioral realms.

In the extended horizon, aspirations extend towards integrating the assessment of behavioral shifts, exploring the profound intersections of GI activities with broader physiological and behavioral outcomes. This progression aims to foster a multi-dimensional understanding,

enabling the linkage of intricate gut biochemical dynamics with observable behavioral manifestations, thus widening the aperture of insights garnered through the PillTrek system. Through these strategic advancements, the PillTrek initiative aims to unveil nuanced pathways of information, facilitate enriched, multi-parameter insights into GI health, and ultimately, contribute significantly to the domains of personalized and precision medicine in GI and CNS health.

BIBILIOGRAPHY

(1) Gao, W.; Emaminejad, S.; Nyein, H. Y. Y.; Challa, S.; Chen, K.; Peck, A.; Fahad, H. M.; Ota, H.; Shiraki, H.; Kiriya, D.; Lien, D.-H.; Brooks, G. A.; Davis, R. W.; Javey, A. Fully Integrated Wearable Sensor Arrays for Multiplexed *in Situ* Perspiration Analysis. *Nature* **2016**, *529* (7587), 509–514. https://doi.org/10.1038/nature16521.

(2) Wilke, K.; Martin, A.; Terstegen, L.; Biel, S. S. A Short History of Sweat Gland Biology. *International Journal of Cosmetic Science* **2007**, *29* (3), 169–179. https://doi.org/10.1111/j.1467-2494.2007.00387.x.

(3) Low, P. A. Evaluation of Sudomotor Function. *Clinical Neurophysiology* **2004**, *115* (7), 1506–1513. https://doi.org/10.1016/j.clinph.2004.01.023.

(4) Klaka, P.; Grüdl, S.; Banowski, B.; Giesen, M.; Sättler, A.; Proksch, P.; Welss, T.; Förster, T. A Novel Organotypic 3D Sweat Gland Model with Physiological Functionality. *PLOS ONE* **2017**, *12* (8), e0182752. https://doi.org/10.1371/journal.pone.0182752.

(5) Elpa, D. P.; Chiu, H.-Y.; Wu, S.-P.; Urban, P. L. Skin Metabolomics. *Trends in Endocrinology & Metabolism* **2021**, *32* (2), 66–75. https://doi.org/10.1016/j.tem.2020.11.009.

(6) Shelley, W. B.; Hurley, H. J. The Physiology of the Human Axillary Apocrine Sweat Gland12. *Journal of Investigative Dermatology* **1953**, *20* (4), 285–297. https://doi.org/10.1038/jid.1953.35.

(7) Sato, K.; Leidal, R.; Sato, F. Morphology and Development of an Apoeccrine Sweat Gland in Human Axillae. *American Journal of Physiology-Regulatory, Integrative and Comparative Physiology* **1987**, *252* (1), R166–R180. https://doi.org/10.1152/ajpregu.1987.252.1.R166.

(8) Heikenfeld, J.; Jajack, A.; Feldman, B.; Granger, S. W.; Gaitonde, S.; Begtrup, G.; Katchman, B. A. Accessing Analytes in Biofluids for Peripheral Biochemical Monitoring. *Nature Biotechnology* **2019**, *37* (4), 407–419. https://doi.org/10.1038/s41587-019-0040-3.

(9) Tripathi, S. R.; Miyata, E.; Ishai, P. B.; Kawase, K. Morphology of Human Sweat Ducts Observed by Optical Coherence Tomography and Their Frequency of Resonance in the Terahertz Frequency Region. *Scientific Reports* **2015**, *5* (1), 9071. https://doi.org/10.1038/srep09071.

(10) Lu, C. P.; Polak, L.; Rocha, A. S.; Pasolli, H. A.; Chen, S.-C.; Sharma, N.; Blanpain, C.; Fuchs, E. Identification of Stem Cell Populations in Sweat Glands and Ducts Reveals Roles in Homeostasis and Wound Repair. *Cell* **2012**, *150* (1), 136–150. https://doi.org/10.1016/j.cell.2012.04.045.

(11) Diao, J.; Liu, J.; Wang, S.; Chang, M.; Wang, X.; Guo, B.; Yu, Q.; Yan, F.; Su, Y.; Wang, Y. Sweat Gland Organoids Contribute to Cutaneous Wound Healing and Sweat Gland Regeneration. *Cell Death & Disease* **2019**, *10* (3), 1–13. https://doi.org/10.1038/s41419-019-1485-5.

(12) Liu, N.; Huang, S.; Yao, B.; Xie, J.; Wu, X.; Fu, X. 3D Bioprinting Matrices with Controlled Pore Structure and Release Function Guide in Vitro Self-Organization of

Sweat Gland. *Scientific Reports* **2016**, *6* (1), 34410. https://doi.org/10.1038/srep34410.

(13) Cui, C.-Y.; Schlessinger, D. Eccrine Sweat Gland Development and Sweat Secretion. *Exp Dermatol* **2015**, *24* (9), 644–650. https://doi.org/10.1111/exd.12773.

(14) Bovell, D. L. The Evolution of Eccrine Sweat Gland Research towards Developing a Model for Human Sweat Gland Function. *Experimental Dermatology* **2018**, *27* (5), 544–550. https://doi.org/10.1111/exd.13556.

(15) Sato, K.; Sato, F. Role of Calcium in Cholinergic and Adrenergic Mechanisms of Eccrine Sweat Secretion. *American Journal of Physiology-Cell Physiology* **1981**, *241* (3), C113–C120. https://doi.org/10.1152/ajpcell.1981.241.3.C113.

(16) Quinton, P. M. Cystic Fibrosis: Lessons from the Sweat Gland. *Physiology* **2007**, *22* (3), 212–225. https://doi.org/10.1152/physiol.00041.2006.

(17) Mihályi, C.; Iordanov, I.; Töröcsik, B.; Csanády, L. Simple Binding of Protein Kinase A Prior to Phosphorylation Allows CFTR Anion Channels to Be Opened by Nucleotides. *Proceedings of the National Academy of Sciences* **2020**, *117* (35), 21740–21746. https://doi.org/10.1073/pnas.2007910117.

(18) Salinas, D. B.; Peng, Y.-H.; Horwich, B.; Wee, C. P.; Frisbee, E.; Maarek, J.-M. Image-Based β-Adrenergic Sweat Rate Assay Captures Minimal Cystic Fibrosis Transmembrane Conductance Regulator Function. *Pediatric Research* **2020**, *87* (1), 137–145. https://doi.org/10.1038/s41390-019-0503-8.

(19) Sonner, Z.; Wilder, E.; Gaillard, T.; Kasting, G.; Heikenfeld, J. Integrated Sudomotor Axon Reflex Sweat Stimulation for Continuous Sweat Analyte Analysis with Individuals at Rest. *Lab on a Chip* **2017**, *17* (15), 2550–2560. https://doi.org/10.1039/C7LC00364A.

(20) Riedl, B.; Nischik, M.; Birklein, F.; Neundörfer, B.; Handwerker, H. O. Spatial Extension of Sudomotor Axon Reflex Sweating in Human Skin. *Journal of the Autonomic Nervous System* **1998**, *69* (2–3), 83–88. https://doi.org/10.1016/S0165-1838(98)00016-2.

(21) Kihara, M.; Opfer-Gehrking, T. L.; Low, P. A. Comparison of Directly Stimulated with Axon-Reflex–Mediated Sudomotor Responses in Human Subjects and in Patients with Diabetes. *Muscle & Nerve* **1993**, *16* (6), 655–660. https://doi.org/10.1002/mus.880160612.

(22) Low, P. A.; Opfer-Gehrking, T. L.; Kihara, M. In Vivo Studies on Receptor Pharmacology of the Human Eccrine Sweat Gland. *Clinical Autonomic Research* **1992**, *2* (1), 29–34. https://doi.org/10.1007/BF01824208.

(23) Ohmi, M.; Tanigawa, M.; Wada, Y.; Haruna, M. Dynamic Analysis for Mental Sweating of a Group of Eccrine Sweat Glands on a Human Fingertip by Optical Coherence Tomography. *Skin Research and Technology* **2012**, *18* (3), 378–383. https://doi.org/10.1111/j.1600-0846.2011.00580.x.

(24) Buono, M. J.; Ball, K. D.; Kolkhorst, F. W. Sodium Ion Concentration vs. Sweat Rate Relationship in Humans. *Journal of Applied Physiology* **2007**, *103* (3), 990–994. https://doi.org/10.1152/japplphysiol.00015.2007.

(25) Ohashi, T.; Gerrett, N.; Shinkawa, S.; Sato, T.; Miyake, R.; Kondo, N.; Mitsuzawa, S. Fluidic Patch Device to Sample Sweat for Accurate Measurement of Sweat Rate

and Chemical Composition: A Proof-of-Concept Study. *Analytical Chemistry* **2020**, *92* (23), 15534–15541. https://doi.org/10.1021/acs.analchem.0c03466.

(26) Simmers, P.; Li, S. K.; Kasting, G.; Heikenfeld, J. Prolonged and Localized Sweat Stimulation by Iontophoretic Delivery of the Slowly-Metabolized Cholinergic Agent Carbachol. *Journal of Dermatological Science* **2018**, *89* (1), 40–51. https://doi.org/10.1016/j.jdermsci.2017.10.013.

(27) Shibasaki, M.; Crandall, C. G. Effect of Local Acetylcholinesterase Inhibition on Sweat Rate in Humans. *Journal of Applied Physiology* **2001**, *90* (3), 757–762. https://doi.org/10.1152/jappl.2001.90.3.757.

(28) Sato, K.; Dobson, R. L. Regional and Individual Variations in the Function of the Human Eccrine Sweat Gland. *Journal of Investigative Dermatology* **1970**, *54* (6), 443–449. https://doi.org/10.1111/1523-1747.ep12259272.

(29) Patterson, M. J.; Galloway, S. D. R.; Nimmo, M. A. Variations in Regional Sweat Composition in Normal Human Males. *Experimental Physiology* **2000**, *85* (6), 869–875. https://doi.org/10.1111/j.1469-445X.2000.02058.x.

(30) Leppäluoto, J. Human Thermoregulation in Sauna. *Annals of Clinical Research* **1988**, *20* (4), 240–243.

(31) *Sauna, sweat and science II – do we sweat what we drink?: Isotopes in Environmental and Health Studies: Vol 55, No 4*. https://www.tandfonline.com/doi/abs/10.1080/10256016.2019.1635125 (accessed 2022-10-02).

(32) Chen, Y.-L.; Kuan, W.-H.; Liu, C.-L. Comparative Study of the Composition of Sweat from Eccrine and Apocrine Sweat Glands during Exercise and in Heat. *International Journal of Environmental Research and Public Health* **2020**, *17* (10), 3377. https://doi.org/10.3390/ijerph17103377.

(33) Lin, S.; Wang, B.; Zhao, Y.; Shih, R.; Cheng, X.; Yu, W.; Hojaiji, H.; Lin, H.; Hoffman, C.; Ly, D.; Tan, J.; Chen, Y.; Di Carlo, D.; Milla, C.; Emaminejad, S. Natural Perspiration Sampling and in Situ Electrochemical Analysis with Hydrogel Micropatches for User-Identifiable and Wireless Chemo/Biosensing. *ACS Sensors.* **2020**, *5* (1), 93–102. https://doi.org/10.1021/acssensors.9b01727.

(34) Souza, S. L.; Graça, G.; Oliva, A. Characterization of Sweat Induced with Pilocarpine, Physical Exercise, and Collected Passively by Metabolomic Analysis. *Skin Research and Technology* **2018**, *24* (2), 187–195. https://doi.org/10.1111/srt.12412.

(35) Moon, J.-M.; Teymourian, H.; De la Paz, E.; Sempionatto, J. R.; Mahato, K.; Sonsa-ard, T.; Huang, N.; Longardner, K.; Litvan, I.; Wang, J. Non-Invasive Sweat-Based Tracking of L-Dopa Pharmacokinetic Profiles Following an Oral Tablet Administration. *Angewandte Chemie* **2021**, *133* (35), 19222–19226. https://doi.org/10.1002/ange.202106674.

(36) Bariya, M.; Li, L.; Ghattamaneni, R.; Ahn, C. H.; Nyein, H. Y. Y.; Tai, L.-C.; Javey, A. Glove-Based Sensors for Multimodal Monitoring of Natural Sweat. *Science Advances* **2020**, *6* (35), eabb8308. https://doi.org/10.1126/sciadv.abb8308.

(37) Lin, P.-H.; Sheu, S.-C.; Chen, C.-W.; Huang, S.-C.; Li, B.-R. Wearable Hydrogel Patch with Noninvasive, Electrochemical Glucose Sensor for Natural Sweat

Detection. *Talanta* **2022**, *241*, 123187. https://doi.org/10.1016/j.talanta.2021.123187.

(38) Sempionatto, J. R.; Moon, J.-M.; Wang, J. Touch-Based Fingertip Blood-Free Reliable Glucose Monitoring: Personalized Data Processing for Predicting Blood Glucose Concentrations. *ACS Sens.* **2021**, *6* (5), 1875–1883. https://doi.org/10.1021/acssensors.1c00139.

(39) Low, P. A.; Caskey, P. E.; Tuck, R. R.; Fealey, R. D.; Dyck, P. J. Quantitative Sudomotor Axon Reflex Test in Normal and Neuropathic Subjects. *Annals of Neurology* **1983**, *14* (5), 573–580. https://doi.org/10.1002/ana.410140513.

(40) Aromdee, C.; Fawcett, J. P.; Ferguson, M. M.; Ledger, R. Serum Pilocarpine Esterase Activity and Response to Oral Pilocarpine. *Biochemical and Molecular Medicine* **1996**, *59* (1), 57–61. https://doi.org/10.1006/bmme.1996.0065.

(41) Herrmann, F.; Mandol, L. Studies of Ph of Sweat Produced by Different Forms of Stimulation. *Journal of Investigative Dermatology* **1955**, *24* (3), 225–246. https://doi.org/10.1038/jid.1955.36.

(42) Verde, T.; Shephard, R. J.; Corey, P.; Moore, R. Sweat Composition in Exercise and in Heat. *Journal of Applied Physiology* **1982**, *53* (6), 1540–1545. https://doi.org/10.1152/jappl.1982.53.6.1540.

(43) Agrawal, K.; Waller, J. D.; Pedersen, T. L.; Newman, J. W. Effects of Stimulation Technique, Anatomical Region, and Time on Human Sweat Lipid Mediator Profiles. *Prostaglandins & Other Lipid Mediators* **2018**, *134*, 84–92. https://doi.org/10.1016/j.prostaglandins.2017.09.007.

(44) Harshman, S. W.; Pitsch, R. L.; Schaeublin, N. M.; Smith, Z. K.; Strayer, K. E.; Phelps, M. S.; Qualley, A. V.; Cowan, D. W.; Rose, S. D.; O'Connor, M. L.; Eckerle, J. J.; Das, T.; Barbey, A. K.; Strang, A. J.; Martin, J. A. Metabolomic Stability of Exercise-Induced Sweat. *Journal of Chromatography B* **2019**, *1126–1127*, 121763. https://doi.org/10.1016/j.jchromb.2019.121763.

(45) Hussain, J. N.; Mantri, N.; Cohen, M. M. Working Up a Good Sweat – The Challenges of Standardising Sweat Collection for Metabolomics Analysis. *The Clinical Biochemist Reviews* **2017**, 38(1), 13–34.

(46) De Giovanni, N.; Fucci, N. The Current Status of Sweat Testing For Drugs of Abuse: A Review. *Current Medicinal Chemistry* **2013**, *20* (4), 545–561. https://doi.org/10.2174/092986713804910139.

(47) Liu, C.; Xu, T.; Wang, D.; Zhang, X. The Role of Sampling in Wearable Sweat Sensors. *Talanta* **2020**, *212*, 120801. https://doi.org/10.1016/j.talanta.2020.120801.

(48) Emaminejad, S.; Gao, W.; Wu, E.; Davies, Z. A.; Yin Yin Nyein, H.; Challa, S.; Ryan, S. P.; Fahad, H. M.; Chen, K.; Shahpar, Z.; Talebi, S.; Milla, C.; Javey, A.; Davis, R. W. Autonomous Sweat Extraction and Analysis Applied to Cystic Fibrosis and Glucose Monitoring Using a Fully Integrated Wearable Platform. *Proceedings of the National Academy of Sciences of the United States of America* **2017**, *114* (18), 4625–4630. https://doi.org/10.1073/pnas.1701740114.

(49) Francis, J.; Stamper, I.; Heikenfeld, J.; Gomez, E. F. Digital Nanoliter to Milliliter Flow Rate Sensor with in Vivo Demonstration for Continuous Sweat Rate Measurement. *Lab on a Chip* **2018**, *19* (1), 178–185. https://doi.org/10.1039/C8LC00968F.

(50) Zhao, F. J.; Bonmarin, M.; Chen, Z. C.; Larson, M.; Fay, D.; Runnoe, D.; Heikenfeld, J. Ultra-Simple Wearable Local Sweat Volume Monitoring Patch Based on Swellable Hydrogels. *Lab on a Chip* **2019**, *20* (1), 168–174. https://doi.org/10.1039/C9LC00911F.

(51) Katseli, V.; Economou, A.; Kokkinos, C. Smartphone-Addressable 3D-Printed Electrochemical Ring for Nonenzymatic Self-Monitoring of Glucose in Human Sweat. *Analytical Chemistry* **2021**, *93* (7), 3331–3336. https://doi.org/10.1021/acs.analchem.0c05057.

(52) Liu, H.; Qing, H.; Li, Z.; Han, Y. L.; Lin, M.; Yang, H.; Li, A.; Lu, T. J.; Li, F.; Xu, F. Paper: A Promising Material for Human-Friendly Functional Wearable Electronics. *Materials Science and Engineering: R: Reports* **2017**, *112*, 1–22. https://doi.org/10.1016/j.mser.2017.01.001.

(53) Zhao, Y.; Zhai, Q.; Dong, D.; An, T.; Gong, S.; Shi, Q.; Cheng, W. Highly Stretchable and Strain-Insensitive Fiber-Based Wearable Electrochemical Biosensor to Monitor Glucose in the Sweat. *Analytical Chemistry* **2019**, *91* (10), 6569–6576. https://doi.org/10.1021/acs.analchem.9b00152.

(54) Huang, X.; Liu, Y.; Chen, K.; Shin, W.-J.; Lu, C.-J.; Kong, G.-W.; Patnaik, D.; Lee, S.-H.; Cortes, J. F.; Rogers, J. A. Stretchable, Wireless Sensors and Functional Substrates for Epidermal Characterization of Sweat. *Small* **2014**, *10* (15), 3083–3090. https://doi.org/10.1002/smll.201400483.

(55) Shu, Y.; Su, T.; Lu, Q.; Shang, Z.; Xu, Q.; Hu, X. Highly Stretchable Wearable Electrochemical Sensor Based on Ni-Co MOF Nanosheet-Decorated Ag/rGO/PU Fiber for Continuous Sweat Glucose Detection. *Analytical Chemistry* **2021**, *93* (48), 16222–16230. https://doi.org/10.1021/acs.analchem.1c04106.

(56) Baker, L. B.; De Chavez, P. J. D.; Ungaro, C. T.; Sopeña, B. C.; Nuccio, R. P.; Reimel, A. J.; Barnes, K. A. Exercise Intensity Effects on Total Sweat Electrolyte Losses and Regional vs. Whole-Body Sweat [Na+], [Cl-], and [K+]. *European Journal of Applied Physiology* **2019**, *119* (2), 361–375. https://doi.org/10.1007/s00421-018-4048-z.

(57) Lee, H.; Song, C.; Hong, Y. S.; Kim, M.; Cho, H. R.; Kang, T.; Shin, K.; Choi, S. H.; Hyeon, T.; Kim, D.-H. Wearable/Disposable Sweat-Based Glucose Monitoring Device with Multistage Transdermal Drug Delivery Module. *Science Advances* **2017**, *3* (3), e1601314. https://doi.org/10.1126/sciadv.1601314.

(58) Tang, W.; Yin, L.; Sempionatto, J. R.; Moon, J.-M.; Teymourian, H.; Wang, J. Touch-Based Stressless Cortisol Sensing. *Advanced Materials* **2021**, *33* (18), 2008465. https://doi.org/10.1002/adma.202008465.

(59) Ichimura, Y.; Kuritsubo, T.; Nagamine, K.; Nomura, A.; Shitanda, I.; Tokito, S. A Fully Screen-Printed Potentiometric Chloride Ion Sensor Employing a Hydrogel-Based Touchpad for Simple and Non-Invasive Daily Electrolyte Analysis. *Analytical and Bioanalytical Chemistry* **2021**, *413* (7), 1883–1891. https://doi.org/10.1007/s00216-021-03156-3.

(60) Nagamine, K.; Mano, T.; Nomura, A.; Ichimura, Y.; Izawa, R.; Furusawa, H.; Matsui, H.; Kumaki, D.; Tokito, S. Noninvasive Sweat-Lactate Biosensor Emplsoying a Hydrogel-Based Touch Pad. *Scientific Reports* **2019**, *9* (1), 10102. https://doi.org/10.1038/s41598-019-46611-z.

(61) Wang, S.; Wu, Y.; Gu, Y.; Li, T.; Luo, H.; Li, L.-H.; Bai, Y.; Li, L.; Liu, L.; Cao, Y.; Ding, H.; Zhang, T. Wearable Sweatband Sensor Platform Based on Gold Nanodendrite Array as Efficient Solid Contact of Ion-Selective Electrode. *Analytical Chemistry* **2017**, *89* (19), 10224–10231. https://doi.org/10.1021/acs.analchem.7b01560.

(62) Heikenfeld, J. Non-Invasive Analyte Access and Sensing through Eccrine Sweat: Challenges and Outlook circa 2016. *Electroanalysis* **2016**, *28* (6), 1242–1249. https://doi.org/10.1002/elan.201600018.

(63) Twine, N. B.; Norton, R. M.; Brothers, M. C.; Hauke, A.; Gomez, E. F.; Heikenfeld, J. Open Nanofluidic Films with Rapid Transport and No Analyte Exchange for Ultra-Low Sample Volumes. *Lab on a Chip* **2018**, *18* (18), 2816–2825. https://doi.org/10.1039/C8LC00186C.

(64) Rebouillat, S.; Pla, F. State of the Art Manufacturing and Engineering of Nanocellulose: A Review of Available Data and Industrial Applications. *Journal of Biomaterials and Nanobiotechnology* **2013**, *4* (2), 165–188. https://doi.org/10.4236/jbnb.2013.42022.

(65) Sen, S.; Martin, J. D.; Argyropoulos, D. S. Review of Cellulose Non-Derivatizing Solvent Interactions with Emphasis on Activity in Inorganic Molten Salt Hydrates. *ACS Sustainable Chemistry & Engineering* **2013**, *1* (8), 858–870. https://doi.org/10.1021/sc400085a.

(66) Yang, Y.; Song, Y.; Bo, X.; Min, J.; Pak, O. S.; Zhu, L.; Wang, M.; Tu, J.; Kogan, A.; Zhang, H.; Hsiai, T. K.; Li, Z.; Gao, W. A Laser-Engraved Wearable Sensor for Sensitive Detection of Uric Acid and Tyrosine in Sweat. *Nature Biotechnology* **2020**, *38* (2), 217–224. https://doi.org/10.1038/s41587-019-0321-x.

(67) Wang, M.; Yang, Y.; Min, J.; Song, Y.; Tu, J.; Mukasa, D.; Ye, C.; Xu, C.; Heflin, N.; McCune, J. S.; Hsiai, T. K.; Li, Z.; Gao, W. A Wearable Electrochemical Biosensor for the Monitoring of Metabolites and Nutrients. *Nature Biomedical Engineering* **2022**, 1–11. https://doi.org/10.1038/s41551-022-00916-z.

(68) Riedl, B.; Nischik, M.; Birklein, F.; Neundörfer, B.; Handwerker, H. O. Spatial Extension of Sudomotor Axon Reflex Sweating in Human Skin. *Journal of the Autonomic Nervous System* **1998**, *69* (2–3), 83–88. https://doi.org/10.1016/S0165-1838(98)00016-2.

(69) Kim, J.; Jeerapan, I.; Imani, S.; Cho, T. N.; Bandodkar, A.; Cinti, S.; Mercier, P. P.; Wang, J. Noninvasive Alcohol Monitoring Using a Wearable Tattoo-Based Iontophoretic-Biosensing System. *ACS Sensors* **2016**, *1* (8), 1011–1019. https://doi.org/10.1021/acssensors.6b00356.

(70) Emaminejad, S.; Gao, W.; Wu, E.; Davies, Z. A.; Yin Yin Nyein, H.; Challa, S.; Ryan, S. P.; Fahad, H. M.; Chen, K.; Shahpar, Z.; Talebi, S.; Milla, C.; Javey, A.; Davis, R. W. Autonomous Sweat Extraction and Analysis Applied to Cystic Fibrosis and Glucose Monitoring Using a Fully Integrated Wearable Platform. *Proceedings of the National Academy of Sciences of the United States of America* **2017**, *114* (18), 4625–4630. https://doi.org/10.1073/pnas.1701740114.

(71) Sempionatto, J. R.; Lin, M.; Yin, L.; De la paz, E.; Pei, K.; Sonsa-ard, T.; de Loyola Silva, A. N.; Khorshed, A. A.; Zhang, F.; Tostado, N.; Xu, S.; Wang, J. An Epidermal Patch for the Simultaneous Monitoring of Haemodynamic and Metabolic

Biomarkers. *Nature Biomedical Engineering* **2021**. https://doi.org/10.1038/s41551-021-00685-1.

(72) Jajack, A.; Brothers, M.; Kasting, G.; Heikenfeld, J. Enhancing Glucose Flux into Sweat by Increasing Paracellular Permeability of the Sweat Gland. *PLoS ONE* **2018**, *13* (7), e0200009. https://doi.org/10.1371/journal.pone.0200009.

(73) Sempionatto, J. R.; Lasalde-Ramírez, J. A.; Mahato, K.; Wang, J.; Gao, W. Wearable Chemical Sensors for Biomarker Discovery in the Omics Era. *Nature Reviews Chemistry* **2022**. https://doi.org/10.1038/s41570-022-00439-w.

(74) Baker, L. B.; Barnes, K. A.; Anderson, M. L.; Passe, D. H.; Stofan, J. R. Normative Data for Regional Sweat Sodium Concentration and Whole-Body Sweating Rate in Athletes. *Journal of Sports Sciences* **2016**, *34* (4), 358–368. https://doi.org/10.1080/02640414.2015.1055291.

(75) Bulmer, M. G.; Forwell, G. D. The Concentration of Sodium in Thermal Sweat. *The Journal of Physiology* **1956**, *132* (1), 115–122. https://doi.org/10.1113/jphysiol.1956.sp005506.

(76) Baker, L. B.; Ungaro, C. T.; Sopeña, B. C.; Nuccio, R. P.; Reimel, A. J.; Carter, J. M.; Stofan, J. R.; Barnes, K. A. Body Map of Regional vs. Whole Body Sweating Rate and Sweat Electrolyte Concentrations in Men and Women during Moderate Exercise-Heat Stress. *Journal of Applied Physiology* **2018**, *124* (5), 1304–1318. https://doi.org/10.1152/japplphysiol.00867.2017.

(77) Baker, L. B.; Stofan, J. R.; Hamilton, A. A.; Horswill, C. A. Comparison of Regional Patch Collection vs. Whole Body Washdown for Measuring Sweat Sodium and Potassium Loss during Exercise. *Journal of Applied Physiology* **2009**, *107* (3), 887–895. https://doi.org/10.1152/japplphysiol.00197.2009.

(78) Sato, K.; Kang, W. H.; Saga, K.; Sato, K. T. Biology of Sweat Glands and Their Disorders. I. Normal Sweat Gland Function. *Journal of the American Academy of Dermatology* **1989**, *20* (4), 537–563. https://doi.org/10.1016/S0190-9622(89)70063-3.

(79) Sato, K. *Reviews of Physiology, Biochemistry and Pharmacology, Volume 79*; Reviews of Physiology, Biochemistry and Pharmacology; Springer-Verlag Springer e-books: Berlin, Heidelberg, 2005.

(80) Czarnowski, D.; Górski, J.; Jóźwiuk, J.; Boroń-Kaczmarska, A. Plasma Ammonia Is the Principal Source of Ammonia in Sweat. *European Journal of Applied Physiology* **1992**, *65* (2), 135–137. https://doi.org/10.1007/BF00705070.

(81) Goodwin, M. L.; Harris, J. E.; Hernández, A.; Gladden, L. B. Blood Lactate Measurements and Analysis during Exercise: A Guide for Clinicians. *Journal of Diabetes Science and Technology* **2007**, *1* (4), 558–569. https://doi.org/10.1177/193229680700100414.

(82) Green, J. M.; Bishop, P. A.; Muir, I. H.; McLester Jr, J. R.; Heath, H. E. Effects of High and Low Blood Lactate Concentrations on Sweat Lactate Response. *International Journal of Sports Medicine* **2000**, *21* (8), 556–560. https://doi.org/10.1055/s-2000-8483.

(83) Fellmann, N.; Grizard, G.; Coudert, J. Human Frontal Sweat Rate and Lactate Concentration during Heat Exposure and Exercise. *Journal of Applied Physiology* **1983**, *54* (2), 355–360. https://doi.org/10.1152/jappl.1983.54.2.355.

(84) Derbyshire, P. J.; Barr, H.; Davis, F.; Higson, S. P. J. Lactate in Human Sweat: A Critical Review of Research to the Present Day. *The Journal of Physiological Sciences* **2012**, *62* (6), 429–440. https://doi.org/10.1007/s12576-012-0213-z.

(85) Sakharov, D. A.; Shkurnikov, M. U.; Vagin, M. Yu.; Yashina, E. I.; Karyakin, A. A.; Tonevitsky, A. G. Relationship between Lactate Concentrations in Active Muscle Sweat and Whole Blood. *Bulletin of Experimental Biology and Medicine* **2010**, *150* (1), 83–85. https://doi.org/10.1007/s10517-010-1075-0.

(86) Green, J. M.; Pritchett, R. C.; Crews, T. R.; McLester, J. R.; Tucker, D. C. Sweat Lactate Response between Males with High and Low Aerobic Fitness. *European Journal of Applied Physiology* **2004**, *91* (1), 1–6. https://doi.org/10.1007/s00421-003-0968-2.

(87) Alvear-Ordenes, I.; García-López, D.; De Paz, J. A.; González-Gallego, J. Sweat Lactate, Ammonia, and Urea in Rugby Players. *International Journal of Sports Medicine* **2005**, *26* (8), 632–637. https://doi.org/10.1055/s-2004-830380.

(88) Buono, M. J.; Lee, N. V. L.; Miller, P. W. The Relationship between Exercise Intensity and the Sweat Lactate Excretion Rate. *The Journal of Physiological Sciences* **2010**, *60* (2), 103–107. https://doi.org/10.1007/s12576-009-0073-3.

(89) Moyer, J.; Wilson, D.; Finkelshtein, I.; Wong, B.; Potts, R. Correlation Between Sweat Glucose and Blood Glucose in Subjects with Diabetes. *Diabetes Technology & Therapeutics* **2012**, *14* (5), 398–402. https://doi.org/10.1089/dia.2011.0262.

(90) Boysen, T. C.; Yanagawa, S.; Sato, F.; Sato, K. A Modified Anaerobic Method of Sweat Collection. *Journal of Applied Physiology* **1984**, *56* (5), 1302–1307. https://doi.org/10.1152/jappl.1984.56.5.1302.

(91) Sakaguchi, K.; Hirota, Y.; Hashimoto, N.; Ogawa, W.; Hamaguchi, T.; Matsuo, T.; Miyagawa, J.-I.; Namba, M.; Sato, T.; Okada, S.; Tomita, K.; Matsuhisa, M.; Kaneto, H.; Kosugi, K.; Maegawa, H.; Nakajima, H.; Kashiwagi, A. Evaluation of a Minimally Invasive System for Measuring Glucose Area under the Curve during Oral Glucose Tolerance Tests: Usefulness of Sweat Monitoring for Precise Measurement. *Journal of Diabetes Science and Technology* **2013**, *7* (3), 678–688. https://doi.org/10.1177/193229681300700313.

(92) Czarnowski, D.; Górski, J. [Excretion of nitrogen compounds in sweat during a sauna]. *Polski Tygodnik Lekarski* **1991**, *46* (8–10), 186–187.

(93) Huang, C.-T.; Chen, M.-L.; Huang, L.-L.; Mao, I.-F. Uric Acid and Urea in Human Sweat. *Chinese Journal of Physiology* **2002**, *45* (3), 109–115.

(94) Al-Tamer, Y. Y.; Hadi, E. A.; Al-Badrani, I. eldin I. Sweat Urea, Uric Acid and Creatinine Concentrations in Uraemic Patients. *Urological Research* **1997**, *25* (5), 337–340. https://doi.org/10.1007/BF01294662.

(95) Ford, E. S.; Li, C.; Cook, S.; Choi, H. K. Serum Concentrations of Uric Acid and the Metabolic Syndrome Among US Children and Adolescents. *Circulation* **2007**, *115* (19), 2526–2532. https://doi.org/10.1161/CIRCULATIONAHA.106.657627.

(96) Zhang, Y.; Guo, H.; Kim, S. B.; Wu, Y.; Ostojich, D.; Park, S. H.; Wang, X.; Weng, Z.; Li, R.; Bandodkar, A. J.; Sekine, Y.; Choi, J.; Xu, S.; Quaggin, S.; Ghaffari, R.; Rogers, J. A. Passive Sweat Collection and Colorimetric Analysis of Biomarkers Relevant to Kidney Disorders Using a Soft Microfluidic System. *Lab on a Chip* **2019**, *19* (9), 1545–1555. https://doi.org/10.1039/C9LC00103D.

(97) Baker, L. B.; Stofan, J. R.; Lukaski, H. C.; Horswill, C. A. Exercise-Induced Trace Mineral Element Concentration in Regional Versus Whole-Body Wash-Down Sweat. *International Journal of Sport Nutrition and Exercise Metabolism* **2011**, *21* (3), 233–239. https://doi.org/10.1123/ijsnem.21.3.233.

(98) Montain, S. J.; Cheuvront, S. N.; Lukaski, H. C. Sweat Mineral-Element Responses during 7 h of Exercise-Heat Stress. *International Journal of Sport Nutrition and Exercise Metabolism* **2007**, *17* (6), 574–582. https://doi.org/10.1123/ijsnem.17.6.574.

(99) Chinevere, T. D.; Kenefick, R. W.; Cheuvront, S. N.; Lukaski, H. C.; Sawka, M. N. Effect of Heat Acclimation on Sweat Minerals. *Medicine & Science in Sports & Exercise* **2008**, *40* (5), 886–891. https://doi.org/10.1249/MSS.0b013e3181641c04.

(100) Ely, M. R.; Kenefick, R. W.; Cheuvront, S. N.; Chinevere, T. D.; Lacher, C. P.; Lukaski, H. C.; Montain, S. J. Surface Contamination Artificially Elevates Initial Sweat Mineral Concentrations. *Journal of Applied Physiology* **2011**, *110* (6), 1534–1540. https://doi.org/10.1152/japplphysiol.01437.2010.

(101) Hadorn, B.; Hanimann, F.; Anders, P.; Curtius, H.-C.; Halverson, R. Free Amino-Acids in Human Sweat from Different Parts of the Body. *Nature* **1967**, *215* (5099), 416–417. https://doi.org/10.1038/215416a0.

(102) Hier, S. W.; Cornbleet, T.; Bergeim, O. The Amino Acids of Human Sweat. *Journal of Biological Chemistry* **1946**, *166* (1), 327–333.

(103) Harvey, C. J.; LeBouf, R. F.; Stefaniak, A. B. Formulation and Stability of a Novel Artificial Human Sweat under Conditions of Storage and Use. *Toxicology in Vitro* **2010**, *24* (6), 1790–1796. https://doi.org/10.1016/j.tiv.2010.06.016.

(104) Zhao, J.; Nyein, H. Y. Y.; Hou, L.; Lin, Y.; Bariya, M.; Ahn, C. H.; Ji, W.; Fan, Z.; Javey, A. A Wearable Nutrition Tracker. *Advanced Materials* **2021**, *33* (1), 2006444. https://doi.org/10.1002/adma.202006444.

(105) Shields, J. B.; Johnson, B. C.; Hamilton, T. S.; Mitchell, H. H. The Excretion of Ascorbic Acid and Dehydroascorbic Acid in Sweat and Urine Under Different Environmental Conditions. *Journal of Biological Chemistry* **1945**, *161* (1), 351–356. https://doi.org/10.1016/S0021-9258(17)41548-1.

(106) Wang, B.; Zhao, C.; Wang, Z.; Yang, K.-A.; Cheng, X.; Liu, W.; Yu, W.; Lin, S.; Zhao, Y.; Cheung, K. M.; Lin, H.; Hojaiji, H.; Weiss, P. S.; Stojanović, M. N.; Tomiyama, A. J.; Andrews, A. M.; Emaminejad, S. Wearable Aptamer-Field-Effect Transistor Sensing System for Noninvasive Cortisol Monitoring. *Science Advances* **2022**, *8* (1), eabk0967. https://doi.org/10.1126/sciadv.abk0967.

(107) Pearlmutter, P.; DeRose, G.; Samson, C.; Linehan, N.; Cen, Y.; Begdache, L.; Won, D.; Koh, A. Sweat and Saliva Cortisol Response to Stress and Nutrition Factors. *Scientific Reports* **2020**, *10* (1), 19050. https://doi.org/10.1038/s41598-020-75871-3.

(108) Torrente-Rodríguez, R. M.; Tu, J.; Yang, Y.; Min, J.; Wang, M.; Song, Y.; Yu, Y.; Xu, C.; Ye, C.; IsHak, W. W.; Gao, W. Investigation of Cortisol Dynamics in Human Sweat Using a Graphene-Based Wireless mHealth System. *Matter* **2020**, *2* (4), 921–937. https://doi.org/10.1016/j.matt.2020.01.021.

(109) Martin, A.; Saathoff, M.; Kuhn, F.; Max, H.; Terstegen, L.; Natsch, A. A Functional ABCC11 Allele Is Essential in the Biochemical Formation of Human Axillary Odor.

Journal of Investigative Dermatology **2010**, *130* (2), 529–540. https://doi.org/10.1038/jid.2009.254.

(110) Cizza, G.; Marques, A. H.; Eskandari, F.; Christie, I. C.; Torvik, S.; Silverman, M. N.; Phillips, T. M.; Sternberg, E. M. Elevated Neuroimmune Biomarkers in Sweat Patches and Plasma of Premenopausal Women with Major Depressive Disorder in Remission: The POWER Study. *Biological Psychiatry* **2008**, *64* (10), 907–911. https://doi.org/10.1016/j.biopsych.2008.05.035.

(111) Marques-Deak, A.; Cizza, G.; Eskandari, F.; Torvik, S.; Christie, I. C.; Sternberg, E. M.; Phillips, T. M. Measurement of Cytokines in Sweat Patches and Plasma in Healthy Women: Validation in a Controlled Study. *Journal of Immunological Methods* **2006**, *315* (1–2), 99–109. https://doi.org/10.1016/j.jim.2006.07.011.

(112) Jones, A. P.; Webb, L. M. C.; Anderson, A. O.; Leonardo, E. J.; Rot, A. Normal Human Sweat Contains Interleukin-8. *Journal of Leukocyte Biology* **1995**, *57* (3), 434–437. https://doi.org/10.1002/jlb.57.3.434.

(113) Buono, M. J. Sweat Ethanol Concentrations Are Highly Correlated with Co-Existing Blood Values in Humans. *Experimental Physiology* **1999**, *84* (2), 401–404.

(114) Lin, S.; Yu, W.; Wang, B.; Zhao, Y.; En, K.; Zhu, J.; Cheng, X.; Zhou, C.; Lin, H.; Wang, Z.; Hojaiji, H.; Yeung, C.; Milla, C.; Davis, R. W.; Emaminejad, S. Noninvasive Wearable Electroactive Pharmaceutical Monitoring for Personalized Therapeutics. *Proceedings of the National Academy of Sciences* **2020**, *117* (32), 19017–19025. https://doi.org/10.1073/pnas.2009979117.

(115) Tsunoda, M.; Hirayama, M.; Tsuda, T.; Ohno, K. Noninvasive Monitoring of Plasma L-Dopa Concentrations Using Sweat Samples in Parkinson's Disease. *Clinica Chimica Acta* **2015**, *442*, 52–55. https://doi.org/10.1016/j.cca.2014.12.032.

(116) Trumbo, P.; Schlicker, S.; Yates, A. A.; Poos, M. Dietary Reference Intakes for Energy, Carbohydrate, Fiber, Fat, Fatty Acids, Cholesterol, Protein and Amino Acids. *Journal of the American Dietetic Association* **2002**, *102* (11), 1621–1630. https://doi.org/10.1016/S0002-8223(02)90346-9.

(117) Wu, G. Amino Acids: Metabolism, Functions, and Nutrition. *Amino Acids* **2009**, *37* (1), 1–17. https://doi.org/10.1007/s00726-009-0269-0.

(118) Lynch, C. J.; Adams, S. H. Branched-Chain Amino Acids in Metabolic Signalling and Insulin Resistance. *Nature Reviews Endocrinology* **2014**, *10* (12), 723–736. https://doi.org/10.1038/nrendo.2014.171.

(119) Wang, T. J.; Larson, M. G.; Vasan, R. S.; Cheng, S.; Rhee, E. P.; McCabe, E.; Lewis, G. D.; Fox, C. S.; Jacques, P. F.; Fernandez, C.; O'Donnell, C. J.; Carr, S. A.; Mootha, V. K.; Florez, J. C.; Souza, A.; Melander, O.; Clish, C. B.; Gerszten, R. E. Metabolite Profiles and the Risk of Developing Diabetes. *Nature Medicine* **2011**, *17* (4), 448–453. https://doi.org/10.1038/nm.2307.

(120) Mayers, J. R.; Wu, C.; Clish, C. B.; Kraft, P.; Torrence, M. E.; Fiske, B. P.; Yuan, C.; Bao, Y.; Townsend, M. K.; Tworoger, S. S.; Davidson, S. M.; Papagiannakopoulos, T.; Yang, A.; Dayton, T. L.; Ogino, S.; Stampfer, M. J.; Giovannucci, E. L.; Qian, Z. R.; Rubinson, D. A.; Ma, J.; Sesso, H. D.; Gaziano, J. M.; Cochrane, B. B.; Liu, S.; Wactawski-Wende, J.; Manson, J. E.; Pollak, M. N.; Kimmelman, A. C.; Souza, A.; Pierce, K.; Wang, T. J.; Gerszten, R. E.; Fuchs, C. S.; Vander Heiden, M. G.; Wolpin, B. M. Elevation of Circulating Branched-Chain

Amino Acids Is an Early Event in Human Pancreatic Adenocarcinoma Development. *Nature Medicine* **2014**, *20* (10), 1193–1198. https://doi.org/10.1038/nm.3686.

(121) Kau, A. L.; Ahern, P. P.; Griffin, N. W.; Goodman, A. L.; Gordon, J. I. Human Nutrition, the Gut Microbiome and the Immune System. *Nature* **2011**, *474* (7351), 327–336. https://doi.org/10.1038/nature10213.

(122) Fernstrom, J. D.; Wurtman, R. J. Brain Serotonin Content: Physiological Dependence on Plasma Tryptophan Levels. *Science* **1971**, *173* (3992), 149–152. https://doi.org/10.1126/science.173.3992.149.

(123) Fernstrom, J. D.; Fernstrom, M. H. Tyrosine, Phenylalanine, and Catecholamine Synthesis and Function in the Brain. *The Journal of Nutrition* **2007**, *137* (6), 1539S-1547S. https://doi.org/10.1093/jn/137.6.1539S.

(124) Dierckx, T.; van Elslande, J.; Salmela, H.; Decru, B.; Wauters, E.; Gunst, J.; Van Herck, Y.; the CONTAGIOUS-consortium; Wauters, J.; Stessel, B.; Vermeersch, P. *The Metabolic Fingerprint of COVID-19 Severity*; preprint; Infectious Diseases (except HIV/AIDS), 2020. https://doi.org/10.1101/2020.11.09.20228221.

(125) Grant, W. B.; Lahore, H.; McDonnell, S. L.; Baggerly, C. A.; French, C. B.; Aliano, J. L.; Bhattoa, H. P. Evidence That Vitamin D Supplementation Could Reduce Risk of Influenza and COVID-19 Infections and Deaths. *Nutrients* **2020**, *12* (4), 988. https://doi.org/10.3390/nu12040988.

(126) Belanger, M. J.; Hill, M. A.; Angelidi, A. M.; Dalamaga, M.; Sowers, J. R.; Mantzoros, C. S. Covid-19 and Disparities in Nutrition and Obesity. *The New England Journal of Medicine* **2020**, *383* (11), e69. https://doi.org/10.1056/NEJMp2021264.

(127) Stefan, N.; Birkenfeld, A. L.; Schulze, M. B. Global Pandemics Interconnected — Obesity, Impaired Metabolic Health and COVID-19. *Nature Reviews Endocrinology* **2021**, *17* (3), 135–149. https://doi.org/10.1038/s41574-020-00462-1.

(128) Wang, J. Electrochemical Biosensors: Towards Point-of-Care Cancer Diagnostics. *Biosensors and Bioelectronics* **2006**, *21* (10), 1887–1892. https://doi.org/10.1016/j.bios.2005.10.027.

(129) Uzun, L.; Turner, A. P. Molecularly-Imprinted Polymer Sensors: Realising Their Potential. *Biosensors and Bioelectronics* **2016**, *76*, 131–144. https://doi.org/10.1016/j.bios.2015.07.013.

(130) Parlak, O.; Keene, S. T.; Marais, A.; Curto, V. F.; Salleo, A. Molecularly Selective Nanoporous Membrane-Based Wearable Organic Electrochemical Device for Noninvasive Cortisol Sensing. *Science Advances* **2018**, *4* (7), eaar2904. https://doi.org/10.1126/sciadv.aar2904.

(131) Newsholme, E. A.; Blomstrand, E. Branched-Chain Amino Acids and Central Fatigue. *The Journal of Nutrition* **2006**, *136* (1), 274S-276S. https://doi.org/10.1093/jn/136.1.274S.

(132) Zuker, M. Mfold Web Server for Nucleic Acid Folding and Hybridization Prediction. *Nucleic Acids Research* **2003**, *31* (13), 3406–3415. https://doi.org/10.1093/nar/gkg595.

(133) Rangel, A. E.; Hariri, A. A.; Eisenstein, M.; Soh, H. T. Engineering Aptamer Switches for Multifunctional Stimulus-Responsive Nanosystems. *Advanced Materials* **2020**, *32* (50), 2003704. https://doi.org/10.1002/adma.202003704.
(134) Pandey, R.; Chang, D.; Smieja, M.; Hoare, T.; Li, Y.; Soleymani, L. Integrating Programmable DNAzymes with Electrical Readout for Rapid and Culture-Free Bacterial Detection Using a Handheld Platform. *Nature Chemistry* **2021**, *13* (9), 895–901. https://doi.org/10.1038/s41557-021-00718-x.
(135) Chenault, J. R.; Thatcher, W. W.; Kalra, P. S.; Abrams, R. M.; Wilcox, C. J. Transitory Changes in Plasma Progestins, Estradiol, and Luteinizing Hormone Approaching Ovulation in the Bovine. *Journal of Dairy Science* **1975**, *58* (5), 709–717. https://doi.org/10.3168/jds.S0022-0302(75)84632-7.
(136) Kim, J.; Jeerapan, I.; Imani, S.; Cho, T. N.; Bandodkar, A.; Cinti, S.; Mercier, P. P.; Wang, J. Noninvasive Alcohol Monitoring Using a Wearable Tattoo-Based Iontophoretic-Biosensing System. *ACS Sensors* **2016**, *1* (8), 1011–1019. https://doi.org/10.1021/acssensors.6b00356.
(137) Oh, S. Y.; Guy, R. H. Effects of Iontophoresis on the Electrical Properties of Human Skin in Vivo. *International Journal of Pharmaceutics* **1995**, *124* (1), 137–142. https://doi.org/10.1016/0378-5173(95)00180-Q.
(138) Ma, D.; Ghoreishizadeh, S. S.; Georgiou, P. Concurrent Potentiometric and Amperometric Sensing With Shared Reference Electrodes. *IEEE Sensors Journal* **2021**, *21* (5), 5720–5727. https://doi.org/10.1109/JSEN.2020.3039567.
(139) Talkhooncheh, A. H.; Yu, Y.; Agarwal, A.; Kuo, W. W.-T.; Chen, K.-C.; Wang, M.; Hoskuldsdottir, G.; Gao, W.; Emami, A. A Biofuel-Cell-Based Energy Harvester With 86% Peak Efficiency and 0.25-V Minimum Input Voltage Using Source-Adaptive MPPT. *IEEE Journal of Solid-State Circuits* **2021**, *56* (3), 715–728. https://doi.org/10.1109/JSSC.2020.3035491.
(140) Kang, D. H. P.; Chen, M.; Ogunseitan, O. A. Potential Environmental and Human Health Impacts of Rechargeable Lithium Batteries in Electronic Waste. *Environmental Science & Technology* **2013**, *47* (10), 5495–5503. https://doi.org/10.1021/es400614y.
(141) Bariya, M.; Nyein, H. Y. Y.; Javey, A. Wearable Sweat Sensors. *Nature Electronics* **2018**, *1* (3), 160–171. https://doi.org/10.1038/s41928-018-0043-y.
(142) He, W.; Wang, C.; Wang, H.; Jian, M.; Lu, W.; Liang, X.; Zhang, X.; Yang, F.; Zhang, Y. Integrated Textile Sensor Patch for Real-Time and Multiplex Sweat Analysis. *Science Advances* **2019**, *5* (11), eaax0649. https://doi.org/10.1126/sciadv.aax0649.
(143) Zamarayeva, A. M.; Ostfeld, A. E.; Wang, M.; Duey, J. K.; Deckman, I.; Lechêne, B. P.; Davies, G.; Steingart, D. A.; Arias, A. C. Flexible and Stretchable Power Sources for Wearable Electronics. *Science Advances* **2017**, *3* (6), e1602051. https://doi.org/10.1126/sciadv.1602051.
(144) Li, J.; Zhao, J.; Rogers, J. A. Materials and Designs for Power Supply Systems in Skin-Interfaced Electronics. *Accounts of Chemical Research* **2019**, *52* (1), 53–62. https://doi.org/10.1021/acs.accounts.8b00486.
(145) Bandodkar, A. J.; Gutruf, P.; Choi, J.; Lee, K.; Sekine, Y.; Reeder, J. T.; Jeang, W. J.; Aranyosi, A. J.; Lee, S. P.; Model, J. B.; Ghaffari, R.; Su, C.-J.; Leshock, J. P.;

Ray, T.; Verrillo, A.; Thomas, K.; Krishnamurthi, V.; Han, S.; Kim, J.; Krishnan, S.; Hang, T.; Rogers, J. A. Battery-Free, Skin-Interfaced Microfluidic/Electronic Systems for Simultaneous Electrochemical, Colorimetric, and Volumetric Analysis of Sweat. *Science Advances* **2019**, *5* (1), eaav3294. https://doi.org/10.1126/sciadv.aav3294.

(146) Reeder, J. T.; Choi, J.; Xue, Y.; Gutruf, P.; Hanson, J.; Liu, M.; Ray, T.; Bandodkar, A. J.; Avila, R.; Xia, W.; Krishnan, S.; Xu, S.; Barnes, K.; Pahnke, M.; Ghaffari, R.; Huang, Y.; Rogers, J. A. Waterproof, Electronics-Enabled, Epidermal Microfluidic Devices for Sweat Collection, Biomarker Analysis, and Thermography in Aquatic Settings. *Science Advances* **2019**, *5* (1), eaau6356. https://doi.org/10.1126/sciadv.aau6356.

(147) Zhao, J.; Lin, Y.; Wu, J.; Nyein, H. Y. Y.; Bariya, M.; Tai, L.-C.; Chao, M.; Ji, W.; Zhang, G.; Fan, Z.; Javey, A. A Fully Integrated and Self-Powered Smartwatch for Continuous Sweat Glucose Monitoring. *ACS Sensors* **2019**, *4* (7), 1925–1933. https://doi.org/10.1021/acssensors.9b00891.

(148) Park, S.; Heo, S. W.; Lee, W.; Inoue, D.; Jiang, Z.; Yu, K.; Jinno, H.; Hashizume, D.; Sekino, M.; Yokota, T.; Fukuda, K.; Tajima, K.; Someya, T. Self-Powered Ultra-Flexible Electronics via Nano-Grating-Patterned Organic Photovoltaics. *Nature* **2018**, *561* (7724), 516–521. https://doi.org/10.1038/s41586-018-0536-x.

(149) Chen, G.; Li, Y.; Bick, M.; Chen, J. Smart Textiles for Electricity Generation. *Chemical Reviews* **2020**, *120* (8), 3668–3720. https://doi.org/10.1021/acs.chemrev.9b00821.

(150) Bandodkar, A. J.; You, J.-M.; Kim, N.-H.; Gu, Y.; Kumar, R.; Mohan, A. M. V.; Kurniawan, J.; Imani, S.; Nakagawa, T.; Parish, B.; Parthasarathy, M.; Mercier, P. P.; Xu, S.; Wang, J. Soft, Stretchable, High Power Density Electronic Skin-Based Biofuel Cells for Scavenging Energy from Human Sweat. *Energy & Environmental Science* **2017**, *10* (7), 1581–1589. https://doi.org/10.1039/C7EE00865A.

(151) Fan, F.-R.; Tian, Z.-Q.; Lin Wang, Z. Flexible Triboelectric Generator. *Nano Energy* **2012**, *1* (2), 328–334. https://doi.org/10.1016/j.nanoen.2012.01.004.

(152) Seung, W.; Gupta, M. K.; Lee, K. Y.; Shin, K.-S.; Lee, J.-H.; Kim, T. Y.; Kim, S.; Lin, J.; Kim, J. H.; Kim, S.-W. Nanopatterned Textile-Based Wearable Triboelectric Nanogenerator. *ACS Nano* **2015**, *9* (4), 3501–3509. https://doi.org/10.1021/nn507221f.

(153) Chen, J.; Huang, Y.; Zhang, N.; Zou, H.; Liu, R.; Tao, C.; Fan, X.; Wang, Z. L. Micro-Cable Structured Textile for Simultaneously Harvesting Solar and Mechanical Energy. *Nature Energy* **2016**, *1* (10), 16138. https://doi.org/10.1038/nenergy.2016.138.

(154) Wang, J.; Li, S.; Yi, F.; Zi, Y.; Lin, J.; Wang, X.; Xu, Y.; Wang, Z. L. Sustainably Powering Wearable Electronics Solely by Biomechanical Energy. *Nature Communications* **2016**, *7* (1), 12744. https://doi.org/10.1038/ncomms12744.

(155) Pu, X.; Liu, M.; Chen, X.; Sun, J.; Du, C.; Zhang, Y.; Zhai, J.; Hu, W.; Wang, Z. L. Ultrastretchable, Transparent Triboelectric Nanogenerator as Electronic Skin for Biomechanical Energy Harvesting and Tactile Sensing. *Science Advances* **2017**, *3* (5), e1700015. https://doi.org/10.1126/sciadv.1700015.

(156) Liu, D.; Yin, X.; Guo, H.; Zhou, L.; Li, X.; Zhang, C.; Wang, J.; Wang, Z. L. A Constant Current Triboelectric Nanogenerator Arising from Electrostatic Breakdown. *Science Advances* **2019**, *5* (4), eaav6437. https://doi.org/10.1126/sciadv.aav6437.

(157) Liu, Z.; Li, H.; Shi, B.; Fan, Y.; Wang, Z. L.; Li, Z. Wearable and Implantable Triboelectric Nanogenerators. *Advanced Functional Materials* **2019**, *29* (20), 1808820. https://doi.org/10.1002/adfm.201808820.

(158) Kwak, S. S.; Yoon, H.; Kim, S. Textile-Based Triboelectric Nanogenerators for Self-Powered Wearable Electronics. *Advanced Functional Materials* **2019**, *29* (2), 1804533. https://doi.org/10.1002/adfm.201804533.

(159) Chen, X.; Song, Y.; Su, Z.; Chen, H.; Cheng, X.; Zhang, J.; Han, M.; Zhang, H. Flexible Fiber-Based Hybrid Nanogenerator for Biomechanical Energy Harvesting and Physiological Monitoring. *Nano Energy* **2017**, *38*, 43–50. https://doi.org/10.1016/j.nanoen.2017.05.047.

(160) Song, Y.; Wang, H.; Cheng, X.; Li, G.; Chen, X.; Chen, H.; Miao, L.; Zhang, X.; Zhang, H. High-Efficiency Self-Charging Smart Bracelet for Portable Electronics. *Nano Energy* **2019**, *55*, 29–36. https://doi.org/10.1016/j.nanoen.2018.10.045.

(161) De Ruiter, C. J.; Verdijk, P. W. L.; Werker, W.; Zuidema, M. J.; De Haan, A. Stride Frequency in Relation to Oxygen Consumption in Experienced and Novice Runners. *European Journal of Sport Science* **2014**, *14* (3), 251–258. https://doi.org/10.1080/17461391.2013.783627.

(162) Kim, J.; Campbell, A. S.; de Ávila, B. E.-F.; Wang, J. Wearable Biosensors for Healthcare Monitoring. *Nature Biotechnology* **2019**, *37* (4), 389–406. https://doi.org/10.1038/s41587-019-0045-y.

(163) Ray, T. R.; Choi, J.; Bandodkar, A. J.; Krishnan, S.; Gutruf, P.; Tian, L.; Ghaffari, R.; Rogers, J. A. Bio-Integrated Wearable Systems: A Comprehensive Review. *Chem. Rev.* **2019**, *119* (8), 5461–5533. https://doi.org/10.1021/acs.chemrev.8b00573.

(164) Yang, Y.; Gao, W. Wearable and Flexible Electronics for Continuous Molecular Monitoring. *Chemical Society Reviews* **2019**, *48* (6), 1465–1491. https://doi.org/10.1039/C7CS00730B.

(165) Heikenfeld, J.; Jajack, A.; Feldman, B.; Granger, S. W.; Gaitonde, S.; Begtrup, G.; Katchman, B. A. Accessing Analytes in Biofluids for Peripheral Biochemical Monitoring. *Nature Biotechnology* **2019**, *37* (4), 407–419. https://doi.org/10.1038/s41587-019-0040-3.

(166) Libanori, A.; Chen, G.; Zhao, X.; Zhou, Y.; Chen, J. Smart Textiles for Personalized Healthcare. *Nature Electronics* **2022**, *5* (3), 142–156. https://doi.org/10.1038/s41928-022-00723-z.

(167) Someya, T.; Bao, Z.; Malliaras, G. G. The Rise of Plastic Bioelectronics. *Nature* **2016**, *540* (7633), 379–385. https://doi.org/10.1038/nature21004.

(168) Gao, W.; Emaminejad, S.; Nyein, H. Y. Y.; Challa, S.; Chen, K.; Peck, A.; Fahad, H. M.; Ota, H.; Shiraki, H.; Kiriya, D.; Lien, D.-H.; Brooks, G. A.; Davis, R. W.; Javey, A. Fully Integrated Wearable Sensor Arrays for Multiplexed in Situ Perspiration Analysis. *Nature* **2016**, *529* (7587), 509–514. https://doi.org/10.1038/nature16521.

(169) Choi, J.; Ghaffari, R.; Baker, L. B.; Rogers, J. A. Skin-Interfaced Systems for Sweat Collection and Analytics. *Science Advances* **2018**, *4* (2), eaar3921. https://doi.org/10.1126/sciadv.aar3921.

(170) Nyein, H. Y. Y.; Bariya, M.; Kivimäki, L.; Uusitalo, S.; Liaw, T. S.; Jansson, E.; Ahn, C. H.; Hangasky, J. A.; Zhao, J.; Lin, Y.; Happonen, T.; Chao, M.; Liedert, C.; Zhao, Y.; Tai, L.-C.; Hiltunen, J.; Javey, A. Regional and Correlative Sweat Analysis Using High-Throughput Microfluidic Sensing Patches toward Decoding Sweat. *Science Advances* **2019**, *5* (8), eaaw9906. https://doi.org/10.1126/sciadv.aaw9906.

(171) Kim, S.; Lee, B.; Reeder, J. T.; Seo, S. H.; Lee, S.-U.; Hourlier-Fargette, A.; Shin, J.; Sekine, Y.; Jeong, H.; Oh, Y. S.; Aranyosi, A. J.; Lee, S. P.; Model, J. B.; Lee, G.; Seo, M.-H.; Kwak, S. S.; Jo, S.; Park, G.; Han, S.; Park, I.; Jung, H.-I.; Ghaffari, R.; Koo, J.; Braun, P. V.; Rogers, J. A. Soft, Skin-Interfaced Microfluidic Systems with Integrated Immunoassays, Fluorometric Sensors, and Impedance Measurement Capabilities. *Proceedings of the National Academy of Sciences of the United States of America* **2020**, *117* (45), 27906–27915. https://doi.org/10.1073/pnas.2012700117.

(172) Son, D.; Lee, J.; Qiao, S.; Ghaffari, R.; Kim, J.; Lee, J. E.; Song, C.; Kim, S. J.; Lee, D. J.; Jun, S. W.; Yang, S.; Park, M.; Shin, J.; Do, K.; Lee, M.; Kang, K.; Hwang, C. S.; Lu, N.; Hyeon, T.; Kim, D.-H. Multifunctional Wearable Devices for Diagnosis and Therapy of Movement Disorders. *Nature Nanotechnology* **2014**, *9* (5), 397–404. https://doi.org/10.1038/nnano.2014.38.

(173) Niu, S.; Matsuhisa, N.; Beker, L.; Li, J.; Wang, S.; Wang, J.; Jiang, Y.; Yan, X.; Yun, Y.; Burnett, W.; Poon, A. S. Y.; Tok, J. B.-H.; Chen, X.; Bao, Z. A Wireless Body Area Sensor Network Based on Stretchable Passive Tags. *Nature Electronics* **2019**, *2* (8), 361–368. https://doi.org/10.1038/s41928-019-0286-2.

(174) Sempionatto, J. R.; Lin, M.; Yin, L.; De la paz, E.; Pei, K.; Sonsa-ard, T.; de Loyola Silva, A. N.; Khorshed, A. A.; Zhang, F.; Tostado, N.; Xu, S.; Wang, J. An Epidermal Patch for the Simultaneous Monitoring of Haemodynamic and Metabolic Biomarkers. *Nature Biomedical Engineering* **2021**, *5* (7), 737–748. https://doi.org/10.1038/s41551-021-00685-1.

(175) Emaminejad, S.; Gao, W.; Wu, E.; Davies, Z. A.; Yin Yin Nyein, H.; Challa, S.; Ryan, S. P.; Fahad, H. M.; Chen, K.; Shahpar, Z.; Talebi, S.; Milla, C.; Javey, A.; Davis, R. W. Autonomous Sweat Extraction and Analysis Applied to Cystic Fibrosis and Glucose Monitoring Using a Fully Integrated Wearable Platform. *Proceedings of the National Academy of Sciences of the United States of America* **2017**, *114* (18), 4625–4630. https://doi.org/10.1073/pnas.1701740114.

(176) Lee, H.; Song, C.; Hong, Y. S.; Kim, M. S.; Cho, H. R.; Kang, T.; Shin, K.; Choi, S. H.; Hyeon, T.; Kim, D.-H. Wearable/Disposable Sweat-Based Glucose Monitoring Device with Multistage Transdermal Drug Delivery Module. *Science Advances* **2017**, *3* (3), e1601314. https://doi.org/10.1126/sciadv.1601314.

(177) Kwon, K.; Kim, J. U.; Deng, Y.; Krishnan, S. R.; Choi, J.; Jang, H.; Lee, K.; Su, C.-J.; Yoo, I.; Wu, Y.; Lipschultz, L.; Kim, J.-H.; Chung, T. S.; Wu, D.; Park, Y.; Kim, T.; Ghaffari, R.; Lee, S.; Huang, Y.; Rogers, J. A. An On-Skin Platform for Wireless Monitoring of Flow Rate, Cumulative Loss and Temperature of Sweat in Real Time.

Nature Electronics **2021**, *4* (4), 302–312. https://doi.org/10.1038/s41928-021-00556-2.

(178) Sonner, Z.; Wilder, E.; Gaillard, T.; Kasting, G.; Heikenfeld, J. Integrated Sudomotor Axon Reflex Sweat Stimulation for Continuous Sweat Analyte Analysis with Individuals at Rest. *Lab on a Chip* **2017**, *17* (15), 2550–2560. https://doi.org/10.1039/C7LC00364A.

(179) Simmers, P.; Li, S. K.; Kasting, G.; Heikenfeld, J. Prolonged and Localized Sweat Stimulation by Iontophoretic Delivery of the Slowly-Metabolized Cholinergic Agent Carbachol. *Journal of Dermatological Science* **2018**, *89* (1), 40–51. https://doi.org/10.1016/j.jdermsci.2017.10.013.

(180) Yu, Y.; Nassar, J.; Xu, C.; Min, J.; Yang, Y.; Dai, A.; Doshi, R.; Huang, A.; Song, Y.; Gehlhar, R.; Ames, A. D.; Gao, W. Biofuel-Powered Soft Electronic Skin with Multiplexed and Wireless Sensing for Human-Machine Interfaces. *Science Robotics* **2020**, *5* (41), eaaz7946. https://doi.org/10.1126/scirobotics.aaz7946.

(181) Song, Y.; Min, J.; Yu, Y.; Wang, H.; Yang, Y.; Zhang, H.; Gao, W. Wireless Battery-Free Wearable Sweat Sensor Powered by Human Motion. *Science Advances* **2020**, *6* (40), eaay9842. https://doi.org/10.1126/sciadv.aay9842.

(182) Yin, L.; Moon, J.-M.; Sempionatto, J. R.; Lin, M.; Cao, M.; Trifonov, A.; Zhang, F.; Lou, Z.; Jeong, J.-M.; Lee, S.-J.; Xu, S.; Wang, J. A Passive Perspiration Biofuel Cell: High Energy Return on Investment. *Joule* **2021**, *5* (7), 1888–1904. https://doi.org/10.1016/j.joule.2021.06.004.

(183) Yin, L.; Kim, K. N.; Lv, J.; Tehrani, F.; Lin, M.; Lin, Z.; Moon, J.-M.; Ma, J.; Yu, J.; Xu, S.; Wang, J. A Self-Sustainable Wearable Multi-Modular E-Textile Bioenergy Microgrid System. *Nature Communications* **2021**, *12* (1), 1542. https://doi.org/10.1038/s41467-021-21701-7.

(184) Xu, F.; Dong, S.; Liu, G.; Pan, C.; Guo, Z. H.; Guo, W.; Li, L.; Liu, Y.; Zhang, C.; Pu, X.; Wang, Z. L. Scalable Fabrication of Stretchable and Washable Textile Triboelectric Nanogenerators as Constant Power Sources for Wearable Electronics. *Nano Energy* **2021**, *88*, 106247. https://doi.org/10.1016/j.nanoen.2021.106247.

(185) Meng, K.; Zhao, S.; Zhou, Y.; Wu, Y.; Zhang, S.; He, Q.; Wang, X.; Zhou, Z.; Fan, W.; Tan, X.; Yang, J.; Chen, J. A Wireless Textile-Based Sensor System for Self-Powered Personalized Health Care. *Matter* **2020**, *2* (4), 896–907. https://doi.org/10.1016/j.matt.2019.12.025.

(186) Polyzoidis, C.; Rogdakis, K.; Kymakis, E. Indoor Perovskite Photovoltaics for the Internet of Things—Challenges and Opportunities toward Market Uptake. *Advanced Energy Materials* **2021**, *11* (38), 2101854. https://doi.org/10.1002/aenm.202101854.

(187) Mathews, I.; King, P. J.; Stafford, F.; Frizzell, R. Performance of III–V Solar Cells as Indoor Light Energy Harvesters. *IEEE Journal of Photovoltaics* **2016**, *6* (1), 230–235. https://doi.org/10.1109/JPHOTOV.2015.2487825.

(188) Espinosa, N.; Hösel, M.; Angmo, D.; Krebs, F. C. Solar Cells with One-Day Energy Payback for the Factories of the Future. *Energy & Environmental Science* **2012**, *5* (1), 5117–5132. https://doi.org/10.1039/C1EE02728J.

(189) Roy, P.; Kumar Sinha, N.; Tiwari, S.; Khare, A. A Review on Perovskite Solar Cells: Evolution of Architecture, Fabrication Techniques, Commercialization Issues

and Status. *Solar Energy* **2020**, *198*, 665–688. https://doi.org/10.1016/j.solener.2020.01.080.

(190) Gao, F.; Zhao, Y.; Zhang, X.; You, J. Recent Progresses on Defect Passivation toward Efficient Perovskite Solar Cells. *Advanced Energy Materials* **2020**, *10* (13), 1902650. https://doi.org/10.1002/aenm.201902650.

(191) Green, M. A.; Dunlop, E. D.; Hohl-Ebinger, J.; Yoshita, M.; Kopidakis, N.; Hao, X. Solar Cell Efficiency Tables (Version 58). *Progress in Photovoltaics: Research and Applications* **2021**, *29* (7), 657–667. https://doi.org/10.1002/pip.3444.

(192) Zheng, H.; Li, D.; Ran, C.; Zhong, Q.; Song, L.; Chen, Y.; Müller-Buschbaum, P.; Huang, W. Emerging Organic/Hybrid Photovoltaic Cells for Indoor Applications: Recent Advances and Perspectives. *Solar RRL* **2021**, *5* (7), 2100042. https://doi.org/10.1002/solr.202100042.

(193) Mallick, A.; Visoly-Fisher, I. Pb in Halide Perovskites for Photovoltaics: Reasons for Optimism. *Materials Advances* **2021**, *2* (19), 6125–6135. https://doi.org/10.1039/D1MA00355K.

(194) Hamann, D.; Thyssen, J. P.; Hamann, C. R.; Hamann, C.; Menné, T.; Johansen, J. D.; Spiewak, R.; Maibach, H.; Lundgren, L.; Lidén, C. Jewellery: Alloy Composition and Release of Nickel, Cobalt and Lead Assessed with the EU Synthetic Sweat Method: THE COMPOSITION OF EARRINGS. *Contact Dermatitis* **2015**, *73* (4), 231–238. https://doi.org/10.1111/cod.12434.

(195) World Health Organization. Regional Office for Europe. (2000). Air Quality Guidelines for Europe, 2nd Ed.. World Health Organization. Regional Office for Europe. Https://Apps.Who.Int/Iris/Handle/10665/107335.

(196) Hailegnaw, B.; Adam, G.; Heilbrunner, H.; Apaydin, D. H.; Ulbricht, C.; Sariciftci, N. S.; Scharber, M. C. Inverted (p–i–n) Perovskite Solar Cells Using a Low Temperature Processed TiO_x Interlayer. *RSC Advances* **2018**, *8* (44), 24836–24846. https://doi.org/10.1039/C8RA03993C.

(197) Venkateswararao, A.; Ho, J. K. W.; So, S. K.; Liu, S.-W.; Wong, K.-T. Device Characteristics and Material Developments of Indoor Photovoltaic Devices. *Materials Science and Engineering: R: Reports* **2020**, *139*, 100517. https://doi.org/10.1016/j.mser.2019.100517.

(198) Steim, R.; Ameri, T.; Schilinsky, P.; Waldauf, C.; Dennler, G.; Scharber, M.; Brabec, C. J. Organic Photovoltaics for Low Light Applications. *Solar Energy Materials and Solar Cells* **2011**, *95* (12), 3256–3261. https://doi.org/10.1016/j.solmat.2011.07.011.

(199) Ho, J. K. W.; Yin, H.; So, S. K. From 33% to 57% – an Elevated Potential of Efficiency Limit for Indoor Photovoltaics. *Journal of Materials Chemistry A* **2020**, *8* (4), 1717–1723. https://doi.org/10.1039/C9TA11894B.

(200) Muhammad, B. T.; Kar, S.; Stephen, M.; Leong, W. L. Halide Perovskite-Based Indoor Photovoltaics: Recent Development and Challenges. *Materials Today Energy* **2022**, *23*, 100907. https://doi.org/10.1016/j.mtener.2021.100907.

(201) Yin, H.; Ho, J. K. W.; Cheung, S. H.; Yan, R. J.; Chiu, K. L.; Hao, X.; So, S. K. Designing a Ternary Photovoltaic Cell for Indoor Light Harvesting with a Power Conversion Efficiency Exceeding 20%. *Journal of Materials Chemistry A* **2018**, *6* (18), 8579–8585. https://doi.org/10.1039/C8TA01728J.

(202) Runa, A.; Feng, S.; Wen, G.; Feng, F.; Wang, J.; Liu, L.; Su, P.; Yang, H.; Fu, W. Highly Reproducible Perovskite Solar Cells Based on Solution Coating from Mixed Solvents. *Journal of Materials Science* **2018**, *53* (5), 3590–3602. https://doi.org/10.1007/s10853-017-1842-7.

(203) Foti, M.; Tringali, C.; Battaglia, A.; Sparta, N.; Lombardo, S.; Gerardi, C. Efficient Flexible Thin Film Silicon Module on Plastics for Indoor Energy Harvesting. *Solar Energy Materials and Solar Cells* **2014**, *130*, 490–494. https://doi.org/10.1016/j.solmat.2014.07.048.

(204) Freitag, M.; Teuscher, J.; Saygili, Y.; Zhang, X.; Giordano, F.; Liska, P.; Hua, J.; Zakeeruddin, S. M.; Moser, J.-E.; Grätzel, M.; Hagfeldt, A. Dye-Sensitized Solar Cells for Efficient Power Generation under Ambient Lighting. *Nature Photon* **2017**, *11* (6), 372–378. https://doi.org/10.1038/nphoton.2017.60.

(205) Sacco, A.; Rolle, L.; Scaltrito, L.; Tresso, E.; Pirri, C. F. Characterization of Photovoltaic Modules for Low-Power Indoor Application. *Applied Energy* **2013**, *102*, 1295–1302. https://doi.org/10.1016/j.apenergy.2012.07.001.

(206) Ylikunnari, M.; Välimäki, M.; Väisänen, K.-L.; Kraft, T. M.; Sliz, R.; Corso, G.; Po, R.; Barbieri, R.; Carbonera, C.; Gorni, G.; Vilkman, M. Flexible OPV Modules for Highly Efficient Indoor Applications. *Flexible and Printed Electronics* **2020**, *5* (1), 014008. https://doi.org/10.1088/2058-8585/ab6e73.

(207) Castro-Hermosa, S.; Lucarelli, G.; Top, M.; Fahland, M.; Fahlteich, J.; Brown, T. M. Perovskite Photovoltaics on Roll-To-Roll Coated Ultra-Thin Glass as Flexible High-Efficiency Indoor Power Generators. *Cell Reports Physical Science* **2020**, *1* (5), 100045. https://doi.org/10.1016/j.xcrp.2020.100045.

(208) Kim, S.; Oh, H.; Kang, G.; Han, I. K.; Jeong, I.; Park, M. High-Power and Flexible Indoor Solar Cells via Controlled Growth of Perovskite Using a Greener Antisolvent. *ACS Applied Energy Materials* **2020**, *3* (7), 6995–7003. https://doi.org/10.1021/acsaem.0c00997.

(209) Dagar, J.; Castro-Hermosa, S.; Gasbarri, M.; Palma, A. L.; Cina, L.; Matteocci, F.; Calabrò, E.; Di Carlo, A.; Brown, T. M. Efficient Fully Laser-Patterned Flexible Perovskite Modules and Solar Cells Based on Low-Temperature Solution-Processed SnO2/Mesoporous-TiO2 Electron Transport Layers. *Nano Research* **2018**, *11* (5), 2669–2681. https://doi.org/10.1007/s12274-017-1896-5.

(210) Steiger, C.; Abramson, A.; Nadeau, P.; Chandrakasan, A. P.; Langer, R.; Traverso, G. Ingestible Electronics for Diagnostics and Therapy. *Nature Reviews Materials* **2019**, *4* (2), 83–98. https://doi.org/10.1038/s41578-018-0070-3.

(211) Kalantar-Zadeh, K.; Ha, N.; Ou, J. Z.; Berean, K. J. Ingestible Sensors. *ACS Sensors* **2017**, *2* (4), 468–483. https://doi.org/10.1021/acssensors.7b00045.

(212) Smith, P. A. The Tantalizing Links between Gut Microbes and the Brain. *Nature* **2015**, *526* (7573), 312–314. https://doi.org/10.1038/526312a.

(213) Yano, J. M.; Yu, K.; Donaldson, G. P.; Shastri, G. G.; Ann, P.; Ma, L.; Nagler, C. R.; Ismagilov, R. F.; Mazmanian, S. K.; Hsiao, E. Y. Indigenous Bacteria from the Gut Microbiota Regulate Host Serotonin Biosynthesis. *Cell* **2015**, *161* (2), 264–276. https://doi.org/10.1016/j.cell.2015.02.047.

(214) Rea, K.; Dinan, T. G.; Cryan, J. F. The Microbiome: A Key Regulator of Stress and Neuroinflammation. *Neurobiology of Stress* **2016**, *4*, 23–33. https://doi.org/10.1016/j.ynstr.2016.03.001.
(215) Bhattacharyya, A.; Chattopadhyay, R.; Mitra, S.; Crowe, S. E. Oxidative Stress: An Essential Factor in the Pathogenesis of Gastrointestinal Mucosal Diseases. *Physiological Reviews* **2014**, *94* (2), 329–354. https://doi.org/10.1152/physrev.00040.2012.
(216) Vernia, P.; Caprilli, R.; Latella, G.; Barbetti, F.; Magliocca, F. M.; Cittadini, M. Fecal Lactate and Ulcerative Colitis. *Gastroenterology* **1988**, *95* (6), 1564–1568. https://doi.org/10.1016/S0016-5085(88)80078-7.
(217) Venton, B. J.; Cao, Q. Fundamentals of Fast-Scan Cyclic Voltammetry for Dopamine Detection. *Analyst* **2020**, *145* (4), 1158–1168. https://doi.org/10.1039/C9AN01586H.
(218) Brodkorb, A.; Egger, L.; Alminger, M.; Alvito, P.; Assunção, R.; Ballance, S.; Bohn, T.; Bourlieu-Lacanal, C.; Boutrou, R.; Carrière, F.; Clemente, A.; Corredig, M.; Dupont, D.; Dufour, C.; Edwards, C.; Golding, M.; Karakaya, S.; Kirkhus, B.; Le Feunteun, S.; Lesmes, U.; Macierzanka, A.; Mackie, A. R.; Martins, C.; Marze, S.; McClements, D. J.; Ménard, O.; Minekus, M.; Portmann, R.; Santos, C. N.; Souchon, I.; Singh, R. P.; Vegarud, G. E.; Wickham, M. S. J.; Weitschies, W.; Recio, I. INFOGEST Static in Vitro Simulation of Gastrointestinal Food Digestion. *Nat Protoc* **2019**, *14* (4), 991–1014. https://doi.org/10.1038/s41596-018-0119-1.